Universität Zürich[UZH]

Physik-Institut

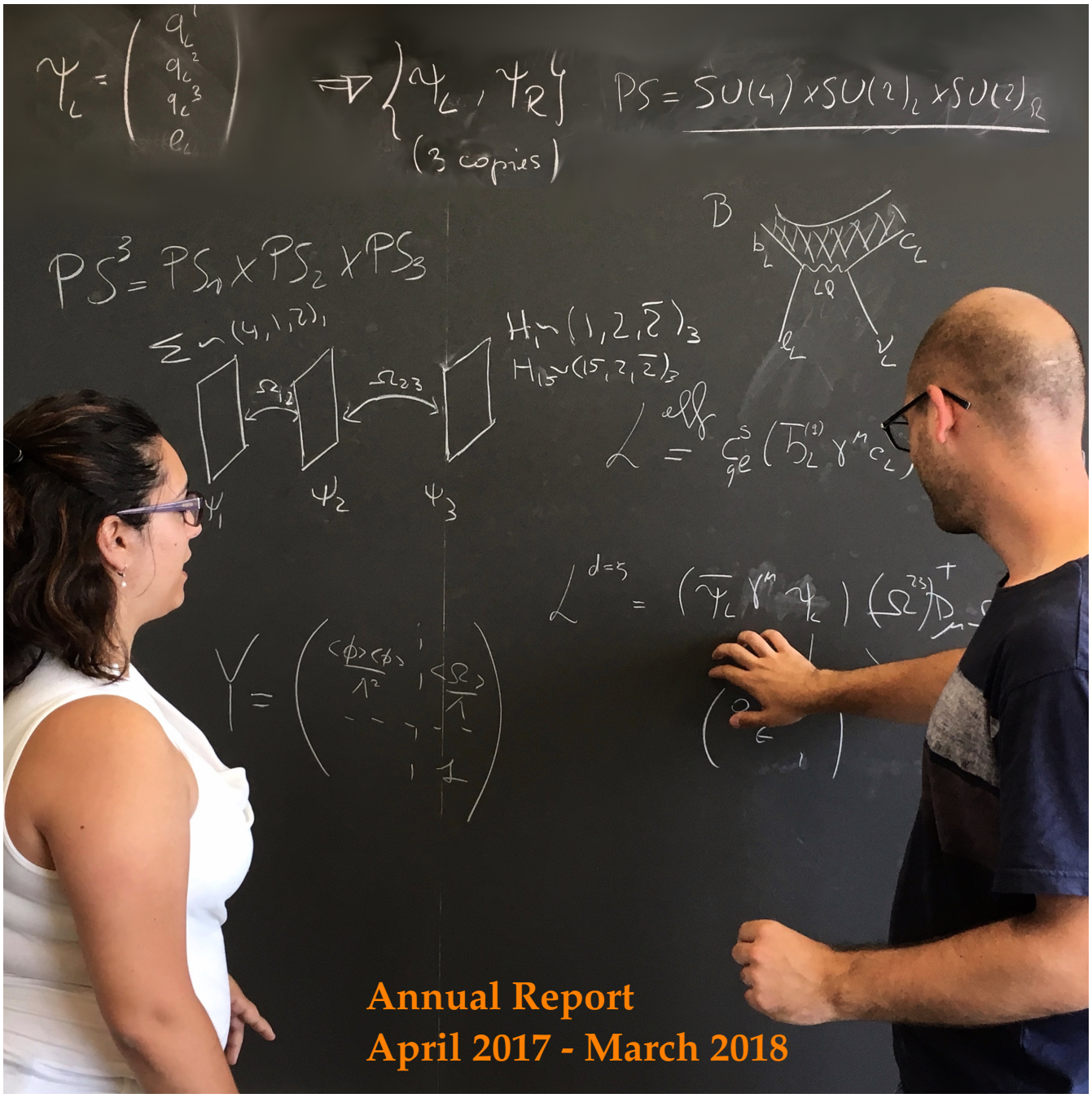

Universität Zürich[UZH]

Physik-Institut

Annual Report
April 2017 - March 2018

Winterthurerstrasse 190, CH-8057 Zürich/Schweiz

Front picture: Members of Isidori's group discussing extensions of the Standard Model motivated by recent results in flavour physics (Sec. 2).

Picture on the back: Sketch of a new algorithm for the calculation of scattering amplitudes in quantum-field theory (Sec. 2).

Secretariat	044 635 5721	sekretariat@physik.uzh.ch
Prof. C. Aegerter	044 635 5813	christof.aegerer@physik.uzh.ch
Prof. L. Baudis	044 635 5777	laura.baudis@physik.uzh.ch
Prof. F. Canelli	044 635 5784	florencia.canelli@physik.uzh.ch
Prof. J. Chang	044 635 5748	johan.chang@physik.uzh.ch
Prof. T. Gehrmann	044 635 5818	thomas.gehrmann@physik.uzh.ch
Prof. M. Gibert	044 635 5753	gibert@physik.uzh.ch
Prof. M. Grazzini	044 635 5806	grazzini@physik.uzh.ch
Prof. M. Greber	044 635 5744	greber@physik.uzh.ch
Prof. G. Isidori	044 635 5751	gino.isidori@physik.uzh.ch
Prof. P. Jetzer	044 635 5819	jetzer@physik.uzh.ch
Prof. B. Kilminster	044 635 5802	ben.kilminster@physik.uzh.ch
Prof. T. Neupert	044 635 4800	titus.neupert@physik.uzh.ch
Prof. J. Osterwalder	044 635 5827	osterwal@physik.uzh.ch
Prof. S. Pozzorini	044 635 6014	pozzorin@physik.uzh.ch
Prof. P. Saha	044 635 6194	psaha@physik.uzh.ch
Prof. A. Schilling	044 635 5791	schilling@physik.uzh.ch
Prof. N. Serra	044 635 5725	nicola.serra@physik.uzh.ch
Prof. A. Signer	056 310 3661	adrian.signer@psi.ch
Prof. U.D. Straumann	044 635 5768	ulrich.straumann@physik.uzh.ch

---

The annual reports are available on the internet: http://www.physik.uzh.ch/reports.shtml.

1 Preface

This annual report gives a flavor of the broad range of research activities carried out at the Department of Physics of UZH. It provides a snapshot of the current state of various longterm projects and highlights in particular the progress achieved over the last year. Presenting these results with pride, we thankfully acknowledge the continued support from the Kanton Zürich, the Swiss National Science Foundation, the European Commission, and others who have made this fundamental research possible. The experimental activities span several subfields of physics, from particle and astroparticle physics, hard and soft condensed matter physics, surface physics and nanoscience, to the physics of biological systems. Theoretical activities include precision calculations of processes in quantum chromodynamics and new theories beyond the standard model of particle physics, astrophysics and general relativity, as well as topological concepts in condensed matter physics. To further increase the diversity of research topics, which is important in particular for the students, other physics-related groups from within the Faculty of Science and beyond were affiliated to our department. This means that their research is also presented on our home page (http://www.physik.uzh.ch/en/research.html), and they can offer Bachelor or Master projects for our students.

An important asset to the research environment in our department are the excellent mechanical and electronics workshops, as well as the efficient IT and administrative support. Thanks to this strong infrastructure department, our research groups are able to make important and highly visible contributions to large international projects at CERN and LNGS.

The past year brought several prestigious new grants to the Department of Physics. Laura Baudis started her ERC Advanced Grant, Titus Neupert received an ERC Starting Grant, adding to the already running Starting Grants of Johan Chang and Nicola Serra and the Consolidator Grant of Stefano Pozzorini. Marta Gibert joined the department in February of this year with her SNF Professorship, setting up a Laboratory for the controlled layer-by-layer growth of transition metal oxides and for studying the physical properties of perovskite heterostructures. In addition, the department will soon host three (!) more SNF Professorships that were awarded in March 2018 and who will start in the course of this year. Finally, Nicola Serra was elected as Physics Coordinator for the MegaScience-Project at the Moscow University for Science and Technology MISis. All these grants bring additional people to the department, which continues to grow. At the end of 2017, there were a total of 163 employees from 32 different countries, distributed over 18 research groups and general services. There is a continuous coming and going of people, with 52 newcomers and 42 departures over the last year. Laboratory and office space is limited, which means that people have to move closer together, and groups have to start sharing offices. The arrival of new SNF professors will help to attract more physics students, in particular in our Master programs, by increasing the diversity of research projects and special lectures.

Student numbers in the physics major Bachelor program have reached a record high, with 68 new students entering the first semester in fall 2017. This is likely a consequence of the excellent outreach efforts over the last several years carried out by many members of the department. Likewise, student numbers in the basic physics lectures that we teach to students from other departments of our faculty and from the Faculty of Medicine, continue to grow. This means that several professors and many PhD students are busy teaching to non-physics majors. In fact, many Master and Bachelor students had to be recruited as tutors for teaching exercise classes for these students.

On November 24, the Department of Physics organized an Alumni Day, with lab tours and poster presentations by the students and postdocs. Three posters were awarded a Poster Prize. The event was very well received by everybody and attracted a good number of 40 former students, postdocs, employees or professors. It will be repeated in similar form, fostering networking and nostalgia. As an immediate outcome, it resulted in the introduction of the new Dectris Prize for excellent Master theses, donated yearly by the company of the same name.

For the first time since the department moved to the Irchel Campus in 1993, the building received a 'face-lift', with walls getting painted, screens being installed for general information and for poster presentations, blackboard walls for informal hallway discussions, new poster frames, and many intermediate and full-size pictures illustrating science in a colorful and artistic way.

The following page will honor Hans-Werner Fink's contributions to the research and teaching at the Department of Physics. He has retired in February of this year. An obituary for Ralph Pixley follows, who has had a significant impact on the department's research and in particular the teaching for half a century.

Zürich, May 2018

Prof. Dr. Jürg Osterwalder

Retirement Prof. Hans-Werner Fink

Hans-Werner Fink was born in 1952 in Salzgitter-Bad, Niedersachsen. He studied physics, mathematics and chemistry at the Technical University of Clausthal where he obtained his diploma in physics in 1979. His thesis was awarded with the E.W. Mueller "Outstanding Young Scientist Award" for the studies on long range interaction between adatom pairs. Three years later Hans-Werner got his PhD from the Technical University of Munich for his studies of the "Atomistics of Monolayer Formation" that he performed in the group of Gert Ehrlich at the University of Illinois at Urbana-Champaign. His engagement concerning the understanding of the interaction of individual atoms on metal surfaces represents an important contribution to the foundation of the field of physics on the nanometer scale. In fact, Hans-Werner was awarded with the Max Auwärter price in 1983 for the discovery of non-pair wise trio interaction.

In 1984 Hans-Werner joined the IBM Zurich Research Laboratory in Rüschlikon – just at the times of the upgrowth of the nobel years. Here he started to develop the Low Energy Electron Point Source (LEEPS) microscope - a novel type of electron microscope based on the principle of inline holography. In the course of these activities he received the IBM Outstanding Innovation Award for the invention of a coherent electron source.

Of great impact certainly was also his work concerning DNA molecules, that Hans-Werner carried out in the later nineteen nineties, when he was a visiting professor at the Physics Institute of the University of Basel. Applying the LEEPS microscope to measure the conductivity of free-standing DNA ropes not only provided insight into a pivotal and highly debated question in life science but also demonstrated the versatility of his new instrument.

In September 1999 Hans-Werner became a professor here at the Physics Institute of the University of Zurich where he eventually moved into newly built and specifically designed laboratory premises to establish a new branch of research involving the novel LEEPS technology. Along the lines of his research he introduced the lecture "Physik auf der Nanometerskala" and made it an inherent part of the lecture calendar.

Over the past two decades he persistently advanced his research with a small team of coworkers making fundamental contributions to the field of coherent optics concerning all, experimental, theoretical as well as computational aspects. Owing to his analytic expertise, intuition and ingenuity Hans-Werner successfully refined the LEEPS technology to become a unique tool for structural analysis of individual proteins. Still, his activities have always been accompanied by little divergent and playful projects.

As a subtle experimentalist he still spends a lot of time in the laboratory to further research with his agile and vigilant spirit. It is hence no surprise that he is going to proceed in a non-strictly academic environment to enhance the LEEPS technology for the purpose of routine pharmaceutical analysis and the in-situ study of chemical bonding among individual ligands.

We thank him for all his valuable achievements and wish him all the best for his plentiful future plans!

Ralph Edward Pixley

September 14, 1929 (Centralia, IL, USA) – March 15, 2018 (Zumikon, CH)

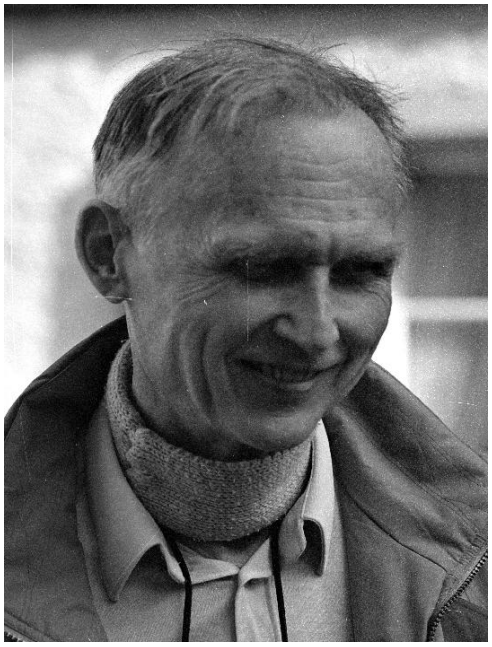

Ralph Edward Pixley studied physics at Drake University, Iowa and obtained his PhD under the supervision of W. Whaling at Caltech. Already during his time as a PhD student, he achieved an important experimental success with the discovery of a new excitation state in the Carbon-12 nucleus at 7.68 MeV which is of central importance to the processes of stellar nucleosynthesis.

As a PostDoc Pixley worked in the Plasma Laboratory in Livermore, at the Brookhaven National Laboratory, at ETH Zurich and at the Centre de Recherche Nucleaire in Strassbourg. In 1963 he joined our department as an "Oberassistent". He lead a group of PhD students, working on the 6 MeV Van de Graaf accelerator. Hans Staub, director of the departement at that time, wrote ".. and he has greatly contributed particularly on the experimental side to our nuclear physics research ... and his experimental and technical abilities are very valuable to us".

Already at that time he was in charge of the advance laboratory course in physics (VP). Staub commented this in his letter ".. developed new experiments .. he is very well liked by the students, particularly since he devotes a lot of time to discussions with them..". The students of that generation indeed remember Pix, as we called him, as our most important contact person for physics, who explained us quantum mechanics, experimental methods and - may be most importantly - statistical analysis and uncertainty calculation methods. He was extremely supportive and patient, but often he concluded at the right moment in "try to find out yourself how it works," an attitutde, which was of invaluable importance for our physics education.

1967 Ralph Pixley was appointed assistent professor at the Stanford University, where he however stayed only for three years. For personal reasons he wished to come back to Switzerland, where he was very welcome at our institute again in 1970.

In the 1980 Ralph Pixley started to contribute significantly to our experiment which measured an upper limit of the neutrino mass by determining the endpoint energy of the tritium decay spectrum. The result of that experiment was for several years very well known as the Zurich neutrino mass, the worlds best mass limit at that time.

After his retirement in 1994 a new endeavour began in our institute, the Zurich Gravitational Constant G measurement. Two 1.1 kg test masses were alternately weighed with a precision balance in the presence of two moveable field masses consisting of liquid mercury, each with mass of 7.5 tons, installed in a quiet place at the Paul-Scherrer-Institut. Ralph Pixley devoted all his energy, great experience and wisdom to the final analysis of the data. In 2006 the final result was published and is now known as the Zurich G value, which is one of the three most precise G measurements existing today.

Ralph's ingenious experimental skills were complemented with his unpretentious appearance and very empathic character. Not many of us knew that he was also a gifted player of the classical guitarre, but once in 1990 he gave in the institute a very nice concert for two guitarrs together with one of the PhD students and he entertained the institute's christmas party with his beautiful music.

Personnel

Scientific personnel

Thea Klæboe	Årrestad	Sec. 9
Mirco	Ackermann	Sec. 14
Prof. Dr. Christof	Aegerter	Sec. 14
Dr. Chanpreet	Amole	Sec. 5
Michele	Atzeni	Sec. 8
Dr. Michael	Baker	Sec. 2
Prof. Laura	Baudis	Sec. 4, 5
Carlo	Bernard	Sec. 13
Dr. Roland	Bernet	Sec. 8
Dr. Christopher	Betancourt	Sec 8, 7
Iaroslava	Bezshyiko	Sec 8, 7
Yanina	Biondi	Sec. 5
Marzia	Bordone	Sec. 2
Yannik	Bötzel	Sec. 3
Adam	Brown	Sec. 5
Ruth	Bründler Denzer	Lab courses
Danyyl	Brzhechko	Sec. 9
Federico	Buccioni	Sec 2
Dr. Annarita	Buonaura	Sec 8, 7
Luca	Buonocore	Sec 2
Dr. Dario	Buttazzo	Sec 2
Dr. Lea	Caminada	Sec. 9
Prof. Florencia	Canelli	Sec. 6, 9
Chiara	Capelli	Sec. 5
Dr. Luca	Castiglioni	Sec. 13
Prof. Johan	Chang	Sec. 11
Dr. Xuan	Chen	Sec 2
Dr. Jaewon	Choi	Sec. 11
Kenny	Choo	Sec. 10
Dr. Marcin	Chrząszcz	Sec. 8
Dr. Leandro	Cieri	Sec 2
Dr. Ashley	Cook	Sec 10
Claudia	Cornella	Sec 2
Paule	Dagenais	Sec 14
Dr. Annapaola	de Cosa	Sec. 9
Riccardo	del Burgo	Sec. 9
Philippe	Denzel	Sec. 3
Daniel	Destraz	Sec. 11
Simone	Devoto	Sec. 11
Silvio	Donato	Sec. 9
David	Dreher	Sec. 14
Adrian	Epprecht	Sec. 13
Dr. Conrad	Escher	
Jonas	Eschle	Sec. 8
Prof. Hans-Werner	Fink	
Dr. Javier	Fuentes Martin	Sec 2
Dr. Arno	Gadola	Sec. 6
Camilla	Galloni	Sec. 9
Dr. Michelle	Galloway	Sec. 5
Dr. Julian	Garcia Pardinas	Sec. 8
Alsu	Gazizulina	Sec. 12
Prof. Thomas	Gehrmann	Sec. 2
Prof. Marta	Gibert Gutierrez	
Frédéric	Girard	Sec. 5
Lisa	Grad	Sec. 13
Elena	Graverini	Sec. 7, 8
Prof. Dr. Massimiliano	Grazzini	Sec. 2
Prof. Thomas	Greber	Sec. 13
Dr. Nicolas	Greiner	Sec. 2
Dr. Admir	Greljo	Sec. 2
Dr. Maria	Haney	Sec. 3
Dr. Adrian	Hemmi	Sec. 13
Dr. Matthias	Hengsberger	Sec. 13
Dr. Roman	Hiller	Sec. 4
Marius	Höfer	Sec. 2
Masafumi	Horio	Sec. 11
Michael	Hotz	Sec. 13
Dr. Tomas	Hreus	Sec. 9
Shang-Xiong	Huang-fu	Sec. 12
Daniel	Hulme	Sec. 2
Agnieszka	Ilnicka	Sec. 2
Dr. Wakiko	Ishibashi	Sec. 3
Prof. Gino	Isidori	Sec. 2
Oleh	Ivashko	Sec. 11
Prof. Philippe	Jetzer	Sec. 3
Dr. Tomas	Ježo	Sec. 2
Dominik	Kara	Sec. 2
Dr. Alexander	Karlberg	Sec. 2
Prof. Benjamin	Kilminster	Sec. 9
Dr. Alexander	Kish	Sec. 4, 5
Pavlo	Kliuiev	Sec. 13
Matthias	König	Sec. 2
Aram	Kostanyan	Sec. 13
Kevin	Kramer	Sec. 11
Rafael	Küng	Sec. 3
Davide	Lancierini	Sec. 8
Flavio	Lanfranconi	Sec. 14
Jean-Nicolas	Lang	Sec. 2
Dr. Andrey	Lebedev	Sec. 2
Dr. Stefanos	Leontsinis	Sec. 9
Federica	Lionetto	Sec. 8
Marianna	Lorenzo	
Archana	Mallavalli	Sec. 14
Dr. David	Marzocca	Sec. 2
Dr. Christian	Matt	Sec. 11
Andrea	Mauri	Sec. 8

Dr. Javier	Mazzitelli	Sec. 2
Vinicius	Mikuni	Sec. 9
Michael	Miloradovic	Sec. 5
Rizalina	Mingazheva	Sec. 5
Jonathan	Mo	Sec. 2
Dr. Claude	Monney	Sec. 13
Dr. Katharina	Müller	Sec. 8
Prof. Titus	Neupert	Sec. 10
Izaak	Neutelings	Sec. 9
Jan	Niehues	Sec. 2
Dr. Zbynek	Novotny	Sec. 13
Seulghi	Ok	Sec. 10
Prof. Jürg	Osterwalder	Sec. 13
Dr. Patrick	Owen	Sec. 8
Julie Charlotte	Pages	Sec. 2
Andrea	Pattori	Sec. 2
Lionel	Philippoz	Sec. 3
Francesco	Piastra	Sec. 5
Deborah	Pinna	Sec. 9
Prof. Stefano	Pozzorini	Sec. 2
Amedo	Primo	Sec. 2
Dr. Albert	Puig Navarro	Sec. 8
Sahil	Puri	Sec. 14
Chloe	Ransom	Sec. 4
Giorgia	Rauco	Sec. 9
Dr. Shayne	Reichard	Sec. 5
Dr. Peter	Robmann	Sec. 9
Prof. Dr. Prasenjit	Saha	Sec. 3
Daniel	Salerno	Sec. 9
Dr. Particia	Sanchez Lucas	Sec. 5
Hayk	Sargsyan	Sec. 2
Andreas	Schärer	Sec. 3
Dr. Lukas	Schertel	Sec. 14
Prof. Andreas	Schilling	Sec. 12
Frank	Schindler	Sec. 10
Dr. Jale	Schneider	Sec. 14
Dr. Marek	Schönherr	Sec. 2
Adrian	Schuler	Sec. 13
Korbinian	Schweiger	Sec. 9
Dr. Claudia	Seitz	Sec. 9
Dr. Lara	Selvaggi	Sec. 14
Prof. Nicola	Serra	Sec. 7, 8
Dr. Andrey	Sidorenko	Sec. 11
Prof. Adrian	Signer	Sec. 2
Dr. Rafael	Silva Coutinho	Sec. 8
PD Dr. Olaf	Steinkamp	Sec. 8
Dr. Barbara	Storaci	Sec. 7, 8
Prof. Ulrich	Straumann	Sec. 6, 8
Denys	Sutter	Sec. 11
Dr. Yuta	Takahashi	Sec. 9
Lakshmi Das	Thazhe Veettil	Sec. 11
Kevin	Thieme	Sec. 5
Sokratis	Trifinopoulos	Sec. 2
Dr. Severine	Urdy	Sec. 14
Dr. Denys	van Dyk	Sec. 2
Dr. Achim	Vollhardt	Sec. 6, 8, 16
Kay	Waltar	Sec. 13
Dr. Qiang	Wang	Sec. 12
Zhenzi	Wang	Sec. 8
Wei	Wang	Sec. 12
Dr. Yuehuan	Wei	Sec. 5
Andreas	Weiden	Sec. 8
Julien	Wulf	Sec. 5
Jeong Yeon	Yook	Sec. 2
Wolf-Dietrich	Zabka	Sec. 13
Xiaofu	Zhang	Sec. 12
Hantian	Zhang	Sec. 2
Max	Zoller	Sec. 2
Dr. Alberto	Zucchetta	Sec. 9

Technical and adminstrative personnel

Dr. Carlos	Abellan Beteta	Sec. 8
Chris	Albrecht	Sec. 15
Dr. Angela	Benelli	Administration
Tiziano	Crudeli	Technical support
Patrick	Donà	Sec. 13
Daniel	Florin	Sec. 16, 6
Brigitte	Freund	Secretariat
Carmelina	Genovese	Secretariat
Lars	Iven	Sec. 5
Andreas	James	Sec. 4,5
Thomas	Kälin	Sec. 13
Simon	Karrer	Sec. 16
Gian	Knüsel	Sec. 15
Paul	Käser	Computing
Bruno	Lussi	Sec. 15
Reto	Maier	Sec. 15
Brandon	Markwalder	Sec. 15
Afrim	Murtezani	Sec. 6
Lucien	Pauli	Lecture demonstrations
Jan Ten	Pierick	Sec. 3
Dominik	Rechsteiner	Sec. 11
Noah	Regensburger	Sec. 15
Monika	Röllin	Secretariat
Gabi	Savill	Administration
Marcel	Schaffner	Sec. 15
Silvio	Scherr	Sec. 15
Regina	Schmid	Secretariat
Karen	Schraader Frigg	Administration
Stefan	Siegrist	Sec. 12
Stefan	Steiner	Sec. 6, 8
Marc	Türler	Administration
Pascal	Weyeneth	Sec. 15
David	Wolf	Sec. 16

Contents

2 Theory of Elementary Particles

M. Baker, M. Bordone, F. Buccioni, L. Buonocore, D. Buttazzo, X. Chen, L. Cieri, C. Cornella, S. Devoto, J. Fuentes-Martin, T. Gehrmann, M. Grazzini, N. Greiner, A. Greljio, M. Höfer, D. Hulme, A. Ilnicka, T. Jezo, D. Kara, A. Karlberg, M. König, G. Isidori, J.N. Lang, J. Mazzitelli, J. Mo, D. Müller, J. Niehues, A. Pattori, S. Pozzorini, A. Primo, H. Sargsyan, A. Signer, M. Schönherr, S. Trifinopoulos, Y. Ulrich, D. van Dyk, J.Y. Yook, H. Zhang, M. Zoller

in collaboration with:
University of Belo Horizonte, CERN, IMSc Chennai, University of Coimbra, TU Dresden, Durham University, University of Edinburgh, INFN and University of Firenze, Freiburg University, University of Granada, Lisbon University, University of Lyon, Stephan Insistue Ljubljana, Mainz University, Michigan State University, University of Milano Bicocca, INFN and University of Milano, MPI Munich, INFN and University of Napoli, Scuola Normale Pisa, INFN and University of Padova, Peking University, University of San Martin, IFIC Valencia, ETH Zürich.

The particle theory group at the Physik-Institut works on a broad spectrum of research projects related to the interpretation of data from high energy particle colliders. These cover precision calculations of benchmark observables, simulation of full collider events, identification of optimal observables for searches and measurements, physics beyond the Standard Model, as well as developments of calculational techniques. We summarize some highlights of last year's research below.

2.1 Theoretical predictions for dark-matter searches at the LHC

The signature of missing transverse energy (MET) recoiling against high-energy jets is one of the most powerful tools in the interpretation of data from hadron colliders. In the Standard Model (SM), MET+jet final states arise from the production of jets in association with electroweak bosons that decay into neutrinos in the processes $pp \to Z(\to \nu\bar{\nu}) + \text{jet}$ and $pp \to W^{\pm}(\to \ell\nu) + \text{jet}$. But MET+jet production is also an almost omnipresent feature of theories of physics beyond the SM (BSM). In particular, MET+jet events are the most powerful probes of dark matter at the LHC. The sensitivity of such searches depends in a critical way on the precision at which the SM background processes $pp \to V+\text{jet}$ with $V = W^{\pm}, Z$ can be controlled. In practice, systematic uncertainties are minimised by performing accurate measurements of $V+$jet processes in control regions dominated by visible signatures, i.e. $\gamma+$jet, $Z(\to \ell^+\ell^-)+$jet or $W(\to \ell\nu)+$jet production with a visible lepton, and extrapolating such measurements to the case of invisible $V+$jet signatures in the region of high transverse-momentum (p_{T}), where a dark-matter signal may show up. Such extrapolations are based on theoretical predictions. In particular, they require a precise theoretical understanding of the correlation between different $V+$jet processes and different p_{T} regions.

In this context, recent advances in perturbative calculations, driven by research at our institute [1–4], have opened the door to significant sensitivity improvements in dark matter searches. A combination of state-of-the-art calculations for all relevant $V+$jet processes was presented in Ref. [5]. Besides including QCD and electroweak (EW) quantum corrections at the highest available order, this study provides the first systematic methodological framework for the application of high-precision theory predictions to MET+jet searches. In particular, we have introduced and applied various new approaches to estimate uncertainties and their correlations across different processes and p_{T} regions.

The long-standing problem of how to treat the correlation of higher-order effects across different $V+$jet processes is addressed by a quantitative method that permits to split QCD effects into universal and process-dependent parts. Amongst others, this is achieved by using a dynamic definition of photons in the high-energy regime. Specifically, we have shown that isolating photons from the surrounding collinear QCD radiation by means of a dynamic cone it is possible to maximise the level of QCD correlation between $\gamma+$jet and $W/Z+$jet production, thereby minimising the uncertainties in the extrapolation from $\gamma+$jet production to dark-matter backgrounds.

Given the strong impact of EW corrections on the shapes of p_{T} distribution for the various V+jet processes and process ratios, NLO EW corrections have been sup-

plemented by the dominant Sudakov EW logarithms at NNLO [6, 7]. Moreover, in order to assess unknown higher-order effects stemming form the interplay of large QCD and EW corrections, we have introduced a dedicated method that allows one to exploit NLO EW calculations for $V + 2$ jet production [2] in order to quantify $\mathcal{O}(\alpha\alpha_S)$ corrections in terms of a simple factorised Ansatz plus extra non-factorising terms. Finally, also the uncertainties associated with parton distribution functions (PDFs) have been assessed in detail.

In Fig. 2.1 we present predictions and uncertainty estimates for the different V+jet processes and process ratios. All sources of QCD and EW uncertainties are combined in quadrature overlaying the remaining PDF uncertainAs a result of the N(N)LO QCD and nNLO EW corrections, the level of theoretical predictions in the p_T distributions for individual V+jet processes reaches the 5–10% level up to about 1 TeV and the 10–20% level up to about 2 TeV. In the process ratios theoretical uncertainties cancel to a large extent. In particular, in the Z/W ratio remaining uncertainties are at the level of only 1–2% up to 1 TeV

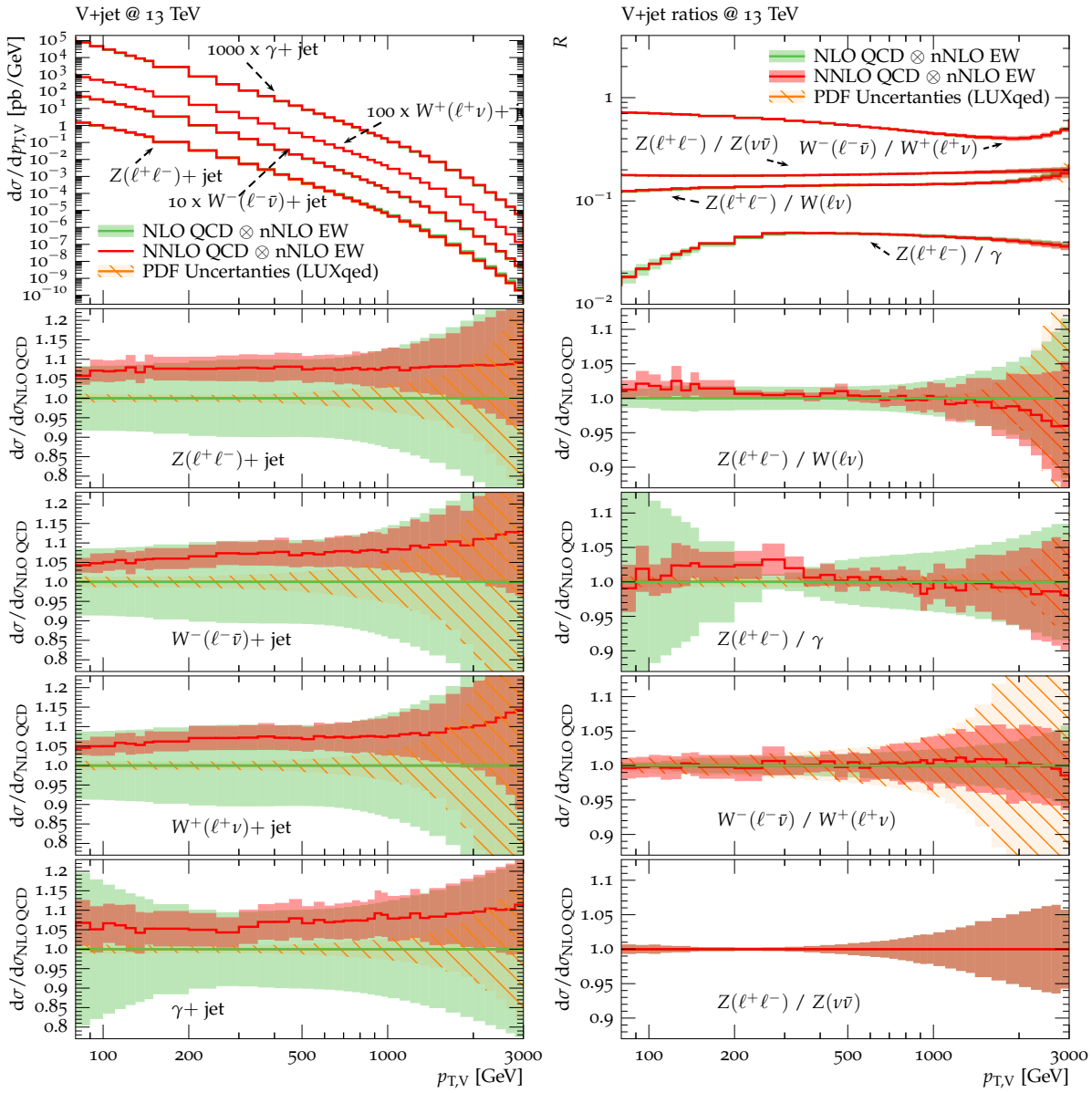

FIG. 2.1 – Theoretical predictions for $V+$jet spectra (left) and ratios (right) at 13 TeV including (N)NLO QCD and nNLO EW corrections. The lower frames show the relative impact of corrections and theory uncertainties. The green and red bands correspond to the combination of perturbative uncertainties, while PDF uncertainties are shown as hashed orange bands. See Ref. [5] for details.

and below 5% up to 2 TeV. Similarly, the Z/γ ratio is constrained at the 5% level up to 2 TeV. Noteworthy, including the NNLO QCD corrections the process ratios remain very stable and in particular within the uncertainty estimates based on NLO QCD. This reflects the fact that QCD uncertainties are very well under control: taking at face value the NNLO QCD systematics we are at the level of few percent all the way up to the multi-TeV scale, and at large p_T we are dominated by EW and PDF uncertainties. The latter are below the perturbative uncertainties in all nominal distributions and all but the W^-/W^+ ratio, where a precise measurement at high p_T could help to improve PDF fits.

Overall, it is possible to obtain precise theoretical control both for vector-boson p_T distributions, and their ratios, at the level of a few percent over a wide range of p_T. These results and the proposed methodology have already been adopted in experimental analyses by ATLAS and CMS, leading to substantial improvements in the sensitivity of dark-matter searches. The benefits of high-precision theoretical calculations are going to be further enhanced once high-luminosity LHC data become available.

[1] S. Kallweit, J. M. Lindert, P. Maierhoefer, S. Pozzorini, and M. Schoenherr, *NLO electroweak automation and precise predictions for W+multijet production at the LHC*, JHEP **04** (2015) 012, [arXiv:1412.5157].

[2] S. Kallweit, J. M. Lindert, P. Maierhofer, S. Pozzorini, and M. Schönherr, *NLO QCD+EW predictions for V + jets including off-shell vector-boson decays and multijet merging*, JHEP **04** (2016) 021, [arXiv:1511.0869].

[3] A. Gehrmann-De Ridder, T. Gehrmann, E. W. N. Glover, A. Huss, and T. A. Morgan, *Precise QCD predictions for the production of a Z boson in association with a hadronic jet*, Phys. Rev. Lett. **117** (2016), no. 2 022001, [arXiv:1507.0285].

[4] A. Gehrmann-De Ridder, T. Gehrmann, E. W. N. Glover, A. Huss, and T. A. Morgan, *The NNLO QCD corrections to Z boson production at large transverse momentum*, JHEP **07** (2016) 133, [arXiv:1605.0429].

[5] J. M. Lindert *et al.*, *Precise predictions for V + jets dark matter backgrounds*, Eur. Phys. J. **C77** (2017), no. 12 829, [arXiv:1705.0466].

[6] J. H. Kuehn, A. Kulesza, S. Pozzorini, and M. Schulze, *One-loop weak corrections to hadronic production of Z bosons at large transverse momenta*, Nucl. Phys. **B727** (2005) 368-394, [hep-ph/0507178].

[7] J. H. Kuehn, A. Kulesza, S. Pozzorini, and M. Schulze, *Electroweak corrections to hadronic production of W bosons at large transverse momenta*, Nucl. Phys. **B797** (2008) 27-77, [arXiv:0708.0476].

2.2 Higgs boson pair production at NNLO

One of the primary goals of the LHC programme in the next decades is the detailed study of Higgs boson properties. In particular, the high-luminosity upgrade of the LHC is expected to provide direct constraints on the Higgs boson trilinear coupling from Higgs boson pair production, which may reveal whether the Higgs potential is indeed Standard-Model like. A detailed theoretical understanding of the Higgs boson pair production processes is thus mandatory. The most important production channel of a pair of Higgs bosons at the LHC is $gg \to hh$, which proceeds through triangular and box diagrams, where the dominant contribution is given by the top quark. Unfortunately, only the triangles are sensitive to the Higgs trilinear coupling, and cancellations among the diagrams, together with the small available phase space, make the cross section extremely small.

The $gg \to hh$ cross section at leading order (LO) is known since quite some time. The next-to-leading-order (NLO) corrections with full top quark mass (M_t) dependence, involving two-loop diagrams with several mass scales, became available only recently [8,9]. Alternatively, to compute yet higher-order perturbative contributions, it is possible to use a Higgs Effective Field Theory approach (HEFT), in which the top quark is integrated out.

In Ref. [10] we have presented a new calculation of the double Higgs cross section at next-to-next-to-leading order (NNLO) in QCD perturbation theory. Our calculation is based on the publicly available computational framework MATRIX [11], which allows the user to perform fully differential NNLO calculations for a wide class of processes at hadron colliders. We start from the exact two-loop amplitude, which is implemented in a dedicated version of MATRIX, and we can thus reproduce the NLO result of Ref. [8,9]. In our reference calculation, denoted by $\text{FT}_{\text{approx}}$, the NNLO contributions are evaluated by using the exact one-loop amplitude for double real emission combined with the real-virtual and double-virtual contributions in the HEFT, but reweighted with the exact Born amplitudes. More precisely, each NNLO contribution is rescaled with the factor

$$\mathcal{R}(ij \to HH + X) = \frac{\mathcal{A}^{\text{Born}}_{\text{Full}}(ij \to HH + X)}{\mathcal{A}^{(0)}_{\text{HEFT}}(ij \to HH + X)}\,. \qquad (2.1)$$

This approximation, which includes the most advanced perturbative information available at present for this process, is denoted by $\text{NNLO}_{\text{FTapprox}}$, and is supposed to provide the best perturbative prediction. Another approximation, denoted by $\text{NNLO}_{\text{NLO}-\text{i}}$, can be obtained

$\sqrt{s}$	13 TeV	14 TeV	27 TeV	100 TeV
NLO [fb]	$27.78\,^{+13.8\%}_{-12.8\%}$	$32.88\,^{+13.5\%}_{-12.5\%}$	$127.7\,^{+11.5\%}_{-10.4\%}$	$1147\,^{+10.7\%}_{-9.9\%}$
$\text{NLO}_{\text{FTapprox}}$ [fb]	$28.91\,^{+15.0\%}_{-13.4\%}$	$34.25\,^{+14.7\%}_{-13.2\%}$	$134.1\,^{+12.7\%}_{-11.1\%}$	$1220\,^{+11.9\%}_{-10.6\%}$
$\text{NNLO}_{\text{NLO-i}}$ [fb]	$32.69\,^{+5.3\%}_{-7.7\%}$	$38.66\,^{+5.3\%}_{-7.7\%}$	$149.3\,^{+4.8\%}_{-6.7\%}$	$1337\,^{+4.1\%}_{-5.4\%}$
$\text{NNLO}_{\text{FTapprox}}$ [fb]	$31.05\,^{+2.2\%}_{-5.0\%}$	$36.69\,^{+2.1\%}_{-4.9\%}$	$139.9\,^{+1.3\%}_{-3.9\%}$	$1224\,^{+0.9\%}_{-3.2\%}$
M_t unc. $\text{NNLO}_{\text{FTapprox}}$	$\pm 2.6\%$	$\pm 2.7\%$	$\pm 3.4\%$	$\pm 4.6\%$
$\text{NNLO}_{\text{FTapprox}}/\text{NLO}$	1.118	1.116	1.096	1.067

TAB. 2.1 – Inclusive cross sections for Higgs boson pair production for different centre-of-mass energies at NLO and NNLO within the considered approximations. Scale uncertainties are reported as superscript/subscript. The estimated top quark mass uncertainty of the $\text{NNLO}_{\text{FTapprox}}$ predictions is also presented. The numerical uncertainties are estimated to be at the per mille level.

by reweighting the exact NLO result for the invariant mass distribution of the Higgs boson pair with the NNLO/NLO ratio obtained in the HEFT. We consider centre-of-mass energies of 13, 14, 27 and 100 TeV. We use the values $M_h = 125\,\text{GeV}$ for the Higgs boson mass and $M_t = 173\,\text{GeV}$ for the pole mass of the top quark. We use the PDF4LHC15 sets of parton distribution functions (PDFs), with parton densities and as evaluated at each corresponding perturbative order (i.e., we use the $(k+1)$-loop running as at N^kLO, with $k = 1, 2$). As renormalisation and factorisation scales, we use the central value $\mu_0 = M_{hh}/2$, and we obtain scale uncertainties via the usual 7-point scale variation.

The approximated NNLO cross sections computed as discussed above are reported in Table 2.1. The NNLO effect ranges from about $+12\%$ at $\sqrt{s} = 13$ TeV to about $+7\%$ at $\sqrt{s} = 100$ TeV. For the considered approximations and collider energies the scale uncertainties are significantly reduced when including the $\mathcal{O}(\text{as}^4)$ NNLO corrections. This reduction is largest for the $\text{NNLO}_{\text{FTapprox}}$ approximation. For instance, at 14 TeV the total scale uncertainty is reduced from about $\pm 13\%$ at NLO to $+2\% - 5\%$ at $\text{NNLO}_{\text{FTapprox}}$, i.e. by about a factor of three. This reduction of the scale uncertainties is stronger as we increase the collider energy and at 100 TeV it approaches a factor of five. As is well known, scale uncertainties can only provide a lower limit on the true perturbative uncertainties. In particular, from Table 2.1 we see that the difference between the NNLO and NLO central predictions is always larger than the NNLO scale uncertainties (although within the NLO uncertainty bands). In any case, the strong reduction of scale uncertainties, together with the moderate impact of NNLO corrections, suggests a significant improvement in the perturbative convergence as we move from NLO to NNLO.

While our calculation includes the exact dependence on the top quark mass up to NLO, at NNLO the top mass effects are included in an approximate way. The $\text{NNLO}_{\text{FTapprox}}$ result represents our best prediction, and for a conservative estimate of the uncertainty of this approximation we compare it against our "next-to-best" prediction. Our estimate for the finite top quark mass uncertainty of our $\text{NNLO}_{\text{FTapprox}}$ result is defined as *half the difference between the* $\text{NNLO}_{\text{FTapprox}}$ *and the* $\text{NNLO}_{\text{NLO-i}}$ *approximations*, and is reported in Table 2.1 for the different values of $\sqrt{s}$. At $\sqrt{s} = 14\,\text{TeV}$ the uncertainty is $\pm 2.7\%$, whereas at $\sqrt{s} = 100\,\text{TeV}$ it increases to $\pm 4.6\%$. A more detailed discussion on this uncertainty and additional results can be found in Ref. [10].

[8] S. Borowka, N. Greiner, G. Heinrich, S. Jones, M. Kerner, J. Schlenk, U. Schubert, and T. Zirke, *Higgs Boson Pair Production in Gluon Fusion at Next-to-Leading Order with Full Top-Quark Mass Dependence*, Phys. Rev. Lett. **117** (2016), no. 1 012001, [arXiv:1604.0644]. [Erratum: Phys. Rev. Lett. **117**,no.7,079901(2016)].

[9] S. Borowka, N. Greiner, G. Heinrich, S. P. Jones, M. Kerner, J. Schlenk, and T. Zirke, *Full top quark mass dependence in Higgs boson pair production at NLO*, JHEP **10** (2016) 107, [arXiv:1608.0479].

[10] M. Grazzini, G. Heinrich, S. Jones, S. Kallweit, M. Kerner, J. M. Lindert, and J. Mazzitelli, *Higgs boson pair production at NNLO with top quark mass effects*, arXiv:1803.0246.

[11] M. Grazzini, S. Kallweit, and M.Wiesemann, *Fully differential NNLO computations with MATRIX*, arXiv:1711.0663.

2.3 Precise predictions for transverse momentum distributions of electroweak bosons

The production of electroweak (EW) gauge bosons with subsequent leptonic decay, known as the Drell–Yan process, is one of the most prominent processes at hadron–hadron colliders such as the LHC. Not only are the gauge bosons produced in abundance, but the clean leptonic signature allows this class of processes to be measured with great precision. As a consequence, the Drell–Yan-like production of W and Z bosons is among the most important 'standard candles' at hadron colliders and, as such, has a wide range of applications.

The transverse-momentum spectrum of the gauge bosons (p_T^V) takes a particularly important role in this respect: Different kinematical regimes of this observable probe various aspects of the predictions, such as resummation and non-perturbative effects at low p_T^V, fixed-order predictions at intermediate to high p_T^V, and also electroweak Sudakov logarithms at very high p_T^V. As such, detailed theory–data comparisons of this observable constitute crucial probes to test the Standard Model (SM) predictions. We recently computed [12] the $\mathcal{O}(\alpha_s^3)$ NNLO QCD corrections to W production at finite transverse momentum with leptonic decay, which is closely related to the Z transverse momentum distribution discussed in Refs. [13–15].

Figure 2.2 shows the normalised transverse-momentum distribution of the W boson in the electron and muon channels. The NLO corrections are between 10–40% with residual scale uncertainties at the level of around $\pm 10\%$. Although the scale-uncertainty bands at NLO mostly cover the experimental data points, systematic differences in the shape between data and the central theory prediction are visible. In view of the experimental precision, this clearly demonstrates the necessity of higher-order predictions with smaller uncertainties in order to discriminate such behaviours. The NNLO corrections are positive and between 5–10% in the intermediate- to high-p_T^W region. Towards lower p_T^W, the NNLO corrections become smaller and turn negative in the lowest-p_T^W bin. The residual scale uncertainties reduce to the level of about $\pm 2\%$ and overlap with the NLO scale bands, exhibiting good perturbative convergence. Most notably, we observe that the shape distortion induced by the NNLO corrections brings the central predictions in line with the measured distributions.

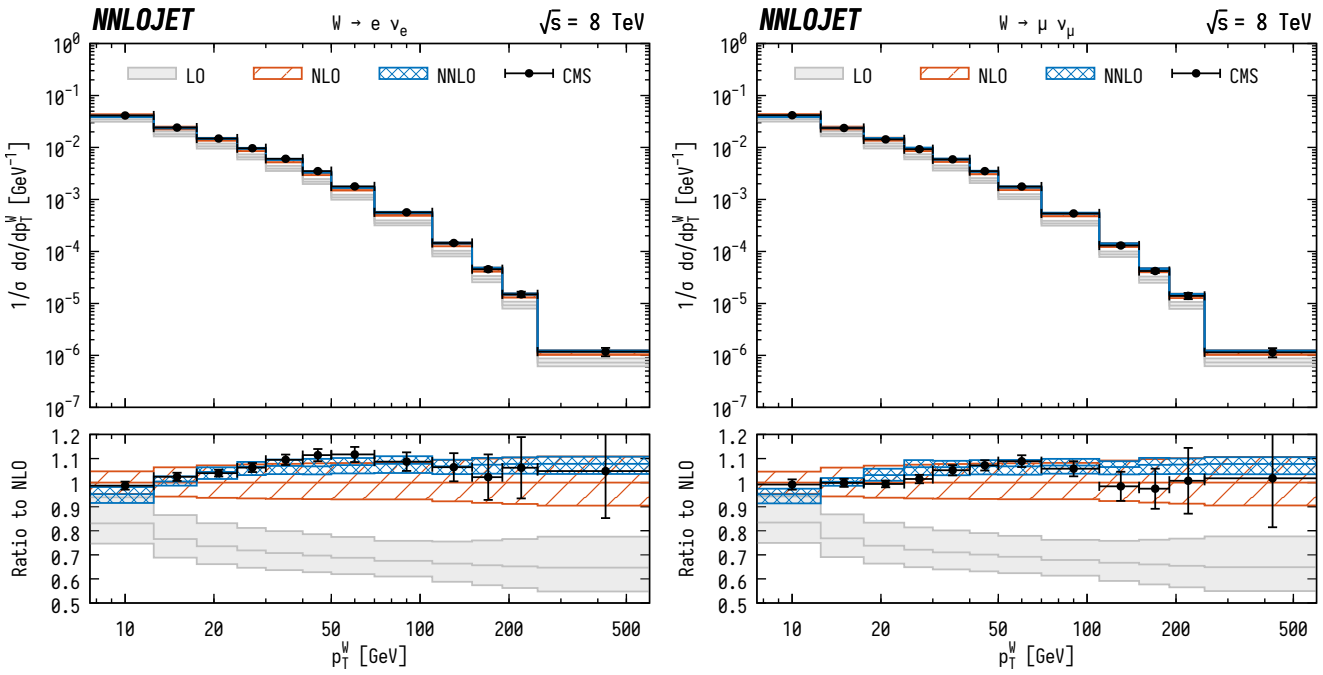

FIG. 2.2 – Normalised p_T^W distribution for $W = W^+ + W^-$ production with subsequent decay into electrons (left) and muons (right). Predictions at LO (gray fill), NLO (orange hatched), and NNLO (blue cross-hatched) are compared to CMS data from Ref. [16]. The bands correspond to scale uncertainties estimated as described in the main text.

Figure 2.3(left) shows the ratio between the normalised distributions of the W boson processes. The ratio is close to one in the lowest p_T^W bin and rises up to ~ 1.1 at $p_T^W \approx 150$ GeV, where it turns over and slowly decreases to 0.9 at $p_T^W = 500$ GeV. The central predictions remain remarkably stable between the different orders, resulting in K-factors that are very close to one. However, the precision of the theory prediction is substantially improved by going to higher orders: While the scale uncertainties at NLO are between $\pm$10–20%, the NNLO corrections reduce the uncertainties to the level of $\pm$5% across most of the p_T^W range, never exceeding $\pm$10%.

The ratio between the Z- and W-boson processes are shown in Fig. 2.3(right). Here, the ratio is again close to one in the low-p_T^V bin and shows a steady increase towards higher p_T^V, reaching about 1.5 at $p_T^V \sim 500$ GeV. As was the case for the W^-/W^+ ratio, the QCD corrections are very stable and leave the central predictions largely unaffected, supporting the expected similarity of QCD corrections between Z and W production. The higher-order corrections however have a big impact on the scale uncertainties, which are reduced by more than a factor of two across almost all p_T^V-bins by going from NLO to NNLO and are at the level of $\pm$5–10%.

The results presented here pave the way towards stress-testing SM predictions using the precise experimental data that are available for the p_T^V spectra and related observables and to reduce theory uncertainties in the extraction of PDFs and parameters such as M_W.

[12] A. Gehrmann-De Ridder, T. Gehrmann, E. W. N. Glover, A. Huss, and D. M. Walker, *NNLO QCD corrections to the transverse momentum distribution of weak gauge bosons*, Phys. Rev. Lett. **120** (2018), no. 12 122001, [arXiv:1712.0754].

[13] A. Gehrmann-De Ridder, T. Gehrmann, E. W. N. Glover, A. Huss, and T. A. Morgan, *The NNLO QCD corrections to Z boson production at large transverse momentum*, JHEP **07** (2016) 133, [arXiv:1605.0429].

[14] A. Gehrmann-De Ridder, T. Gehrmann, E. W. N. Glover, A. Huss, and T. A. Morgan, *NNLO QCD corrections for Drell-Yan p_T^Z and φ observables at the LHC*, JHEP **11** (2016) 094, [arXiv:1610.0184].

[15] R. Gauld, A. Gehrmann-De Ridder, T. Gehrmann, E. W. N. Glover, andat the LHC,A. Huss, *Precise predictions for the angular coefficients in Z-boson production*, JHEP **11** (2017) 003, [arXiv:1708.0000].

[16] CMS Collaboration, V. Khachatryan *et al.*, *Measurement of the transverse momentum spectra of weak vector bosons produced in proton-proton collisions at $\sqrt{s} = 8$ TeV*, JHEP **02** (2017) 096, [arXiv:1606.0586].

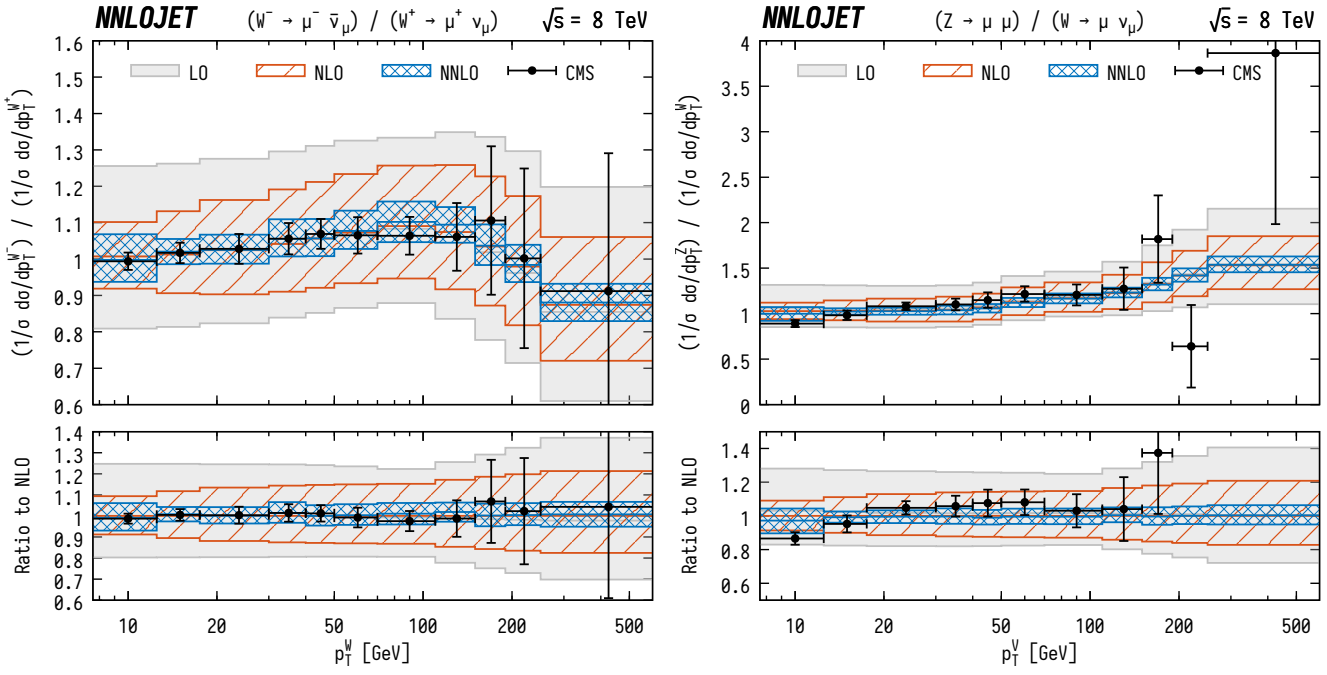

FIG. 2.3 – Ratio of normalised p_T^W distributions between W^- and W^+ production (left) and between Z and $W = W^+ + W^-$ production (right) in the muon channel. Predictions at LO (gray fill), NLO (orange hatched), and NNLO (blue cross-hatched) are compared to CMS data from Ref. [16]. The bands correspond to scale uncertainties estimated as described in the main text.

2.4 Regularization-scheme dependence

Intermediate results in perturbative higher-order calculations in gauge theories such as QED or QCD suffer from divergences. In order to give these expressions a well-defined mathematical meaning, a regularization is needed. For a final physical result, the regularization can be removed and a finite, regularization-scheme independent answer is obtained.

For most calculations, conventional dimensional regularization (CDR) is used, whereby the dimension for all quantities is moved away from the physical value of 4 to $D \equiv 4 - 2\epsilon$. The singularities then manifest themselves as poles in $1/\epsilon$. While this is a very elegant and powerful method there are circumstances where other methods are advantageous.

Broadly speaking there are two classes of schemes. First there are variations of CDR where only some quantities are moved to D dimensions and others are kept in 4 dimensions. Second, there are schemes that work entirely in 4 dimensions and define subtraction terms to regularize the singularities. Some schemes offer various advantages for the computation of particular parts of a full physical result. For example, numerical methods often rely on some quantities being defined in strictly four dimensions. In order to be able to combine separate parts computed with different regularization schemes it is mandatory to precisely understand their relation and how to convert a partial result from one scheme to another.

Our group has worked on a consistent formulation of several schemes and their comparison to others. Following a workshop that took place at the University of Zurich, this has culminated in an article [17] that compares and translates the various schemes. Virtually all international groups working on this topic have participated and new relations between proposed regularization schemes have been discovered.

Among the long-standing problems of CDR is the treatment of γ_5, an inherently four-dimensional object that cannot be defined consistently in D dimensions. Building on [17], we have revisited this problem and studied how to consistently implement γ_5 in schemes other than CDR [18]. The clarification of such technical questions opens the possibility to develop more efficient computational techniques for theories that involve γ_5.

[17] C. Gnendiger *et al.*, *To d, or not to d: recent developments and comparisons of regularization schemes*, Eur. Phys. J. **C77** (2017), no. 7 471, [arXiv:1705.0182].

[18] C. Gnendiger and A. Signer, γ_5 *in FDH*, arXiv:1710.0923.

2.5 Flavour physics within and beyond the Standard Model

Continuing the research line started in 2015, also in 2017 we have devoted most of our research efforts on analysing origin and implications of the evidences of Lepton Flavour Universality (LFU) violations observed in B physics. We have analysed this phenomenon both from a pure phenomenological perspective and in the context of motivated extensions of the Standard Model (SM). Our research has been articulated along two main directions.

- *New physics analyses based on Effective Theory approaches and simplified models.*
  Completing the work started in 2015, we have presented an extensive analysis (and a complete solution) of the problem of combining the two sets of anomalies, namely i) the breaking of τ–μ universality in $B \to D^{(*)}\ell\nu$ decays and ii) the breaking of μ–e universality in $B \to K\ell^+\ell^-$ decays, within a common Effective Field Theory approach [19]. Using the same approach, we have investigated the possible implication of these anomalies on rare K decays. As we have shown [20], the $K \to \pi\nu\bar{\nu}$ decays could be particularly interesting probes of LFU breaking dynamics, being the only kaon decays with third-generation leptons (the τ neutrinos) in the final state. Last but not least, using a representative class of simplified models describing the observed LFU effects, we have analysed the implications of the flavour-conserving, non-universal, quark-lepton contact interactions on $pp \to \ell^+\ell^-$ processes at the LHC [21].

- *UV completions.*
  A significant step forward has been made on the attempt to find motivated ultraviolet (UV) completions for the simplified models addressing these anomalies. In Ref. [22] the first full-fledged UV complete and calculable gauge model which incorporates the vector lepton-quark as leading mediator for the anomalies has been identified. The model is based on the gauge group $SU(4) \times SU(3) \times SU(2) \times U(1)$, which is assumed to be spontaneously broken to the SM around the TeV scale. A more ambitious attempt has been presented in Ref. [23], with a renormalizable model able to explain the SM flavor hierarchies while, at the same time, accommodating the recent experimental hints of LFU violations in B decays. The latter solution, which can be viewed as a non-trivial extension toward higher energies of the work in Ref. [22], is based on a three-site Pati-Salam gauge group, whose breaking chain down to the SM is illustrated in Figure 2.4. The model is consistent with low- and

high-energy bounds and predicts a rich spectrum of new states at the TeV scale that could be probed in the near future by the high-p_T experiments at the LHC.

[19] D. Buttazzo, A. Greljo, G. Isidori, and D. Marzocca, *B-physics anomalies: a guide to combined explanations*, JHEP **11** (2017) 044, [arXiv:1706.0780].

[20] M. Bordone, D. Buttazzo, G. Isidori, and J. Monnard, *Probing Lepton Flavour Universality with $K \to \pi\nu\bar{\nu}$ decays*, Eur. Phys. J. **C77** (2017), no. 9 618, [arXiv:1705.1072].

[21] A. Greljo and D. Marzocca, *High-p_T dilepton tails and flavor physics*, Eur. Phys. J. **C77** (2017), no. 8 548, [arXiv:1704.0901].

[22] L. Di Luzio, A. Greljo, and M. Nardecchia, *Gauge leptoquark as the origin of B-physics anomalies*, Phys. Rev. **D96** (2017), no. 11 115011, [arXiv:1708.0845].

[23] M. Bordone, C. Cornella, J. Fuentes-Martin, and G. Isidori,*A three-site gauge model for flavor hierarchies and flavor anomalies*, Phys. Lett. **B779** (2018) 317-323, [arXiv:1712.0136].

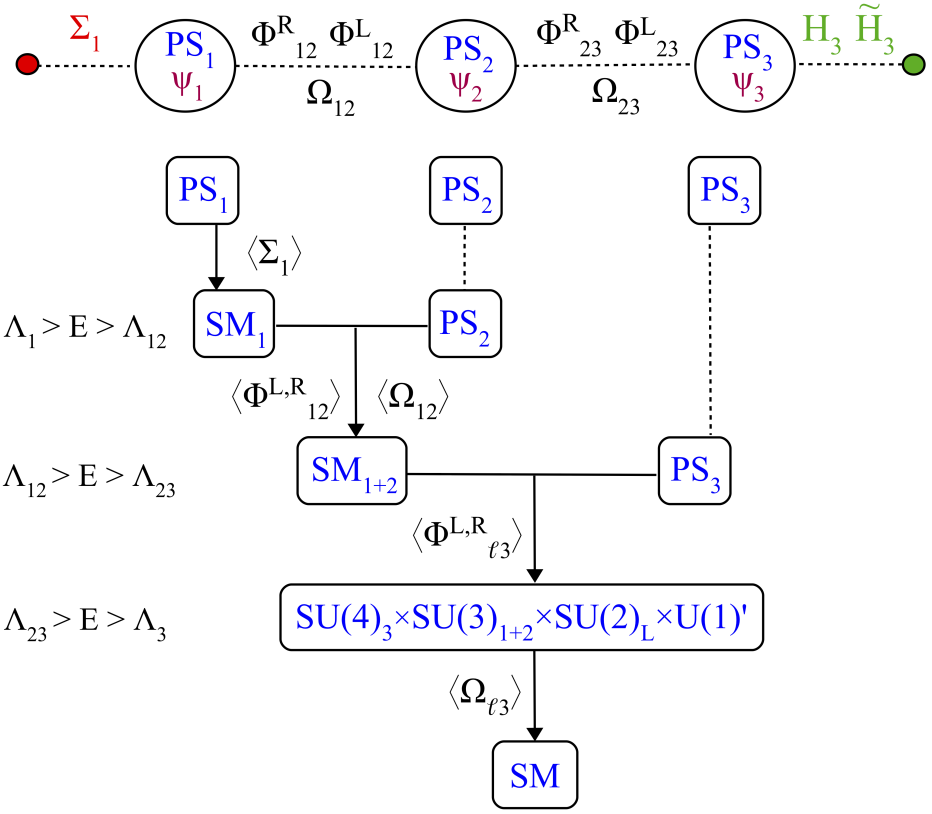

FIG. 2.4 – Symmetry breaking sequence for the three-site Pati-Salam model presented in Ref. [23].

3 Astrophysics and General Relativity

Y. Boetzel, P. Denzel, M. Haney, W. Ishibashi, Ph. Jetzer, R. Küng, A. Schärer, L. Philippoz, P. Saha, J. Su, J. ten Pierick

Newtonian gravity is adequate for most astrophysical phenomena, but for situations involving very strong gravitational fields (or cosmological distances, or the effect of gravity on light, or simply extremely precise measurements), relativistic gravity is needed. After more than a hundred years, Einsteinian gravity continues to pass all tests thrown at it, and meanwhile reveals new insights into the Universe through the recent observations of gravitational waves (GW). Exploring various aspects of general relativity (GR) is our area of research.

3.1 Gravitational Waves

One of the predictions of GR is the existence of GW. In analogy to electromagnetism, accelerating masses cause local perturbations in spacetime geometry that propagate at the speed of light. Indirect observational evidence for GW has existed since 1974, through the measurements of the orbital decay of binary pulsars like the Hulse-Taylor pulsar (PSR B1913+16). Efforts to directly measure the extremely tiny effects of a passing GW on Earth have been ongoing since the 1960s, with the development of resonant bar detectors and subsequently laser interferometry. On 14 September 2015, the two instruments of the Laser Interferometer Gravitational-Wave Observatory (LIGO) detected the GW signal GW150914 from the inspiral and subsequent merger of two stellar-mass black holes, marking the first direct detection of GW and the first observation of a binary black hole merger. Further black hole coalescing events have been detected since then, in joint observation with the European Virgo detector. In October 2017, the LIGO-Virgo collaborations and their partner observatories announced the first joint observation of a neutron star merger in GW and the electromagnetic spectrum, inaugurating a new era in multi-messenger astronomy. As a member of the LIGO Scientific Collaboration (LSC) and as part of the LISA Pathfinder (LPF) and Laser Interferometer Space Antenna (LISA) science teams, our group is directly involved in the efforts of both ground-based and space-borne GW observatories.

3.1.1 LISA Pathfinder

Ph. Jetzer is member of the LISA Pathfinder (LPF) Science Working Team, of the LISA Consortium Board and of the ESA LISA Science Study Team. LISA Pathfinder is a European Space Agency (ESA) mission launched on December 3, 2015. The mission has terminated in July 2017. LPF's goal was to place two test masses in a nearly perfect gravitational free-fall, and control and measure their relative motion with unprecedented accuracy, at the level required for a future space-based gravitational wave (GW) observatory, such as LISA (see Fig. 3.1). The latest results have been published in February 2018 and show an improvement with respect to the previous ones.

The demonstration of the LPF's key technologies opens the door to the development of LISA, which will be capable of detecting gravitational waves emanating from a wide range of objects in the universe. In November 2013, ESA selected *The Gravitational Universe* as the science theme to be explored by ESA's Large class mission L3. Following the success of LPF, the Laser Interferometer Space Antenna (LISA) was selected as the L3 mission by ESA in June 2017.

3.1.2 Gravitational Waves, LIGO and LISA

The scope of LISA is to detect and study low-frequency GW from about 0.1 mHz to 1 Hz, thus complementing ground-based gravitational observatories. LISA opens

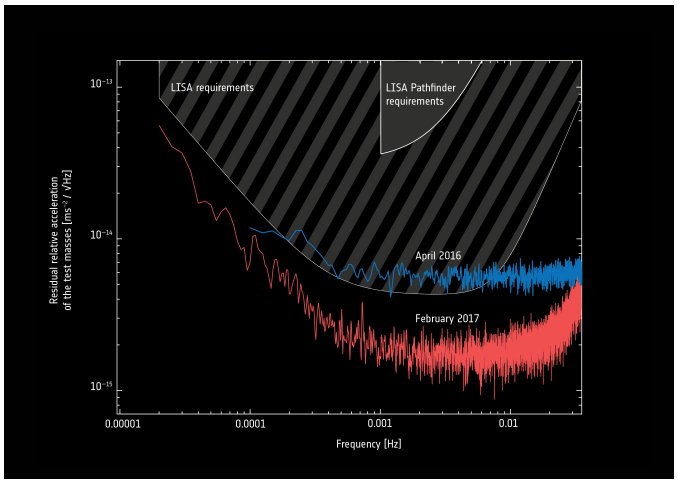

FIG. 3.1 – Analysis of the LISA Pathfinder mission results towards the end of the mission (red line) compared with the first results published shortly after the spacecraft began science operations (blue line). The initial requirements (top, wedge-shaped area) and that of the future GW detection mission LISA (middle, striped area) are included for comparison, and show that it far exceeded expectations. Copyright ESA/LISA Pathfinder collaboration.

new possibilities for astrophysical studies by allowing, for instance, to detect supermassive black holes (typically of $10^6 - 10^7\ M_\odot$) merging at cosmological distances. Mergers of a supermassive black hole with another compact object (such as another black hole or a neutron star) produce a very clean GW signal which LISA will be able to measure with high precision. Alternative gravity theories would influence the dynamics of such mergers, and hence LISA is expected either to directly see the imprints of certain alternative theories or to put severe constraints on them. Another class of objects, which will be observed by LISA, are ultra-compact binaries, in particular binaries of white dwarfs in our Galaxy. They are important sources of GW in the mHz frequency range. Moreover, it will be possible to detect or put strong constraints on the primordial GW background, which – as the cosmic microwave background – is a leftover from the Big Bang.

Members of our group are working on various theoretical aspects of LISA-related GW science. As members of the LIGO Scientific Collaboration (LSC), we are contributing to the theoretical groundwork for the LIGO-Virgo detectors and are directly involved in the analysis of GW data.

According to GR, GW possess two tensor polarizations. Deviation from GR can however lead to the appearance of additional modes: up to two scalar ones (a massive longitudinal mode and a massless transverse mode), as well as two vector modes. Detecting (or not) such additional modes can be a powerful tool to test GR and put constraints on alternative theories of gravity. Lionel Philippoz is investigating the limits that could be provided on the various polarization modes by several configurations of LISA, as well as correlations of Earth-based and space-borne detectors which have been proposed in the past years, and the possibilities to extract that information from a given GW signal. This study focus primarily on a stochastic GW background which could originate from the early universe, and better constraints on that signal are of importance for cosmology. In his master thesis, Adrian Boîtier studied the future GW detectors ET and DECIGO and their inclusion in a network of existing detectors in order to establish the sensitivity curves for the various polarization modes of GW, in the case of a GW background and point sources.

Yannick Boetzel is studying theoretical aspects of GW from compact binaries in eccentric inspiralling orbits. In particular he could already provide an elegant analytic solution to the 3PN-accurate Kepler equation, associated with the 3PN-accurate generalized quasi-Keplerian parameterization for compact binaries in eccentric orbits. This is an important step to model accurate GW templates from compact binaries in inspiralling eccentric orbits. For his master thesis, Michael Ebersold studied the Hansen coefficients, used to describe the Keplerian motion of binary systems, in a post-Newtonian setting.

In March 2017, Philippe Jetzer, Maria Haney and Yannick Boetzel joined the GEO600 collaboration and were subsequently approved for membership in the LIGO Scientific Collaboration (LSC), establishing the first LSC group in Switzerland. We have committed a contribution to LSC research that includes template waveform development for the GW search and parameter estimation efforts, as well as tests of GR with GW data from binary black hole mergers. At present, Y. Boetzel and M. Haney have (respectively) promised 50% and 90% of their research time to LSC-approved projects, with Ph. Jetzer serving as the PI of the group. A focus of our LSC work is the development of accurate and efficient GW templates, as well as studying their implications for improved GW search and parameter estimation methods. In particular, we model GW signals that take previously unmodeled effects like spin precession and orbital eccentricity of compact binary GW sources into account, broadening the parameter space for GW searches and eliminating systematic biases in GW source parameter estimation. Additionally, we develop new data analysis pipelines that aim to test and constrain possible strong-field deviations from GR with GW data.

A number of recent investigations have explored several plausible astrophysical mechanisms for the formation and merger of LIGO relevant compact binaries which retain non-negligible eccentricities throughout their lifetime, through dynamical-formation scenarios that take place in dense stellar environments. These investigations suggest that $\sim$ 1% of all black hole binary mergers could be detected with non-negligible eccentricity, and that ground-based GW observatories could potentially detect up to 10 eccentric inspirals per year up to redshift $z \sim 0.2$, with eccentricities as high as 0.9 when the signals enter the detector band. Even one confident detection of an eccentric black hole binary would give very strong evidence for the preferred formation channel of binary black holes (BBH). However, it has been shown that a large fraction of GW signals from binary coalescence with non-negligible eccentricities will be missed by the current template searches, since the quasi-circular waveform families employed in those searches are substantially suboptimal to detect GWs from compact binaries with eccentricities > 0.05. This is mainly due to the significant dephasing and the amplitude modulations that are expected to occur in eccentric GW signals. Third-generation ground-based detectors like the Einstein Telescope (ET) and space-based GW observatories like LISA will have much improved sensitivities in the low-frequency regime and are expected to observe stellar-mass BBH like GW150914 a significant time before merger, when eccentricity effects may be expected to be non-negligible. It has been estimated that LISA should

resolve eccentricities $e_0 \geq 0.01$ and may even be able to detect 90% of binaries inspiraling along orbits with $e_0 \geq 0.001$. Therefore, it is highly desirable to incorporate effects of residual orbital eccentricity in the source modeling for data analysis with present and future generations of GW observatories.

As active member of the *Waveforms* working group of the LSC, we develop codes for the LIGO Algorithm Library (LAL) that provide ready-to-use, post-Newtonian (PN) accurate inspiral templates for compact binaries in inspiraling eccentric orbits, and develop the necessary data analysis tools that would enable the LSC to use these templates for the estimation of GW source parameters and eventually for GW searches.

M. Haney is working to improve previously developed time-domain and frequency-domain GW models of eccentric binary inspiral [1], with the aim of achieving templates with a PN accuracy that is comparable to that of the widely used quasi-circular inspiral approximants. With collaborators at UIB Palma, she has begun to study data analysis implications of a ready-to-use, 'effective eccentric variant' of the non-precessing IMRPhenomD waveform family, with the aim of including eccentricity as an integral part of the phenomenological modeling process. (Phenomenological frequency-domain waveform models have become standard tools for the GW data analysis of black-hole merger events with LIGO and Virgo.) This preliminary Phenom model for eccentric coalescence was developed and implemented for data analysis during LIGO's first observing run, restricted to non-spinning black holes and incorporating the effects of small orbital eccentricities during the inspiral regime. With the help of hybrid waveforms that include information from numerical relativity simulations of eccentric black-hole coalescence, she has started to explore the accuracy of the model over the parameter space and work towards improving the phenomenological modeling of the waveforms. The long-term goal of this project is the development of an accurate and computationally efficient frequency-domain inspiral-merger-ringdown (IMR) GW model for generic binaries with both eccentricity and spin precession. With collaborators at INFN Trento and Cardiff University, she is employing these models of compact binary coalescence with non-negligible eccentricity for a performance comparison of the modeled (circular template-based) and unmodeled (burst) pipelines of the LSC. Such a systematic study of the effects of eccentricity on GW searches will lead to a better understanding of certain search characteristics, such as estimates of sensitivity, upper limits on events rates, systematics of parameter estimation, estimation of the background. Y. Boetzel is working on a new, generic Fourier-domain inspiral model that combines effects of eccentricity and spin precession, which can prove to be a crucial tool to probe waveform systematics in GW source parameter estimation. A first publication is currently under review by Physical Review D, and a timely software implementation of these waveforms in the LIGO Algorithm Library (LAL) is ongoing. Other eccentricity-related projects for the LSC include work by M. Haney to explore the possibility of using parameterized tests of GR violations in GW data (with gIMR waveform models) to extract information about the eccentricity of a binary system, to study a possible connection between the inspiral coefficients in the gIMR analysis and plausible eccentricity effects. For the second part of his master thesis, Michael Ebersold studies the nonlinear memory effect of eccentric binary systems, extending work by Favata to the post-Newtonian regime. GW memory is a (as-of-yet unobserved) strong-field effect, i.e. a permanent displacement of spacetime arising from a non-oscillatory contribution to the GW polarizations due to an interaction of the GW with themselves. Although memory effects in the GW signal from an individual merger event have signal-to-noise ratios that are too small to be resolved by ground-based detectors, it has been shown that a cumulative stacking of signal-to-noise ratio from GW measurements of many binary black hole mergers can lead to a detection of GW memory in principle. With collaborators at INFN Trento, we are probing the prospects for detection of GW memory from a population of eccentric binary black hole mergers, with the potential to provide hints for the understanding of formation channels of black holes, even in the absence of an unambiguous detection of a black hole merger event with significant eccentricity.

Compact binaries in hyperbolic orbits are plausible GW sources for the currently available and upcoming GW observatories. Though compact binaries in hyperbolic orbits are expected to be rare GW events, close encounters of an unbound binary containing a neutron star may be associated with electromagnetic flares. This feature makes binaries on hyperbolic orbits interesting candidates for triggered GW burst searches. Additionally, there has been significant interest from within the LSC to explore hyperbolic waveform models in the context of a possible application in classifying sine-Gaussian glitches in GW detector data. For his master thesis, Oliver Fischer has calculated the radiated energy and power spectrum during a hyperbolic encounter, checking and correcting the results from [2]. With collaborators at TIFR Mumbai and Seoul National University, M. Haney has developed PN-accurate 'burst' templates for compact binaries in unbound orbits, by computing 3PN-accurate quasi-Keplerian parameterization and extending previous efforts in De Vittori et al. (2014) [2] to compute the orbital dynamics of hyperbolic binaries. A publication introducing this waveform model is currently under review by Physical Review D, with ongoing work towards an im-

plementation of hyperbolic waveforms in the LAL software and an exploration of the data analysis implications of certain memory effects in the GW polarization states.

As part of the R&D efforts of the Testing GR working group of the LSC, M. Haney has developed a new data analysis infrastructure that generically tests for imprints of (GR violating) gravitational dipole radiation on GW signals from compact binary coalescence, and obtains constraints on certain specific mechanisms for the emission of dipole radiation. This pipeline has passed internal review by the LSC and has been used as a standard test of GR in GW data during the recent second observing run (O2) of Advanced LIGO. Efforts are ongoing to extend and improve the dipole radiation test by working towards including higher-order dipole radiation effects in GW phasing that are important at higher frequencies, particularly during the late inspiral and the merger.

Recently and prompted by the detection of GW170817 (see Fig. 3.2), M. Haney and collaborators at TIFR Mumbai have started to study effects of magnetic dipole-dipole interaction in binary neutron star mergers on the GW phasing of frequency-domain waveforms of such systems [3]. The aim of this project is a possible distinction of binary neutron stars (BNS) with magnetic dipole moments from neutron star - black hole sources, by studying the systematic bias on the chirp mass that is estimated from GW data.

M. Haney has also devoted a substantial amount of time to service work for the LSC. She has been running data analysis for the binary black hole and BNS events detected during LIGO-Virgo's second observing run, and is a member of the team that is tasked with writing the LSC-Virgo collaboration paper that will detail tests of GR for the neutron star merger GW170817. She has also served as an internal LSC reviewer for several publications and data analysis software. Crucially, she was involved in efforts to develop and review (for the data analysis of GW170817) accurate and efficient inspiral-merger-ringdown models for BNS mergers that augment binary black hole model with numerical-relativity-tuned tidal effects. A short author list publication on this work is currently under review by Physical Review D.

[1] S. Tanay, M. Haney, and A. Gopakumar, Phys. Rev. D **93**, 064031 (2016)

[2] L. De Vittori, A. Gopakumar, A. Gupta, and Ph. Jetzer, Phys. Rev. D **90** (2014) 124066

[3] K. Ioka, and K. Taniguchi, Astrophys. J. **537**, 327–333 (2010)

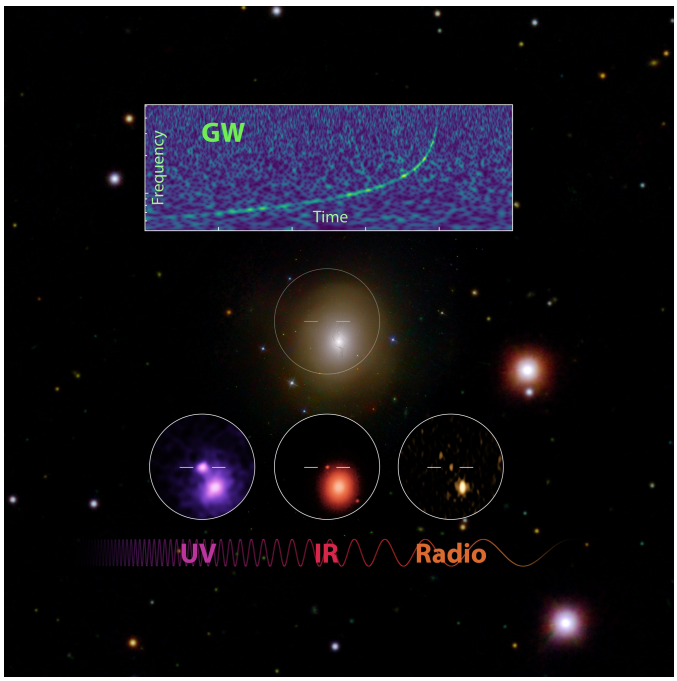

FIG. 3.2 – Detection of the GW170817 neutron star merger in gravitational waves (LIGO-Virgo) and electromagnetic radiation in ultra-violet (Swift satellite), infrared (Gemini-South Telescope) and radio (Very Large Array).
Copyright Robert Hurt (Caltech/IPAC), Mansi Kasliwal (Caltech), Gregg Hallinan (Caltech), Phil Evans (NASA) and the GROWTH collaboration .

3.2 Gravitational Lensing

The concepts of gravitational lensing – specifically that light is affected by both space and time parts of the metric, unlike Newtonian bodies, which are affected only by the time part – are too well known to need elaborating here. Nowadays, however, gravitational lensing is valued, more than as a test of GR, as a way of detecting matter that would be otherwise invisible.

On the scale of galaxies and clusters of galaxies, gravitational lensing is very important as a probe of dark matter. Extracting the information on mass distributions, however, requires solving a non-trivial inverse problem. R. Küng, P. Denzel and P. Saha, together with external collaborators, have worked on the problem of mapping a mass distribution from lensing observables. One part of this work is the development of an improved method for modeling galaxy lenses and furthermore, a theoretical formulation and computational interface to enable modeling in a citizen-science context. The other aspect is mapping and interpreting dark-matter structure in strong-lensing galaxy-clusters.

3.3 Space clocks and relativity

Together with the academic guest Dr. Jianfeng Su, Qiang Wang and Qinghua Wang from Spectratime in Neuchâtel, we studied the possibility to detect GW by putting very accurate atomic clocks on satellites on particular orbits. The result of this investigation has been published in the journal Classical and Quantum Gravity [4].

Also using spacecraft clocks, we investigated the possibility of measuring frame dragging by planets in a paper which appeared in Frontiers in Astronomy and Space Science [5].

Together with Fupeng Zhang at Sun Yat-Sen University in Guangzhou, China, P. Saha continued studying the relativistic spacetime expected around the Galactic-center black hole with the help of natural clocks. In a paper in the Astrophysical Journal [6], they conclude that if (as expected) the next generation of radio telescopes finds a pulsar in close orbit around the black hole (comparable to known stars), the black-hole spin and its orientation could be measured.

[4] J. Su *et al.*, Class. Quantum Grav. **35**, 085010 (2018)

[5] A. Schärer *et al.*, Front. Astron. Space Sci. **4**, 11 (2017)

[6] F. Zhang, and P. Saha, Astrophys. J. **849**, 33 (2017)

3.3.1 ACES workshop

On 29 and 30 June 2017 we organized at the Irchel campus of University of Zürich the ACES workshop, the first of a series. ACES (Atomic Clock Ensemble in Space) is a space mission at whose heart is an ensemble of atomic clocks on board the international space station (ISS) and microwave and optical links to compare the onboard clocks to clocks on the ground. It features a cold atom clock (PHARAO) and a hydrogen maser, built in Switzerland, that will bring unprecedented accuracy into space, together with world-wide dissemination of its time-scale to ground clocks. The launch of ACES/PHARAO is expected for 2020. The science objectives are in fundamental physics, time/frequency metrology, cold-atom space physics, study of the ionosphere and geodesy. One of its primary goals is a measurement of the gravitational redshift, a central prediction of Einstein's GR and a fundamental constituent of the Einstein Equivalence Principle, the experimental foundation of all metric theories of gravitation. The workshop brought together the scientific community interested in the results of ACES/PHARAO in all domains, from theoretical physics to cold atoms and application in geodesy and atmospheric studies. It consisted of invited and contributed presentations on the details of ACES, data analysis and scientific applications. The aim of the workshop was to prepare the scientific community for the upcoming launch and scientific exploitation of the data.

3.4 Scalar-Tensor Theories

Scalar-tensor theories are a promising class of alternative theories of gravitation. They contain, in addition to the metric tensor of GR, a scalar degree of freedom. Upcoming precision experiments might detect violations of general relativity, which could be explained by such theories. Together with Manuel Hohmann from the University of Tartu, Estonia, Andreas Schärer investigated multi-scalar-tensor theories. These theories are a further generalization which contain multiple such scalar fields. The results have been published in Physical Review D [7].

Simone Bavera in his master thesis studied the role of the boundary terms which appear in the Einstein-Hilbert action.

[7] M. Hohmann, and A. Schärer,
Phys. Rev. D **96**, 104026 (2017)

4 Neutrinoless Double Beta Decay with GERDA and LEGEND

Laura Baudis, Roman Hiller, Michael Miloradovic, Rizalina Mingazheva, Chloe Ransom

in collaboration with: INFN Laboratori Nazionali del Gran Sasso LNGS, Jagellonian University Cracow, Institut für Kern- und Teilchenphysik Technische Universität Dresden, Joint Institute for Nuclear Research Dubna, Institute for Reference Materials and Measurements Geel, Max Planck Institut für Kernphysik Heidelberg, Universitá di Milano Bicocca e INFN Milano, Institute for Nuclear Research of the Russian Academy of Sciences, Institute for Theoretical and Experimental Physics Moscow, Russian Research Center Kurchatov Institute, Max-Planck-Institut für Physik München, Dipartimento di Fisica dell Universitá di Padova e INFN, Physikalisches Institut Eberhard Karls Universität Tübingen.

(GERDA and LEGEND Collaborations)

4.1 Introduction

Neutrinos are the only known elementary particles that are Majorana fermion candidates, implying that they would be their own antiparticles. The most sensitive and perhaps only practical probe for the Majorana nature of neutrinos is an extremely rare nuclear decay process called neutrinoless double beta decay ($0\nu\beta\beta$), where a nucleus with mass number A and charge Z decays by emitting two electrons and changes its charge by two units (A,Z)$\longrightarrow$(A,Z+2) + 2e$^-$. The observation of this decay would mean that the lepton number is violated by two units, and would yield information on the neutrino mass scale via the so-called effective neutrino Majorana mass $\langle m_{\beta\beta}\rangle = |\Sigma_i U_{ei}^2 m_i|$, where the sum is over the neutrino mass eigenstates m_i, and U_{ei}, the corresponding entries in the lepton mixing matrix, are complex numbers. The related, two-neutrino double beta decay mode ($2\nu\beta\beta$) is allowed in the Standard Model and has been observed in more than 10 nuclei. In this case, the sum energy of the two electrons is a continuum, while for the $0\nu\beta\beta$-decay the distinct signature is a peak at the Q-value, the mass difference between mother and daughter nucleus.

Experiments can observe a certain decay rate in a detector, the half-life of which is inversely proportional to $\langle m_{\beta\beta}\rangle^2$:

$$\frac{1}{T_{1/2}^{0\nu}} = \frac{\langle m_{\beta\beta}\rangle^2}{m_e^2} G^{0\nu} |M^{0\nu}|^2, \tag{4.2}$$

assuming that the decay is mediated by the exchange of a light Majorana neutrino, and where m_e is the mass of the electron, while $G^{0\nu}$ and $M^{0\nu}$ are the phase space factor and the nuclear matrix element, respectively. Recent experimental limits on $T_{1/2}^{0\nu}$ and $\langle m_{\beta\beta}\rangle$ are of the order $T_{1/2}^{0\nu} \geq 10^{25}$-$10^{26}$ y and $\langle m_{\beta\beta}\rangle \leq 0.06 - 0.4$ eV, using a variety of nuclei and detector technologies.

4.2 The GERDA Experiment

The GERDA experiment aims to detect the $0\nu\beta\beta$ decay of ^{76}Ge, and is currently acquiring science data in its second phase at the Laboratori Nazionali del Gran Sasso (LNGS). GERDA uses high-purity germanium diodes, enriched in ^{76}Ge. The diodes, arranged in seven strings, act simultaneously as the detector and source material and are submerged in liquid argon (LAr). A water Cherenkov veto surrounds the LAr cryostat, to reject interactions from cosmic muons. Filled with ultra-pure water, the water tank also provides shielding against external radiation. The LAr cryostat is instrumented as a veto against background events from Compton scatters. It is equipped with photomultiplier tubes and silicon photomultipliers (SiPMs) to detect the scintillation light induced by interactions in the argon, triggered by an event in a germanium detector. The upgraded instrument is described in [1], and the latest results from this second phase of the project can be found in [2, 3]. The next phase, called GERDA-Upgrade is a step towards a 200 kg stage, to be constructed at LNGS by the new collaboration, LEGEND [4], which itself is the precursor of a future, ton-scale ^{76}Ge experiment. The aimed sensitivities are $T_{1/2}^{0\nu\beta\beta} > 10^{26}$ y and $T_{1/2}^{0\nu\beta\beta} > 10^{27}$ y for GERDA-Upgrade and the 200 kg stage, respectively.

[1] M. Agostini *et al.* [GERDA Collaboration], arXiv:1710.07776 [nucl-ex], accepted in EPJ-C.

[2] M. Agostini *et al.*, [GERDA Collaboration] Nature **544** (2017) 47-52.

[3] M. Agostini *et al.* [GERDA Collaboration], Phys. Rev. Lett. **120** (2018) no.13, 132503

[4] N. Abgrall *et al.* [LEGEND Collaboration], AIP Conf. Proc. **1894** (2017) no.1, 020027, [arXiv:1709.01980]

4.3 Search for the $0\nu\beta\beta$-decay

GERDA has been successfully operated in its second phase starting from December 2015. Over this period, the experiment has achieved the lowest background ever in the region of interest for the neutrinoless double beta decay ($Q_{\beta\beta}\pm25$ keV) (see Table 4.1). In consequence, less than one background event for the designed exposure of 100 kg·y [5] is expected. This low-background level has been achieved thanks to enhanced background rejection algorithms, and to the upgrade campaign in the summer 2015, which included the instrumentation of the liquid argon veto, the addition of 30 Broad Energy Germanium (BEGe) detectors (total mass of 20.0 kg) to the enriched coaxial detectors (15.6 kg), and the decreasing background levels of materials surrounding the detectors. The achieved energy resolution at $Q_{\beta\beta}$ at full width half maximum (FWHM) is about 3 and 4 keV for the BEGe and coaxial detectors, respectively. The latest results include data sets published in [5] and [6]. The summary of the obtained exposure and measured background index (events per keV·kg·y) during the second phase are summarised in the Table 4.1. The analysis includes in addition physics data accumulated during the first phase of the experiment, which makes 23.5 kg·y in total [7]. The efficiency ϵ is given by the product of the ^{76}Ge isotope fraction (∼87%), the active volume fraction (85%/89%), the efficiency of $0\nu\beta\beta$ event reconstruction at full energy in a single detector (∼92%), the efficiency of the pulse shape discrimination algorithm (79%-87%) and the liquid argon veto acceptance (98%).

Figure 4.1 shows the overall energy spectrum accumulated for the enriched BEGe detectors prior and after applied cuts for background rejection. The zoom into the region of interest in Fig. 4.2 shows the data from Phase I, as well as the Phase II data divided into enriched coaxial and BEGe detectors. The analysis range is from 1930 keV to 2190 keV, excluding indicated intervals which correspond to known peaks predicted by the background model.

TAB. 4.1 –
Summary of the exposure, resolution (FWHM), efficiency and expected background contribution for two Phase II data sets in GERDA.

Data set	exp.	resolution	efficiency	background
	kg·y	keV		$\frac{10^{-3}\text{cts}}{\text{keV·kg·y}}$
Coaxial	5.0	4.0(2)	0.53(5)	$3.5^{+2.1}_{-1.5}$
BEGe	18.2	2.93(6)	0.60(2)	$1^{+0.6}_{-0.4}$

After all the event selection criteria were applied and the region of interest around the Q-value of the decay was unblinded, four events were observed for BEGe and coaxial detectors, respectively (as seen in Fig. 4.2) for Phase II data. Since there are no events close to $Q_{\beta\beta}$ we place a 90% C.L. lower limit of $T^{0\nu}_{1/2} > 8.0\times10^{25}$ y on the decay half-life derived from a frequentist analysis, with a median sensitivity of 5.8×10^{25} y [6].

[5] M. Agostini *et al.*, [GERDA Collaboration] Nature **544** (2017) 47-52.

[6] M. Agostini *et al.* [GERDA Collaboration], Phys. Rev. Lett. **120** (2018) no.13, 132503

[7] M. Agostini *et al.*, Phys. Rev. Lett. **111** (2013) 122503.

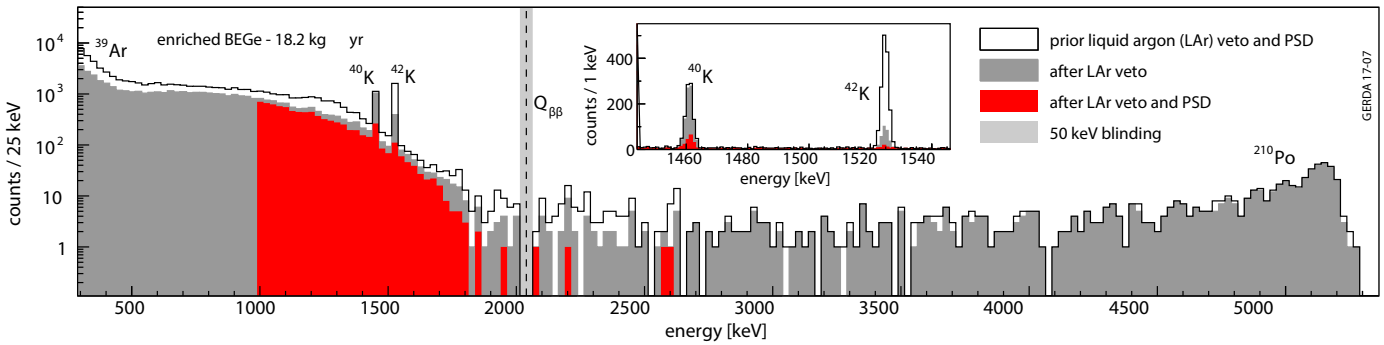

FIG. 4.1 – Energy spectra of Phase II BEGe detectors prior to liquid argon veto and PSD cuts (open histogram), after the LAr veto (dark grey) and after all event selection criteria (red). The inset shows the spectrum in the energy region of the gamma lines from ^{40}K and ^{42}K. The blinded region of ±25 keV around $Q_{\beta\beta}$ is indicated with the grey vertical band.

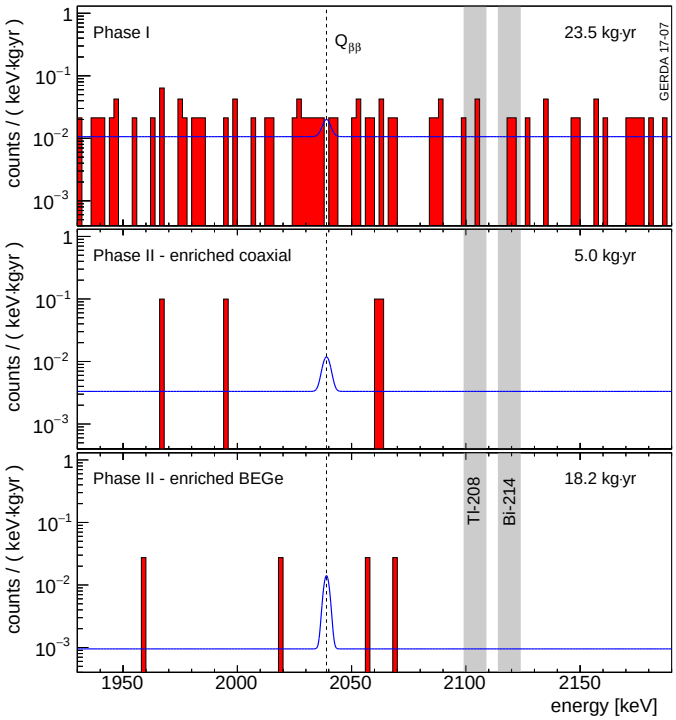

FIG. 4.2 – Energy spectra in the analysis range for Phase I and Phase II coaxial and BEGe detectors, respectively, after all the event selection criteria are applied (red histograms). The grey vertical bands indicate the intervals excluding known gamma lines. A hypothetical $0\nu\beta\beta$ signal for $T^{0\nu}_{1/2} = 8.0\times10^{25}$ y together with the expected background is also shown (blue lines).

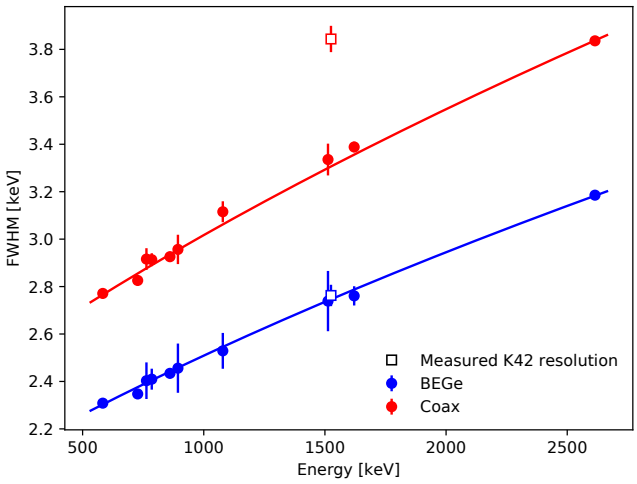

FIG. 4.3 – Combined energy resolution curves for BEGe (blue) and coaxial (red) detectors using data acquired with the ^{228}Th calibration sources (filled symbols). The estimated resolution based on low-background data using the ^{42}K line at 1525 keV is also shown for comparison (open symbols). The observed systematic difference for coaxial detectors is currently under investigation.

4.4 Energy calibration and resolution

Knowledge of the energy scale and resolution of the GERDA detectors is required for all physics analyses. In addition, the energy resolution at the Q-value of $0\nu\beta\beta$ decay is a strong prior for the sensitivity. Germanium detectors have excellent resolutions, of about 3-4 keV at FWHM, which improves the sensitivity for all peak searches. The array is calibrated by temporarily exposing the germanium detectors to ^{228}Th sources on an approximately weekly basis. Our group is jointly responsible for performing the weekly calibrations and for analysing and evaluating the calibration data.

The combined analysis for the energy resolution at $Q_{\beta\beta}$ is shown in Fig. 4.3. Since the GERDA background level is very low, as explained in section 4.3, there are few gamma lines whose resolution can be used as a cross-check for this analysis. The resolution of the ^{42}K line at 1525 keV is also shown in Fig. 4.3. For the coaxial detectors, the resolution in physics data is somewhat poorer than expected from calibration data. The reason for this is not yet clear, and investigations are ongoing.

We have studied systematic uncertainties on the energy scale determination, by considering deviations in the observed peak positions of the combined calibration spectra from their literature values. These could be caused by non-linearities present in the energy scale. For the BEGe and coaxial detectors, we estimate an uncertainty in the energy scale at $Q_{\beta\beta}$ of 0.2–0.3 keV and 0.2–0.4 keV respectively.

The relatively short half-life of ^{228}Th of 1.9 y requires that the three sources be replaced regularly. We are currently producing the new sources, in collaboration with the company Eckert & Ziegler, Mainz University and the Paul Scherrer Institute, with the deposition of thorium on gold foils foreseen for June this year. The deposition will be followed by the encapsulation and subsequent characterisation of the produced sources, including the determination of their activities and cryogenic tests. The current GERDA sources were also produced and characterised by our group [8], and we will follow a similar recipe for this round of calibration sources.

[8] L. Baudis *et al.*,
Journal of Instrumentation **10**, 12 (2015) P12005.

4.5 Background model and pulse shape simulations

We are part of the background modelling effort in the GERDA collaboration. It is based on Monte Carlo simulations of radioactive isotope decays in the detector materials [9], together with measured radioactivity levels using low-background germanium spectroscopy.

So far, the focus of the collaboration was on the enriched germanium detectors, which are used for the main

physics analysis of the $0\nu\beta\beta$-decay channel. Recently, we have started to investigate the natural (non-enriched) germanium detectors (placed on the central detector string in GERDA), with the goal of including these in the overall background model. These detectors, while fewer in number than the enriched diodes (3 diodes, with a total mass of 7.6 kg), have the advantage that the background due to the $2\nu\beta\beta$-decay is lower, as ^{76}Ge is present in natural Ge with an abundance of 7.8%. The energy spectrum thus provides complementary information on some background components. As an example, additional ^{214}Bi peaks are visible and will provide clues on the source location, which depends on the ratio of observed peak intensities. Our preliminary background model for the natural Ge detectors is shown in Fig. 4.4. No major discrepancies in peaks are visible that allude to other potential components that could be fit to the data. Some smaller differences have been investigated and excluded as being from additional radioactivity. Several ^{214}Bi peaks not visible in the enriched coaxial detector spectrum are revealed in a zoom into the background region visible in the lower part of Fig. 4.4. These stem mostly from ^{214}Bi, while ^{85}Kr and ^{39}Ar peaks are visible as well.

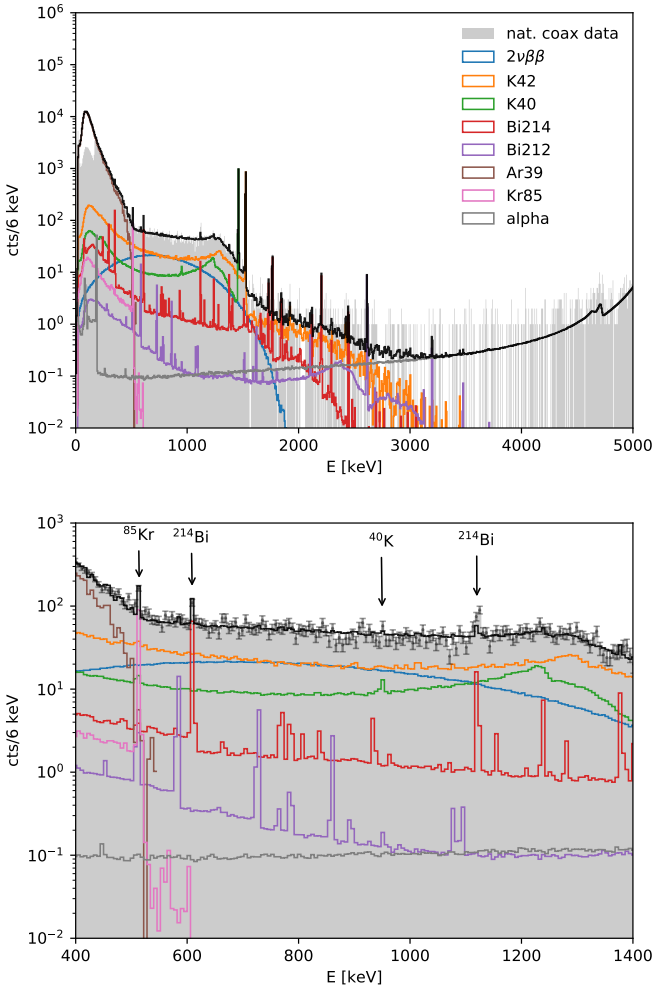

FIG. 4.4 – Preliminary background model fit of Monte Carlo simulations of the most dominant background components to data of the validated dataset of the natural coaxial detectors (grey). Top: Full energy range from 0 to 3000 keV. Bottom: Zoom into range from 400 to 1400 keV revealing peaks which are only visible for natural coaxial detectors.

Currently, all the background model simulations are limited to the energy deposition inside the germanium detectors and do not include the signal generation in the Ge diodes. The impact of the detector response and signal processing, as well as the pulse shape properties required for pulse shape discrimination (PSD) are thus not accounted for. We have developed tools in order to integrate the Monte Carlo simulations of the background (based on Geant4) into the pulse shape simulation software. The main goal is to perform an end-to-end simulation of GERDA events and to develop a background model after PSD, which can be directly compared with data. To this end, we have first developed an interface that extracts the detector geometries and transforms the Monte Carlo hits into the detector frame based on the geometries. The subsequent field simulations in each detector then use the extracted geometries.

To validate the pulse shape simulation results, we have performed a first comparison between averaged simulated pulses created with hits from simulations of the double escape peak (DEP) of the ^{208}Tl line with real pulses taken from the DEP in GERDA Phase II calibration data. The result is shown in Fig. 4.5. The simulation agrees well with the data up to a 2% level, where the op-

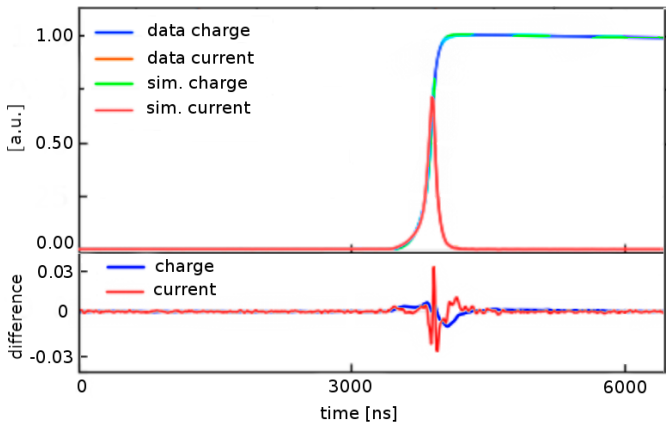

FIG. 4.5 – Averaged waveforms of events in the Double Escape Peak of ^{208}Tl from pulse shape simulations and recorded data. Top: Average simulated charge and current pulses (green, red) of BEGe detectors from calibration data in comparison to the corresponding average data pulses (blue, orange) from calibration data. Bottom: The difference between simulations to data for charge (blue) and current (red) pulses.

timisation of the simulation parameters is expected to further reduce this in the future. Our next step is to run the simulated pulses through the entire GERDA data production chain, and after validating the calibration spectra, to build a background model which incorporates PSD.

[9] M. Agostini *et al.*, Eur. Phys. J. C (2014) **74**: 2764.

4.6 The GERDA Upgrade and LEGEND

Considering the background level and energy resolution achieved by GERDA [10, 11], the projected sensitivity on $T_{1/2}^{0\nu\beta\beta}$ surpassed 10^{26} y in early 2018 - the first experiment to do so. A major data release is planned for summer 2018, with the unblinding of the new data sets scheduled for May. With its unprecedented low background, GERDA remains in the "background-free" regime, where the sensitivity grows linearly with exposure. Thus, to fully exploit the potential of the experiment, we are upgrading the detector and increase the target mass to achieve a higher final exposure by the end of 2019.

In May 2018, all the detector strings will be extracted from the liquid argon and modified as follows: The three natural germanium detectors with a mass of 7.6 kg, together with the lightest (800 g) enriched coaxial type detector, will be replaced by five newly built, enriched inverted coaxial type detectors [12] with a total mass around 9 kg. With the increased target mass of enriched germanium GERDA will have caught up the lost uptime due to the hardware upgrade within a few months. This will be the first time that this new detector type will be operated long-term in liquid argon, thus providing a vital test for the next-generation experiment LEGEND, which is to employ inverted coaxial detectors on a larger scale.

Apart from installing new detectors, we aim to suppress the background in GERDA even further, by introducing two modifications. The optical fibre shroud around the detector strings will be replaced by a new, denser one to improve the efficiency of the liquid argon veto. We will also replace part of the cables to reduce the radioactivity inside the cryostat. Should GERDA observe a first signal, it will benefit from a lower background level, because the sensitivity for signal detection is more sensitive to background and can still be improved. If no signal will be detected, we will demonstrate that an even lower background index is achievable, which will be a crucial step towards the ambitious background goals of LEGEND.

Finally, smaller repairs and modifications are planned: The amplifiers of three detectors were damaged by power surges and will be repaired. All amplifiers will be modified to avoid similar damage in the future and reduce their noise. A few detectors with an increased leakage current will be etched for stabilising their performance. The detector holders will be modified to operate all detectors upright to avoid additional leakage current due to particulates accumulating on the groove between the electrodes if it is faced upwards.

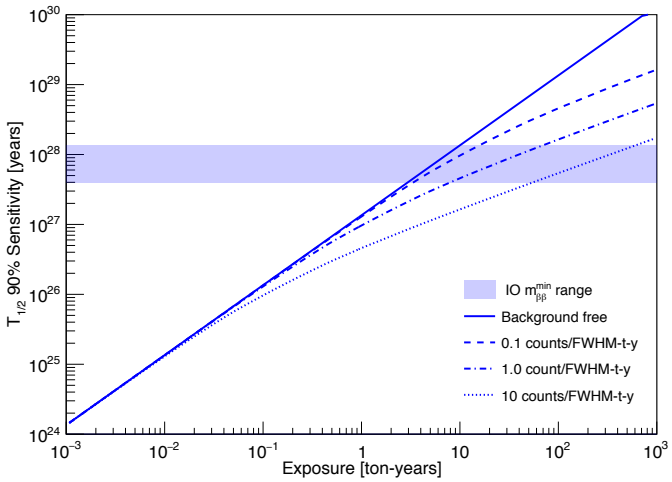

FIG. 4.6 – Sensitivity for a signal discovery in LEGEND, shown as the half-life sensitivity versus exposure. The four curves imply different background scenarios, and the horizontal light blue region shows the effective Majorana neutrino range for the inverted mass ordering scenario.

Once GERDA Phase II ends in late 2019, the cryostat will be modified for housing the first stage of LEGEND [13], the LEGEND-200 experiment. This experiment will combine enriched germanium detectors from GERDA, the Majorana Demonstrator, as well as newly produced diodes to achieve a target mass of 200 kg. The aim is to operate in background-free mode up to an exposure of 1000 kg·y and thus to increase the sensitivity to the half-life by one order of magnitude (Fig. 4.6). LEGEND will be a first step towards a ton-scale germanium experiment. A ton-scale experiment would probe the inverted neutrino mass ordering scenario.

[10] M. Agostini *et al.*, Nature **544** (2017) 47-52.

[11] M. Agostini *et al.*, Phys. Rev. Lett. **120** (2018) 132503.

[12] A Domula *et al.*,
Nucl. Instrum. Meth. A **891** (2018) 106-110.

[13] N. Abgrall *et al.* [LEGEND Collaboration], AIP Conf. Proc. **1894** (2017) no.1, 020027, [arXiv:1709.01980]

5 Dark Matter Search with XENON and DARWIN

Laura Baudis, Yanina Biondi, Adam Brown, Chiara Capelli, Michelle Galloway, Frédéric Girard, Lars Iven, Andreas James, Shingo Kazama, Alexander Kish, Francesco Piastra, Shayne Reichard, Patricia Sanchez Lucas, Kevin Thieme, Julien Wulf

in collaboration with: Columbia University, UCLA, UCSD, INFN, University of Münster, Coimbra University, Subatech, The Weizmann Institute of Science, University of Mainz, MPIK Heidelberg, Rice University, University of Bologna, Nikhef, Purdue University, RPI, NYAD, The University of Chicago, Stockholm University, Albert Einstein Center for Fundamental Physics Bern, University of Tokyo, Kobe University, Nagoya University, LAL, LPNHE

XENON and DARWIN Collaborations

5.1 Introduction

Overwhelming evidence supports a model of our Universe where dark matter outnumbers baryonic matter by a factor of 5 [1]. One compelling dark matter candidate is a Weakly Interacting Massive Particle (WIMP) with a mass $\sim$1 GeV/c^2-10 TeV/c^2, which arises naturally in various extensions to the Standard Model of particle physics [2]. In the field of direct dark matter detection, dual-phase liquid xenon (LXe) Time Projection Chambers (TPCs) have demonstrated rapid progress during the past decade [3–6], and are among the main technologies for probing the allowed parameter space for WIMPs with masses above a few GeV. LXe is intrinsically radio-pure, is capable of powerful self-shielding, and is sensitive to low-energy nuclear recoils (NRs) with good energy resolution. The simultaneous detection of ionisation signals down to the single electron level, together with prompt scintillation down to a few keV, enables 3D position sensitivity for fiducialisation of the target volume. Particularly attractive is also the scalability of a LXe TPC to contain a homogeneous target of several tons. In such large detectors, neutrons can be distinguished from WIMP-induced NRs due to their multiplicity. This makes LXe TPCs unique in their potential to identify dark matter-induced signals.

XENON is an international collaboration of 164 scientists from 21 institutions with the goal to directly detect dark matter particles in an ultra-sensitive, low-background detector, using the liquified noble gas xenon as a target material. The current phase of the project, XENON1T, is a dual-phase TPC with a total mass of LXe of 3.3 t, out of which 2.0 t are in the active target [7]. The detector and its sub-systems are in operation in Hall B of the Laboratori Nazionali del Gran Sasso (LNGS) and the science data taking started in autumn 2016. World-leading results from a first run were published in 2017 [5], and the analysis of the data collected in the subsequent run is in its final stage. The expected sensitivity from this second run is shown in Fig. 5.1.

The upgrade to the XENONnT phase, planned for 2019, will enable XENON to continue leading the direct detection field in the next few years with a sensitivity to dark matter cross sections down to 10^{-48} cm^2 [8]. Figure 5.1 shows the projected sensitivity to spin-independent WIMP-nucleon interactions as a function of WIMP mass, for an exposure of 20 t·y in XENONnT.

[1] P.A.R. Ade et al., Astron. Astrophys., 594:A13, (2016).

[2] G. Bertone, Particle Dark Matter (2013).

[3] A. Tan et al. (PandaX Collaboration), Phys. Rev. Lett. 117(12):121303, (2016).

[4] D.S. Akerib et al. (LUX Collaboration), Phys. Rev. Lett. 118, 021303 (2017).

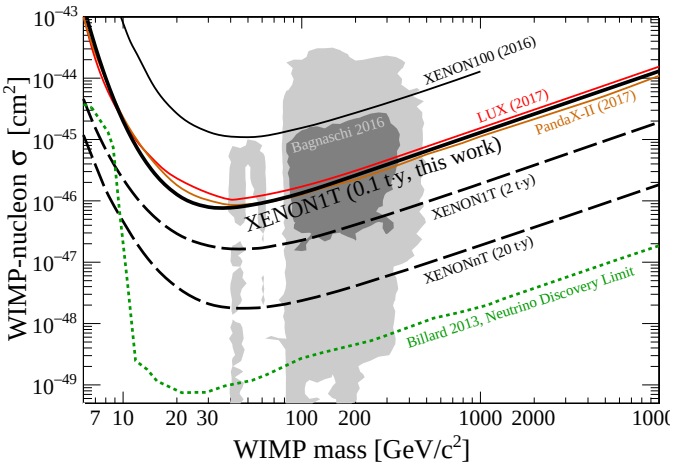

FIG. 5.1 – The projected sensitivity to spin-independent WIMP-nucleon interactions for XENON1T and for XENONnT (dashed black line), assuming an exposure of 20 t·y. Also shown are current results, the sensitivity of XENON1T using 2 t·y of data, and the neutrino discovery limit (dashed orange).

[5] E. Aprile et al., Phys. Rev. Lett. 119, 181301 (2017).
[6] X. Cui et al. (PandaX Collaboration), Phys. Rev. Lett. 119, 181302 (2017).
[7] E. Aprile et al. (XENON Collaboration), Eur. Phys. J. C (2017) 77: 881.
[8] E. Aprile et al., Phys. Rev. D 94 no.12, 122001 (2016).

5.2 Status and First Results from the XENON1T

The XENON1T experiment has collected data with 278.8 days total live time, split into two science runs of 32.1 days (SR0) and 246.7 days (SR1). SR0 was collected between October 2016 and January 18, 2017, when a magnitude 5.7 earthquake caused a two week downtime [9]. SR1 began immediately afterwards and was concluded on February 8, 2018, while the detector continues to run and collect data. The main operational difference between the two science runs is the cathode voltage, which was lowered from -12 kV for SR0 to -8 kV for SR1. All key detector parameters are continuously monitored to ensure operational stability. The LXe level is 2.5 mm above the gate electrode, within sensor reading fluctuations of 2% RMS. The LXe temperature and gaseous xenon pressure were constant at -96.0°C and 1.94 bar, respectively, both $<$0.02% RMS. 32 PMTs are ignored for the analysis, the majority of them (26 PMTs) due to gas leaks into the tubes, and the remaining due to low single photo-electron (SPE) efficiency.

In November 2017 the first WIMP-search results [10] from the XENON1T experiment were published, based on the SR0 science data. Given the 1042 kg fiducial volume this corresponds to an exposure of 35.6 t day. Six background sources are considered in the search region: electronic recoils due to internal and external radioactive contamination, nuclear recoils due to radiogenic neutrons, coherent neutrino-nucleus scattering, accidental coincidences of unrelated prompt scintillation ($S1$) and ionization ($S2$) signals, inward-reconstructed events which occurred on the PTFE walls of the TPC, and finally a small uniform background component to account for elastic recoil (ER) events with anomalous S2 area. The ER and NR components distributions are calibrated using injected ^{220}Rn and an external ^{241}AmBe source respectively. Both calibrations and the dark matter search data are shown in Fig. 5.2 together with the ER and NR models.

The data in a predefined box were blinded until the event selection and background models had been fixed. 99% of the ER band was left unblinded using this selection. Additionally, a small fraction of the total exposure (four live days, corresponding roughly to the XENON100 exposure) were left unblinded. After unblinding, 63 events remain in the search region: $cS1 \in [3, 70]$ and $cS2_b \in [50, 800]$, where $cS1$ and $cS2b$ are the corrected $S1$ signals and the corrected $S2$ signals from the bottom array, respectively. One event at $cS1 = 68.0$ PE, observed in the initial 4-day unblinded data, is at an extreme $(cS1, cS2_b)$ location for all background and signal models. Another event at $cS1 = 26.7$ PE is at the -2.4σ ER quantile. The background components, together with a mass-dependent signal model are considered independently to produce a limit on the WIMP-nucleon interaction cross-section using an extended unbinned profile likelihood. The resulting limit is shown in Fig. 5.3. The strongest limit is 7.7×10^{-47} cm^2 for 35 GeV/c^2 WIMPs.

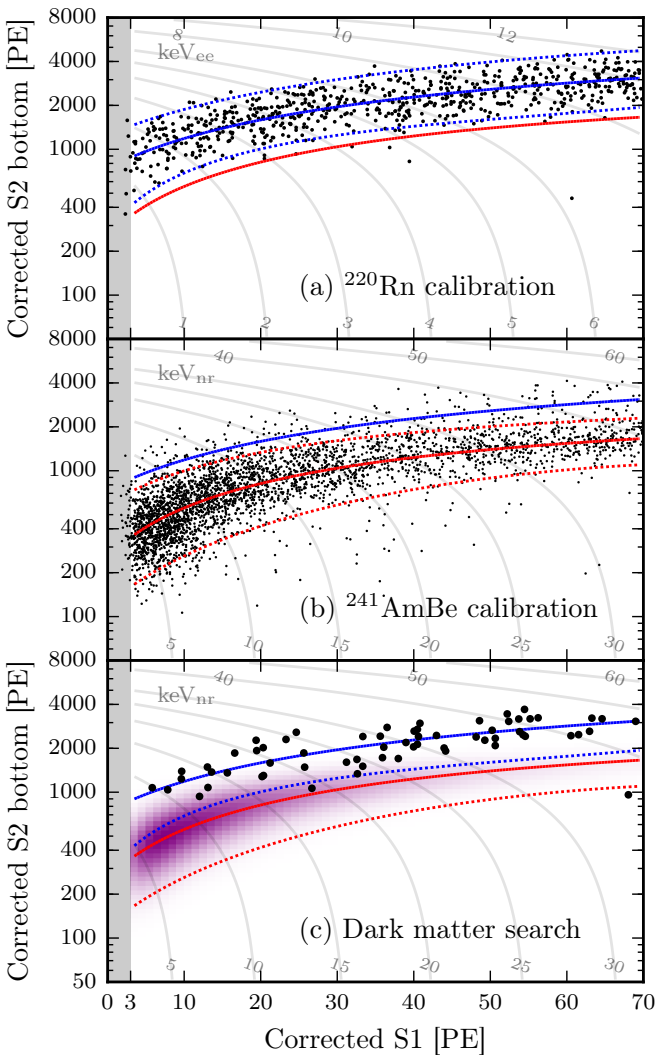

FIG. 5.2 – Observed data in $cS2_b$ vs $cS1$ for (a) ^{220}Rn elastic recoil calibration, (b) ^{241}AmBe calibration, and (c) dark matter search data. Solid and dotted lines are the median and $\pm 2\sigma$ quantiles in $cS2_b$ of the elastic recoil (blue) and nuclear (red) models. The purple shading in (c) shows the signal model for a 50 GeV/c^2 WIMP.

Our research group at the University of Zurich was responsible for significant parts of the analysis for these results, including the development of interaction vertex reconstruction algorithms using a neural network; spatially-dependent signal corrections to compensate for variations in the S2 signal area of up to around 15%; and data-quality selection criteria. In addition we continue to be responsible for ensuring and monitoring the long-term stability of the PMTs and their in-situ calibration using external LEDs. Apart from the standard, spin-independent WIMP analysis, we are leading a few other analysis channels, such as the search for the neutrinoless double beta decay of ^{136}Xe, a search for SuperWIMPs, a search for inelastic WIMP scatters on ^{129}Xe and ^{131}Xe, and detection of solar neutrinos via neutrino-electron scatters.

[9] USGS Database, https://earthquake.usgs.gov

[10] E. Aprile et al., Phys. Rev. Lett. 119, 181301 (2017).

[11] D.S. Akerib et al., Phys. Rev. Lett. 118, 021303 (2017).

[12] A. Tan, et al., Phys. Rev. Lett. 117(12):121303, (2016).

[13] E. Aprile et al., Phys. Rev. D 94 no.12, 122001 (2016).

5.3 The XENONnT Experiment

In parallel to the ongoing operation of the XENON1T detector and analysis of the collected science data, we are working on the upgrade to the XENONnT TPC, which will increase the active LXe target mass to 6 t, improving the sensitivity to WIMP-nucleon interaction by an order of magnitude. Our group is co-responsible for the design and fabrication of the new TPC, for the characterisation measurements and selection of the photosensors, design and production of the PMT voltage-divider circuits, design and production of low-noise, dual-output amplifier boards, cabling on the cold, xenon side, and measurements of the radioactivity levels in the construction materials, including the photosensors.

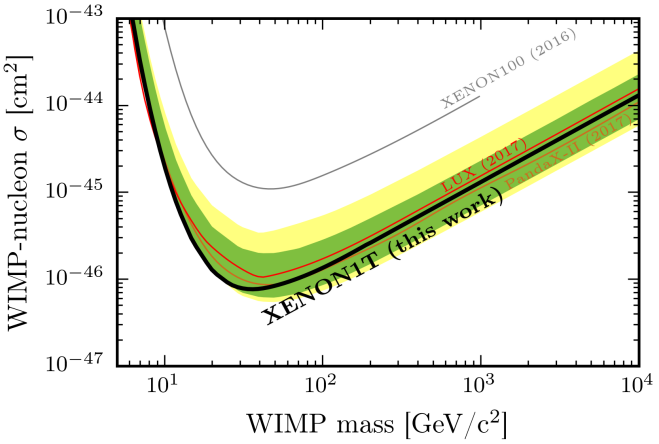

FIG. 5.3 – The limit on the spin-independent WIMP-nucleon cross section at 90% confidence level as a function of WIMP mass for the first result of XENON1T (black line). Green and yellow shading shows the one- and two-sigma sensitivity bands for the same data. Results from LUX [11] (red line), PandaX [12] (brown line) and XENON100 [13] (grey line) are shown for comparison.

Photosensors

As shown in Fig. 5.4, the active volume of LXe in the XENONnT experiment will be equipped with 494 R11410-21 Hamamatsu 3-inch PMTs. These will be assembled in two arrays of 253 (top) and 241 (bottom), to detect both primary and secondary Xe scintillation light with a high collection efficiency and granularity for event vertex reconstruction. Departing from the previous designs for XENON100 and XENON1T, the top PMT array features a pattern of closest hexagonal packing and is more resilient to possible non-functional channels thanks to the increased PMT density. The precision of the xy-position reconstruction is expected to be 10 mm (at 1 σ) at low energies, as in XENON1T.

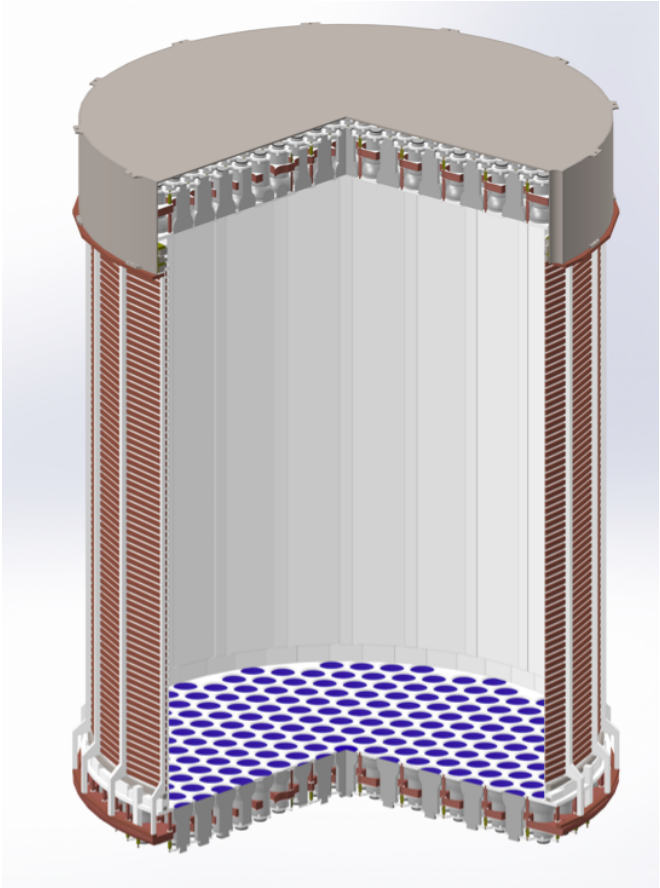

FIG. 5.4 – Technical drawing of the XENONnT time-projection chamber. The scintillation and electroluminescence signals are detected by a total of 494 Hamamatsu R11410-21 PMTs, installed in two arrays above (253 units) and below (241 units) the active LXe target.

Most of the photosensors currently operated in the XENON1T experiment will be re-used for XENONnT, hence about 260 units were newly procured and distributed between the Universities of Stockholm and Zurich for characterisation in LXe. First, the general performance at room temperature is characterised by determining parameters such as amplification gain, dark count and after-pulse rates, timing and performing a HV scan. The measurement of the after-pulse spectra [14] before and after cooling down the PMTs in LXe is of most interest in order to identify potential openings of micro-leaks during the cooling down process.

During cryogenic tests the PMTs are operated in LXe and tested in conditions very similar to those of operation in the XENONnT detector, including gaseous xenon. Our MarmotX xenon detector at the University of Zurich can simultaneously test 10 PMTs distributed in two arrays of 5 PMTs each. Typically the photosensors undergo two cool-down cycles, and are operated one week in LXe and one week in gaseous xenon, and the amplification gain and dark count rate are continuously monitored. We also perform light stress tests, in which the PMTs are exposed to a relatively large amount of light for a certain period of time, thus emulating the conditions of detector calibrations with radioactive sources.

Over the course of six months, a total of 129 PMTs have been tested in liquid and cold gaseous xenon, out of these 51 in MarmotX. So far, ten units were rejected due to failures and sent to Hamamatsu Photonics to be replaced, including eight with identified xenon ion after-pulses and hence leaks in the vacuum seal. Presently we are measuring several replacement units, combined with the characterisation of a pre-amplified signal read-out circuit, which has been recently developed by our group and may allow to improve the signal quality in future experiments.

We have designed and, after extensive tests, produced new, 16 channel NIM amplifier boards for XENONnT, with dual gain output: a high-gain stage with with non-inverting voltage gain of 20 (gain 10 into 50 Ohm load) and a low- gain stage with non-inverting voltage gain of 1 (gain 0.5 into 50 Ohm load). The high-gain stage operates from DC to 250 MHz, the low-gain stage from DC to 200 MHz. Both stages have a 50 Ohm output impedance and are designed to drive 50 Ohm loads. The aim is to increase the dynamic range of the detector, where the gain-20 signal will be used for the low-energy searches, while the gain-1 signal will be employed for the double beta decay search and for the characterisation of the background up to energies of a few MeV.

The Gator low-background counting facility

Much of the material screening for XENONnT, particularly the PMTs, will be performed using the Gator high-purity germanium spectrometer that is owned by the University of Zurich [15]. Its radiopurity and excellent energy resolution ($\sigma_E < 1$ keV at $E \sim 1$ MeV) allow for low-background material radioassay. The spectrometer is shielded from cosmic radiation by operating it in an ultra-low background facility at LNGS at the same depth as the XENON1T detector.

An upgrade of the enclosure for the Gator spectrometer was performed in 2017, with the primary objective of improving the sealing to the external environment in order to reduce radon diffusion into the cavity. The new shielding includes well-sealed ports and edges, a gate valve to isolate the sample loading box, and hermetic electrical feedthroughs to prevent air leaks. Additionally, a new, top-loading glovebox was designed in order to improve the ergonomics for inserting samples. The new design is shown schematically in Fig. 5.5 (Top).

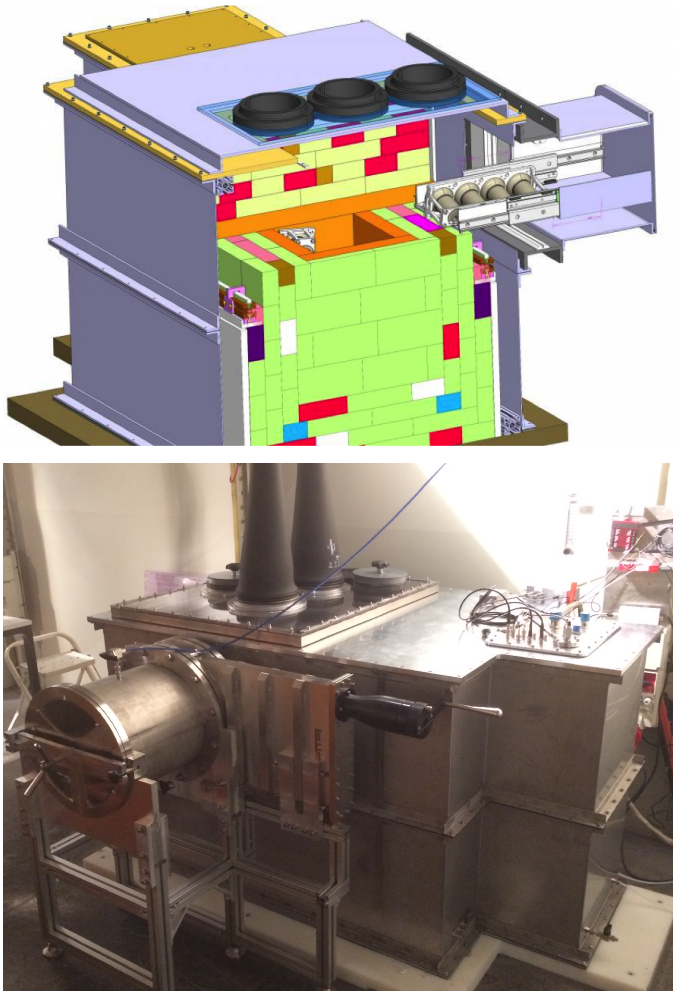

FIG. 5.5 – Top: The design of the new Gator enclosure. It includes well-sealed ports and edges, a gate valve to isolate the screening sample loading box, hermetic electrical feedthroughs to prevent air leaks as well as a new, top-loading glovebox. Bottom: A picture of the new Gator enclosure after assembly was completed in August 2017.

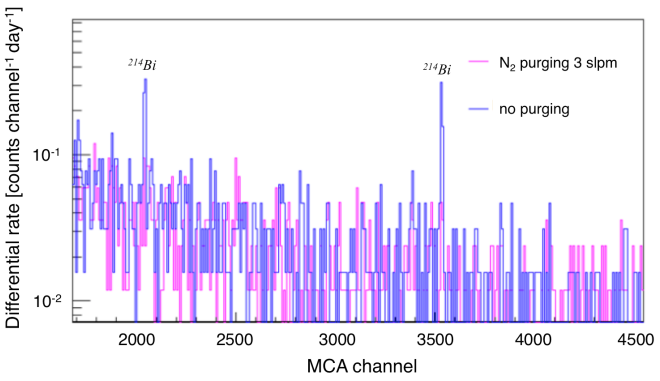

FIG. 5.6 – Disappearance of the ^{214}Bi daughters of radon from a state with no nitrogen flow (blue) and after purging at 3 slpm (pink).

The materials for the housing were procured and tested at UZH, and the construction of the new enclosure, including all of the welded seams, was performed in the UZH machine shop. The new enclosure was shipped to the underground facility at LNGS and installed in August 2017. Prior to installation, the low-background lead and copper shielding was disassembled and cleaned in an ultrasonic bath with ethanol in order to remove any contaminants or dust that accumulated since its initial installation. The shielding was then reassembled and the new closure installed, as shown in Fig. 5.5 (Bottom).

The nitrogen flow rate into the detector cavity was optimised for radon reduction. Initial tests at 3 slpm showed a reduction in radon daughters, as shown by the reduced activity of the ^{214}Bi lines in Fig. 5.6. The upgrade also provided the opportunity to reduce the contribution from induced electromagnetic interfernce: with new electrical feedthroughs and shielding, the noise level was reduced by ∼30%, particularly in the low-energy regime. The detector is now fully operational and acquiring background data specifically to prepare for screening the PMTs for the XENONnT detector.

[14] P. Barrow et al., JINST 12(01):P01024 (2017).

[15] L. Baudis et al., JINST 6, P08010 (2011).

5.4 R&D for the DARWIN Observatory

The new Xurich LXe TPC has been designed and built to investigate the microphysics of particle interactions in LXe at energies below 50 keV, which are relevant for many of the rare event searches using xenon as target material. The instrument and its calibration measurements are described in detail in [16]. The energy calibration is performed with ^{83m}Kr, providing low-energy lines at 9.4 keV and 32.1 keV uniformly distributed within the target volume [17]. These are tagged by exploiting their double-S1

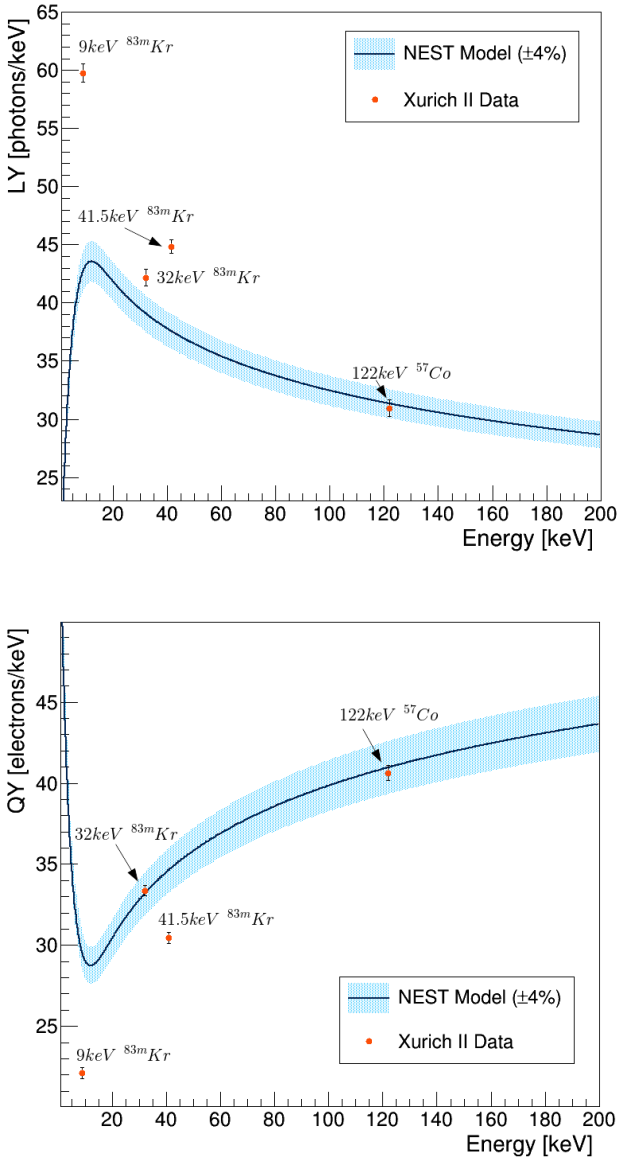

FIG. 5.7 – The scintillation light yield (top) and comparison between the absolute ionisation charge yield (bottom) of liquid xenon for ^{57}Co and ^{83m}Kr energy lines measured with the Xurich TPC, and comparison with the prediction by the NEST model [18].

and double-S2 topology, given the measured half-life of the first excited state at 9.4 keV of (155±1) ns.

We have performed systematic measurements of the absolute scintillation light and ionisation charge yields of LXe in response to electronic recoils [16], with the results for a drift field of 1050 V/cm shown in Fig. 5.7. A comparison with the empirical NEST model [18] suggests that the light (charge) yield at low energies is higher (lower) than the predictions. These discrepancies are currently under investigation, in particular we will compare the data with a new version of NEST.

The absolute calibration is used to predict the poten-

tial of our detector to observe low-energy nuclear recoils, where the energy threshold is estimated based on the predictions of the NEST model [18]. An analysis threshold of 2 PE corresponds to a mean number of 10.5 primary photons, which translates to an energy threshold of (2.3−2.7) keV in nuclear recoil equivalent, depending on the drift field.

The Xenoscope Project

In October 2017, the European Research Council (ERC) funded project Xenoscope has started. The goal of Xenoscope is to conduct research towards the construction of a 50 t LXe observatory, DARWIN [19]. This research is focused on the optimisation of the light collection in a large TPC, on a full-scale TPC demonstrator, as well as on the mitigation of background radioactivity through an extensive material screening campaign. In addition, new shielding schemes will be studied through geometrical optimisation of the detector design.

In the first part of the project, Multi-Pixel Photon Counters (MPPCs), a new type of light sensors based on a solid-state, silicon photo-multiplier (SiPM) technology, will replace the photomultiplier tubes in the Xurich TPC [16]. The upgrade will happen in two phases. First, the top PMT will be replaced by a MPPC array shown in Fig. 5.8. After a series of calibration runs, the bottom PMT will be replaced by a SiPM array, allowing for a direct comparison of the performance of SiPMs to that of PMTs. The Xurich detector will be calibrated using radioactive sources such as ^{83m}Kr, ^{37}Ar (to be produced at PSI as part of this project), ^{57}Co, AmBe and neutrons from a deuterium fusion generator.

The main project aiming at the optimisation of the light collection is the upgrade of the MarmotX detector [20], which is currently used for qualification tests of the XENONnT PMTs, to a two-phase TPC. This cylindrical detector of 15 cm diameter and 10 cm height will be the first LXe TPC to incorporate a 4π light coverage: a top and bottom arrays of 60 SiPM modules (1.2×1.2 cm^2 from Hamamatsu Photonics) each, and 5 SiPMs rings composed of 28 SiPM modules each, for a total of 140 SiPM modules. The design of the detector will be optimised by Monte Carlo simulations of the light collection efficiency and simulations of the drift field by boundary element methods.

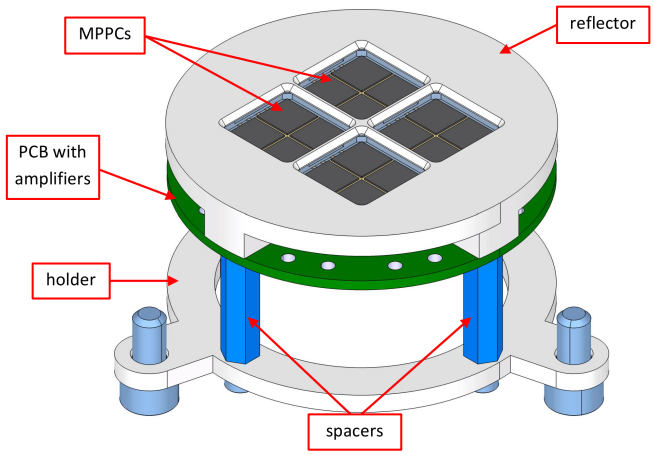

FIG. 5.8 – The top MPPC array which will replace the 2-inch top PMT in the Xurich TPC. It is made out of four 1.2×1.2 cm^2 units from Hamamatsu Photonics, for 16 channels in total.

Finally, the Xenoscope project also aims at the construction of a LXe TPC demonstrator that will be used to investigate the possibility to drift electrons over 2.6 m. This demonstrator will have the full height of the future DARWIN TPC, but will have a diameter of merely 20 cm, incorporating a total of 325 kg of LXe. A LXe filtration system will also be developed to ensure a sufficiently large electron lifetime (≥1 ms) required to drift and extract electrons in the gas phase.

[16] L. Baudis et al., Eur. Phys. J. C, 78 (2018).

[17] A. Manalaysay et al., Rev. Sci. Instrum. 81, 073303 (2010).

[18] M. Szydagis et al., JINST 6, P10002 (2011); M. Szydagis, A. Fyhrie, D. Thorngren and M. Tripathi, JINST 8 C10003 (2013).

[19] J. Aalbers et al. (DARWIN Collaboration), JCAP 1611, 11, 017 (2016).

[20] P. Barrow et al., JINST 12, P01024 (2017).

6 Very High Energy Gamma Ray Astronomy with CTA

F. Canelli, D. Florin, A. Gadola, A. Murtezani, S. Steiner, U. Straumann, A. Vollhardt, D. Wolf

in collaboration with: MPI für Kernphysik Heidelberg, Universität Erlangen, Universität Innsbruck, Universität Tübingen and over 210 institutes from 32 countries

(CTA)

The Cherenkov Telescope Array (CTA) represents the next generation of Imaging Atmospheric Cherenkov Telescopes (IACTs). IACTs, like the present H.E.S.S. [1], MAGIC [2], and VERITAS [3] are ground-based mirror telescopes used to detect gamma rays of energies from several 10 GeV up to hundreds of TeV. Sources of such very high energy (VHE) gamma rays are both galactic and extragalactic, including quasars, supernovae and their remnants, gamma-ray bursts, and possibly dark matter annihilations. The signal is a faint (100 photons/m^2 @ E_γ = 1 TeV) and very fast (few ns) Cherenkov light flash, produced in the shower developing in the Earth's atmosphere after an initial $\gamma \rightarrow e^+e^-$ pair production, allowing the reconstruction of the primary gamma ray's energy and direction. With more than 100 telescopes which will be located in the northern and southern hemispheres, CTA will be the world's largest and most sensitive high-energy gamma-ray observatory. A comprehensive survey of planned research activities with CTA has recently been published [4].

The CTAO gGmbH ("gemeinnützige Gesellschaft mit beschränkter Haftung" according to German law) with official seat in Heidelberg is the interim legal entity to prepare construction and operation of the CTA observatories. In the past year the organisation concentrated to work towards creating a final legal entity in the form of an European Research Infrastructure Consortium (ERIC) with Italy as hosting country. It is expected, that sometime in 2019 the ERIC could officially start. Meanwhile the headquarters have been established in Bologna, Italy, with a growing number of employees, including a CTA project manager. The detailed planning of the infrastructure on the two observatory sites in La Palma (Canary Islands) and at the European Southern Observatory (ESO) area in Chile made significant progress and first geotechnical studies of the sites have revealed promising results. U. Straumann, acted as the director of the CTAO gGmbH until February 2018.

The Zurich group continued to be involved in the design and prototype construction of three projects for CTAO: Camera frontend electronics and mechanical body with safety and power for FlashCam, mirror actuators as well as the master clock for the whole telescope array.

In 2017 our longstanding mechanical technician, Stefan Steiner, went to retirement. Thanks to his wide technical experience, and his strong commitment and dedication the Zurich designs of the mirror actuators and the camera bodies have reached technical maturity and prototypes are now being tested by several other groups. We are happy to welcome his successor Afrim Murtezani in the Zurich CTA team.

[1] B. Opitz *et al.*, (HESS collaboration), AIP Conf. Proc. 1223 (2010) 140.

[2] J. A. Coarasa *et al.*, (MAGIC collaboration), J. Phys. Soc. Jap. Suppl. 77B (2008) 49.

[3] D. Hanna *et al.*, (VERITAS collaboration), J. Phys. Conf. Ser. 203 (2010) 012118.

[4] B.S. Acharya *et al.*, (Cherenkov Telescope Array Consortium), arXiv:1709.07997.

6.1 FlashCam camera body

The FlashCam camera [5] is the first fully digital Cherenkov telescope camera and will suit the mid-size telescope of CTA. The UZH group contributions to the camera have been the development and production of prototype series of the photon-detector modules, which have been handed over to the University of Erlangen for a future mass-production. The second large contribution is the design and production of the whole camera body mechanics including the camera safety control, the power control and distribution, as well as the cooling. The first prototype body was tested in 2015 on a telescope prototype in Berlin and staffed with electronics in Heidelberg during 2016 and 2017. In autumn 2017 the camera was mounted again on the telescope in Berlin, where it became fully operational in a very short period of time and was commissioned successfully in all aspects.

Based on lessons learned the camera body and safety cabinet was slightly improved in several aspects and two new bodies (see Fig. 6.1) have been assembled during 2017. They are considered to be the final versions and will be subject to a review to be organized by the CTAO management. If things go well the two bodies could become the first production camera bodies.

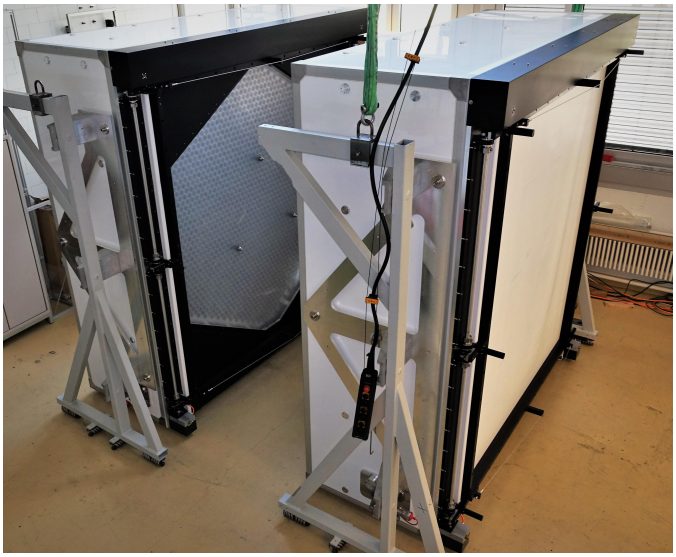

FIG. 6.1 – Two prototype camera bodies for FlashCam cameras in the Zurich workshop, ready-to-ship. The front lid is closed on the right box and opened on the left box.

6.2 Mirror actuator

The 220 actuator sets, which were produced in 2015 are now being installed on the first large scale telescope prototype (LST) which is presently under construction on La Palma (see figure 6.2). First operation is foreseen during summer 2018.

Each set of actuators consists of two actuators and one fix point, allowing to control the direction of a single mirror facet. During the past year several small aspects of the design have been improved, including adjustments of mechanical construction tolerances, stability against corrosion, maintainability and measures to optimise mass production. Several details on the mechanical interfaces to the telescope structures have been adjusted as well.

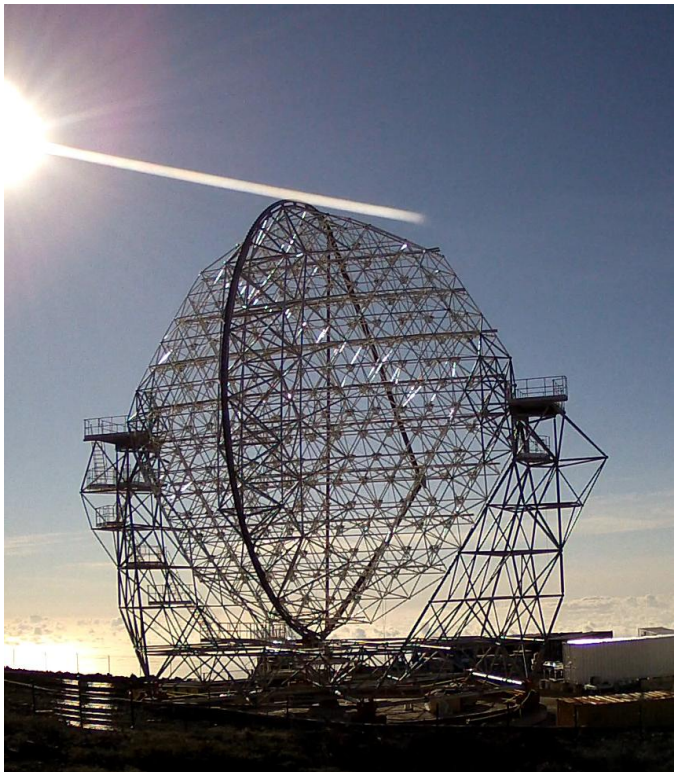

FIG. 6.2 – Prototype LST under construction on La Palma (Canary Islands), picture taken on April 3, 2018

As a next step the Zurich group prepares the production of a new series of 60 prototype sets of actuators to be tested against the specifications as input for the upcoming reviews to be organized by the CTAO management. In parallel to these activities the planning and coordination of the mass production of roughly 12'000 single actuators has started in very close contact with the CTAO management.

[5] G. Pühlhofer *et al.*, (FlashCam Collaboration), arXiv 1211.3684 [astro-ph.IM] (2012).

7 Particle Physics with the SHiP experiment

C. Betancourt, I. Bezshyiko, A. Buonaura, E. Graverini, N. Serra, B. Storaci (till December 2017)

The full SHiP collaboration consists of 52 institutes from Bulgaria, Chile, Denmark, France, Germany, Italy, Japan, Russia, Sweden, Switzerland, Turkey, Ukraine, the United Kingdom and the United States of America.

(SHiP Collaboration)

SHiP is a newly proposed experiment at the CERN SPS accelerator. A 400 GeV proton beam will be dumped on a heavy target in order to produce 2×10^{20} proton-target interactions in five years [1, 2]. After the target there is a hadron stopper, followed by a system of shielding magnets to sweep muons away from the fiducial decay volume. This is followed by a neutrino detector which has a modular structure and employs the Emulsion Cloud Chamber technology. The main unit of the detector is the brick where lead plates acting as passive material for neutrino interactions are interleaved with emulsion films which are tracking devices with micrometric resolution. The main purpose of the neutrino detector is to perform the first direct observation of the tau anti-neutrino, hence it is placed in a magnetic field so to allow the reconstruction of the charge of the τ lepton daughters and hence discriminate ν_τs from $\bar{\nu}_\tau$s. The neutrino detector is followed by a magnetic spectrometer, contained in a 50 m long vessel of pyramidal frustum shape, to measure the charge and the momentum of muons produced in charged current muon neutrino interactions or in $\tau \to \mu$ decays. A straw tagger is placed in vacuum 5 m downstream of the entrance lid of the vessel. An additional background tagger surrounds the fiducial decay volume, its walls enclose 30 cm of liquid scintillator. The Hidden Sector (HS) detector will comprise: a tracking system placed in vacuum at the end of the vessel, made of 5 m long straw tubes organized in 4 stations in a magnetic field of 1 Tm; a high-accuracy timing detector; and a particle identification system featuring electromagnetic and hadronic calorimeters followed by a muon system made of four active layers interlaced with iron.

Several models with Hidden Particles can be tested at the SHiP experiment. In particular, Sterile Neutrinos at the GeV scale can solve several open problems of the Standard Mode, including the asymmetry between matter and anti-matter [3]. These particles can be produced by heavy mesons decays (charmed and beauty mesons). The SHiP sensitivity to Heavy Neutral Leptons (HNLs) are shown in Fig. 7.1 for two different coupling schemes. These studies have been conducted by E. Graverini and N. Serra. Active neutrino cross-sections and angular distributions will also be studied, thanks to a dedicated detector placed between the target and the hidden sector detector [1].

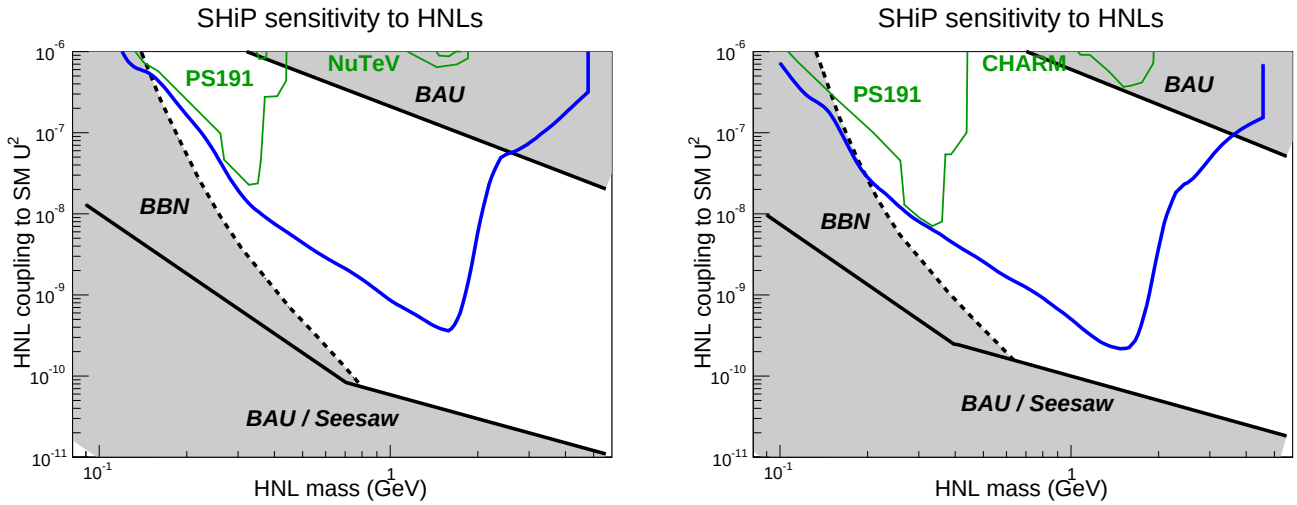

FIG. 7.1 – SHiP's sensitivity to HNLs assuming normal (left) or inverted (right) hierarchy of SM neutrino masses. The parameter space of the νMSM is superimposed.

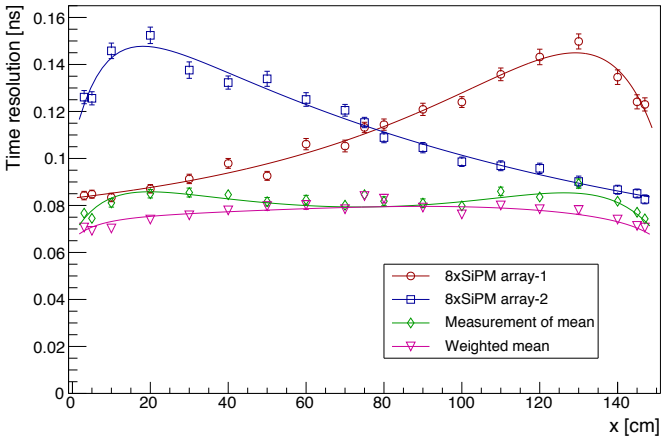

FIG. 7.2 – Time resolution as a function of position along a plastic EJ-200 scintillating bar with dimensions $150 \times 6 \times 1$ cm^3 and read out on both ends with an array of 8 SiPMs.

Our group is taking a leading role in the design and construction of the SHiP veto timing detector. This detector is vital to reject combinatorial di-muon background by requiring events be coincidence in time within 100 ps or less. We have been one of the main proponents of a plastic scintillator based detector read out by arrays of silicon photomultipliers (SiPMs) [4, 5].

Preliminary tests conducted at UZH involved characterisation of several SiPM devices. Tests compared the breakdown voltage, single photon timing resolution, dark count rate, cross talk probability and gain of different type of devices. A comparison of similar devices from different manufacturers was also performed. Measurements of the time resolution of single plastic scintillating bars read out on both ends by an array of SiPMs was also investigated using a radioactive source.

Test-beam measurements at CERN were carried out in June and October 2017 on bars of different types and geometries read out by SiPM arrays. The main results of these studies was the measurements of a time resolution 80 ps along a bar of dimensions $150 \times 6 \times 1$ cm^3 read out on both ends by arrays of 8 SiPMs, as shown in Fig. 7.2. These results were extrapolated to a bar with a length of 170 cm, close to the final proposed bar geometry, indicating a resolution of 85 ps along the bar. Additionally, a custom designed ASIC for read out of SiPM arrays, called MUSIC and developed by the University of Barcelona, was tested for the first time during these test-beams. These measurements paved the way for the design of a timing detector prototype. The prototype will consist of 20 scintillating bars of dimensions $168 \times 6 \times 1$ cm^3, read out on both ends by an array of 8 SiPMs. The data acquisition system will consist of MUSIC boards and SAMPIC waveform digitisers.

Since the Technical Proposal was submitted in 2015, the optimisation phase of the SHiP detector has started.

In preparation for the Technical Design Report, the idea to gain acceptance for Hidden Particle searches by placing the decay volume closer to the beam dump has been explored. Our group gave a crucial contribution proposing to use a conical vacuum vessel, with a shape reproducing the development of the muon free region along the beam axis, thus allowing to gain efficiency and reduce muon induced background.

After the feasibility of such a shaped decay vessel was confirmed by engineers, the subsequent step in the optimisation phase was to study how to shorten the muon shield. The aim of these studies was the optimisation of the shield in order to reduce the amount of iron used, hereby reducing cost while maintaining the same level of muon flux reduction. New methods have been developed for the simulation and the optimisation of shielding magnets taking into account the total mass of the magnets as well as the muon hits in the spectrometer. Our group played a major role in the optimisation of the active muon shield. We showed that is possible to reduce the muon rate to the level of 3×10^5 muons/spill, which is considered to be sufficiently low even though the muon shield was shortened from 53 m to 34 m. This allowed to increase the acceptance for hidden sector particles at the same time reducing the iron by more than 1000 ton (from 2896 to 1845 tons) with respect to the Technical Proposal. These studies are documented in Ref. [6]. The reoptimized SHiP detector is shown in Fig. 7.3.

Aiming the SHiP experiment to be a zero-background experiment, possible background sources to hidden particle searches have to be studied carefully. One of the most dangerous background in searches for hidden particles consists of neutrino interactions. The flux of neutrinos is estimated to be 10^{11} neutrinos per spill, inducing around 7 millions interactions in the proximity of the fiducial volume for 2×10^{20} PoTs.

We simulated a large sample of neutrino interactions and studied the background as a function of the pressure in the vacuum vessel, showing that a pressure of 10^{-3} mbar is sufficient to reduce to a negligible level the number of neutrino interactions in the air. We also studied background rejections by using kinematic selection and veto systems, demonstrating the possibility to reduce the background level to < 0.1 events for 5 nominal years of running.

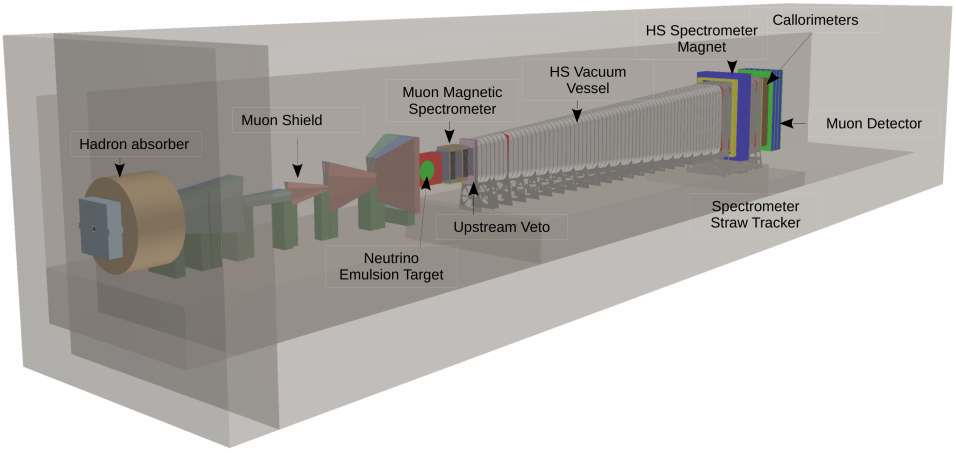

FIG. 7.3 – Overview of the SHiP detector. From left to right: the target, followed by the hadron stopper, the muon shield, the neutrino and Light-Dark-Matter detector (emulsion detector and muon magnetic spectrometer), the Hidden Sector vacuum vessel and the Hidden Sector spectrometer. The latter consists of straw tube tracking stations, a dipole magnet, a veto-timing detector, a calorimeter system and a muon system.

[1] W. Bonivento *et al.*, arXiv:1310.1762, SPSC-EOI-010.

[2] M. Anelli *et al.*, [SHiP Collab.], arXiv: CERN-SPSC-2015-016.

[3] A. Takehiko, S. Blanchet and M. Shaposhnikov, Phys. Lett. B631 151-156 (2005) CERN-SHiP-NOTE-2016-005.

[4] C. Betancourt *et al.*, Journal of Instrumentation 12, P11023 (2017).

[5] C. Betancourt *et al.*, Journal of Instrumentation 12, C02058 (2017).

[6] A. Akmete *et al.*, The SHiP Collaboration, JINST (1748- 0221-12-05-P05011).

8 Particle Physics with LHCb

C. Abellan Beteta, M. Atzeni, R. Bernet, Ch. Betancourt, Ia. Bezshyiko, A. Buonaura (since September 2017), M. Chrząszcz[1] (till August 2017), J. Eschle (since February 2018), J. García Pardiñas (since February 2018), E. Graverini, D. Lancierini (since September 2017), F. Lionetto, A. Mauri, K. Müller, P. Owen, A. Puig Navarro, N. Serra, R. Silva Coutinho, St. Steiner (till July 2017), O. Steinkamp, B. Storaci (till December 2017), U. Straumann, A. Vollhardt, Z. Wang (since January 18) and A. Weiden

[1] also at Henryk Niewodniczanski Institute of Nuclear Physics, Polish Academy of Sciences, Kraków, Poland

The full LHCb collaboration consists of 74 institutes from Brazil, China, Colombia, France, Germany, Ireland, Italy, Poland, Romania, Russia, Spain, Switzerland, the Netherlands, Ukraine, the United Kingdom and the United States of America.

(LHCb Collaboration)

LHCb is a heavy flavour physics experiment at the Large Hadron Collider (LHC) [1] at CERN, optimised for precision tests of the Standard Model (SM) and for indirect searches for physics beyond the Standard Model (BSM) via precision measurements of *CP* violating phases and rare heavy-quark decays. The detector is designed as a forward dipole spectrometer and is fully instrumented in the pseudorapidity range $2 < \eta < 5$, including detectors for precise vertex and track reconstruction, electromagnetic and hadronic calorimeters and detectors for efficient particle identification. The forward acceptance and the ability to trigger on particles with relatively low transverse momentum allow to probe particle production in a unique kinematic range. Many physics analyses go beyond the initial heavy-flavour physics programme and have established LHCb in the wider particle physics community as a successful general-purpose detector in the forward region. These features will be further strengthened in the upgrade of the experiment, foreseen to be installed in the next long shutdown of the LHC in 2019/2020.

Our group is responsible for the operation and maintenance of silicon micro-strip detectors in the tracking system and we contribute to R&D for the upgrade of the tracking detector. Furthermore, our group makes significant contributions to measurements in a variety of rare b-hadron decays and to measurements sensitive to parton densities.

Members of our group hold various positions of responsibility inside the collaboration: Katharina Müller has been a member of the LHCb Speakers Bureau since 2016 and chairs this body since October 2017. Patrick Owen and Albert Puig Navarro are conveners of the semileptonic and rare decays physics analysis working groups, respectively, while Rafael Silva Coutinho has been appointed convener of the rare electroweak penguins sub-working group in January 2018. Barbara Storaci was project leader of the Silicon Tracker project until she left the field in January 2018. Carlos Abellan has been appointed deputy project leader of the Silicon Tracker project in January 2018. The work of our group members has also been rewarded with grants and prizes: Rafael Silva Coutinho was awarded an SNF ambizione grant; Elena Graverini won a UZH Forschungskredit to continue her research upon completion of her PhD thesis in our group in March 2018; Jonas Eschle won a UZH Semester prize for his Bachelor thesis that he completed in our group in summer 2017. Nicola Serra has been appointed successor of Ulrich Straumann upon the latter's retirement from his professorship at our institute in June 2018.

[1] LHCb Collab., JINST 3 S08005 (2008).

8.1 LHCb performance and plans

The LHCb experiment has collected high-quality data with an efficiency exceeding 90% since the startup of the LHC in 2010. During Run 1, which lasted from 2010 till 2012, the LHC collided protons with collision energies of 7 and 8 TeV and LHCb collected a data sample corresponding to an integrated luminosity of 3 fb^{-1}. Most analyses discussed in the following sections are based on this data sample. After a first long shutdown (LS1) in 2013/2014, the LHC resumed operation for Run 2 in 2015, now colliding protons at a collision energy of 13 TeV. For LHCb, the increase in collision energy means a two-fold increase in the production cross section for b quarks. Combined with significant improvements in trigger and selection efficiencies for interesting events, this allows the

experiment to collect interesting b decays at more than twice the rate compared to Run 1. LHCb has already collected data corresponding to an integrated luminosity of 3.7 fb^{-1} in Run 2 and we expect this number to grow to more than 5 fb^{-1} by the end of Run 2 at the end of 2018. Combined with the increased b production cross section and selection efficiency, this implies for most of the analyses discussed below a more than four-fold increase in the numbers of selected signal events compared to the published results.

The scientific output of the collaboration is prolific and well recognized in the community. More than 420 papers on physics analyses have been submitted to peer-reviewed scientific journals and have collected more than 20'000 citations. On average, about 300 oral presentations at international conferences have been assigned by the LHCb Speaker's Bureau per year since 2013.

A comprehensive upgrade of the LHCb detector is planned to be installed during the second long shutdown (LS2) of the LHC in 2019/2020. The goal of this upgrade is two-fold: firstly, relevant detectors will be upgraded to finer granularity, to allow collecting data at a five times higher instantaneous luminosity; secondly, the first, hardware-based level of the current trigger system is going to be abolished to allow selecting interesting events with higher efficiency. Abolishing the hardware trigger requires to read out the full detector and operate a software trigger at the LHC bunch-crossing rate of 40 MHz.

The LHCb collaboration has submitted an expression of interest [2] for further upgrades of the detector in the subsequent long shutdowns of the LHC in 2024-2026 (LS3) and 2030 (LS4). Our group is getting involved in simulation studies and detector R&D for these upgrades.

[2] LHCb Collab., CERN-LHCC-2017-003.

8.1.1 TT detector performance

E. Graverini, A. Mauri, O. Steinkamp, B. Storaci

The Tracker Turicensis (TT) is a large surface silicon microstrip detector installed in front of the magnet of the LHCb spectrometer. The TT was developped and built by our group. It has continued to perform well also in 2017. At the end of the year, more than 99.5% of its 143'360 readout channels were fully operational. One out of the 1050 silicon sensors seems to have developed a bad bias-voltage contact inside the detector box. Simulation studies have shown that the effect on physics analyses is negligible. It has therefore been decided to not attempt a repair in order to avoid the risk associated with opening the detector. In view of the harsh radiation environment at the LHC, the monitoring of radiation damage in the silicon detectors remains an important task. Leakage currents in the detector are monitored continuously and regular charge-collection efficiency scans allow to determine the bias voltage at which the silicon sensors fully deplete. The analysis of these bias-voltage scans has been a topic of the PhD thesis of Elena Graverini. A paper describing the method and results is currently under collaboration-wide review. The results of our studies agree well with expectations from a detailed model calculation. Based on these results, we expect no degradation of the detector performance until its foreseen replacement during the LHCb upgrade in LS2.

8.2 LHCb upgrade

C. Abellan, Ch. Betancourt, Ia. Bezshyiko, O. Steinkamp

Despite its excellent performance, the current TT detector will have to be replaced as part of the LHCb upgrade in LS2, since its front-end readout electronics is not compatible with the upgraded readout scheme. The replacement for the TT, dubbed Upstream Tracker (UT), is being developed by a collaboration including our group as well as CERN and six institutions from Italy, Poland and the US [3]. One of the most critical items is the development of the front-end readout chip (SALT). Carlos Abellan has made major contributions towards tests on prototype chips and our group has taken the full responsibility for the development of test infrastructure for the quality assurance of the final chips. In particular, Iaroslava Bezshyiko is developing readout and analysis software for this project as part of her PhD thesis in our group. Exploiting his expertise in FPGA programming, Carlos Abellan has also taken the responsibility for the development of the UT specific firmware needed to process the detector data in the LHCb readout boards.

[3] LHCb Collab., CERN-LHCC-2014-001.

8.3 Physics results

The LHCb collaboration has published about 50 papers on physics analyses during the past year [4], covering a wide range of topics. A brief summary of a few selected highlights is given here, followed by slightly more detailed discussions of analyses with direct contributions from our group.

One of the LHCb results that echoed most in the particle physics community is the measurement of the ratio of branching fractions [5]

$$R(K^*) = \frac{\mathcal{B}(B^0 \to K^* \mu\mu)}{\mathcal{B}(B^0 \to K^* ee)}$$

in two regions of the squared dilepton invariant mass (q^2). In the SM, this quantity is expected to be very

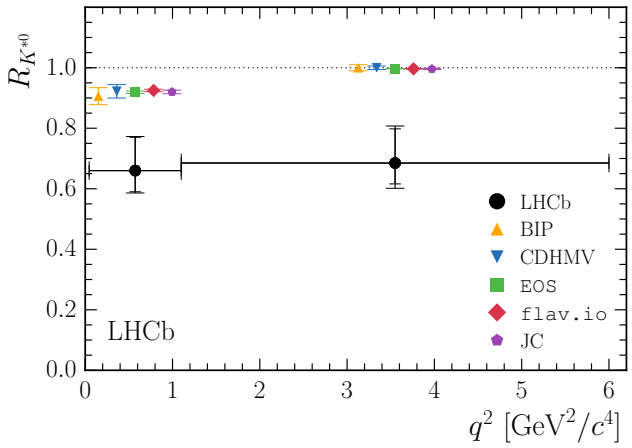

FIG. 8.1 – Comparison of the LHCb measurements of $R(K^*)$ with Standard-Model predictions: BIP [6] CDHMV [7], `EOS` [8], `flav.io` [9] and JC [10]. Data points for the predictions are displaced horizontally for clearer presentation.

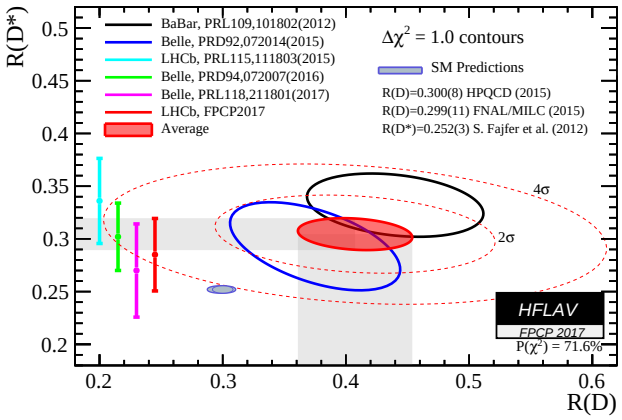

FIG. 8.2 – Measured values for $R(D^{(*)})$ and $R(D)$ by the BaBar, Belle and LHCb experiments. The Standard Model prediction is also shown.

close to unity, with only small deviations due to the mass difference between muons and electrons. The LHCb results are lower than predicted in the SM as is shown in Fig. 8.1. Intriguingly, the measured value (especially that in the region $1.1 < q^2 < 6.0$ GeV^2) is numerically coherent with a set of anomalous results by LHCb, consisting of the observables P_5' [11, 12] and the ratio of branching fractions $R(K^*) = \mathcal{B}(B^0 \to K^*\mu\mu)/\mathcal{B}(B^0 \to K^*ee)$ [5]. Our group is involved in a variety of measurements that are aimed at clarifying the origin of these anomalies, as discussed in Sec. 8.3.1.

The Lepton Flavour Universality (LFU) ratio $R(D^{(*)}) = \mathcal{B}(B \to D^{(*)}\tau\nu)/\mathcal{B}(B \to D^{(*)}\mu\nu)$ has been measured by LHCb [13] as well as by the experiments BaBar [14, 15] and Belle [16, 17]. The LHCb measurement used the decay $\tau \to \mu\nu_\tau\overline{\nu}_\mu$ to reconstruct the τ lepton. The results from all three experiments are higher than the value expected in the SM. Combined, the measurements deviate by about four standard deviations from SM predictions, as summarized in Fig. 8.2 (reproduced from Ref. [18]). Recently, LHCb has published a new measurement of $R(D^*)$ using the hadronic decay mode of the τ lepton, $\tau \to 3\pi\nu_\tau$. The result of this measurement is compatible with the SM as well as with previous measurements [19]. While its overall uncertainty is larger than those of the earlier measurements, it has different systematics. Future improvements of this measurement with larger statistics will provide an important consistency check.

In addition, LHCb has measured the LFU ratio $R(J/\psi) = \mathcal{B}(B_c \to J/\psi\tau\nu)/\mathcal{B}(B_c \to J/\psi\mu\nu)$ [20] for the first time. This measurement is still limited by statistics due to the small production rate of B_c mesons. However, it provides an important proof of principle, since in the future it will be important to measure LFU ratios in complementary channels. Our group is working towards a measurement in related decays with higher statistics, as described in Sec. 8.3.3.

LHCb has made many high-impact measurements that demonstrate it should be considered not only a dedicated B-physics experiment but rather a general purpose experiment covering the forward direction at the LHC. For instance, the collaboration reported the first observation of the doubly charmed baryon Ξ_{cc}^{++}, using the decay channel $\Lambda_c^+ K^-\pi^+\pi^-$ [21]. Also, LHCb presented the first measurement of the effective lifetime of the decay $B^0_{(s)} \to \mu^+\mu^-$ [22]. LHCb has also contributed to searches for Hidden Sector particles, for example setting limits on the existence of Dark Photons [23].

[4] http://lhcb.web.cern.ch/lhcb/

[5] LHCb Collab., Phys. Rev. Lett. **113** (2014), 151601.

[6] M. Bordone, G. Isidori and A. Pattori, Eur. Phys. J. C**76** (2016) 440.

[7] B. Capdevila, S. Descotes-Genon, L. Hofer and J. Matias, JHEP **04** (2017) 016.

[8] N. Serra, R. Silva Coutinho and D. van Dyk, Phys. Rev. D **95** (2017) 035029.

[9] D. Straub *et al.*, flav-io/flavio v0.19

[10] S. Jäger and J. Martin Camalich, Phys. Rev. D **93** (2016) 014028.

[11] LHCb Collab., Phys. Rev. Lett. **111** (2013) 191801.

[12] LHCb Collab., JHEP **02** (2016) 104.

[13] R. Aaij *et al.* [LHCb Collab.], Phys. Rev. Lett. 115 (2015) 111803, arXiv:1506.08614

[14] J. P. Lees *et al.* [BaBar Collab.], Phys. Rev. Lett. **109**, 101802 (2012).

[15] J. P. Lees *et al.* [BaBar Collab.], Phys.Rev.D **88**, 072012 (2013).
[16] M. Huschle *et al.* [Belle Collab.], Phys. Rev. D **92**, 072014 (2015).
[17] A. Abdesselam *et al.* [Belle Collab.], arXiv:1603.06711
[18] Heavy Flavour Averaging Group (HFLAV), https://hflav.web.cern.ch/
[19] R. Aaij *et al.* [LHCb Collaboration], arXiv:1708.08856.
[20] R. Aaij *et al.* [LHCb Collaboration], arXiv:1711.05623
[21] R. Aaij *et al.* [LHCb Collaboration], Phys. Rev. Lett. **119** (2017) 112001.
[22] R. Aaij *et al.* [LHCb Collaboration], Phys. Rev. Lett. **118** (2017) 191801.
[23] R. Aaij *et al.* [LHCb Collaboration], Phys. Rev. Lett. **120** (2018) 061801.

8.3.1 Study of $b \to s\ell^+\ell^-$ transitions

M. Atzeni, A. Mauri, E. Graverini, F. Lionetto, P. Owen, A. Puig Navarro, N. Serra, R. Silva Coutinho, Z. Wang

Recent studies of rare semileptonic decays of beauty mesons, mediated through virtual quantum loops, reported intriguing discrepancies with SM predictions, in particular in angular analyses of the $B \to K^{*0}\mu^+\mu^-$ decay [24] and ratios of branching fractions of $B^{(+,0)} \to K^{(+,*0)}\mu^+\mu^-$ and $B^{(+,0)} \to K^{(+,*0)}e^+e^-$ [25,26]. Whilst the individual significances of the present results are still inconclusive, these deviations seem to form a coherent pattern. Global fits to all these observables report deviations from SM predictions at the level of four standard deviations [27].

In order to achieve a further understanding on the nature of these anomalies, our group is involved in several key measurements testing LFU. The primary goal of our effort is to perform an angular analysis of the decay $B^0 \to K^{*0}e^+e^-$ and compare the results with those obtained in $B \to K^{*0}\mu^+\mu^-$.As a first step towards this goal, measurements of the difference of *CP*-averaged angular observables in the decay $B^0 \to K^{*0}e^+e^-$ have been performed in a simplified counting experiment using the data of $3\,\text{fb}^{-1}$ collected in Run 1. The results are found to be comparable with those obtained in the decay $B^0 \to K^{*0}\mu^+\mu^-$ and compatible with SM predictions within their currently still significant statistical uncertainties. This analysis has been the main topic of the PhD thesis of Federica Lionetto. We also pursue for the first time a full simultaneous amplitude analysis of the muonic and electronic decay modes, which we find to have a compelling discovery potential, as discussed in Sec. 8.3.2. Finally, complementary measurements of ratios of branching fractions, *e.g.* $R_{K\pi} = \mathcal{B}(B^0 \to K\pi\mu^+\mu^-)/\mathcal{B}(B^0 \to K\pi e^+e^-)$ and $R_{K\pi\pi} = \mathcal{B}(B^+ \to K\pi\pi\mu^+\mu^-)/\mathcal{B}(B^+ \to K\pi\pi e^+e^-)$ are led by our group. For the electron modes these are also first observations of the respective decays.

[24] R. Aaij *et al.* [LHCb Collab.], JHEP **02** (2016) 104.
[25] R. Aaij *et al.* [LHCb Collab.], PRL **113** (2014), 151601.
[26] R. Aaij *et al.* [LHCb Collab.], JHEP **08** (2017) 055.
[27] B. Capdevila *et al*, **1801** (2018) 093.

8.3.2 Towards establishing New Physics in $B \to K^{*0}\ell^+\ell^-$ decays

A. Mauri, N. Serra, R. Silva Coutinho

Deviations from SM predictions in angular analyses of the decay mode $B \to K^*\mu^+\mu^-$, notably in the observable P_5', have been suggested as potential signatures of Physics Beyond the SM (BSM). However, non-perturbative QCD contributions, that are difficult to assess reliably from first principles, could either mimic or camouflage BSM effects. We investigate the prospects to disentangle these effects in an unbinned amplitude analysis of this decay mode, relying on state-of-the-art parametrisations of non-perturbative contributions [28]. A simultaneous analysis of theory predictions, measurements of semileptonic decays and measurements of the hadronic decays $B \to K^*J/\psi$ and $B \to K^*\psi(2S)$ is performed to control systematic uncertainties related to the model dependence on direct fits to the underlying Wilson Coefficients.

The deviations observed in angular observables, combined with measurements of R_K and R_{K^*}, hint towards a possible violation of LFU. We propose a novel approach to independently and complementary probe this hypothesis by performing a simultaneous amplitude analysis of the decay modes $B^0 \to K^{*0}\mu^+\mu^-$ and $B^0 \to K^{*0}e^+e^-$ [29]. This method enables the direct determination of observables that encode potential non-equal couplings of muons and electrons, and are found to be insensitive to non-perturbative QCD effects. If the current hints for deviations are indeed due to BSM effects, our approach could allow a discovery of these effects with the dataset collected in Run 2. Figure 8.3 illustrates the usefulness of the method by combining the information from angular analyses and branching ratio measurements.

[28] M. Chrzaszcz, A. Mauri, N. Serra, R. Silva Coutinho and D. van Dyk, arXiv:1805.06378.
[29] A. Mauri, N. Serra and R. Silva Coutinho, arXiv:1805.06401.

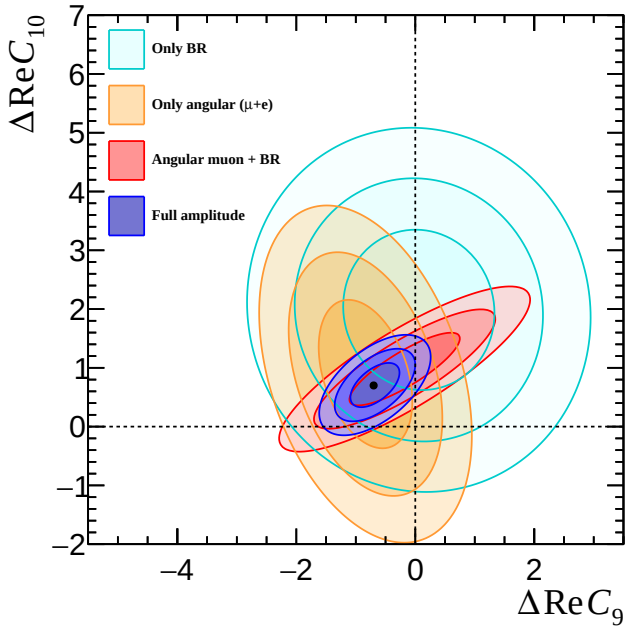

FIG. 8.3 – Projected sensitivity to BSM effects in the Wilson Coefficients $\mathcal{C}_9$ and $\mathcal{C}_{10}$ for the expected statistics after Run 2. The relative contributions (1, 2, 3 σ contours) from each step of the analysis are shown in different colours, together with the result of the full amplitude method.

8.3.3 Semileptonic decays

Ia. Bezshyiko, A. Buonaura, E. Graverini, P. Owen, J. Pardiñas, N. Serra

The strongest evidence for a possible violation of LFU is currently seen in measurements of the branching fractions of semileptonic decays involving a τ lepton, in particular the measurement of the observables $R(D)$ [30,31] and $R(D^*)$ [30–32]. The observed enhancement can be explained in many extensions to the SM, which preferentially couple to third generation leptons. Examples are models with an additional charged Higgs boson or a leptoquark.

Our group is involved in a measurement of $R(D^+) = \mathcal{B}(B \to D^+\tau\nu)/\mathcal{B}(B \to D^+\mu\nu)$, which has the potential to disentangle enhancements to the observables $R(D)$ and $R(D^*)$. An illustration of the sensitivity for $R(D^+)$ is shown in Fig. 8.4. We are also involved in preparations for a test of Lepton Universality in the ratio $R(\Lambda_c^*) = \mathcal{B}(\Lambda_b^0 \to \Lambda_c^*\tau\nu)/\mathcal{B}(\Lambda_b^0 \to \Lambda_c^*\mu\nu)$, which will be one of the main topics for the PhD thesis of Iaroslava Bezshyiko. The measurement of $R(\Lambda_c^*)$ provides complementary information to those of $R(D)$, $R(D^*)$ and $R(D^+)$, since it concerns the decay of a fermion, which behaves differently under the laws of angular momentum conservation. In preparation for this measurement, we have been involved in a phenomenological analysis of the decay, designed to control uncertainties related to QCD effects [34].

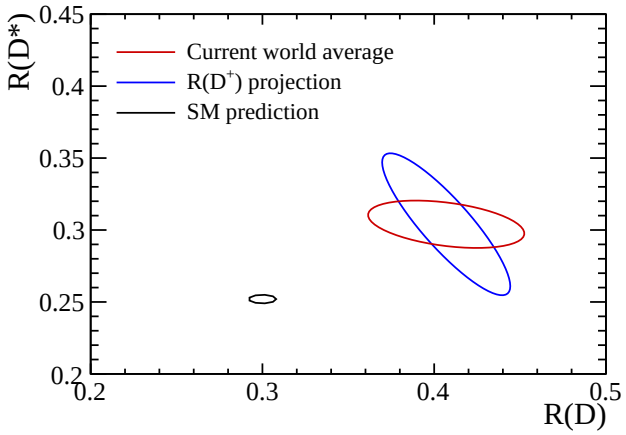

FIG. 8.4 – Projection for the observable $R(D^+)$ for Run 2 of LHCb, compared with the current world average [33] of the observable $R(D^{(*)})$. This measurement has the potential to break the correlation between $R(D)$ and $R(D^*)$.

[30] J. P. Lees *et al.* [BaBar Collab.], Phys.Rev.D **88**, 072012 (2013).

[31] M. Huschle *et al.* [Belle Collab.], Phys. Rev. D **92**, 072014 (2015).

[32] LHCb Collab., Phys. Rev. Lett. **115** (2015) 111803.

[33] HFAC Collaboration http://www.slac/stanford.edu/xorg/hfag

[34] P. Böer *et al.*, arXiv:1801.08367

8.3.4 Charmless *b*-hadron decays

J. García Pardiñas, R. Silva Coutinho

Measurements of time-dependent *CP*-violating asymmetries in decays of B_s^0 mesons to two vector mesons, such as $\phi(1020)$ or $K^*(892)$, provide sensitive probes for as-yet undiscovered heavy particles that can enter in penguin quantum loops. Our group has been involved in the updated measurement of the *CP*-violating phase $\phi_s^{s\bar{s}s}$ and triple-product asymmetries in $B_s^0 \to \phi\phi$ decays using an integrated luminosity of 5.0 fb^{-1} [35]. The results are found to be consistent with the hypothesis of *CP* conservation. Moreover, an improved limit has been set on the branching fraction of the decay $B^0 \to \phi\phi$ [35].

The decay $B_s^0 \to K^{*0}(\to K^+\pi^-)\overline{K}^{*0}(\to K^-\pi^+)$ is another example of a transition dominated by gluonic penguins, in this occasion with a $b \to sd\bar{d}$ quark content. A key feature of this decay mode is the possibility to control the theoretical uncertainty on the associated phase $\phi_s^{d\bar{d}}$ via a U-spin analysis of the decay $B^0 \to K^{*0}\overline{K}^{*0}$.

The first measurement of $\phi_s^{d\bar{d}}$ has been recently performed using the Run 1 data set [36]. To increase the available statistics, not only the $K^{*0}(\overline{K}^{*0})$ resonance was inspected, but also several scalar, vector and tensor $K\pi$ components present in a two-dimensional $K\pi$ mass window from 750 to 1600 MeV/c^2. The *CP*-violating phase has found to be compatible with SM predictions within uncertainties. The longitudinal polarisation fraction of the $B_s^0 \to K^{*0}\overline{K}^{*0}$ decay has been found to be lower than predicted by the SM, confirming an earlier measurement [37].

Our group has also contributed to Dalitz-plot analyses of the decay mode $B^0 \to K_S^0\pi^+\pi^-$. The *CP* asymmetry between the conjugate $\bar{B}^0 \to K^*(892)^-\pi^+$ and $B^0 \to K^*(892)^+\pi^-$ decay rates is determined to be -0.308 ± 0.062, constituting the first observation of a non-vanishing *CP* asymmetry in this mode [38]. Furthermore, our group is leading the update of the search for *CP* violation in the decay $\Lambda_b^0 \to K_S^0 p\pi^-$. The asymmetry in this decay mode is expected to be large and its measurement has the potential to yield the first observation of *CP* violation in the b-hadron sector.

[35] LHCb Collab., LHCb-CONF-2018-001, https://cds.cern.ch/record/2314360.

[36] LHCb Collab., J. High Energy Phys. **03** (2018) 140.

[37] LHCb Collab., Phys. Lett. B**709** (2012) 50.

[38] LHCb Collab., arXiv:1712.09320, to appear in PRL

8.3.5 Measurements sensitive to parton distributions

M. Chrząszcz, K. Müller, A. Weiden

Measurements of the production cross-section of electroweak bosons constitute an important test of the SM at LHC energies. Since predictions in perturbative quantum chromodynamics are known at the percent level, these measurements are sensitive to the momentum distribution of the partons in the proton. Inclusive measurements of electroweak boson production as well as measurements of electroweak boson production with jets have been performed by LHCb in the past years in various decay channels with significant contributions from our group [39–42]. Many of these measurements are now entering precision area aiming to reach systematic uncertainties below the %-level.

Andreas Weiden performs in his PhD thesis a measurement of low mass Drell-Yan production down to masses of 10 GeV^2. He developed new methods to control the backgrounds at low masses which are hardly distinguishable from signal. A different approach is taken in the Bachelor thesis of Thomas Neuer who uses machine learning techniques to distinguish signal from background. The two different approaches can in the end be used to study systematic effects.

[39] LHCb Collab., Phys. Lett B**776** (2017) 430.

[40] LHCb Collab., JHEP **09** (2016) 136.

[41] LHCb Collab., JHEP **05** (2016) 131.

[42] LHCb Collab., Phys. Lett. **B767** (2017) 110.

[43] LHCb Collab., JHEP **08** (2011) 034.

8.4 Outreach activities

K. Müller, A. Puig Navarro, O. Steinkamp

Besides our contributions to the LHCb detector and physics analyses, members of our group have also engaged in a variety of outreach activities. We participated with a stand at "Scientifica 2017", the Zurich Science days organised jointly by UZH and ETHZ. We carried out advanced training days in particle physics for high-school teachers and organised the International Masterclass in particle physics [44] for high-school students. O. Steinkamp and A. Puig Navarro contributed to the Outreach, education and diversity session at the 2017 edition of the EPS Conference on High Energy Physics [45, 46]. K. Müller has been appointed Swiss representative in the International Particle Physics Outreach Group (IPPOG).

[44] http://physicsmasterclasses.org/

[45] A. Puig Navarro *et al.* [LHCb Collab.], PoS(EPS-HEP2017)565

[46] O. Steinkamp *et al.* [LHCb Collab.], PoS(EPS-HEP2017)569

8.5 Summary and Outlook

The LHCb experiment has again performed very well throughout the 2017 LHC run, operating stably and collecting high-quality data with high efficency. The LHCb collaboration has continued to produce physics analyses of high quality, resulting in about 50 publications in peer-reviewed journals and more than 300 oral presentations at international conferences. Analyses of the data collected in Run 2 data are ongoing and significant improvements in the precision of many measurements are expected in the near future. The preparation of the LHCb upgrade for the long shutdown LS2 in 2019/2020 is underway and studies for further upgrades in LS3 and LS4 are starting.

Our group has continued to make important contributions to the operation of the experiment, to physics analyses and to the preparation for the upgrade.

9 Particle physics with the CMS experiment at CERN

T. Årrestad, D. Brzhechko, L. Caminada, F. Canelli, A. de Cosa, P. Bärtschi, R. del Burgo, S. Donato, C. Galloni, M. Gienal, T. Hreus, St. Leontsinis, B. Kilminster, I. Neutelings, D. Pinna, G. Rauco, P. Robmann, D. Salerno, K. Schweiger, C. Seitz, Y. Takahashi, A. Zucchetta

in collaboration with: CMS - Collaboration

The CMS experiment acquired a record year of data in 2017, collecting over 50 fb^{-1} of proton-proton collisions with a center of mass energy of 13 TeV. A new pixel detector, built largely at UZH in collaboration with PSI and ETH, was installed in February 2017, just prior to this data taking period. This detector provided improved vertex resolution for primary and secondary production of charged particles, and higher hit efficiencies and rate capabilities.

Here we present an overview of our CMS activities. Our major activity in 2017 was calibrating and understanding the data from the new 4-layer Phase 1 pixel detector system. We have also begun design studies of a future pixel detector upgrade for the Phase 2 operation of the LHC (HL-LHC). Our group has taken responsibility for a pixel detector that will extend CMS tracking coverage to a more forward detector region; it is envisioned to be ready in 2024. Besides our work on the original and upgraded pixel detectors, we are also involved in trigger development and monitoring as well as physics data analysis on a number of different topics.

Our physics analysis program addresses fundamental questions in particle physics. After the discovery of a Higgs particle at the LHC [1], studies of its properties are among the primary goals. We are testing the fermionic couplings of the Higgs boson, with several analyses geared towards its couplings to tau leptons, top quarks, and bottom quarks. We are testing several theoretical models which could extend the Standard Model (SM), by directly searching for new particle states of mass up to 4 TeV. These generate loop corrections with the necessary cancellations to stabilize the Higgs boson mass. Models such as supersymmetry (SUSY), extra dimensions, and vector-like quarks justify the low Higgs boson mass, and predict a wide range of new particles, which we are sifting through CMS data to observe. We have also begun a new analysis program, testing for violations of lepton flavor universality.

Members of our group play important coordination roles. In the period covered by this report, S. Donato lead the High Level Trigger (HLT) group. C. Seitz acted as subgroup convener within the inclusive SUSY physics group. A. de Cosa led the pixel monitoring group, and was subgroup convener within the Beyond 2 Generations physics group, C. Galloni was convener of the tau lepton identification group. S. Donato and L. Caminada are members of the Swiss Tier 3 computing steering committee. F. Canelli is on the CMS Management Board, and B. Kilminster is on the Management Board for the Phase 2 upgrade and the Tracker group.

[1] ATLAS collaboration, Phys. Lett. B **716** (2012) 29; CMS collaboration, Phys. Lett. B **716** (2012) 30.

9.1 The CMS experiment

CMS [2] is one of the multipurpose detectors at the LHC. It consists of different layers of detectors optimized for position and energy measurements of particles produced in collisions. An all-silicon tracker, an electromagnetic calorimeter, and a hadronic sampling calorimeter are all contained within a large-bore 3.8 T superconducting solenoid. Beyond the solenoid there are four layers of muon detectors. The CMS tracker is composed of the inner pixel detector and the outer silicon strip detector. The upgraded pixel detector, installed in 2017, consists of four barrel layers (BPIX) at 2.9, 6.8, 10.9, and 16.0 cm, and three forward/backward disks at longitudinal positions of $\pm$32, 36, and 46 cm, and extending in radius from about 6 to 15 cm. The high segmentation of the pixel detector allows for high-precision tracking in the region closest to the interaction point. The pixel detector information is crucial for primary vertex and pile-up vertex reconstruction, and identification of long-lived τ-leptons and B-hadrons. The performance of this newly installed pixel detector has been excellent. The barrel pixel detector was built with major contributions from the Swiss Consortium of PSI, ETH and the University of Zurich.

[2] CMS collaboration, JINST **3** (2008) S08004.

9.2 Detector maintenance and operation

The pixel detector is a central component in the reconstruction of high-quality data used in CMS physics anal-

yses. With more than 100 million channels, it provides most of the data of the CMS experiment, allowing precise tracking of charged particles near the point of their creation. Our group made significant contributions to the operation of the pixel detector as well as the re-calibration during technical stops of the accelerator. We are responsible for the monitoring of detector performance and operational parameters, which are crucial in order to respond with preventive actions that ensure high-quality data.

In particular, we keep track of the evolution of the radiation damage to the silicon sensors with increasing luminosity, measuring threshold and noise distributions, as well as pixel hit resolutions, and determine the impact of dynamic inefficiencies in the pixels. As responsible for monitoring the effect of radiation on the health of the pixel detector, we developed a robust system to verify the evolution of the leakage current in the silicon sensors as a function of the integrated luminosity, and hence, on the radiation dose absorbed by the system. Figure 9.1 shows how the leakage current circulating in the sensors increases with the increase in integrated luminosity, for the four barrel layers. The pixel hit resolution of all regions of the pixel detector is studied to verify the detector is operating optimally and the reconstruction parameters are properly set (see Fig. 9.2).

During the last two months of 2017 operation, an issue with the DC-DC converters used in the power system of the pixel detector occurred. An increasing number of DC-DC converters failed, such that 67 out of 1128 converters were unresponsive by the end of the run. In order to investigate the problem and ensure the best possible performance during 2018, the pixel system was extracted for repair in the technical stop at the end of 2017. Within less than a month, we were able to replace all DC-DC converters with new components, substitute modules in the innermost layer that had been damaged as a consequence of the DC-DC converter failure, and resolve system-level

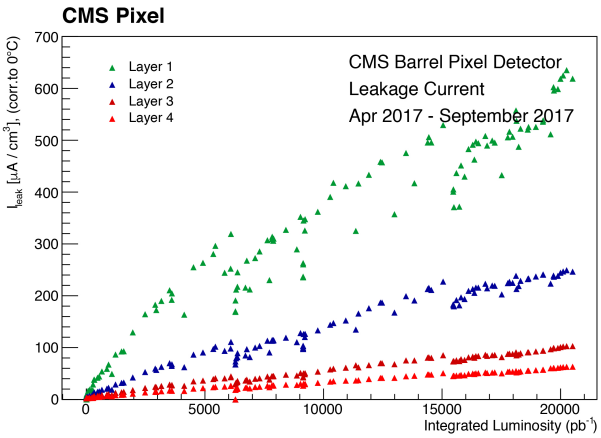

FIG. 9.1 – The CMS Phase 1 pixel detector leakage current per unit of silicon volume for the four barrel layers as a function of the integrated luminosity.

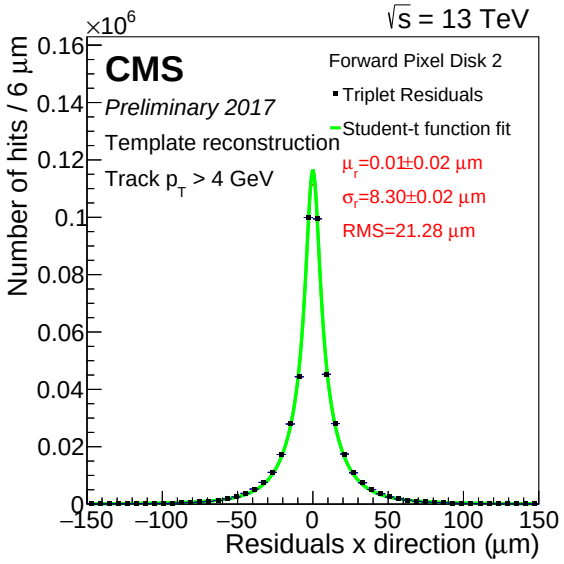

FIG. 9.2 – Resolution in transverse direction of one of the disks of the pixel detector with 2016 data, as determined by interpolating tracks through layers of the detector.

problems with individual power and readout groups that had prevented some fraction of the detector (4%) from being operational in 2017. At the beginning of March 2018 we reinstalled the pixel detector in CMS and our effort on commissioning, and calibration was completed in time to record the first data of 2018. The performance of the DC-DC converters is being closely monitored and preventive measures have been put in place to mitigate potential losses. Figure 9.3 shows UZH and PSI members replacing DC-DC converters at CMS. It has since been determined that the problem is due to a defect in the CERN chip responsible for controlling

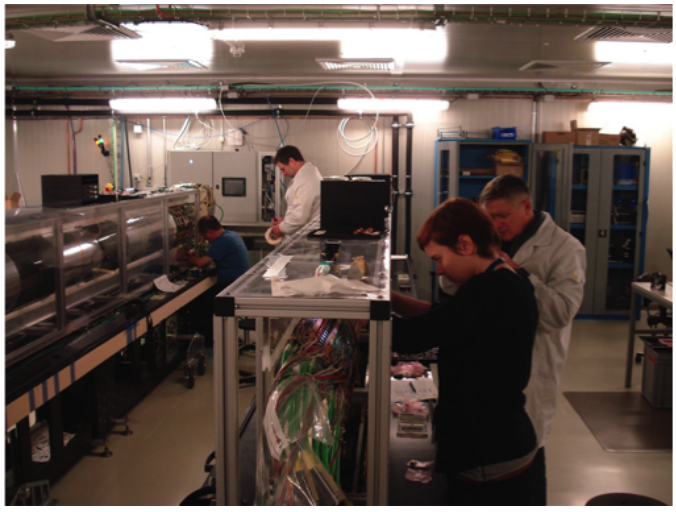

FIG. 9.3 – Replacement of BPIX DC-DC convertors in clean room at surface of CMS experimental area by UZH and PSI members in early 2018.

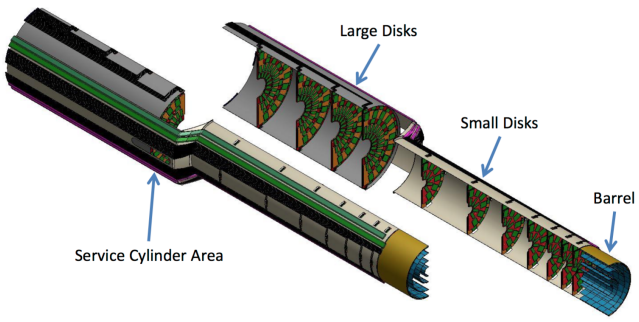

FIG. 9.4 – A quarter of the proposed phase 2 pixel detector for the CMS upgrade. The detector barrel section is composed of four cylindrical layers, while the forward region is composed of seven small disks and four large disks.

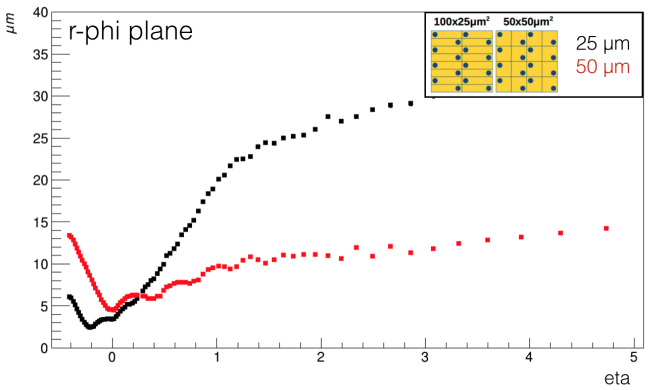

FIG. 9.5 – Resolution (r-ϕ vs η) of different simulated pixel sizes for the phase 2 pixel detector.

the DC-DC converter, and the CERN microelectronics group has now developed a fix, so that we will again replace all the DC-DC converters at the end of 2018.

Our group is also involved in another key part of the CMS detector, the HLT system. One group member is in charge of the group dedicated to the trigger menu integration and trigger code development in the HLT. The main responsibility is to guarantee that the trigger software works properly, and to keep it updated with the changes proposed by the physics analysis groups. This task is very important since any error in the trigger might compromise the data taking of the whole CMS experiment. Our group also monitors and studies the online performance of the triggers that include b-tagging, these are crucial in many physics analyses in CMS.

9.3 Upgrades

The upgraded pixel detector is designed to provide optimal performance for the whole Phase 1 operation, until the third long shutdown of the accelerator (2023-2025), when a new pixel detector for the High Luminosity LHC (HL-LHC) will be installed (Phase 2). The Phase-2 CMS pixel detector is composed of three parts, a barrel detector and two detectors composed of disks. The UZH CMS group will be constructing the large disk detectors (see Fig. 9.4). To meet the challenges arising from the increased luminosity of the machine, we are already now performing R&D for the next generation of pixel systems. In particular, efforts are ramping up to evaluate the performance of different designs concerning the number and positioning of the pixel layers, the optimal pixel size as well as the overall mechanical design and technical implementation. We have studied different geometries of Phase 2 pixel detector sensors by fully simulating the relative angles of particles reaching the detector, the drift of electrons and holes, the effect of the CMS magnetic field, as well as digitization and clustering. Some results are shown in Fig. 9.5, and have been used to optimize the detector pixel sizes. Our group is also researching the possibility to add a layer of tracking that can also provide precise timing resolution, in order to reduce pileup and identify Higgs boson production with forward jets. We are currently testing the timing resolution of low gain avalanche diode sensors (LGADs) with sources as shown in Fig. 9.6. The ultimate sensitivity we hope to achieve is to measure the time a charged particle passes through the detector with a timing resolution of 30 ps.

9.4 Higgs Properties

9.4.1 Higgs boson couplings to top quarks

The Higgs boson couples strongly only to the top quark. The search for the Higgs boson produced in association with a top-quark pair ($t\bar{t}H$) is the only way to directly probe this coupling and, among $t\bar{t}H$ channels, the

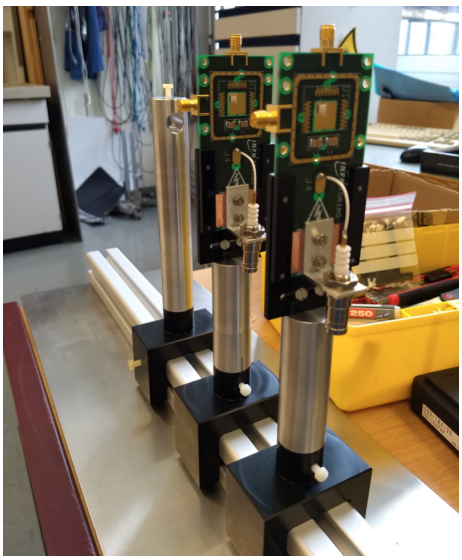

FIG. 9.6 – Part of a setup for testing the timing resolution of LGAD sensors for the Phase-2 CMS pixel detector with a radioactive source.

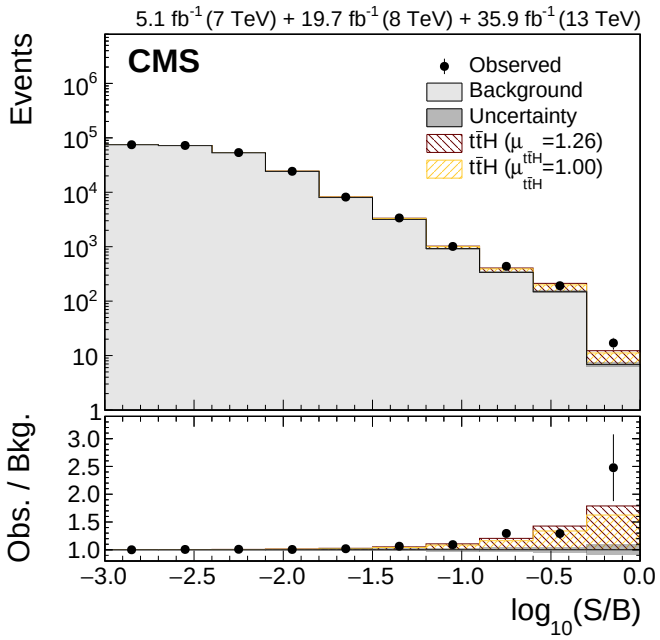

FIG. 9.7 – Observation of $t\bar{t}H$ by the CMS collaboration. The shaded histogram shows the expected background distribution, with different signal hypotheses considered shown stacked on the background. In the SM, the multiplier of the expect signal is $\mu_{t\bar{t}H} = 1$, while the best fit signal is observed to be 1.26. The lower panel shows the ratios of the expected signal and observed results relative to the expected background.

search for the Higgs boson decaying into b quarks probes the largest Higgs branching ratio of $H \to bb$ ($\sim$ 58%), and its measurement allows a constraint purely on third-generation Higgs boson couplings.

One achievement this year has been to analyze fully-hadronic $t\bar{t}H$ final states of only quarks. Although this final state represents the largest branching ratio, it is the most challenging analysis due to the large contamination from SM background processes. After events are selected, a jet-based quark-gluon discriminator is used in an event-based likelihood ratio to differentiate between events containing jets originating from light-flavour quarks and events containing jets from gluons. Finally, a matrix element method (MEM) is used for optimal discrimination between the $t\bar{t}H$ signal and SM background processes and for the ultimate signal extraction.

The results of the fully hadronic $t\bar{t}H$ analysis [3] were included in the overall $t\bar{t}H$ combination at CMS [4] of all individual final-state searches of the Higgs boson performed at CMS at centre-of-mass energies of 7, 8 and 13TeV. The combination provides the first-ever observation of $t\bar{t}H$ production, with an observed significance of 5.2 standard deviations, and the most precise measurement of the $t\bar{t}H$ cross section to date, with a best fit signal strength of $\hat{\mu} = 1.26^{+0.31}_{-0.26}$, see Fig. 9.7. Without the fully-hadronic search, the measurement would have

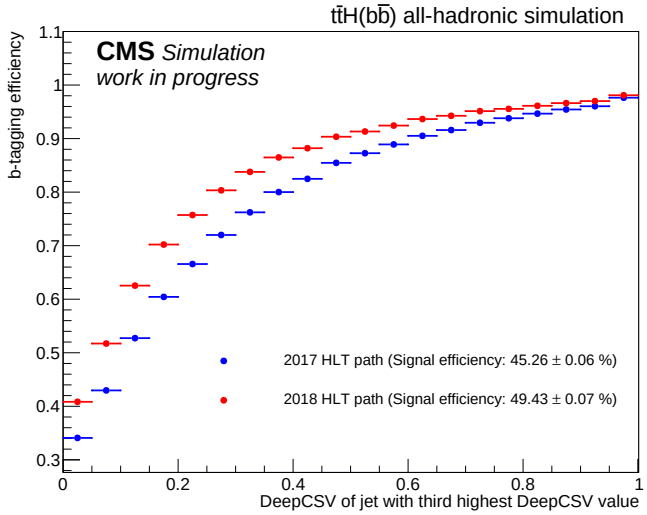

FIG. 9.8 – Improvement in the b-tagging efficiency for $t\bar{t}H(b\bar{b})$ fully-hadronic analysis made possible by utilizing a new HLT path with an improved b-tagging algorithm.

fallen short of the 5 standard deviations required to claim an observation [5].

With this measurement already made, we are now improving the future data sample size by optimizing the trigger selection of $t\bar{t}H$ events as in Fig. 9.8. We have also started a measurement of the $t\bar{t} + b\bar{b}$ inclusive cross section in the all-hadronic channel, which represents a large background for our search, and have developed new methods to reduce the QCD multijet background using a combination of two different boosted decision trees. The first results of these new methods are summarized in Table 9.1, that shows the yields of the expected signal and background processes after using our background rejection methods.

[3] CMS collaboration, arXiv:1804.03682 submitted to JHEP.

[4] CMS collaboration, Phys. Rev. Lett. 120 (2018) 231801.

[5] D. Salerno, CERN-THESIS-2018-026

Process	Yields
Other backgrounds	50100±300
Multijet	31000±200
Total bkg.	81100±400
$t\bar{t} + b\bar{b}$	8000±100
S/B	0.09
Data	89350

TAB. 9.1 – Expected yields for signal and backgrounds for the $t\bar{t} + b\bar{b}$ cross section measurement using 35.9 fb^{-1} of data collected by the CMS experiment in 2016, with statistical uncertainties.

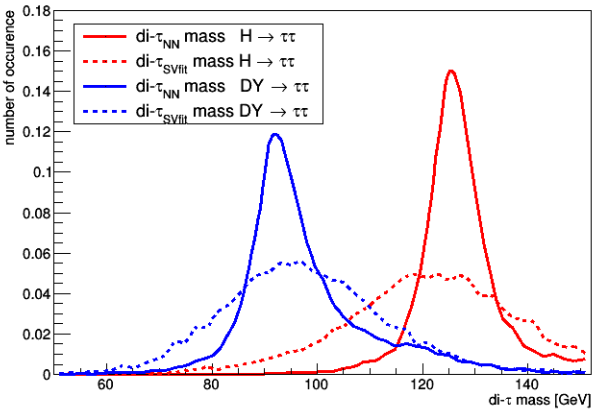

FIG. 9.9 – Improvement in the mass resolution using our Neutral Network (NN) algorithm compared to the default SVfit method used for the Higgs observation. The improvement is shown both for reconstructed Higgs bosons as well as Drell Yan (DY) events, which peak at the Z boson mass.

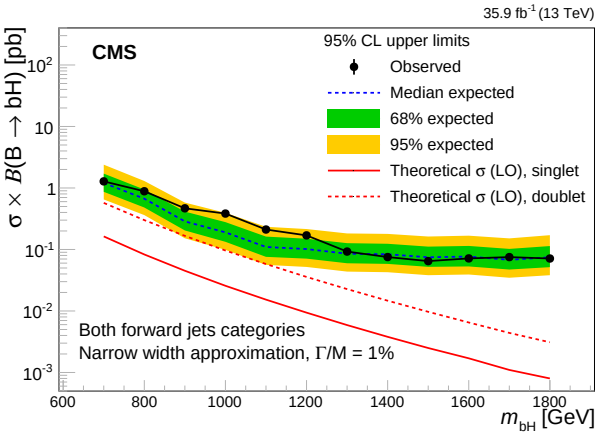

FIG. 9.10 – Results of a search for the single production of vector-like quarks B that decay to a b quark and a Higgs boson in fully-hadronic events with highly-boosted topologies. Upper limits at the 95% CL are set on the product of the B quark production cross section and branching fraction as a function of the signal mass, assuming narrow-width resonances of the resonance mass for the B quark.

9.4.2 Higgs boson coupling to τ leptons

In 2016, our CMS group reported the first observation of the Higgs boson decaying to tau leptons, for which we contributed to the analysis, the tau identification and scale factors, and as main editors of the observation publication [6]. We have now developed a new algorithm for improving the mass reconstruction of Higgs bosons decaying to tau leptons. Since tau leptons produce unmeasurable neutrinos in their decays, the Higgs boson mass is not fully constrained, therefore, a special algorithm (SVfit) has been traditionally used to calculate the most probable Higgs boson candidate mass. Using a machine learning algorithm, we have been able to greatly improve the mass resolution with respect to SVfit for particles decaying into two tau leptons, as shown in Fig. 9.9.

9.5 Searches for new phenomena

Our group is mainly focused on searching for new physics beyond the SM (BSM). We search for natural extensions that can solve inadequacies of the SM, such as its failure to predict a dark matter (DM) candidate, and its inability to explain the exceptionally low mass of the Higgs boson. We consider additional symmetries and extra dimensions that predict new particles, and also search for DM produced in our detectors. A new area of research in this period has been to directly probe for particles that may explain anomalies seen in indirect measurements seen with the LHCb experiment and other experiments focusing on b-quark physics.

9.5.1 Search for vector-like quarks

Many extensions of the SM, such as composite Higgs, extra dimensions, and little Higgs, predict the existence of a new class of heavy quarks, named vector-like quarks (VLQ) The existence of such particles would represent a solution to the hierarchy problem. Single electroweak production of VLQs has not yet been well-explored, despite the production being dominant above masses of 700 GeV. Our group has made a significant impact in the search for singly produced VLQs, carrying out two different searches, looking for massive B and T VLQs. Our focus is on two specific final states: $T \to tZ \to bq\bar{q}\nu\nu$ and $B \to bH \to bb\bar{b}$.

These new heavy resonances may decay into highly boosted quarks and bosons, whose decay products are merged into a unique “fat" jet, for which we use special techniques for identification. Our search for a vector-like quark particle, B, has been performed with an integrated luminosity of 35 fb^{-1} delivered by the LHC in 2016 and recently published [7]. The search focused on the hadronic final state of $B \to bH \to bb\bar{b}$ production channel. Advanced techniques of boosted Higgs boson production identification have been employed together with data-based methods to estimate background contributions. For the first time, in addition to narrow widths resonances, more realistic scenarios of resonance widths corresponding to 10, 20 and 30% of the resonance mass have been investigated. Results of the search are shown in Fig 9.10.

[6] A. M. Sirunyan *et al.* [CMS Collaboration], Phys. Lett. B **779**, 283 (2018), arXiv:1708.00373.

[7] CMS collaboration, JHEP 06 (2018) 031.

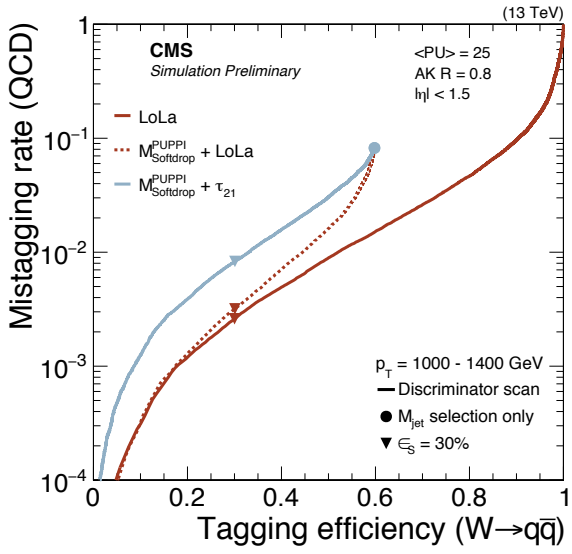

FIG. 9.11 – Performance of the LoLa algorithm for identifying boosted, hadronically-decaying bosons, as compared to the standard algorithm of PUPPI and Softdrop. Shown are curves comparing the efficiency for tagging a signal W-boson jet with the probability for mistagging a QCD-produced jet.

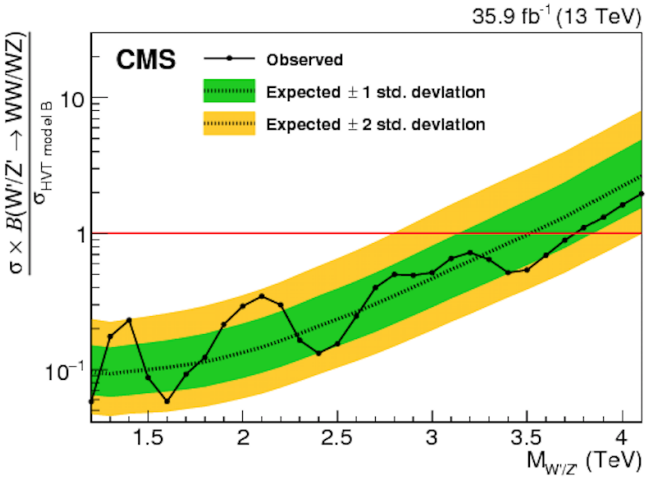

FIG. 9.12 – 95% exclusion bounds on the signal strength (product of theoretical cross section and the branching fraction to WW and ZZ) for spin-1 particles predicted by the triplet hypothesis of the HVT model B.

9.5.2 Search for heavy resonances in diboson events

The UZH group plays a leading role in searches for heavy resonances, with masses larger than 1 TeV, decaying into a pair of SM bosons (W, Z, or the Higgs boson). These heavy resonances are predicted by a large number of theoretical models that extend the SM and provide an explanation for the hierarchy problem. The most credited theories include extra dimensions, composite Higgs, heavy vector-triplets, and additional $U(1)$ gauge groups [8]. These models predict the presence of massive spin-0 Radions, spin-2 Gravitons, or spin-1 heavy W' or Z' bosons which may decay with a significant branching fraction into SM bosons.

As a consequence of the heavy mass of the new particles, and the large Lorentz boost of the decay products, the pair of particles originating from the decay of the SM bosons usually have a small angular separation and special identification and reconstruction techniques must be employed. We have designed a new machine-learning algorithm for identifying boosted bosons, called LoLa, which provides an improvement in identification efficiency over the standard tagging algorithm that uses PUPPI [9] and Soft Drop [10] (see Fig. 9.11).

During the last year, our group produced several new results using the 2016 dataset, which was a factor of 5 larger than the previously available dataset of 13 TeV center-of-mass collisions. Using events identified as containing hadronically-decaying boosted jets, where we have the largest statistics, we are able to search for heavy resonances, and interpret them as bulk gravitons, heavy vector triplet W′ and Z′ resonances, and excited quarks. We have set upper limits on the cross sections for such particles, for masses up to 5.0 TeV [11]. Figure 9.12 shows constraints on one of these models. We have also searched for new particles decaying to a W or Z boson and a Higgs boson, such that the Higgs boson is boosted and decays into b quarks that are overlapping in a single jet. Our search considers events in which the W or Z bosons decay leptonically into zero, one, or two leptons (see Fig. 9.13).

Beyond this, we have searched for a high mass resonance decaying to two Higgs bosons ($X \to HH \to b\bar{b}\tau^-\tau^+$). Our new results using the 2016 dataset extend the search range for such particles up to 4 TeV, and a publication is in its final stages of review within CMS. The results put constraints on BSM radion particles, as shown in Fig. 9.14. The preliminary result [15] is almost fully reviewed and expected to be submitted for publication in the next month.

[8] K. Agashe *et al.*, Phys. Rev. D **76** (2007) 036006;
L. Randall, R. Sundrum,
Phys. Rev. Lett. **83** (1999) 3370;
D. Marzocca *et al.*, JHEP **08** (2012) 013;
R. Rattazzi *et al.*, JHEP, 2011(10), 2011;
D. Pappadopulo *et al.*, arXiv:1402.4431.

[9] D. Bertolini *et al.*, JHEP **2014** (2014) 59.

[10] A. J. Larkoski *et al.*, JHEP **05** (2014) 146.

[11] A. M. Sirunyan *et al.* [CMS Collaboration], Phys. Rev. D **97**, no. 7, 072006 (2018), arXiv:1708.05379.

[12] CMS Collaboration, CMS-PAS-B2G-17-004.

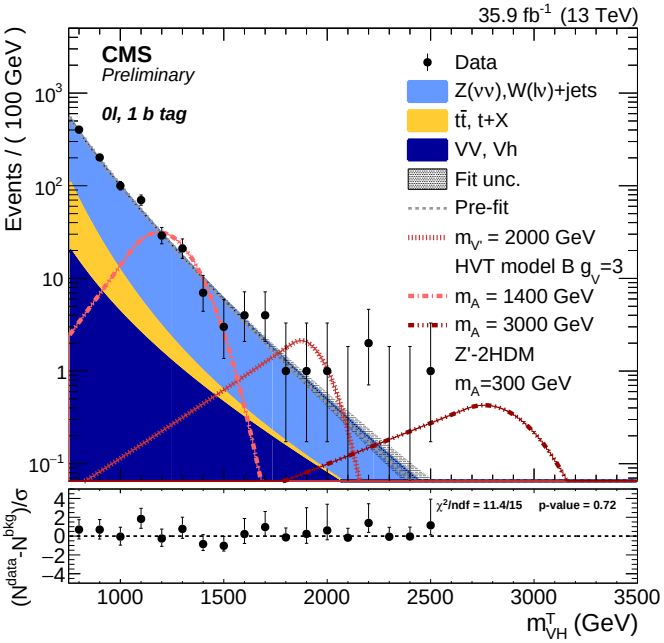

FIG. 9.13 – Observed data in the 0 lepton, 1 b-tag category. The filled areas represent the contribution of the main backgrounds (W, Z + jets, $t\bar{t}$, SM diboson). The dotted lines represent the different beyond-the-SM signal hypotheses tested: a heavy Z' that decays to a Z and a Higgs boson, or a heavy Z' that decays in a Higgs boson and DM particles, the latter mediated by a heavy pseudoscalar boson (Z'-2HDM model).

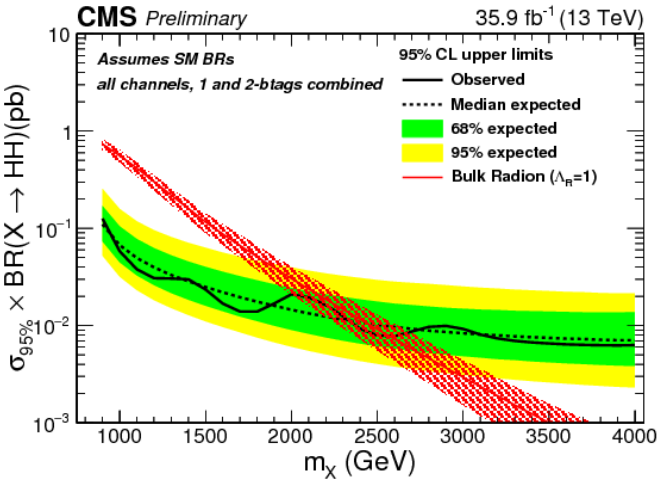

FIG. 9.14 – Observed 95% CL upper limits on $\sigma\,\mathcal{B}$(X(spin-0)→HH). Expected limits are shown with ±1 and ±2 standard deviation uncertainty bands. The $\ell\tau_h$ and $\tau_h\tau_h$ final states, and one and two b-tagged sub-jet categories are combined in the limits. The solid line and the dashed area correspond to the cross sections predicted by the radion model and the related theoretical uncertainties.

[13] A. M. Sirunyan *et al.* [CMS Collaboration], Eur. Phys. J. C **77**, no. 9, 636 (2017), arXiv:1707.01303.

[14] A. Zucchetta [CMS Collaboration], PoS DIS **2017**, 286 (2018).

[15] CMS Collaboration, CMS-PAS-B2G-17-006.

9.5.3 Supersymmetry (SUSY)

One of the favored extensions of the SM is SUSY, predicting a variety of new particles at the TeV scale, that differ in spin from their SM counterparts. SUSY provides an elegant solution to some of the shortcomings of the SM, including the hierarchy problem and the nature of DM.

One SUSY model describes the pair production of gluinos, where each gluino decays into two top quarks and the lightest supersymmetric particle, which does not interact and escapes detection. Our group has been part of the efforts to search for this type of decay in the exclusive single lepton final state, which has the advantage of a large branching ratio and a fairly clean SM background, mainly originating from top quark pair production with additional jets. Multiple exclusive search regions are defined, by binning events in various kinematic variables. The observed data in each of these regions is compared with the expected SM background, which is estimated by data driven techniques. We observe good agreement between the prediction and data and can place limits on the gluino pair production cross section as a function of neutralino and gluino mass, as shown in Fig. 9.15. The results are based on the full dataset of 35.9 fb^{-1} collected during 2016 and have been published in [16] and [17]. Gluino masses are excluded up to 1800 GeV.

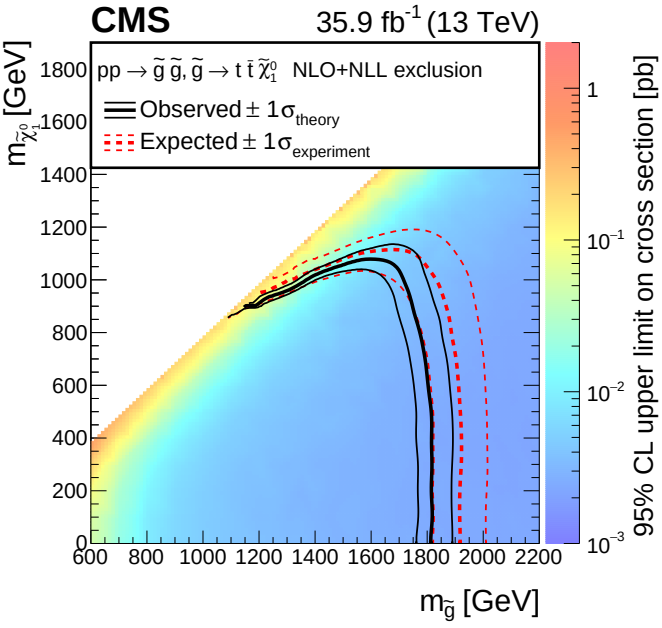

FIG. 9.15 – The results of a supersymmetric search, shown as limits on the gluino pair production cross section as a function of the neutralino and gluino masses. Gluino masses can be excluded up to 1800 GeV.

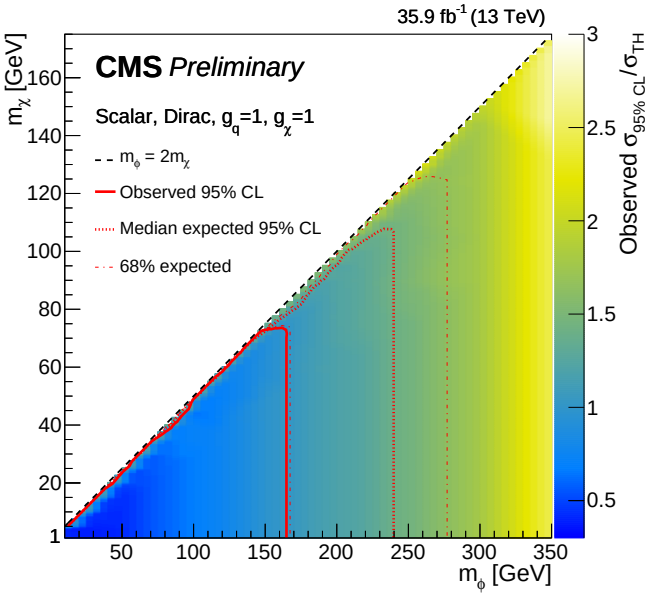

FIG. 9.16 – Results on the search for DM produced in association with a top quark pair. Expected and observed 95% CL upper limits are shown on the ratio of the DM production cross section to the model expectation as a function of the scalar mediator mass (m_{MED}), with the single-lepton and fully-hadronic channels combined. A DM mass of 1 GeV is assumed [19].

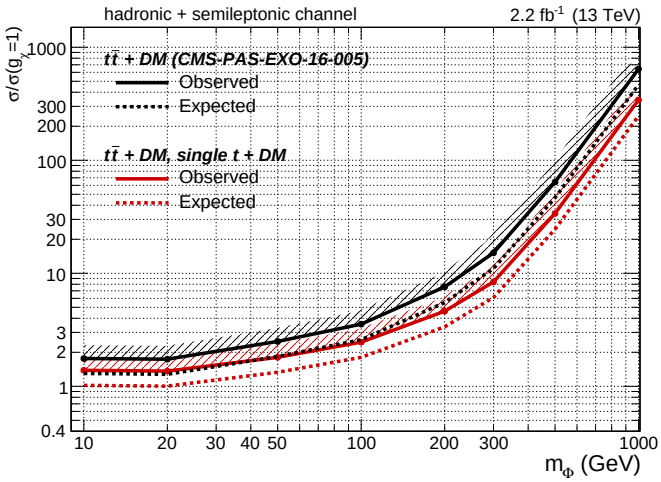

FIG. 9.17 – Comparison between the expected and observed exclusion limits on the signal strength by considering the contribution of the single top quark and DM production summed to the top quark pair production, as originally considered by CMS. A significant improvement in sensitivity is observed when considering the new DM production mechanism.

[16] CMS Collaboration, *Phys. Lett. B* 780 (2018) 384.

[17] CMS Collaboration, *Phys. Rev. D* 95, 012011 (2017).

9.5.4 Search for dark matter particles with top quarks

In several new physics models, a weakly interacting massive particle arises naturally as a DM candidate. So far, however, there is no established knowledge about its properties and interactions with ordinary matter. DM may couple to matter in proportion to mass, leading to DM being produced with top quarks at the LHC [18].

The DM particle would escape detection, therefore the signature of this type of event is large missing energy recoiling against the top quarks. Our group has made a significant impact on this search with 8 TeV and the 13 TeV data collected in 2015, the latter was published in 2017 [19]. We have developed a new and improved analysis, for which we had performed detailed studies of the different model parameters in the context of simplified models, namely the couplings strengths involved and the dependency of the analysis sensitivity on different DM and mediator mass hypotheses. Results with an integrated luminosity of 35 fb^{-1} delivered by the LHC in 2016 are shown in Fig. 9.16. Preliminary results can be found at [20], and a journal publication is currently in preparation. In addition to top quark pairs, DM can also be produced in association with a single top quark [21], [22]. Our group discovered this alternate signal mechanism, and previously produced a phenomenology paper discussing its improvement in sensitivity. This year, the analysis was developed and applied to CMS data, and is expected to become public in 2018. We have found that the exclusion limits can be improved by $30-90\%$ by including the single top quark processes, depending on the assumed scalar mediator mass, as can be seen in Fig. 9.17.

[18] D. Abercrombie *et al.*, arXiv:1507.00966.

[19] CMS collaboration, Eur. Phys. J. C 77 (2017) 845.

[20] CMS collaboration, CMS-EXO-16-049.

[21] D. Pinna *et al.*, arXiv:1701.05195.

[22] D. Pinna, CERN-THESIS-2017-211

9.5.5 Search for leptoquarks

The LHCb experiment and other dedicated B physics experiments have reported an increasing set of experimental anomalies in semi-leptonic B-meson decays, appearing in both charged and neutral currents. Ongoing work to solidify the understanding of these effects is reported by LHCb in Section 8. The particle physics community is now confronting these two 4σ deviations from the SM [23, 24]. The UZH theory group has brought forth

some interesting BSM models to explain these anomalies with new particles called leptoquarks that have an enhanced coupling to third generation particles, as explained in Section 2. In the past year, our CMS group has searched directly for these particles, considering events in which a hypothetical, third-generation leptoquark is produced singly, decaying to a tau lepton and b quark. Since the single production cross section of leptoquarks grows with the Yukawa coupling λ at the LQ-lepton-quark vertex, it can extend the mass range of leptoquark searches at high values of λ. Results of this search are shown in Fig. 9.18, and have been submitted for peer review for publication.

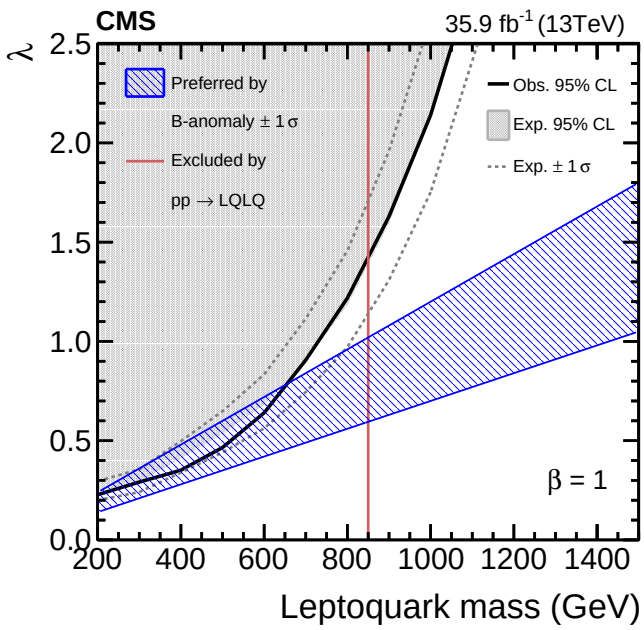

FIG. 9.18 – The red line shows the 95% CL upper limit of leptoquark masses excluded through searches for LQ-pair production, while the black (gray) line shows the 95% CL observed (expected) upper limit on singly-produced leptoquarks, as a function of the Yukawa coupling λ at the LQ-lepton-quark vertex. The blue band represents the range of mass and coupling preferred by B anomalies .

[23] Y. Amhis *et al.*, Heavy Flavor Averaging Group, "Averages of b-hadron, c-hadron, and τ-lepton properties as of summer 2016," arXiv:1612.07233.

[24] W. Altmannshofer and D. M. Straub, "Implications of $b \to s$ measurements," arXiv:1503.06199.

10 Condensed matter theory group

Titus Neupert, Ashley Cook, Seulgi Ok, Frank Schindler, and Kenny Choo

The condensed matter theory group studies topological phenomena in electronic systems. Numerical and analytical tools are used to model phases of matter and understand their unique physical properties. The term topology refers to a field of mathematics that is concerned with the relations of objects to each other if one allows for smooth deformations of these objects. Objects that can be transformed into each other by smooth deformations are said to be topologically equivalent. For example, one can smoothly deform a donut into a coffeecup but not a donut into a muffin. Thus a donut and a muffin are topologically different. Applying the same concepts to phases of quantum matter yields phenomena that are universal and surprisingly robust to perturbations. They are often related to measurable observables which are universally quantized, such as the Hall conductivity in the integer quantum Hall effect.

Topological systems can be strongly interacting, in which case we are often interested in phenomena related to so-called topological orders. Topologically ordered phases of matter are best understood in quasi two-dimensional systems with an energy gap at zero temperature, and are characterized by emergent fractionalized excitations. These so-called anyons could be used in future quantum computing devices. Our research group is interested in a conceptual understanding of topological order and its generalization, for example to three dimensions as well as in the question how such states can be realized and manipulated. One of the projects completed this year [1] is concerned with this latter problem: we pioneered the numerical study of heterostructures that combine a fractional quantum Hall state with a superconducting state. We showed that topological degrees of freedom emerge at the interface between the two. In another numerical study [2] we investigate the nature of phase transitions between two-dimensional topologically ordered states and trivial ones, relating them to accidental degeneracies in band structures.

The iconic model for strongly interacting phases of matter (topological or not) is the Hubbard model. Over the past year, we studied numerically its topological aspects [3]. In an experimental collaboration the effects of spin-orbit coupling for excitations of a Mott insulating state [4] were investigated.

We are also interested in weakly or non-interacting systems, in which case interesting topological phenomena result from the band theory of solids. Such topological band characterizations were first discovered for insulating systems. The classic example in this category is the integer quantum Hall effect with its quantized topological Hall conductivity. It was recently joined by time-reversal symmetric insulators with topological properties. All these systems are defined by the existence of boundary modes which cannot be removed by boundary perturbations that respect the symmetries protecting the topological character, such as time-reversal symmetry. Time-reversal symmetric topological insulators exist in two and three spatial dimensions and are characterized by a single Kramers pair of edge modes and a single, non-degenerate Dirac surface state, respectively.

More recently, the notion of topological band structures was extended from insulators to metals and semimetals. This direction of research characterizes symmetry-protected degeneracies in momentum space by topological numbers, showing that they are generic and can be robust against a large class of perturbations. The degeneracies give rise to so-called Weyl or Dirac semimetals on which we have devoted a series of works over the past years. We highlight below one paper in which the annihilation of Weyl nodes is observed when the material is exposed to a strong magnetic field [5].

Finally, our research group is always interested in pioneering new methods to study phases of matter theoretically. An emergent direction in condensed matter physics is to employ machine learning algorithms in various contexts. We contributed to this effort with a study that uses an artificial neural network for phase classification based on numerical data [6], which we discuss in detail below.

[1] C. Repellin *et al.*, *Numerical investigation of gapped edge states in fractional quantum Hall-superconductor heterostructures*, npj Quantum Materials **3**, 14 (2018).

[2] S. Kourtis *et al.*, *Weyl-type topological phase transitions in fractional quantum Hall like systems*, Phys. Rev. B **96**, 205117 (2017).

[3] W.-L. Tu *et al.*, *Competing orders in the Hofstadter t-J model*, Phys. Rev. B **97**, 035154 (2017).

[4] L. Das *et al.*, *Spin-Orbital Excitations in Ca_2RuO_4 Revealed by Resonant Inelastic X-ray Scattering*, Phys. Rev. X **8**, 011048 (2018).

[5] C.-L. Zhang *et al.*, *Magnetic-tunnelling-induced Weyl node annihilation in TaP*, Nature Physics **13**, 979986 (2017).

[6] F. Schindler *et al.*, *Probing many-body localization with neural networks*, Phys. Rev. B **95**, 245134 (2017).

10.1 Simulation of parafermion heterostructures

While the fractional quantum Hall (FQH) effect remains of tremendous interest for realizing myriad phases ranging in complexity from Laughlin states all the way to states with non-Abelian quasiparticles such as Majorana fermions and Fibonacci anyons, experimental exploration of these systems has remained limited. The challenges are two-fold in experimentally confirming states with non-Abelian quasiparticles. First, these states can only be accessed under extreme experimental conditions, as they are protected by very small energy gaps. Second, the topological information is encoded in degenerate ground states or the state of quasiparticles, making it intrinsically hard to measure and manipulate.

To address these challenges, we undertook extensive numerical calculation of a FQH system that is coupled to a superconductor using exact diagonalization. More explicitly, we consider a bilayer FQH system, with magnetic field perpendicular to the layers, where the orientation of the field for one layer is opposite to that for the other layer, a construction that permits gapping out of the edge states with an interlayer superconducting pairing.

Our calculations are performed on a cylinder geometry in which the bilayer FQH droplet has two edges (Fig. 10.1). To make numerics feasible, we restricted our study to the subspace of zero energy bulk and edge excitations of the Laughlin $\nu = 1/3$ state in each layer. We find a three-fold ground state degeneracy of the gapped edge states, which can be understood as follows: By introducing a gap, the superconducting coupling turns the bilayer quantum Hall state with edges into a single-layer quantum Hall state on a manifold without boundary. This manifold is topologically equivalent to a torus, where the space between the two layers becomes the interior of the torus (Fig. 10.1 c)). On the torus, a Laughlin state at filling $\nu = 1/3$ has a three-fold ground state degeneracy, which is topologically equivalent to the three ground states we observe in the superconducting bilayer system.

As we demonstrate in this work, charge pumping can permute these ground states and provide evidence of their topological nature. Suppose we start with a state $|\Psi_0\rangle$ that has charge 0 on both edges. As unit ϕ_0 spin flux is adiabatically inserted, charge is transferred from the left to the right edge, so that the resulting state is $|\Psi_+\rangle$. The other ground states are expected to transform into one another analogously: $|\Psi_+\rangle \to |\Psi_-\rangle$, $|\Psi_-\rangle \to |\Psi_0\rangle$. Thus, after insertion of a quantum of spin flux, we expect to obtain a permutation of the three ground states.

To further support our claim that the heterostructure realizes the desired topological superconducting edges, we calculated the spectral flow that corresponds to the 6π Josephson effect. In the thermodynamic limit, in which the three ground states of interest are degenerate, the *ground state* of the system does not return to itself when φ is advanced by 2π. Rather, it evolves into another degenerate ground state and

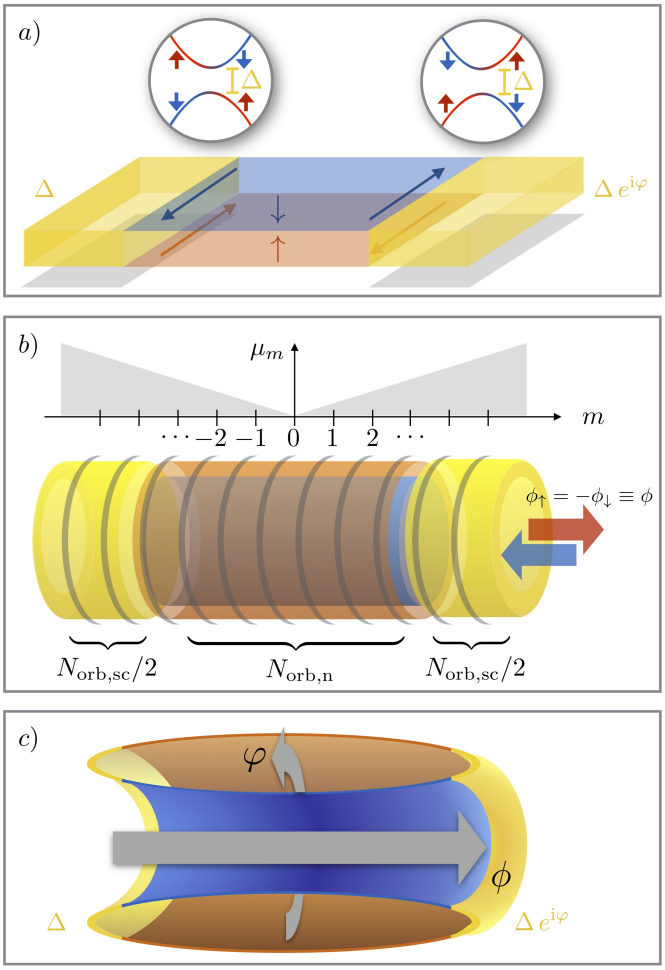

FIG. 10.1 – Schematics of the physical geometry and the one used for the numerical investigation.
a) Fractional topological insulator heterostructure in which carriers with spin up and down (red and blue) form a fractional quantum Hall state with opposite chirality. Proximity to superconducting reservoirs (yellow) induces a superconducting gap in their edge channels. To study the Josephson effect, arelative phase φ between the left and right superconducting order parameter is included.
b) When imposing periodic boundary conditions along the edges, resulting in a cylinder geometry, each edge carries a topological degree of freedom. The boundary conditions can be twisted by inserting a flux ϕ into the cylinder for spin up electrons and $-\phi$ for spin down electrons. In the Landau gauge orbitals are localized along the cylinder, where we consider $N_{\mathrm{orb,n}}$ and $N_{\mathrm{orb,sc}}$ normal and superconducting orbitals, respectively. The typical separation between orbitals is $2\pi\ell_B^2/L_y$, where L_y is the cylinder perimeter. The droplet is confined by a linear potential μ_m.
c) With the counter-propagating edges gapped out, the bilayer FQH state on the cylinder is topologically equivalent to a single layer FQH state on a torus, where the fluxes ϕ and φ run through its two noncontractible cycles and can be used to explore its topological ground state degeneracy. It is thus topologically equivalent to the ground state degeneracy of the gapped edge modes.

only after φ is advanced by 6π does the system return to its initial state, because the elementary excitations of the superconducting edge are Cooper-paired quasiparticles of charge $2e/3$, delocalized along the cylinder perimeter, which tunnel across the bulk gap.

System sizes in this work were limited, but we were nevertheless able to demonstrate four key features: (i) the edges develop a spectral gap induced by the superconducting coupling, (ii) the expected number of three nearly degenerate ground states without any charge imbalance between the two halves of the system, (iii) charge pumping can permute the ground states, and (iv) the system exhibits a 6π-periodic Josephson effect. For each signature, we discussed the suitable parameter regime. Our work provides the first quantitative study of fractional edge modes coupled to superconducting leads in a fully microscopic model and should serve as an important foundation for future work.

10.2 Annihilating Weyl fermions with a magnetic field

Weyl semimetals display the most elementary topological band degeneracies [7]: two bands in a three-dimensional band structure are degenerate in an isolated point in momentum space. Away from this singular point, the bands generically disperse linearly. Quasi-particle excitations near the degeneracy point (Weyl node) are described by the Weyl equation, hence the name. These quasiparticles have a number of unique properties when it comes to their electromagnetic response. In some precise sense, they can be regarded as magnetic monopoles in momentum space and are associated with a topological charge ± 1.

In the most widely studied class of Weyl semimetals, the Weyl nodes arise from spin-orbit coupling which can be thought of as a perturbation to a more symmetric band structure. As a result, Weyl nodes of opposite charge come in pairs that in many cases are separated by a small distance Δk_{W} in momentum space.

When the material is exposed to an strong external magnetic field, Weyl fermions generate a very distinct quasi-one-dimensional band structure of dispersing Landau levels. Apart from two sets of Landau levels above and below the Weyl node, respectively, there is a single 'chiral' Landau level that disperses linearly across the energy of the Weyl node. The sign of the associated velocity is given by the topological charge of the Weyl node. Because of this chiral Landau level, a single Weyl fermion cannot become insulating when exposed to a magnetic field.

Tantalum phosphide (TaP) is a Weyl semimetal [8] with two relevant features: Its Weyl nodes are very close to the Fermi level and their separation in momentum Δk_{W} is rather small as shown in Fig. 10.2 a). We studied the transport properties of TaP when exposed to a strong magnetic field. The field orientation was chosen such that the Weyl nodes are separated in momentum space perpendicular to the magnetic field B, this corresponds to 0° in Fig. 10.2 c). In this configuration, the chiral Landau levels of the two Weyl nodes with opposite velocity cross as shown in Fig. 10.2 b). For small fields, this crossing is only hybridizing by an exponentially small amount in the ratio of $\Delta k_{\mathrm{W}}^{-1}$ and the magnetic length $\ell \propto 1/\sqrt{B}$. The magnetic length is the typical length scale on which the magnetic field breaks the translational symmetry of the system. As the field is increased, a noticeable hybridization appears as soon as $\ell^{-1} \sim \Delta k_{\mathrm{W}}$ and the system turns into an insulator.

In the transport measurement, this change in the electronic structure manifests itself in a dramatic change and sign reversal in the Hall conductivity at around $B = 30$ T as shown in Fig. 10.2 c). This field scale is in very good agreement with the expectation from our theoretical calculations.

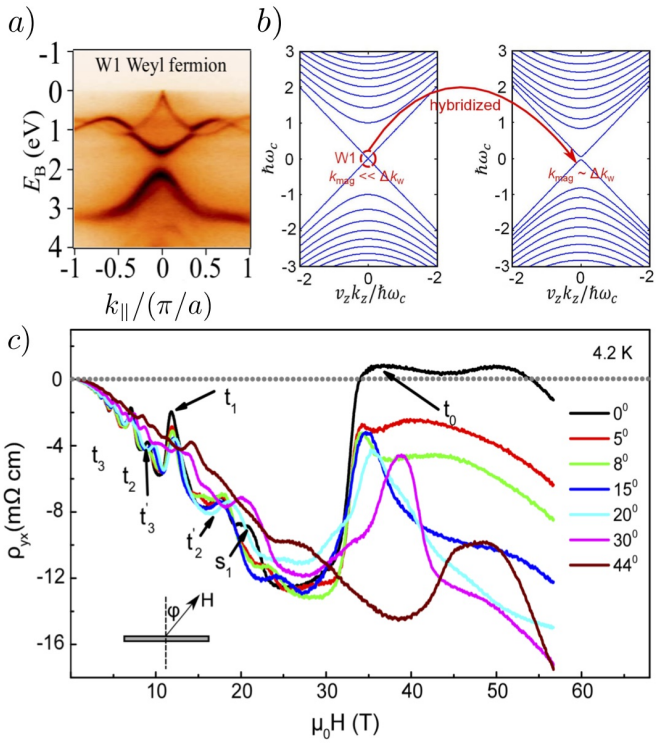

FIG. 10.2 – Magnetic field induced annihilation of Weyl fermions in the band structure of TaP.
a) Angle-resolved photoemission spectroscopy image of a Weyl node in TaP, visible as a linear band crossing near the Fermi level.
b) Schematic of how a strong magnetic field hybridizes two Weyl nodes in the Landau level band structure in TaP: The two Weyl nodes are at the same momentum k_z and have opposite chirality. Thus they come with linearly and oppositely dispersing Landau levels which cross each other at small fields. As the inverse magnetic length becomes of the same scale as the transverse Weyl node separation in momentum space, the linear Landau levels hybridize. The transport properties of the material change drastically.
c) Hall conductivity as a function of magnetic field. The critical field where the Weyl node Landau levels annihilate is manifest via a drastic jump and sign reversal of the Hall conductivity (0° trace).

The residual conductivity for $B > 30$ T comes from other Fermi pockets in the Brillouin zone that are unrelated to the Weyl node.

[7] B. Yan, *et al. Topological Materials: Weyl Semimetals*, Ann. Rev. Cond. Matt. Phys. **8**, 337-354 (2017).

[8] S.-Y. Xu, *et al. Experimental discovery of a topological Weyl semimetal state in TaP*, Science Advances **1**, e1501092 (2015).

10.3 Machine learning for detecting phase transitions

Artificial intelligence is widely employed in science and information technology whenever large amounts of data need to be analyzed or classified. Machine learning techniques and neural networks in particular are becoming a more and more widespread tool also in statistical and condensed matter physics. A typical class of tasks for neural networks are classification problems, for instance to identify whether images show cats or dogs. Classification, for instance that of phases of (quantum) matter based on various observables, is a prominent task in condensed matter physics.

In this project, which is our first venture into the field of machine learning, we used a neural network for exactly that task – a binary phase classification – based on numerically obtained data [9]. The two phases to be distinguished are a thermalizing and a localized phase of a Heisenberg spin chain in a random field. The Hamiltonian is strongly interacting and the phase with strong random field is called many-body localized. Many-body localization means that a system keeps a memory of its initial condition for arbitrary long times for states at high energies/temperatures [10]. The quantum entanglement is not scrambled as in a conventional, thermalizing system. As a consequence, many-body localized states do not follow the conventional rules of quantum statistical mechanics and in particular violate ergodicity. These properties and their potential for quantum information storage make them an important current research field.

However, there are many open questions about the properties of the many-body localized phase and the associated phase transition. It is not clear, which observable is best suited to detect the phase transition from numerical data on finite-size systems. This is where neural networks become useful. We taught a neural network and entanglement fingerprint of typical states well in the localized and well in the thermalizing phase of the spin chain and then asked it to classify the same entanglement fingerprint for states in the transition region to determine the phase boundary. The fingerprint we used is the so-called entanglement spectrum [11] (defined as the spectrum of the reduced density matrix when one half of the spin chain is traced over). The entanglement spectrum was shown to contain a lot of universal information about quantum phases via its level statistics, gaps between levels, degeneracies of levels and more.

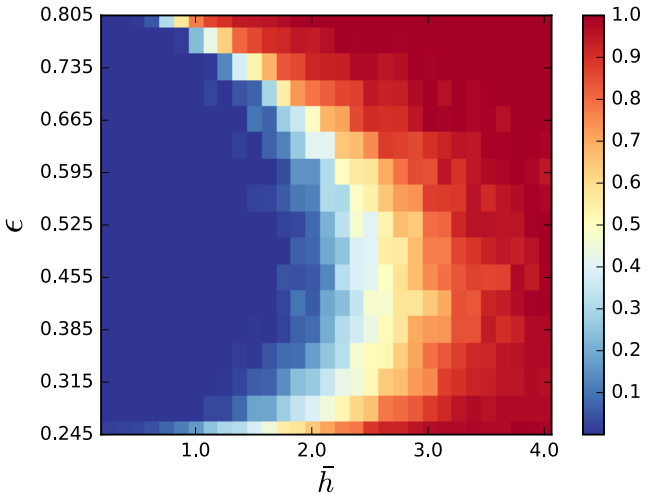

FIG. 10.3 – Phase diagram of a spin-1/2 Heisenberg chain in a random field obtained using a neural network. The horizontal axis is the strength of the disorder field, the vertical axis is energy density (the classification is valid for arbitrary excited states). The blue region is thermalizing, while the red region is in a many-body localized phase.

We did not teach the neural network which features in the entanglement spectrum of the spin chain are relevant for the classification. Rather, we later used the technique of hallucinogenic dreaming to determine what properties the network had learned. (This was the first time the technique was applied to condensed matter physics.) It turned out that the network had correctly learned a known power-law feature of the entanglement spectrum.

Most importantly, however, the neural network was able to pin down the phase transition very sharply, even by only looking at individual eigenstates of the spin-chain Hamiltonian. The phase boundary shown in Fig. 10.3 is in quantitative agreement with previous results, but needs much less numerical input to be computed. Our neural network approach is a combination of a so-called supervised and an unsupervised technique in that we do not a priori know where the phase transition is. To enhance the performance, we invented an algorithm called confidence optimization, which incentives the confident classification of the states near the phase transition. This work was an interesting first venture into the field of machine learning, on which we will follow up with diverse further projects.

[9] F. Schindler *et al.*, *Probing many-body localization with neural networks*, Phys. Rev. B **95**, 245134 (2017).

[10] A. Soluyanov *et al.*, *Type-II Weyl semimetals*, Nature **527**, 495-498 (2015).

[11] H. Li, *et al.*, *Entanglement Spectrum as a Generalization of Entanglement Entropy: Identification of Topological Order in Non-Abelian Fractional Quantum Hall Effect States*, Phys. Rev. Lett. **101**, 010504 (2008).

11 Superconductivity and Magnetism

L. Das, D. Sutter, O. Ivashko, D. Destraz, K. Kramer, D. Rechsteiner, C. E. Matt, J. Choi, M. Horio & J. Chang

in collaboration with: Paul Scherrer Institute (M. Dantz, Y .Tseng, D. E. McNally, N. Plumb, M. Shi, & T. Schmitt), EPFL Lausanne (G. Gatti, N. E. Shaik, H. M. Rønnow & M. Grioni), University of Zurich (F. Schindler, A. Cook & T. Neupert), University of Central Lancashire, UK (P. G. Freeman), Technical University of Denmark, Denmark (N. B. Christensen), Dipartimento di Fisica 'E. R. Caianiello', Salerno-Italy (F. Forte, V. Granata, R. Fittipaldi, M. Cuoco & A. Vecchione), The University of Tokyo, Japan (S. Pyon), Okayama University, Japan (K. Kudo & M. Nohara), Weizmann Institute of Science, Israel (M. Hücker), Deutsches Elektronen-Synchrotron DESY, Germany (M. von Zimmermann)

Our group is carrying out experimental research on strongly correlated electron systems using complementary synchrotron and laboratory based techniques. In this report, we highlight three different experiments. First, we have continued our work on the puzzling Mott insulating state of Ca_2RuO_4 by combining absorption and resonant inelastic x-ray spectroscopies. We have been able to reveal the intricate interplay between crystal-field and orbital degrees of freedom. Our second highlight is on a high-temperature superconductor where, by means of angle resolved photoemission, we have uncovered the orbital hybridisation at the Fermi level. It is discussed how this impacts on superconductivity. Finally, we have also studied the interplay between charge ordering and superconductivity in the $Ir_{1-x}Pt_xTe_2$ system.

11.1 Mott-Mechanism of Ca_2RuO_4 revealed

Spin-orbit coupling (SOC) is a central thread in the search for novel quantum material physics. A particularly promising avenue is the combination of SOC and strong electron correlations in multi-orbital systems. This scenario is realised in heavy transition metal oxides composed of 4*d* and 5*d* elements. Of particular interest is the complex regime where SOC and crystal-field energy scales are comparable. Here Ca_2RuO_4 is a topical material that displays a wealth of physical properties. Current-induced giant diamagnetic response (the strongest diamagnetism among non-superconducting materials) was recently reported [1]. Also, neutron and Raman scattering experiments have shown evidence for a dispersive Higgs mode [2, 3]. Experimental studies of angle-resolved photoemission spectroscopy and band structure calculations on the paramagnetic insulating phase of Ca_2RuO_4 have supported evidence for a band-Mott insulating ground state [4] due to interplay between Coulomb interaction and Hund's coupling. The rich and myriad phenomenology of Ca_2RuO_4 is hence attributed to various energy scales – Coulomb interaction U, Hund's coupling J_H, crystal-field splitting δ and SOC λ.

We have studied the magnetically ordered phase of Ca_2RuO_4 at $T = 16$ K, using O K edge Resonant Inelastic X-ray Scattering (RIXS) [5]. Four excitations have been identified – two low energy excitations labelled *A* and *B* at 80 meV and 400 meV respectively and two high energy excitations labelled *C* and *D* at 1.3 eV and 2.2 eV respectively as indicated in Fig. 11.1. The *A* and *B* branches are interpreted to be arising from composite spin-orbital excitations due to SOC and the high-energy excitations, dubbed *C* and *D*, arise from singlet-triplet excitations at the Ruthenium site set by energy scale of Hund's coupling.

A light polarisation analysis was carried out yielding information about the internal structure of these excitations. The momentum dependent analysis of the *A* and *B* peaks were made. Even though the dispersion of the

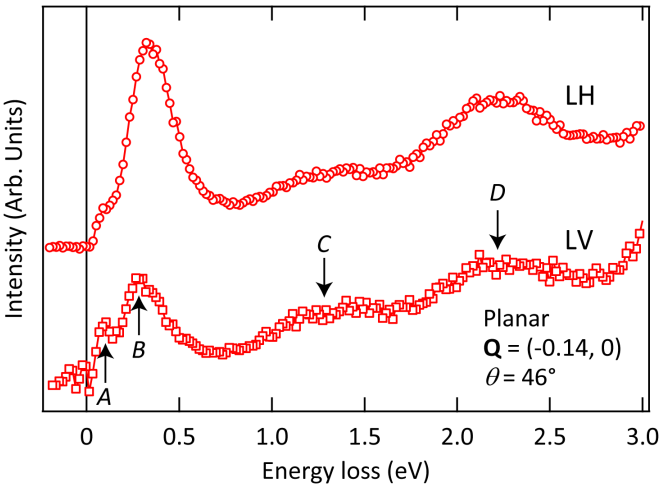

FIG. 11.1 – Planar RIXS spectra, recorded with LH and LV light polarisation for incident angle (momentum transfer) as indicated. The elastic scattering contribution is subtracted. Vertical arrows indicate the four excitations labelled *A*, *B*, *C* and *D*.

A peak was not discernible with our current resolution, the B peak showed a weak dispersion consistent with its propagating nature. Further, with the light polarisation analysis of the x-ray absorption and the RIXS spectra, we were able to characterise the Mott-active Ruthenium orbitals involved in the absorption processes. Our results are consistent with the picture of an almost completely filled d_{xy} orbital (becoming inaccessible to absorption processes) and half-filled $d_{xz/yz}$ orbitals involved in the Mott transition, thus, playing a pivotal role in creating the unique band-Mott insulating state of Ca_2RuO_4.

To understand the nature of the high energy excitations (C and D), a model cluster of two Ru sites connected to one planar oxygen site was used. The model was evaluated using material specific values of the energy scales: crystal field splitting $\delta = 0.3$ eV, SOC $\lambda = 0.075$ eV, Coulomb interaction $U = 2$ eV and Hund's coupling $J_H = 0.5$ eV. With this model, the spectral features named C and D were found to arise from singlet and triplet excitations at Ru site, with the energy given by $2J_H$ and $4J_H$, respectively. To describe the nature of the low-energy excitations (A and B), the eigenstates of the Hamiltonian of the single Ru site was considered and good agreement with the experimental data was obtained. In summary, we demonstrated that Ca_2RuO_4 is an example of a combined band-Mott insulator. The low-energy excitations of this ground state consists of damped dispersive spin-orbiton quasiparticles.

[1] C. Sow *et al.*, Science **358**, 1084 (2011)

[2] A. Jain *et al.*, Nat. Phys. **13**, 633 (2017)

[3] S.-M. Souliou *et al.*, Phys. Rev. Lett. **119**, 067201 (2017)

[4] D. Sutter *et al.*, Nat. Commun. **8**, 15176 (2017)

[5] L. Das *et al.*, Phys. Rev. X **8**, 11048 (2018)

11.2 Orbital Hybridisation in a Cuprate Superconductor

In the quest to improve superconducting transition temperatures in layered copper-oxide compounds (cuprates), it is important to identify the influencing factors of the transition temperature T_c. In single-layer cuprate superconductors, the particular crystal field environment of the copper oxide octahedra causes the nine $3d$-electrons to fill the t_{2g} manifold and leaves the e_g-states 3/4 filled [6]. Although superconductivity is promoted within the copper-oxide layers, the apical oxygen possibly plays a crucial role in defining T_c [7, 8]. The distance of the apical oxygen to the CuO_2-plane d_A then controls the hybridisation strength between the filled d_{z^2} -band and the metallic $d_{x^2-y^2}$ -band. Generally, in the single-layered materials T_c seems to correlate with larger d_A [9], thus suggesting

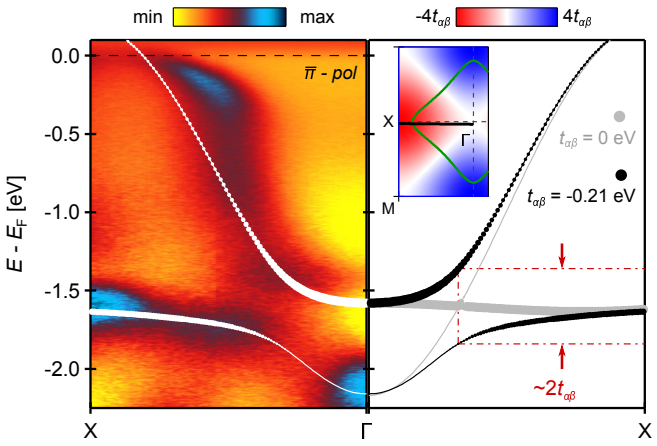

FIG. 11.2 – Avoided band crossing. Left panel: Ultraviolet ARPES data recorded along the anti-nodal direction using 160 eV linear horizontal polarised photons. Right panel: Tight-binding model of the $d_{x^2-y^2}$ and d_{z^2} bands along the anti-nodal direction. The gray lines are the model prediction in absence of inter-orbital hopping ($t_{\alpha\beta} = 0$) between $d_{x^2-y^2}$ and d_{z^2}. In this case, the bands are crossing near the Γ-point. This degeneracy is lifted once a finite inter-orbital hopping parameter is considered. For the solid black lines $t_{\alpha\beta} = -210$ meV and other hopping parameters have been adjusted accordingly. The inset indicates the Fermi surface (green line) and the Γ−X cut directions. The coloured background displays the amplitude of the hybridisation term $\Psi(\mathbf{k})$ that vanishes on the nodal lines.

a sabotaging role of orbital hybridisation for superconductivity. However, the d_{z^2} -band has never been directly identified by angle-resolved photoemission spectroscopy (ARPES) studies.

In a recent experiment [10], we have resolved the d_{z^2}-band in La-based single-layer compounds with ultraviolet and soft X-ray ARPES measurements. We have pinned down the orbital character in three different ways. Firstly, our observations are consistent with density functional theory (DFT) calculations, suggesting the existence of the d_{z^2}-band below the $d_{x^2-y^2}$-band. Secondly, by using matrix element selection rules of the optical transition we can test the orbital character by varying the measurement geometry and light polarisation [11]. The incident light and the electron detector slit define a global mirror-plane. With respect to this plane one can assign the parity for the electromagnetic light field and the parity of the orbitals. For the free electron final state (even parity), the selection rules dictate if the photocurrent for a certain orbital-driven band vanishes or not. Thirdly, using soft X-rays, we were able to probe the band structure in k_z-direction and observed dispersive features of the d_{z^2}-band beyond matrix element effects, in contrast to the non-dispersive $d_{x^2-y^2}$-band.

Experimental data and DFT results have been parametrised using a two-orbital tight binding model [11]. Crucially, there is a hybridisation term $\Psi(\mathbf{k}) = 2t_{\alpha\beta}[\cos(k_x a) - \cos(k_y b)]$ between the $d_{x^2-y^2}$ and d_{z^2} orbitals, with the hopping parameter $t_{\alpha\beta}$ that characterises the strength of orbital hybridisation. If one describes the two observed bands independently with $t_{\alpha\beta} = 0$, they would cross each other along the antinodal (Γ–X) direction which is not observed experimentally (see Fig. 11.2). From the avoided band crossing, we directly estimate a hybridisation term of $t_{\alpha\beta} \approx 200$ meV. Furthermore, in contrast to the widely used single-band tight binding parametrisation, our two-band model allows a unification of t'_α/t_α ratios for all single-layer compounds, where t_α is the nearest neighbour hopping and t'_α is the next nearest neighbour hopping for the $d_{x^2-y^2}$ orbitals. It has been argued that orbital hybridisation - of the kind reported here - is unfavourable for superconducting pairing [7,12]. It thus provides an explanation for the varying $T_c^{\max}$ across single-layer cuprate materials.

[6] J. Fink *et al.*, J. Res. Dev. **33**, 372 (1989)

[7] H. Sakakibara *et al.*, Phys. Rev. Lett. **105**, 057003 (2010)

[8] Y. Ohta *et al.*, Phys. Rev. B **43**, 2968-2982 (1991)

[9] E. Pavarini *et al.*, Phys. Rev. Lett. **87**, 047003 (2001)

[10] C. Matt, D. Sutter *et al.*, Nat. Commun. **9**, 972 (2018)

[11] C. B. Bishop *et al.*, Phys. Rev. B **93**, 224519 (2016)

[12] H. Sakakibara *et al.*, Phys. Rev. B **85**, 064501 (2012)

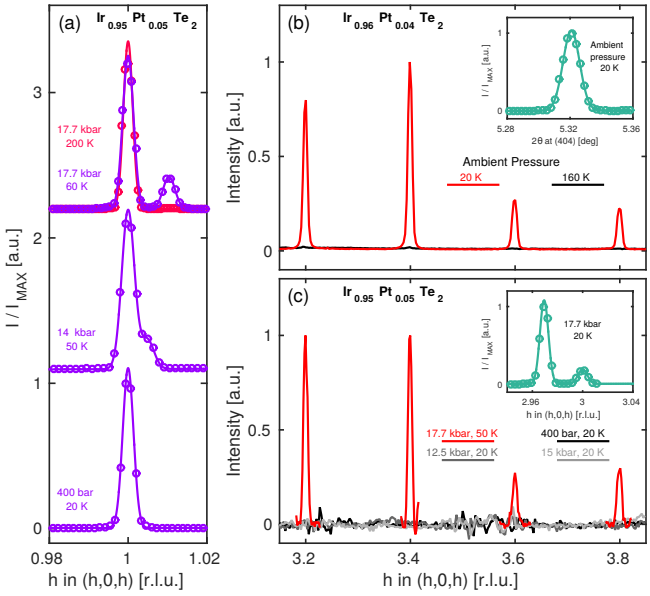

FIG. 11.3 – Lattice and charge ordering reflections in $Ir_{1-x}Pt_xTe_2$. (a) Bragg peak $(1,0,1)$ reflection measured in $Ir_{0.95}Pt_{0.05}Te_2$ as a function of pressure as indicated. Solid lines are Gaussian fits to the data. (b) Ambient pressure x-ray diffracted intensity measured on $Ir_{0.96}Pt_{0.04}Te_2$ along the $(1,0,1)$ direction for 20 K (red line) and 160 K (black line) respectively. (c) Scan as in (b) but measured at base temperature (20 K) on $Ir_{0.95}Pt_{0.05}Te_2$ for pressures as indicated. The slightly worse signal-to-noise level stems from the necessary background subtraction of signal originating from the pressure cell.

11.3 Charge-Stripe Order and Superconductivity in $Ir_{1-x}Pt_xTe_2$

$IrTe_2$ is an interesting system because of a large SOC on the Ir site [13, 14]. It also displays high-temperature charge ordering, and superconductivity can be induced by Pt or Pd substitution that in turn quenches the charge order [15–17]. Several studies concluded in favour of a conventional *s*-wave pairing symmetry [18,19]. It remains however to be understood how charge order, lattice symmetry and superconductivity interfere. In the parent compound $IrTe_2$, charge order coincides with a lowering of the crystal structure symmetry (from hexagonal $P\bar{3}m1$ to monoclinic $C2/m$) [15].

We carried out a combined resistivity and x-ray diffraction study of $Ir_{1-x}Pt_xTe_2$, as a function of chemical substitution and hydrostatic pressure near the critical composition $x_c \sim 0.045$ [20]. Just below this critical composition, we find a temperature independent charge ordering modulation vector $(1/5, 0, 1/5)$ (see Fig. 11.3(b)). This signifies a difference from the parent compound where the ground state charge modulation is $(1/8, 0, 1/8)$ [21]. Our pressure experiments were carried out just above x_c (namely at $x = 0.05$) in a compound with a superconducting ground state and no evidence of charge order at, and around, ambient conditions $1 - 400$ bar. With increasing pressure, we find a lowering of lattice symmetry, evidenced by a Bragg peak splitting above $p_{c1} \sim 11.5$ kbar (see Fig. 11.3(a)). This breaking of the hexagonal lattice symmetry appears without any trace of charge ordering that emerges only for pressures above $p_{c2} \sim 16$ kbar (see Fig. 11.3(c)). Since the charge ordering is intimately related to the shorter lattice parameter (inset of Fig. 11.3(c)), we conclude that charge ordering is lattice – rather than electronically – driven.

We also dealt with the interplay between charge ordering and superconductivity. The temperature versus Pt substitution phase diagram suggests that these two phases are competing, since superconductivity appears only after charge ordering is quenched. From resistivity data we observe a gradual broadening of the transition (as a function of pressure for $x = 0.05$ system), to a point where zero resistance is not observed. This is consistent with Kosterlitz-Thouless transition [22, 23] scenario where an exponential drop in resistivity is predicted. In $Ir_{1-x}Pt_xTe_2$ it is know that charge order generates two

dimensional walls of low density-of-states [24, 25]. It is therefore not inconceivable that superconductivity is suppressed inside these walls. Hence there exists a possible physical mechanism for two-dimensional superconductivity in $Ir_{1-x}Pt_xTe_2$. Further experimental evidence supporting this scenario would be of great interest. Another plausible scenario to describe the broad resistive transition is granular superconductivity. We notice, however, that the pressure induced crystal domain formation initially have no influence on superconductivity. Explaining our data in terms of granular superconductivity is therefore not straightforward.

[13] B. J. Kim *et al.*, Phys. Rev. Lett. **101**, 076402 (2008)
[14] M. Moretti Sala *et al.*, Phys. Rev. B **89**, 121101 (2014)
[15] S. Pyon *et al.*, J. Phys. Soc. Jpn. **81**, 053701 (2012)
[16] J. Yang *et al.*, Phys. Rev. Lett. **108**, 116402 (2012)
[17] S. Pyon *et al.*, Physica C **494**, 80 (2013)
[18] S. Y. Zhou *et al.*, Europhys. Lett. **104**, 27010 (2013)
[19] D. J. Yu *et al.*, Phys. Rev. B **89**, 100501 (2014)
[20] O. Ivashko *et al.*, Sci. Rep. **7**, 17157 (2017)
[21] K.-T. Ko *et al.*, Nat. Commun. **6**, 7342 (2015)
[22] Q. Li *et al.*, Phys. Rev. Lett. **99**, 067001 (2007)
[23] L. Benfatto *et al.*, Phys. Rev. B **80**, 214506 (2009)
[24] G. L. Pascut *et al.*, Phys. Rev. Lett. **112**, 086402 (2014)
[25] G. L. Pascut *et al.*, Phys. Rev. B **90**, 195122 (2014)

12 Phase transitions, materials and applications

A. Gazizulina, S. Huangfu, A. Schilling, S. Siegrist, Q. Wang, W. Wang and X. Zhang

in collaboration with: University of Bern (K. Krämer), Deutsches Zentrum für Luft- und Raumfahrt (Prof. Alexei Semenov), Paul-Scherrer Institut (Dr. Marisa Medarde), Paul-Scherrer Institut (Dr. Ekaterina Pomjakushina, Dr. Vladimir Pomjakushin), McMaster University (Dr. Hanna Dabkowska), Max Planck Institute for Chemical Physics and Solids, Dresden (Prof. Claudia Felser), Universidad del Pais Vasco (Prof. Evgeny Sherman), Academy of Sciences of Uzbekistan (Prof. Abdulla Rakhimov), Leibniz-Institut für Festkörper- und Werkstoffforschung (IFW) (Dr. Vladimir Kataev), Helmholtz Research Centre Dresden-Rossendorf (Dr. Tobias Förster), Radboud University Nijmegen (Dr. Laurens Peters), Universitetet i Stavanger (Prof. Diana Quintero Castro), Helmholtz Zentrum für Materialien und Energie HZB (Dr. Illya Glavatskyy), Laboratoire National des Champs Magnetiques Intenses (lmcmi) (Dr. Albin De Muer), Deutsches Zentrum für Luft- und Raumfahrt (Dr. Heinz Wilhelm Hübers), Karlsruhe Institut für Technologie (Dr. Konstantin Ilín), National Institute of Standards and Technology (Dr. Sae Woo Nam), University of Geneva (Dr. Jeremie Teyssier), Dresden High Magnetic Field Laboratory (Dr. Sergei Zherlitsyn)

12.1 Superconducting nanowire single photon detectors (SNSPDs)

12.1.1 Criteria for choosing materials for SNSPDs

For superconducting photon detectors, the amount of photon energy consumed in breaking Cooper pairs is one of the most essential factors determining their detection efficiency. The energy of the incident photon is dissipated mainly through electron electron and electron-phonon interactions. The more energy is transferred into the electron subsystem, the higher the detection efficiency that can be expected. The likelihood for energy absorption through electron-electron interaction is $p_{e-e} \propto 1/\tau_{e-e}$ with the electron-electron interaction time τ_{e-e}, while $p_{e-ph} \propto 1/\tau_{e-ph}$ describes the corresponding contributions due to the interaction with the phonon subsystem. We have proposed a detailed model, concluding that materials with a large τ_{e-ph}/τ_{e-e} ratio (i.e., $p_{e-e} >> p_{e-ph}$) ensure that the photon energy can be effectively transferred to the material, and a more effective detector can be fabricated [1].

In a real material, the temperature dependences of τ_{e-ph} and τ_{e-e} near the critical temperature T_c can be determined by the magneto-transport measurements. From the excess magneto-conductance, the inelastic scattering time τ_i, containing a combination of τ_{e-ph} and τ_{e-e}, can be obtained at different temperatures and fitted with contributions of a weak localization effect, the Aslamazov-Larkin and Maki-Thompson fluctuation mechanisms, and the contribution from the suppression of the electronic density of states due to the formation of short lifetime Cooper pairs, respectively. In Fig. 12.1 we show the result of such fits to the excess magneto-conductance measured on a 4 nm-thick WSi film at different temperatures.

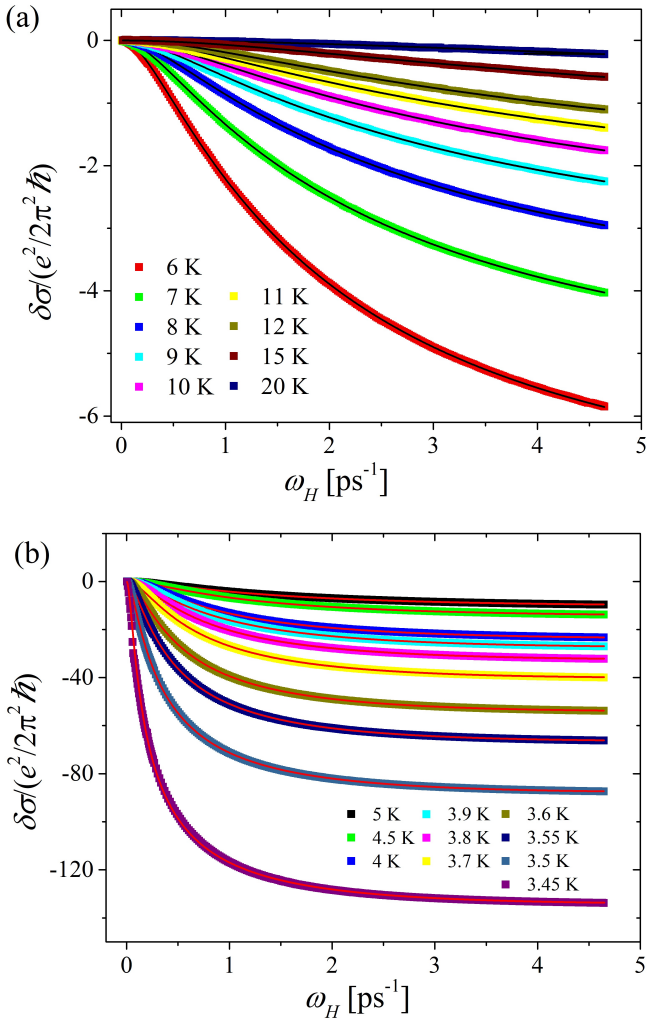

FIG. 12.1 – Best fits to the excess magneto-conductance of a 4 nm-thick WSi film at different temperatures.

The resulting temperature dependence of τ_i is shown in Fig. 12.2. From these data, we were able to extract the magnitudes and temperature dependences of τ_{e-e}, τ_{e-ph}, and a characteristic electron-fluctuation time τ_{e-fl} [1]. The temperature dependence of τ_{e-ph} follows αT^{-3} with $\alpha = 4.8\times10^3$ psK^3, which corresponds to τ_{e-ph} = 122 ps at the critical temperature (3.44 K) and 75 ps at 4 K. Sidorova et al. recently also studied the electron-phonon relaxation time in a 3.4 nm thick WSi film using an amplitude-modulated absorption of sub-THz radiation (AMAR) method, and τ_{e-ph} was estimated to be in the range of 100-200 ps at 3.4 K [2], which coincides well with our result from the magneto-resistance method. With respect to the contribution from the electron electron interaction, we obtain a temperature dependence $\tau_{e-e} = \beta T^{-1}$ with $\beta = 60$ psK, with $\tau_{e-e} = 17.4$ ps at T_c. Generally speaking, materials with a large τ_{e-ph}/τ_{e-e} ratio, such as WSi ($\tau_{e-ph}/\tau_{e-e} \approx 6.9$ for a 4 nm film at T_c) [1] or MoN ($\tau_{e-ph}/\tau_{e-e} \approx 11$ [3]), are more suitable for SNSPD applications as compared to conventional superconducting materials, such as NbN ($\tau_{e-ph}/\tau_{e-e} \approx 1$) [3].

[1] Zhang X., Lita A., Sidorova M., Q. Wang V., Verma and, Nam S., Semenov A., and Schilling A, *Superconducting fluctuations and characteristic time scales in amorphous wsi*, accepted in Phys. Rev. B, arXiv:1712.05019, 2017.

[2] Sidorova M., Semenov A., Korneev A., Chulkova G., Korneeva Yu., Mikhailov M., Devizenko A., Kozorezov A., and Goltsman G., *Electron-phonon relaxation time in ultrathin tungsten silicon film*, arXiv:1607.07321, 2016.

[3] Korneeva Y., Florya I., Vdovichev S., Moshkova M., Simonov N., Kaurova N., Korneev A., and Goltsman G., *Electron-phonon relaxation time in ultrathin tungsten silicon film*, IEEE Trans. Appl. Supercond., 27:2201504, 2017.

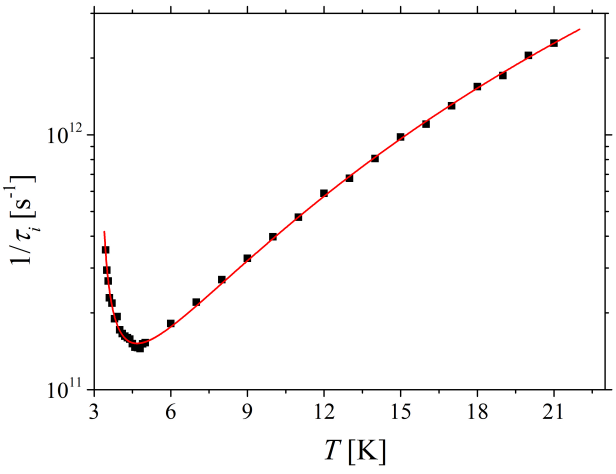

FIG. 12.2 – Measured inelastic scattering rate for a 4-nm thick WSi film.

12.1.2 X-ray single-photon detectors (X-SNSPDs)

Based on our previous experience with optical superconducting nanowire single-photon detectors (SNSPDs), we had extended their application range to the X-ray regime (see last annual reports and Refs. [4, 5]). These detectors had been structured from Nb, TaN and WSi superconducting films, and were successfully operating around liquid helium temperatures ($T \approx 4$ K).

In order to achieve a wider range of applicability, we are now attempting to adapt the same detection scheme to high-temperature superconductor films, with the potential to fabricate a detector operating at liquid nitrogen temperature (77 K). Although there are no reports on the successful implementation and operation of optical SNSPDs based on these materials in the literature, the preconditions for fabricating corresponding X-SNSPDs are more favorable. The reason is that SNSPDs for optical wavelengths require small dimensions of the superconducting wires, of the order of nanometers in width and thickness, which are difficult to produce and handle with ceramic high-temperature superconductors without significant degradation of their superconducting properties. By contrast, X-SNSPDs can (and should) be made from thick films to increase the absorption probability of X-ray photons, and the use of wide wires may also be feasible. We started with a simple bridge made of a commercial 150 nm thick $YBa_2Cu_3O_7$ film via electron beam lithography. Fig. 12.3 shows the SEM image of the 2.5 µm wide bridge with a critical temperature $T_c = 84$ K. Corresponding current-voltage I-V curves at $T = 72$ K and 76 K are shown in Fig. 12.4. The expected hysteretic behavior and the characteristic transition to the normal state at a well-

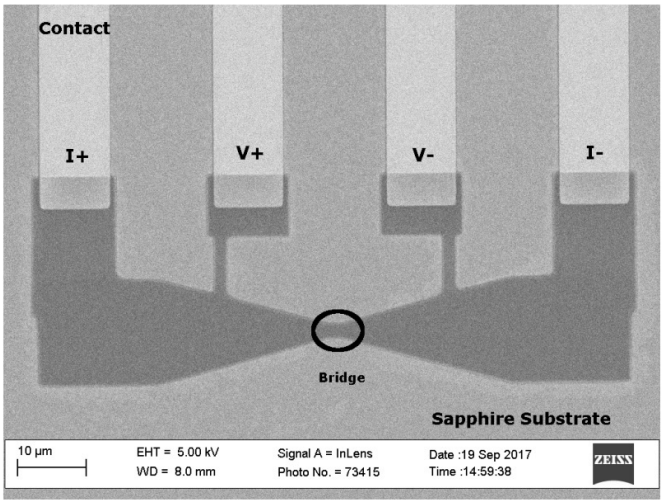

FIG. 12.3 – SEM image of the 2.5 µm wide $YBa_2Cu_3O_7$-bridge. The gold contacts for four-point measurements are indicated as (V+; V-; I+; I-).

defined critical current I_c are visible only at 72 K. The finite slope at small voltages is due to the circuit resistance. A well-defined I_c is crucial for the operation of the detector, because sharp detectable voltage pulses upon photon absorption are generated only if part of the current-biased superconductor becomes suddenly temporarily normal conducting.

For an X-ray detection measurement, we operated the $YBa_2Cu_3O_7$-bridge with 99 % of I_c at T = 72 K and irradiated it using an X-ray source with a W-target operating at 30 keV and 1.5 mA. After 20 min integration time, only 2 detection events were recorded. A detailed analysis showed that these detection events were most probably caused by thermal fluctuations in the bridge. As the $YBa_2Cu_3O_7$ film showed signs of degradation upon nano-fabrication, we are now working with 300 nm thick $(Bi, Pb)_2Sr_2Ca_2Cu_3O_{10}$ films with T_c = 108 K which are much more robust against oxygen loss as compared to $YBa_2Cu_3O_7$ films [6, 7] (in collaboration with A. Matsumoto, NIMS, Tsukuba, Japan).

[4] Inderbitzin K., Engel A., and Schilling A., *Soft x-ray single-photon detection with superconducting tantalum nitride and niobium nanowires*, IEEE Trans. Appl. Supercond., 23:2200505, 2013.

[5] Zhang X., Wang Q., and Schilling A., *Superconducting single x-ray photon detector based on $W_0.8Si_0.2$*, AIP Advances, 6:115104, 2016.

[6] Russek S., Sanders S., Roshko A., and Ekin J., *Surface degradation of superconducting $YBa_2Cu_3O_7$ thin films*, Appl. Phys. Lett., 64:3649, 1988.

[7] Maeda H., Tanaka Y., Fukutomi M., and Asano T., *Synthesis of BiSrCaCuo ceramics with large intergrowth defects*, Jpn. J. Appl. Phys., 27:209, 1994.

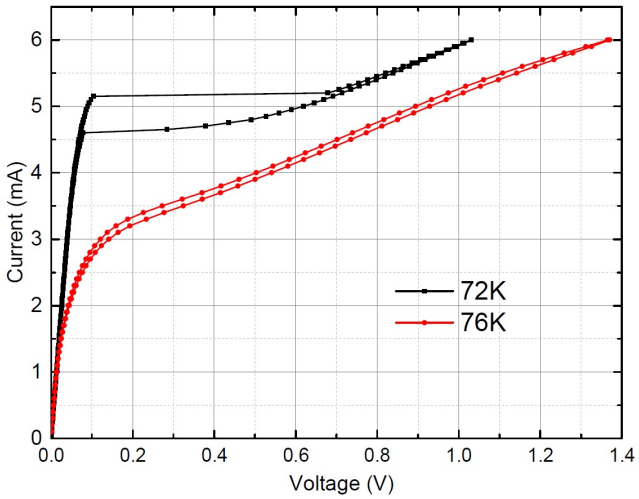

FIG. 12.4 – I-V curves of the $YBa_2Cu_3O_7$-bridge.

12.2 New results on the system $Ba_{3-x}Sr_xCr_2O_8$

The solid-solution $B_{3-x}Sr_xCr_2O_8$ was described in detail in the annual reports from previous years. To be short, these compounds are dimerized spin $\frac{1}{2}$ systems with a strong antiferromagnetic interaction that leads to a singlet ground state and energetically separated triplet states. This separation can be closed by a magnetic field (at a critical field H_{c1}) due to the Zeeman effect, thereby introducing antiferromagnetic order. This state resembles a Bose-Einstein condensate of magnetic quasiparticles, so called 'triplons'. In the past years we had studied the dependence of the magnetic interactions and the critical fields as functions of x by various techniques, and we showed that these quantities can be tuned between the extremal values in $Sr_3Cr_2O_8$ and $Ba_3Cr_2O_8$ [8,9].

Last year we have continued this line of research, e.g., by Raman spectroscopy measurements (in collaboration with Univ. of Geneva, Dr. J. Teyssier) on single crystals of $Ba_{0.2}Sr_{2.8}Cr_2O_8$ and $Ba_{0.1}Sr_{2.9}Cr_2O_8$, to study a high-temperature structural phase transition from hexagonal to monoclinic upon lowering the temperature.

To complete the magnetic phase diagram of $Ba_{0.1}Sr_{2.9}Cr_2O_8$ presented in Ref. [9], we have performed a series of ultrasound velocity measurements on single crystals of $Ba_{0.1}Sr_{2.9}Cr_2O_8$ at the Dresden High Magnetic Field Laboratory (in collaboration with Dr. S. Zherlitsyn) using a pulse-echo method with a phase-sensitive detection technique. The ultrasound frequencies ranged between 5 and 500 MHz, with magnetic field pulses up to almost 60 T during 120 ms. In Fig. 12.5(left) we show the relative changes of the sound velocity, exhibiting two distinct features around 30 T and 50 T, respectively. The corresponding magnetic phase diagram is shown in Fig. 12.5(right), together with respective data taken from the literature for $Sr_3Cr_2O_8$ (x = 3) [10].The nature of the phase labeled as 'magnonic liquid' in Fig. 12.5(right) and in Ref. [10] is still a matter of debate. While it is clear that it represents a state outside the antiferromagnetic 'dome' (here labeled as 'magnonic superfluid' [10]), little is known about its microscopic origin.

[8] Gazizulina A., Quintero-Castro D., and Schilling A., *Single-crystal growth and study of the mixed spin-dimer system $Ba_{3-x}Sr_xCr_2O_8$*, Physical Review B, 96:184201, 2017.

[9] Grundmann H., Gazizulina A., Schilling A., von Rohr F., Forster T., and Peters L., *Tuning the critical magnetic field of the triplon Bose-Einstein condensation in $Ba_{3-x}Sr_xCr_2O_8$*, New J. Phys., 18:033001, 2016.

[10] Wang Z., Quintero-Castro D., Zherlitsyn S., Yasin S., Skourski Y., and Loidl A., *Field-induced magnonic liquid in the 3d spin-dimerized antiferromagnet $Sr_3Cr_2O_8$*, Phys. Rev. Lett., 116:147201, 2016.

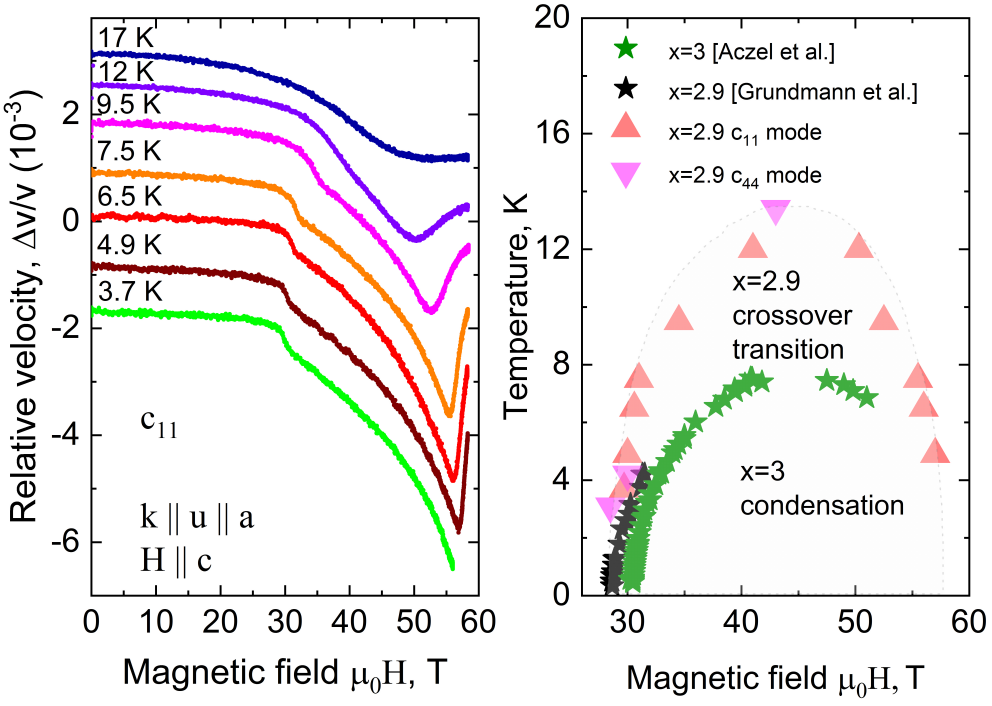

FIG. 12.5 – Left: changes in the sound velocity of a $Ba_{0.1}Sr_{2.9}Cr_2O_8$ single crystal in pulsed magnetic fields. Right: extracted magnetic phase diagram, together with data from our Ref. [9] and Ref. [10].

12.3 Investigations on $Pr_4Ni_3O_8$, a trilayer nickelate

The trilayer nickelates $La_4Ni_3O_8$ and $Pr_4Ni_3O_8$ (Fig. 12.6) show a large orbital polarization with unoccupied Ni *3d* states that are predominately $d_{(x^2-y^2)}$ in character, with a low spin configuration for dopants (Ni^{2+} holes), and a high degree of hybridization between Ni *3d* and O *2p* states [11]. This is very reminiscent of the situation met in the well-known superconducting copper oxides.

In their stoichiometric composition, the filling of the *3d* states corresponds, in the language of the cuprates, to a state which is highly overdoped with holes. Most interestingly, $Pr_4Ni_3O_8$ has indeed been reported to be metallic [11], while $La_4Ni_3O_8$ is not. It is therefore natural to attempt to change the number of charge carriers in these compounds by doping, possibly up to the level of reaching an antiferromagnetic insulating phase, which would then be an analogue to the 'parent structure' of the cuprates [12], and to examine their physical properties.

In Fig. 12.7 we show a series of magnetic hysteresis loops of $Pr_4Ni_3O_8$, suggesting that the compound is, in fact, ferro- or ferrimagnetic. We have also studied the preparation conditions and possibilities to change the cation and anion stoichiometry of $Pr_4Ni_3O_8$. While cation substitution by atoms of different valency (e.g., by partially replacing Pr^{3+} with Ce^{4+}) was not successful, we succeeded in varying the oxygen content to a large extent

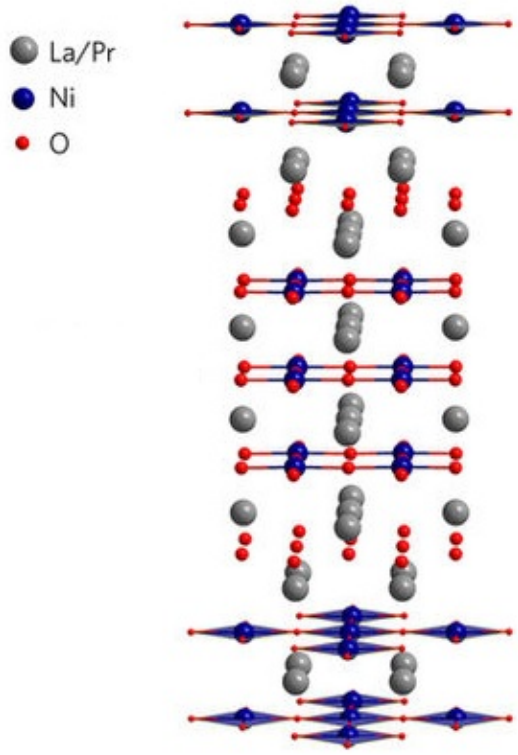

FIG. 12.6 – Crystal structure of the trilayer nickelates $La_4Ni_3O_8$ and $Pr_4Ni_3O_8$ (taken from Ref. [11]).

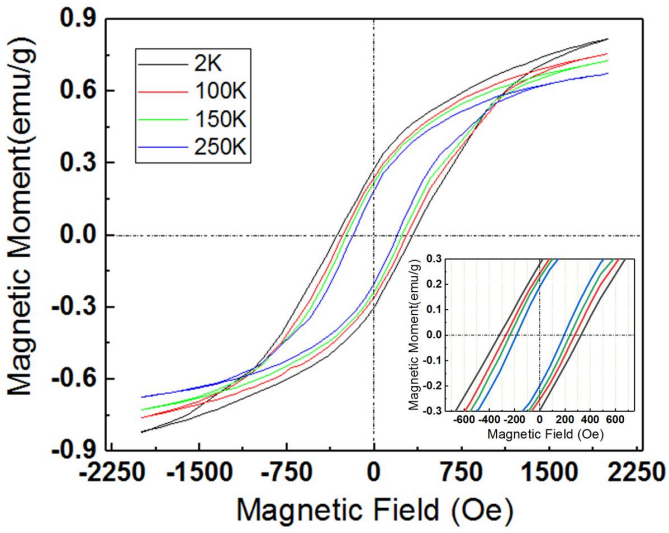

FIG. 12.7 – Magnetic hysteresis loops of $Pr_4Ni_3O_8$ measured at 2K, 100K, 150K and 250K.

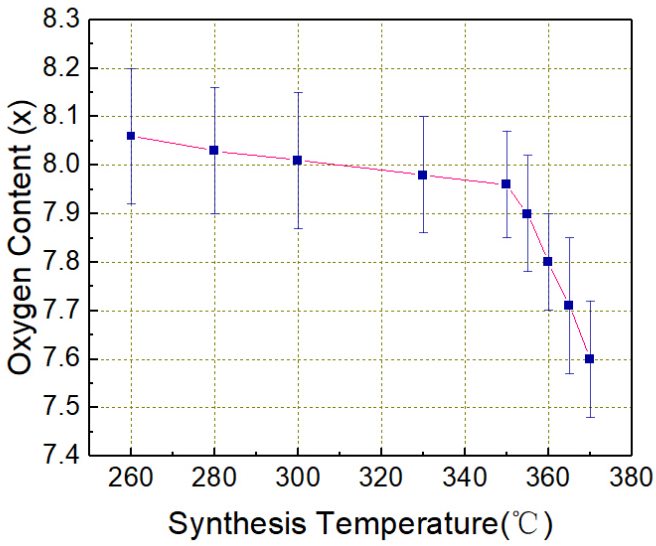

FIG. 12.8 – : Oxygen content of $Pr_4Ni_3O_8$ as a function of synthesizing temperature.

by adjusting the synthesizing temperature of $Pr_4Ni_3O_8$ in a mixture of N_2/H_2 while maintaining the crystal structure intact. In Fig. 12.8, we show the dependence of the oxygen content which we determined by titration techniques, on the respective synthesizing temperature.

Based on these investigations, we plan to perform a neutron-scattering study (in collaboration with V. Pomjakushin, PSI Villigen), to investigate the details of the oxygen sublattice in oxygen-deficient $Pr_4Ni_3O_8$.

[11] Zhang J., Botana A., Freeland J., Phelan D., Zheng H., Pardo V., Norman M., and Mitchell J., *Large orbital polarization in a metallic square-planar nickelate*, Nature Physics, 13:864, 2017.

[12] Botana A., Pardo V., and Norman M., *Electron doped layered nickelates: Spanning the phase diagram of the cuprates*, Physical Review Materials, 1:021801, 2017.

13 Surface Physics

M. Hengsberger, L. Castiglioni, C. Monney, A. Hemmi, Z. Novotny, R. Totani, C. Bernard, A. Epprecht, L. Grad, P. Kliuiev, A. Kostanyan, A. Schuler, K. Waltar, W.-D. Zabka, J. Chen, F. Cossalter, M. Hotz, P. Kretz, H. Nussbaumer, D. Schachtler, B. Tobler, B. Salzmann, P. Dona, T. Kälin, T. Greber, and J. Osterwalder

Our laboratory is equipped for the investigation of surface and interface phenomena at the atomic level, for the preparation and characterization of clean single-crystalline surfaces, metal and molecular monolayer films, as well as sp^2-bonded single layers on surfaces that we exfoliate from metals with wet transfer methods. In addition, we are part of a user consortium of the soft x-ray beamline *PEARL (PhotoEmission and Atomic Resolution Laboratory)* at the Swiss Light Source. Our group has built and commissioned a compact and mobile angle-resolved photoemission (ARPES) instrument, while a second ARPES spectrometer has been successfully fitted with a high-harmonic gas jet source for producing short VUV light pulses.

The research carried out during the report period can be grouped into four topics:

- 2D materials
  Monolayer hexagonal boron nitride (*h*-BN) and graphene are grown by chemical vapor deposition (CVD) on metal surfaces. The present efforts focus on the delamination of theses single-layer materials from their growth substrate. For this purpose we develop wet transfer protocols that allow transfer of large-area hexagonal boron nitride onto arbitrary substrates. This project is pursued within the European FET Flagship Graphene (see Section 13.1).

- Adsorbed molecular catalysts and photosensitizers
  Within the University Research Priority Program *Light to Chemical Energy Conversion* (LightChEC) we develop and characterize model electrode surfaces for solar water splitting. Studied systems include monolayers of catalyst molecules on oxide semiconductor surfaces and self-assembled monolayers of photosensitizer molecules on ultrathin oxide films. Section 13.2 describes the preparation of ultrathin crystalline alumina films and the *in situ* adsorption of organometallic rhenium complexes with covalent linkers from solution in a specifically designed satellite chamber of our electron spectrometer.

- Ultrafast processes at surfaces
  Within the NCCR *Molecular Ultrafast Science and Technology* (MUST) the group investigates dynamical processes at surfaces on the pico- and femtosecond time scale by means of pump-probe photoemission experiments. This year we report on a polarization-sensitive terahertz pulse reconstruction scheme. It may be obtained from momentum-resolved photoelectron streaking data and recovers the field amplitudes and phase in THz laser pulses (see Section 13.3). This work is relevant for experiments at free electron lasers that use THz pump and x-ray probe pulses.

- Spin shuttles
  Fullerenes with magnetic endohedral units (*spin shuttles*) like $HoSc_2N@C_{80}$ are investigated in view of their magnetic properties. In this context we demonstrated that the molecular conformation may be changed with an external magnetic field [1] and that these nanometer sized molecules realize the smallest compass. This project bases on a collaboration with the IFW Dresden where the molecules are produced and purified.

We like to highlight the award of a Semesterpreis to Björn Salzmann for his Bachelor thesis *Doping Graphene on SiO_2 using X-rays*. Furthermore we organized within the Sino Swiss Science and Technology (SSSTC) cooperation a small international *workshop on endohedral single molecule magnets* in Castasegna.

In the following, three highlights of last year's research are presented in more detail.

[1] A. Kostanyan *et al.*,
Phys. Rev. Lett. **119**, 237202 (2017).

13.1 Centimeter-Sized Single-Orientation Hexagonal Boron Nitride

In collaboration with: Huanyao Cun, Ke Liu, Duncan T. L. Alexander, Aleksandra Radenovic, École Polytechnique Fédérale de Lausanne, Switzerland, Armin Kleibert, Swiss Light Source, Paul Scherrer Institut, Switzerland, Benjamin Probst, Department of Chemistry, Universität Zürich, Michael Weinl, Matthias Schreck, Institut für Physik, Universität Augsburg, Germany.

In this project we are producing single-layer material like graphene or hexagonal boron nitride (*h*-BN) on single-crystalline transition metal surfaces. The chemi-

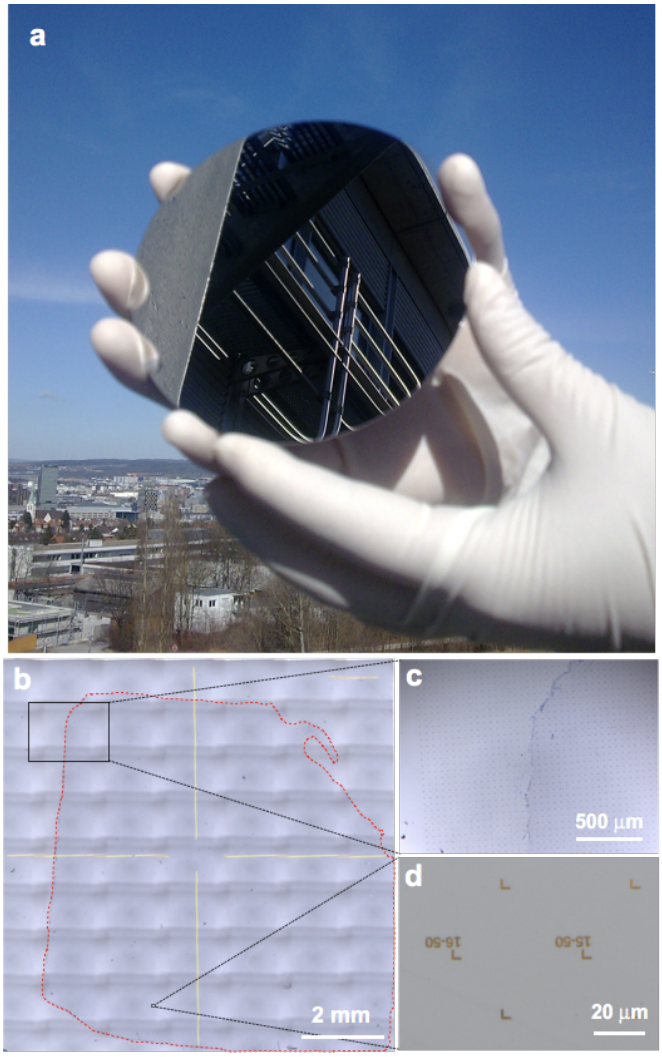

FIG. 13.1 – (a) Photograph of a four-inch wafer in Zürich air on which single layer *h*-BN may be grown. (b-d) Optical microscopy from single layer *h*-BN transferred on a 90 nm SiO_2/Si wafer. (b) 9.5 x 9.5 mm^2 where 64 individual frames are stitched together. The red line marks the boundary of the transferred *h*-BN. (c) Single frame from (b) containing the *h*-BN border. The single layer on the right side appears darker. (d) Zoom in where the gold markers that allow to find the same coordinates in different instruments are the only inhomogeneities. Data from [2].

cal vapor deposition growth method bears the advantage of scalability and substrate based functionalisation. Fig. 13.1(a) shows a four-inch wafer substrate with a single-crystalline metal film that is used in our lab for the production of single orientation *h*-BN on large areas. For applications in electronic devices, or as ultimately thin membranes, the material has to be transferred to insulating substrates or onto supporting grids. For *h*-BN, wet transfer methods that rely on electrochemical hydrogen-bubble production at the interface between the monolayer and the transition metal rhodium (111) surface yield flakes in the 20 µm size range. In a significant leap we succeeded to transfer centimeter sized single-layer *h*-BN onto arbitrary substrates [2]. Similar to the delamination of graphene from Ir(111) [3], the process involves an additional step prior to the H_2-bubbling, where the *h*-BN on Rh substrate is electrochemically treated in a tetraoctylammonium bromide (TOABr) solution in acetonitrile. After the TOA *h*-BN treatment transfer rates above 90% are obtained. Figures 13.1(b)-(d) show transferred centimeter sized single-layer, single-orientation *h*-BN on a 90 nm SiO_2/Si(001) wafer chip with micrometer sized gold markers that serve for navigation at the nanometer scale. The images are obtained with an optical microscope in air. The optical contrast of a single layer *h*-BN that may be used for identification of the transferred material on 90 nm SiO_2/Si is shown in Fig. 13.1(c). Although the centimeter sized *h*-BN does not (yet) meet the performance of the µm sized flakes that are exfoliated from *h*-BN single crystals [4], our material opens new perspectives for applications of monolayer-thick hexagonal boron nitride. It was demonstrated that it can protect germanium from oxidation at elevated temperatures, and that in functionalized form it can be used as an ion conducting membrane in a liquid [2], which was highlighted in Science [5].

[2] H.Y. Cun *et al.*, Nano Lett. **18**, 1205 (2018).

[3] L. Koefoed *et al.*, J. Phys. D: Appl. Phys. **48**, 115306 (2015).

[4] T. Taniguchi, and K. Watanabe, J. Cryst. Growth, **303**, 525 (2007).

[5] S. Vignieri and J. Smith, Science, **359**, 649 (2018).

13.2 Growth and functionalization of ultrathin crystalline alumina films

In collaboration with: Mathias Mosberger, Benjamin Probst and Roger Alberto, Chemistry Department, Universität Zürich (URPP LightChEC).

We investigated the growth of ultrathin crystalline alumina films and their functionalization with organometallic rhenium complexes. These are synthetically versatile photo- and redox active compounds and can be incorporated into efficient homogeneous photocatalytic systems [6].

Ultrathin alumina films grown by selective oxidation on NiAl(110) substrates are a prototypical example for ultrathin wide gap insulators with a minimum thickness of two atomic layers [7]. The structural changes in these crystalline films were studied systematically when the thickness is increased. The long-range order that does not

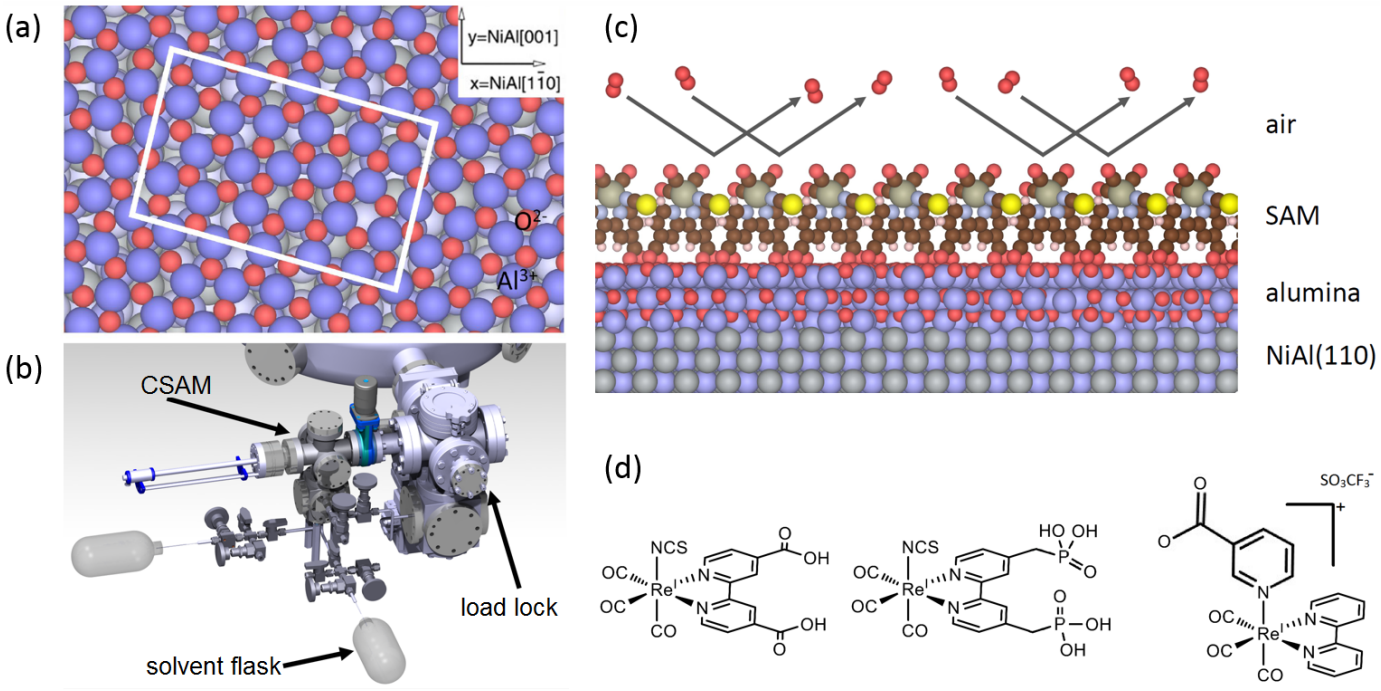

FIG. 13.2 – (a) Structure of a two-atomic-layers thick alumina film grown on NiAl(110) (unit cell marked in white, based on the model from Ref. [9]). (b) 3D rendering of the developed chamber (SAMcham) for self-assembled monolayers SAM deposition without exposing the samples to air. (c) Illustration of the produced metal-insulator-SAM heterostructure and the passivation effect. The SAM passivates the substrate in air. (d) Structure formulae of rhenium based organometallics with covalent linkers that were successfully attached to ultrathin alumina films.

relate to any bulk structure, is imposed by the crystallized interface, and is characterized by a rather large surface unit cell as shown in Fig. 13.2(a). This surface unit cell formed at the interface persists in thicker films. In contrast, the short-range ordering changes upon film growth and is attributed to the formation of subnanometer-sized $\gamma - Al_2O_3$-type nuclei inside the larger unit cell [8].

These ultrathin alumina films are prepared in ultra-high vacuum systems. The instability of these films under ambient conditions limits the possibilities of applications of these systems when the thickness of the insulating oxide film is crucial for device performance. Therefore, a chamber was developed and attached to our UHV system that allows to directly deposit organometallic rhenium complexes from solution with covalent linkers as illustrated in Fig. 13.2(b). Self-assembled monolayers (SAM) can thus be formed from a solution without sample exposure to air. The molecular layer acts as a capping layer, passivating the ultrathin oxide film against corrosion under ambient conditions (Fig. 13.2(c)). This method for molecule attachment was demonstrated to work for various photoactive organometallics (Fig. 13.2(d)), which allowed to compare their adsorption behavior and electronic level alignment to the substrate.

[6] B. Probst *et al.*, Inorg. Chem. **48**, 1836 (2009).

[7] Q.-H. Wu *et al.*, Int. Rev. Phys. Chem. **28**, 517 (2009).

[8] W.-D. Zabka *et al.*, Phys. Rev. B, **96**, 155420 (2017).

[9] G. Kresse *et al.*, Science, **308**, 1440 (2005).

13.3 Polarization-sensitive pulse reconstruction by momentum-resolved photoelectron streaking

In collaboration with: Johannes Haase (Laboratory for Catalysis and Sustainable Chemistry, Paul Scherrer Institute, Switzerland), Jeroen A. van Bokhoven (Department of Chemistry, ETH Zurich, Switzerland), Matteo Lucchini (Physics Department, Politechnico di Milano, Italy) (NCCR MUST).

Many pump-probe experiments nowadays aim at the investigation and manipulation of ultrafast dynamic processes at surfaces [10]. For instance, a THz pulse can interact with the dipole moment of adsorbed molecules and induce coherent atomic motion [11]. The structural dynamics of such motion is accessible via , e.g., x-ray photoelectron diffraction (XPD) [12]. A decisive experimental parameter in these types of experiments is the time-dependent strength and orientation of the electric field in close proximity to the surface under investigation. This effective electric field often results from the superposition of an incoming and reflected laser pulse and has a complex nature varying in space and time. In this work [13],

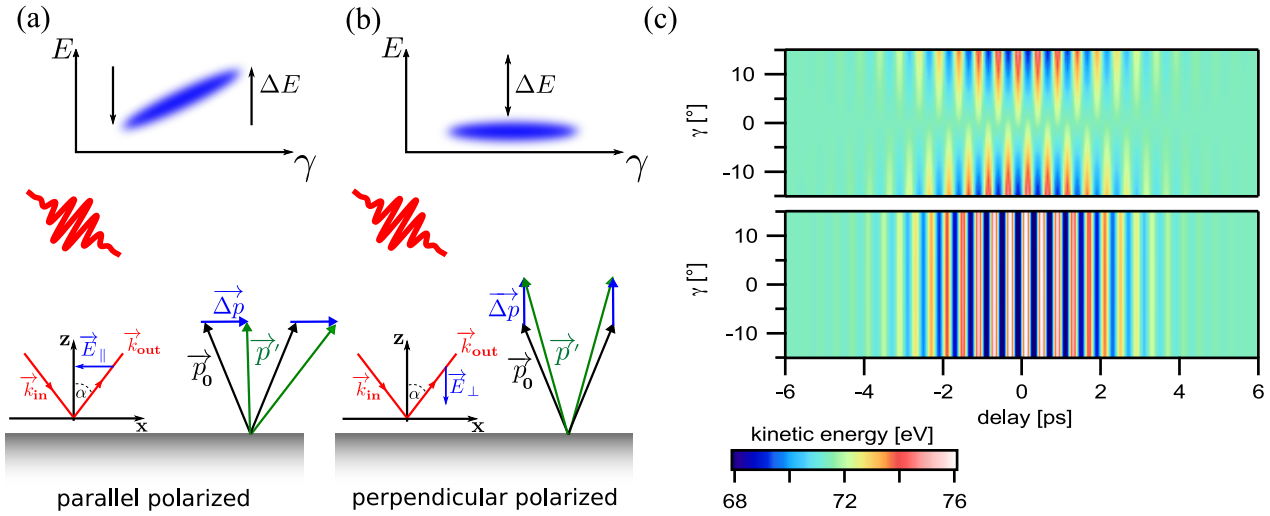

FIG. 13.3 – Schematic illustration of the effects of THz field components polarized parallel and perpendicular to the surface on the x-ray-emitted photoelectron momentum distribution (from [13]). (a) Effect of the electric field component parallel to the surface. The effective electric field due to superposition of incoming and reflected THz light with wavevectors $\vec{k}_{in}$ and $\vec{k}_{out}$ induces a momentum change $\vec{\Delta p}$ to the initial electron momentum $\vec{p}_0$ which results in a final momentum $\vec{p}\,'$. The effect on the detected electron distribution as measured in the two-dimensional electron analyzer is depicted at the top. γ is the detector angle and E the kinetic energy. (b) Same as in (a) but for the THz field component perpendicular to the surface. (c) COM maps of photoelectrons with an initial kinetic energy of 72 eV interacting with a Gaussian-shaped THz pulse with a peak amplitude of 10^7 V/m ($\lambda = 150$ µm, FWHM = 5 ps). The presented COM maps are shown for the case of a transparent substrate, i.e. with no reflection present. The anti-symmetric (top) and symmetric (bottom) energy shifts with respect to the normal emission direction $\gamma = 0°$ are hallmarks of the parallel and perpendicular field component.

we developed a pulse metrology to reconstruct the effective electric field components parallel and perpendicular to arbitrary metallic or dielectric surfaces by means of THz-field modified electron momentum distributions as measured in photoelectron spectroscopy experiments.

Photoelectrons are generated by a short x-ray pulse at a solid surface and undergo a momentum change due to interaction with a few-cycle THz pulse. The electron analyzer is capable of tracking changes in both, electron kinetic energy and angular distribution. Assuming a linearly polarized electric field, the effect of field components purely parallel and perpendicular to the surface is schematically shown in Fig. 13.3. Panel (a) elucidates the change to the detected electron distribution induced by a parallel field component. A parallel component leads to a lateral shift in the momentum distribution and hence to energy shifts that are roughly anti-symmetric to the normal emission direction. The perpendicular component in Fig. 13.3(b) causes a symmetric change in the momentum distribution and a symmetric energy offset relative to the interaction-free distribution. For each angular channel of the detector an energetic center of mass (COM) position can be determined that reflects the position of, for instance, an elastic photoemission line. THz-field induced changes in the electron distribution can then be followed in COM maps as shown in Fig. 13.3(c). These maps present the COM position of the electron distribution color-coded as a function of detector angle γ and relative delay between x-ray and THz pulse. The anti-symmetric energy modifications along the angle-dispersive axis due to the parallel field component Fig. 13.3(c, top), as well as the symmetric changes due to the perpendicular component Fig. 13.3 (c, bottom) are apparent. Our model uses the kinetic energy offset along the normal emission channel ($\gamma = 0°$) and the tilt angle of the COM distribution along the angle-dispersive axis as measures for the electron momentum added by the THz field which in turn can be related to the THz field components. We tested the validity of our model at different interfaces described by their optical constants. By using a Monte Carlo approach we were able to simulate artificial pump-probe experiments on a variety of substrates and with different optical parameters of the x-ray and THz pulse. We could validate our reconstruction approach by comparing the obtained field amplitudes to those calculated by Fresnel's equations and suggest suitable photoelectron energy regimes for optimal field reconstruction.

[10] J.L. LaRue *et al.*, Phys. Rev. Lett. **115**, 036103 (2015).

[11] S.S. Dilhon *et al.*, J. Phys. D: Appl. Phys. **50**, 043001 (2017).

[12] M. Greif *et al.*, Struct. Dyn. **2**, 035102, (2015).

[13] K. Waltar *et al.*, Opt. Express **26**, 8364-8374 (2018).

14 Disordered and Biological Soft Matter

M. Ackermann, C.M. Aegerter, F. Atzeni, P. Dagenais, D. Dreher, A. Keller (till March 2018), F. Lanfranconi (till December 2017), A. Mallavalli, S. Puri, S. Scheibler (Master student), L. Schertel , J. Schneider, L. Selvaggi, T. Stöckli (Master student) and S. Urdy (till July 2017)

in collaboration with: Institute of Molecular Life Sciences (K. Basler, T. Aegerter-Wilmsen, L. Pelkmans, D. Brunner), ETH Zürich (P. Koumoutsakos), MPI für Planzenforschung Köln (R.S. Smith), University of Fribourg (A. Jazwinska), University of Bern (C. Kulemeier, S. Robinson), Biozentrum Basel (M. Affolter), University of Konstanz (G. Aubry, G. Maret), MPI für Selbstorganisation Göttingen (C.C. Maass), Deutsches Luft- und Raumfahrtzentrum (M. Sperl), Université Joseph Fourier Grenoble (S. Skipetrov), Université Paris Denis Diderot (F. Graner), Technion Haifa (E. Akkermans).

In the group of disordered and biological soft-matter, we are interested in the behaviour of disordered materials outside of equilibrium, where instabilities arise, which lead to emergent structures. In particular, we are currently studying three overarching themes: The first is concerned with light transport in disordered, multiple-scattering media, where we aim at understanding, controlling and using multiply scattered light. In terms of understanding, we are also studying fundamental properties of multiple-scattering transport, such as the influence of path-reciprocity and Mie-scattering in the context of Anderson localisation and photonic band gaps. On the side of controlling light transport, we are using wavefront shaping to structure the illumination behind turbid layers, effectively compensating the multiple scattering. This can then be used in creating microscopy techniques that are capable to image structures in turbid media. Such novel imaging techniques for instance come into play in the second class of problems we are interested in, namely the regulation of biological development via mechanical forces. This is studied in the growth of the Drosophila wing and its folds as well as in the regeneration of fins of the zebrafish. The control of developmental processes by mechanical forces is also studied less in the context of direct growth regulation, but more in the context of shaping three dimensional structures as a driver of morphogenesis. This is studied in detail in the process of dorsal closure in Drosophila embryos. In all of this, the mechanical characterization of the materials in question is of paramount importance and we are using novel force techniques at the appropriate force levels ranging from nano Newtons to micro Newtons. The third theme finally, which complements these biological systems, consists of physical model systems that are far outside of equilibrium, such as granular gases and foams. These are studied in diamagnetic levitation in order to obtain information on long time dynamics, which is otherwise masked by the effects of gravity. In this way, we can study the overall properties of instabilities in disordered non-equilibrium systems.

Last years progress in the subjects of light transport in photonic glasses, imaging in turbid media, as well as the study of elastic properties of biological materials, such as the cytoplasm of the Drosophila embryo, its wing imaginal disc, and the bending stiffness of the zebrafish caudal fin are discussed in detail below.

14.1 Near field effects in the light transport through photonic glasses

In the study of light transport in photonic glasses, several aspects of light scattering are of importance. The refractive index difference determines the scattering strength, which is however also influenced by the size of the scatterers by the appearance of resonances due to Mie-scattering. Finally, in densely packed samples, positional correlations between the particles are of importance and have to be considered as well. We have recently developed and tested an extension of the energy coherent potential approximation [1], which takes into account collective effects of the scatterer arrangement [2]. In the case of weakly scattering polystyrene particles, we have been able to show that the scattering strength and the effective refractive index describe the experimental findings well, including the resonant effects due to the size of the particles, which is comparable to the wavelength of light. This can be seen in Fig. 14.1, where the scattering strength of several samples is shown as a function of the particle size. In addition to our data, the theory also describes data from [3]. The scattering strength in these experiments was determined from the width of the coherent backscattering cone [4]. With a working theory as this, capable of describing light transport in dense high index materials, it becomes possible to design materials that come close to the transition point to Anderson localisation [5, 6].

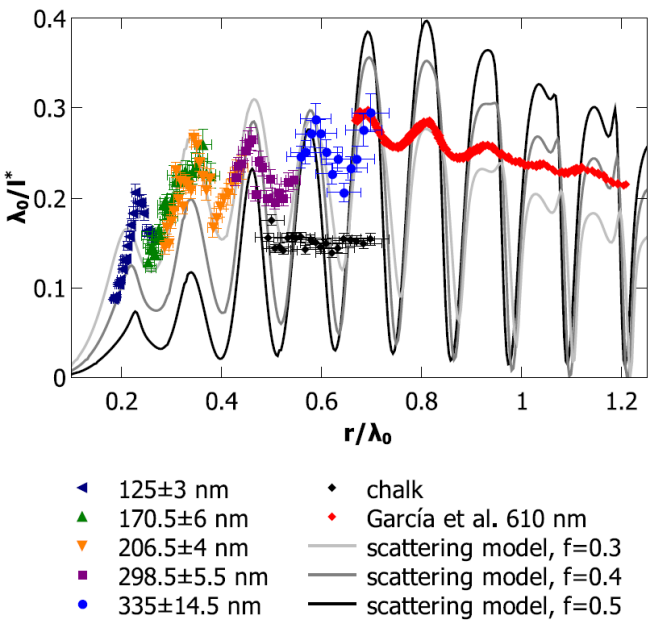

FIG. 14.1 – Scattering strength of photonic glasses made of almost mono-disperse polystyrene particles. Changing the wave-length of the scattered light, as well as the particle size, the full range of relative particle sizes can be studied and resonance effects due to Mie-scattering can be observed. The theoretical model describes our data, as well as those of García well, with a slight underestimation of the filling fraction.

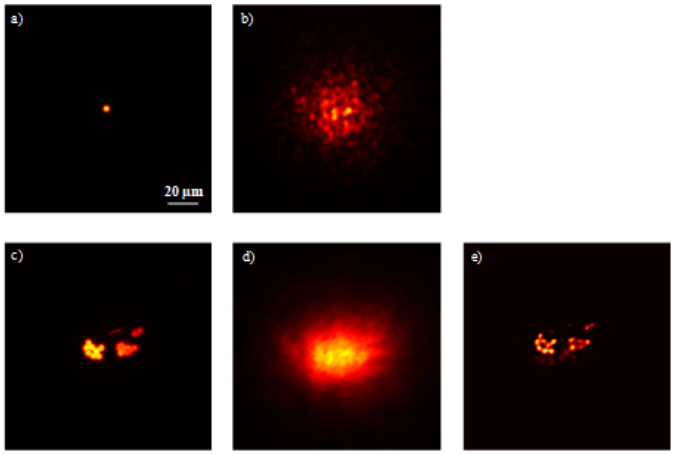

FIG. 14.2 – a) The image of a single fluorescent bead used as guide star. b) The same scene as in a) scrambled by the scattering layer indicating the PSF of the system. c) The image of a fluorescent scene. d) The same scene as in c) scrambled after passing the same part of the turbid medium. e) Reconstruction of the fluorescent scene seen in c) by deconvoluting image d) with image b) using blind deconvolution with 80 iterations. The distance between the fluorescent sample and the scattering medium was set to 5 mm.

[1] K. Busch and C.M. Soukoulis,
Phys. Rev. Lett. **75** 3445 (1995).

[2] G. Aubry, L. Schertel, M. Chen, H. Weyer, C. M. Aegerter, S. Polarz, H. Cölfen, and G Maret,
Phys. Rev. A **96** 043871 (2017).

[3] P. D. García, R. Sapienza, J. Bertolotti, M. D. Martín, A. Blanco, A. Altube, L. Vi na, D. S. Wiersma, and C. López, Phys. Rev. A **78**, 023823 (2008).

[4] S. Fiebig, C.M. Aegerter, W. Bührer, M. Störzer, G. Montambaux, E. Akkermans, and G. Maret,
Europhys. Lett. **81**, 64004 (2008).

[5] P.W. Anderson, Phys. Rev. **109**, 5 (1958).

[6] M. Störzer, P. Gross, C.M. Aegerter, and G. Maret,
Phys. Rev. Lett. **96**, 063904 (2006).

14.2 Deconvolution techniques for imaging in turbid media

In recent years, we have made great progress in controlling light transport through turbid media, developing fluorescence microscopy [7] in three dimensions [8], without direct optical access [9]. However in the context of structured illumination [10] and single plane illumination microscopy [11], which we have shown can work in a turbid environment, it can be of interest to determine the fluorescent structures via de-convolution techniques. This is of particular interest in biological situations, where the turbidity is detrimental to imaging, however not purely random. Here, we have recently adapted a method of using a guide star [12] for the determination of the point spread function (PSF) of the imaging system. As can be seen in Fig. 14.2, this works even in a situation where imaging is otherwise impossible [13]. This points a way apply to single plane illumination [11] in actual biological settings.

[7] I. M. Vellekoop and C.M. Aegerter,
Opt. Lett. **35**, 1245 (2010).

[8] G. Ghielmetti and C.M. Aegerter,
Opt. Express **20**, 3744 (2012).

[9] G. Ghielmetti and C.M. Aegerter,
Opt. Express **22**, 1981 (2014).

[10] A. Malavalli, M. Ackermann, C.M. Aegerter,
Opt. Express (2016).

[11] J. Schneider and C.M. Aegerter,
Journal of the European Optical Society **14**, 7 (2018).

[12] E. Edrei and G. Scarcelli,
Nature Scientific Reports **6**, 33558 (2016)

[13] J. Schneider and C.M. Aegerter
to be published (2018).

14.3 Determining the bending stiffness of live zebrafish fins

In the study of the influence of hydrodynamic forces on the growth and regeneration of zebrafish fins [14], we are studying how the fins are deformed during swimming and what forces are acting on these fins. This is in order to correlate the forces with growth patterns and growth rates that determine the size and structure of the zebrafish fins. For making the connection between deformation and forces quantitative, we need to determine the mechanical properties of live zebrafish fins, where the bony rays as well as the soft interray tissue is of interest. For this purpose, we have built a setup with which to determine the bending stiffness of the entire fin in a position dependent manner, see Fig. 14.3 [15]. With this, we can see that the bending stiffness of the fins is mainly determined by the bony rays, since a disruption of the interray tissue between the tissue does not influence the values for bending stiffness we obtain. The stiffness of the bones that we find is in good agreement with a scaled down value determined from the amputated rays bluegill sunfish [16], which are much larger than zebrafish and where the stiffness is therefore easier to determine. However, by bending only part of the fin, we are effectively stretching the interray tissue (see Fig. 14.4b) in addition to the bending. By cutting the tissue at the point of bending, we can separate these two contributions and hence obtain a determination of the effective elastic moduli of not only the bony rays, but also of the interray tissue, which is more than three orders of magnitude softer than the rays and is of the order of a few kPa.

[14] C. Pfefferli, and A. Jazwinska, Regeneration **2** 72 (2015).

[15] S. Puri, T. Aegerter-Wilmsen, A. Jazwinska, and C.M. Aegerter, Journal of experimental Biology **221**, 17077 (2018).

[16] B.E. Flammang, S. Alben, P.G.A. Madden, and G.V. Lauder, J. Morphol. **274**, 1044-1059 (2013).

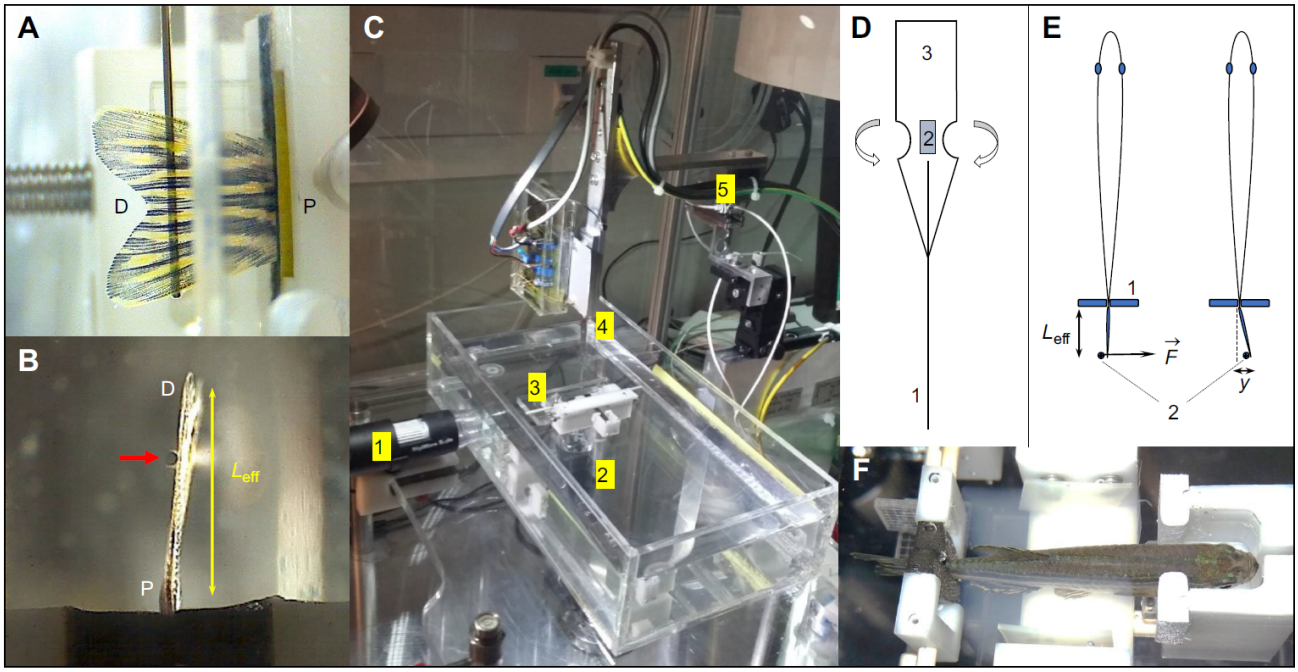

FIG. 14.3 – (A) Side-view of a lined force attack from the deflection pin onto the fin surface (D: distal end of the fin; P: proximal end of the fin). (B) Bottom-view showing the pin (red arrow) at a certain effective beam length from the fixation (black foam pads). (C) Overall impression of the measurement setup showing a water basin, two camera positions (1., 2.) as in (A) and (B) respectively, a fish holding device (3.) as also shown again in (F) and the sensor construct (4.) mounted onto piezo-based positioners (5.). (D) Design of the sensor construct with strain gages (2.) mounted onto a spring sheet (3.) together with the deflection pin (1.) that leads to the base of the strain gages to increase the effective bending moment together with the specialized geometry of the spring sheet (3.). (E) Measurement principle illustrating the deflection pin (2) applying a force at a certain proximal-distal position (effective beam length, Leff) leading to a certain displacement y. The fish peduncle is held by two opposing foam pads (1) as also shown in figure (B). (F) Zebrafish holding device showing an anesthetized adult specimen.

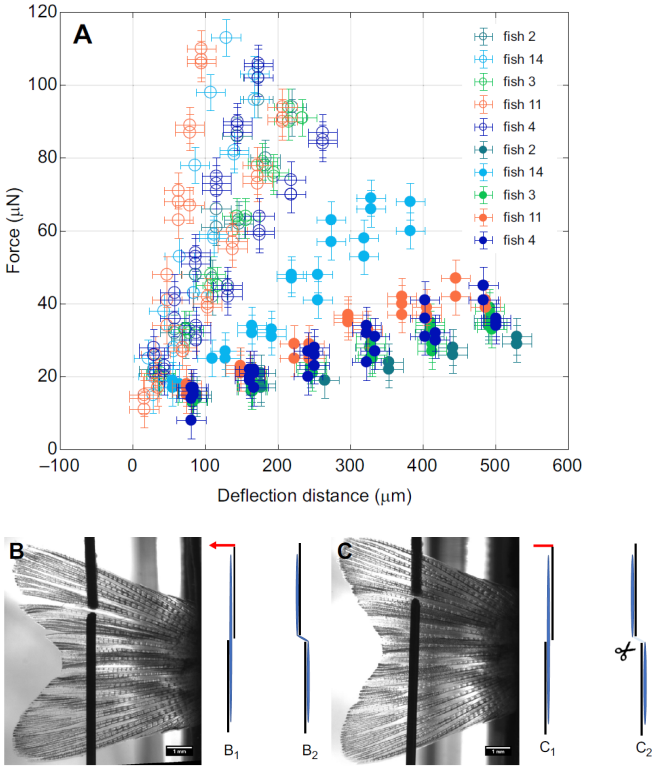

FIG. 14.4 – (A) The force extension curves for 5 fish are shown, while circled data points indicate measurements on intact tissues (B). At the same time data points (non-circled) are shown for surgically disrupted tissues (C), (error bars for deflection distance correspond to standard deviations (±20μm), equally for force (±5μN). Measurements were performed at the same positions in each fin, once between the 4th and 5th ray (B, C) and once between the 6th and 7th ray (not shown). The illustrations (B1, B2, C1, C2) represent front views. B1 and C1 represent the initial starting position, before a deflection (indicated by a red arrow) has occurred that would result in the configurations B2 and C2 respectively.

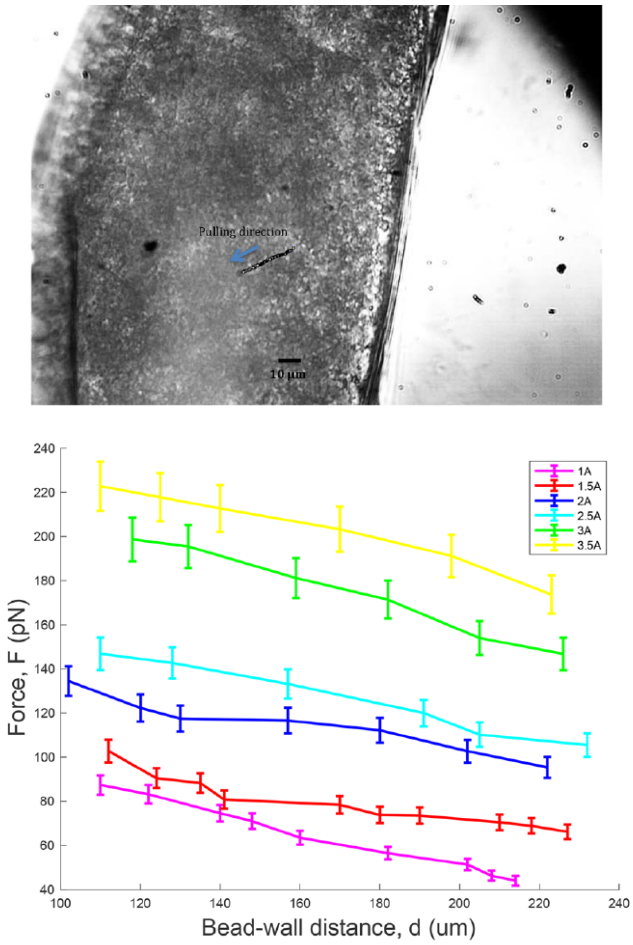

FIG. 14.5 – Top: Trace of a 2.8 μm bead pulled with a constant magnetic force inside a fly embryo. The field of view is 275 μm × 206 μm. Bottom: Force calibration curves of 2.8 μm Dynabeads for different current values.

14.4 Determining the viscoelastic properties of the cytoplasm in Drosophila embryos

In the context of morphogenesis, we are studying the process of dorsal closure in the Drosophila embryo [17]. Here, we are interested into how mechanical forces shape a tissue and actively lead to contractions [18]. For this purpose, the mechanical properties of tissues and cytoplasms in the Drosophila embryo. Given that we want to be able to actively apply forces and the scale of the forces present in embryos, we have built a magnetic tweezer setup [19], which is able to apply forces of the order of several hundred pico Newton onto super-paramagnetic beads that can be injected into the embryo at an early stage (see Fig. 14.5) and then positioned to a desired part of the embryo, such that they are incorporated into tissues of choice. With this, we have been able to determine the visco-elastic properties of the cytoplasm of mid-stage Drosophila embryos [19], where the viscous part is in reasonable agreement with a previous determination at the same stage of development that was done using passive microrheology [20].

[17] J. Solon, A. Kaya-Copur, J. Colombelli, D. Brunner, Cell **137**, 1331 (2009).

[18] T. Idema, J.O. Dubuis, L. Kang, M.L. Manning, P.C. Nelson, T. C. Lubensky, and A.J. Liu, PLoS One **8**, e77216 (2013).

[19] L. Selvaggi, L. Pasykarnakis, D. Brunner, and C.M. Aegerter, Review of Scientific Instruments **89** 045106 (2018).

[20] A.D. Wessel, M. Gumalla, J. Grosshans, and C.F. Schmidt, Biophys. J. **108**, 1899 (2015).

14.5 The influence of geometry on the elastic properties of the Drosophila wing imaginal disc

We have in the past extensively studied the mechano-regulation of growth in the Drosophila wing imaginal disc, where we have modelled the process [21, 22] and shown that mechanical feedback in growth regulation can lead to a size determination as well as uniform growth in the presence of growth factor gradients. In addition, we have shown that there are mechanical stresses present in the wing disc [23] and that mechanical tension can lead to an increase in cell division rates [24]. When studying these regulation mechanisms on a cellular level, the forces acting on individual cells need to be known even though the application of force is on the entire tissue level. Therefore, we have recently started to investigate how applied loads are distributed in the tissue and which parts of the tissue get stressed most. For this purpose, we have combined the stretching apparatus used previously [24] with a confocal microscope, such that the deformations of the tissue as well as the cells can be determined concurrently with the application of a mechanical load. This is shown in Fig. 14.6, where it can be seen that much of the initial elongation of the tissue is due to an unfolding of the corrugated structure.

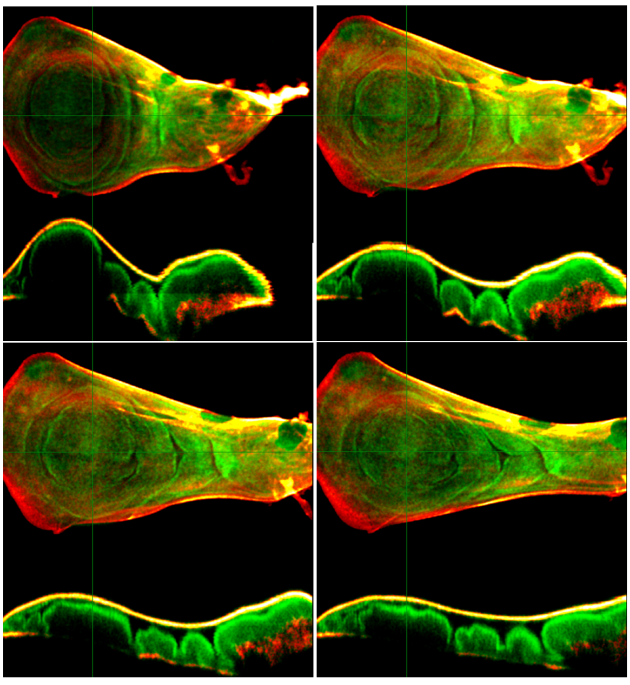

FIG. 14.6 – Deformation experiment, three-dimensional confocal microscopy images of 0 µm (top left), 30 µm (top right), 50 µm (bottom left) and 70 µm (bottom right) deformation of fixed boundary. The extracellular matrix is in red and the apical side of the tissue in green.

This leads to a strongly non-linear behaviour in the force-extension curve, shown in Fig. 14.7. After the unfolding, the extracellular matrix (ECM) surrounding the tissue (marked in red in Fig. 14.6) begins to experience the mechanical load. Since ECM is a dense network of collagen fibres, it is much stiffer than the rest of the tissue, such that its stretching requires more force, thus leading to an increase in the slope of the force extension curve. We have also modelled this computationally [25], where the non-linear response is reproduced reasonably well even using completely linear materials, see Fig. 14.7.

Thanks to the computational modelling, we can therefore now also have a picture of which parts of the tissue experience the most stress in a stretching experiments, such that the cellular mechanism can be investigated experimentally. This is shown in Fig. 14.8, where the deformation of the modelled wing disc is comparable to that of the experiment, but we in addition can determine the shear and normal stresses spatially resolved, showing that they are localised mostly in the ECM, as well as close to the folds.

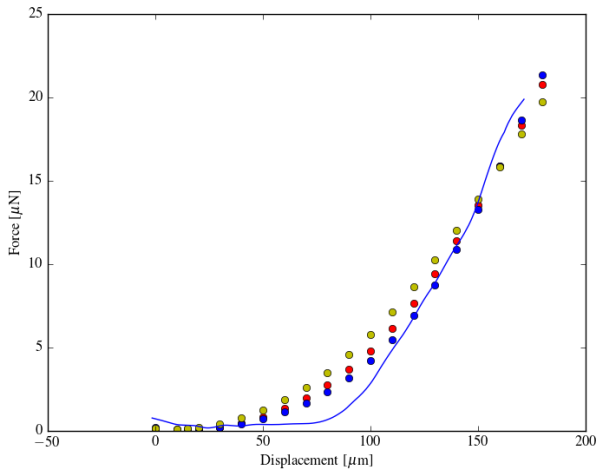

FIG. 14.7 – Solid line: Force extension curve averaged over nine subsequent extensions. The force extension curve is highly non-linear with a strong increase in its slope at an extension of roughly 80 µm, where the overall response stiffens by at least an order of magnitude. The fact that the extension returns to zero when the force is reduced indicates that the tissue reacts elastically on the time scale of the experiment, which is 900 s. The symbols show modelled force displacement curves with an overall elastic modulus of 1.1 kPa and an outside layer of ECM with a higher modulus by a factor of 50 (blue dots) and 100 (red dots). The yellow dots are as the red ones, but with additionally a harder layer on the apical side with a 100 times higher modulus than the entire wing disc.

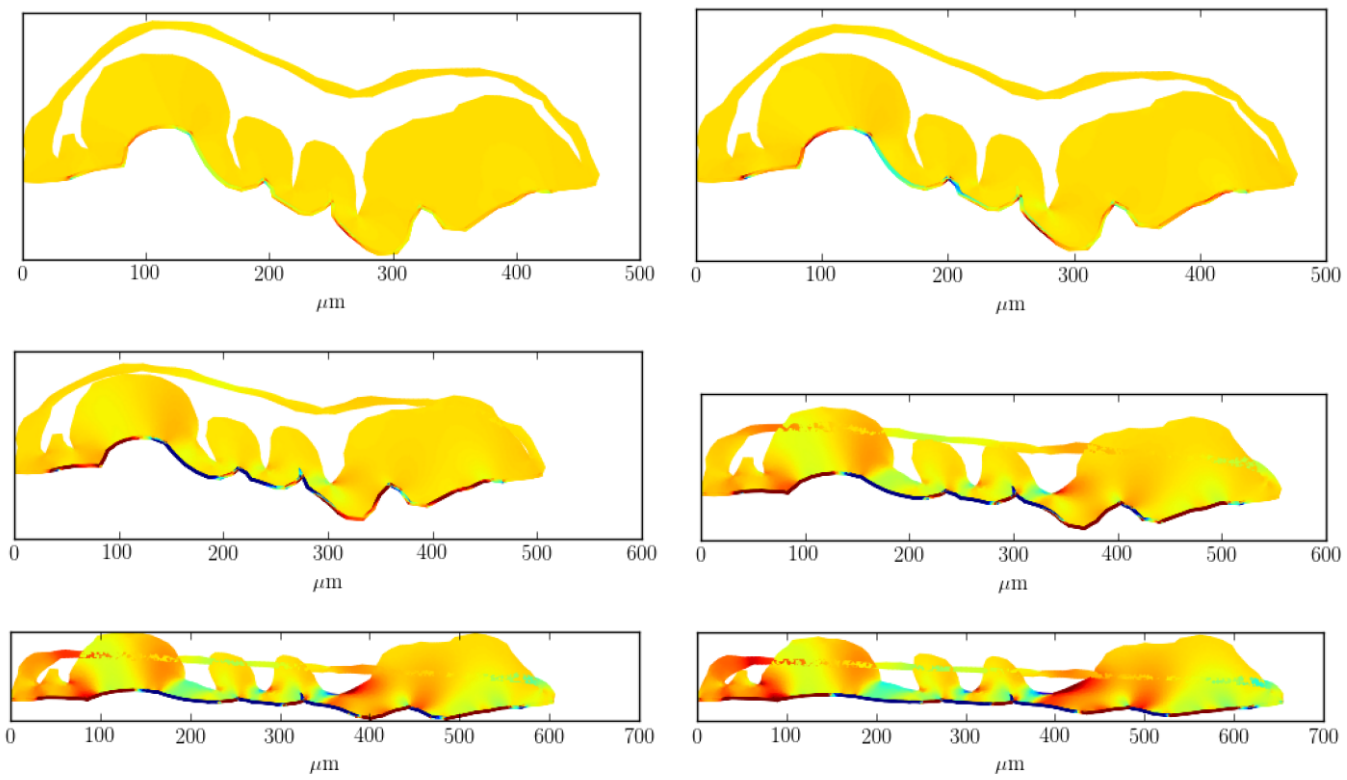

FIG. 14.8 – Modelled deformation history: color coded is the shear component σ_{xy} of the Cauchy stress tensor. The color scale varies from -0.03 MPa (blue) to 0.015 MPa (red).

[21] T. Aegerter-Wilmsen, C.M. Aegerter, E. Hafen, and K. Basler,
Mechanisms of Development **124**, 318 (2007).

[22] T. Aegerter-Wilmsen, M.B. Heimlicher, A.C. Smith, P. Barbier de Reuille, R.S. Smith, C.M. Aegerter, and K. Basler, Development **139** 3221 (2012).

[23] U. Nienhaus, T. Aegerter-Wilmsen, and C.M. Aegerter,
Mechanisms of Development **126**, 942 (2009).

[24] T. Schluck, U. Nienhaus, T. Aegerter-Wilmsen, and C.M. Aegerter,
PLoS One **8**, e76171 (2013).

[25] A. Keller, F. Lanfranconi, and C.M. Aegerter,
to be published (2018).

15 Mechanical Workshop

C. Albrecht, B. Lussi, R. Maier, M. Schaffner, S. Scherr, G. Knüsel, B. Markwalder, P. Weyeneth, N. Regensburger

Infrastructure

A new high performance precision band saw was purchased for the raw material storage to guarantee an excellent cutting quality for materials with up to 265 mm in diameter (Fig. 15.1).

The big lathe was relocated to the student workshop in order to create more space in the main workshop (Fig. 15.2). This space was needed for the installation of the new high-performance, milling - turning and machining centre in the physics workshop in December. This new machine, allows now to carry out turning and milling operations of highly complex components on one single machine (Fig. 15.3). To promote the exchange with many of our customers from various institutes of UZH, ETH Zurich, universities of applied sciences, as well as the customers of the material storage, our annual aperitif was organized in autumn.

FIG. 15.1 – High performance precision band saw.

FIG. 15.2 – Relocation of the big lathe to the student workshop.

FIG. 15.3 – New high-performance, milling - turning and machining centre. The top figure shows the transport through the corridor.

Personnel

Brandon Markwalder and Pascal Weyeneth completed their practical apprenticeship examination with very good results (see Fig. 15.4 and 15.5) and our second year apprentice Gian Knüsel has passed the part examination at the end of his second year with great success. Due to the large volume of orders Brandon Markwalder worked in our workshop until the end of October after his apprenticeship.

First of August 2018 Noah Regensburger started the four-year apprenticeship as a polymechanic EFZ. Noah has already settled in very well to his work and has integrated well into our team.

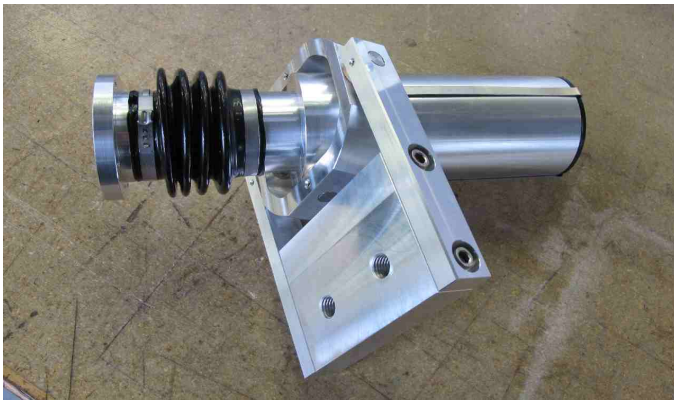

FIG. 15.4 – Masterpiece from Brandon: mirror actuator for CTA.

FIG. 15.5 – Masterpiece from Pascal: spindle stopper for the lathe.

Teaching

As every year our annual workshop courses for bachelor students, which took place in August/September 2017 and January/February 2018 were attended with great enthusiasm. In Autumn 2016 ETHZ apprentices trained their welding skills in our workshop (Fig. 15.6).

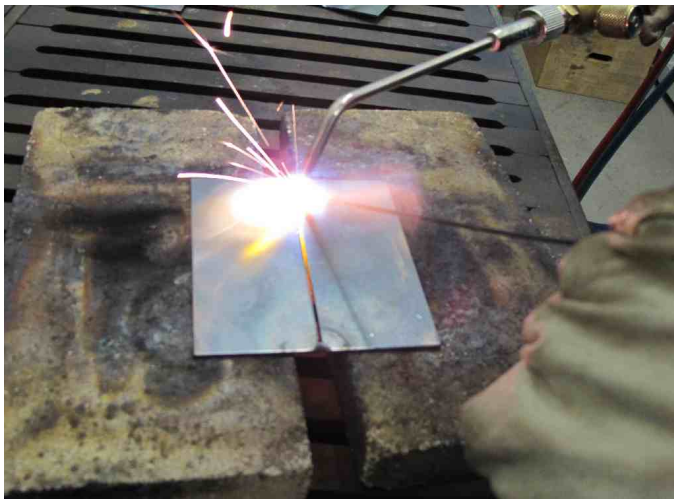

FIG. 15.6 – ETHZ apprentices trained their welding skills in our workshop.

Projects

Last year, our workshop was involved in various internal and external projects. In the following some projects are listed to which we significantly contributed:

- LGAD Telescope (Sec. 9)
  For the group of Ben Kilminster we designed and built the telescope to test LGAD (low-gain avalanche detectors) in our workshop (Fig. 15.7).

FIG. 15.7 – Telescope to test LGAD.

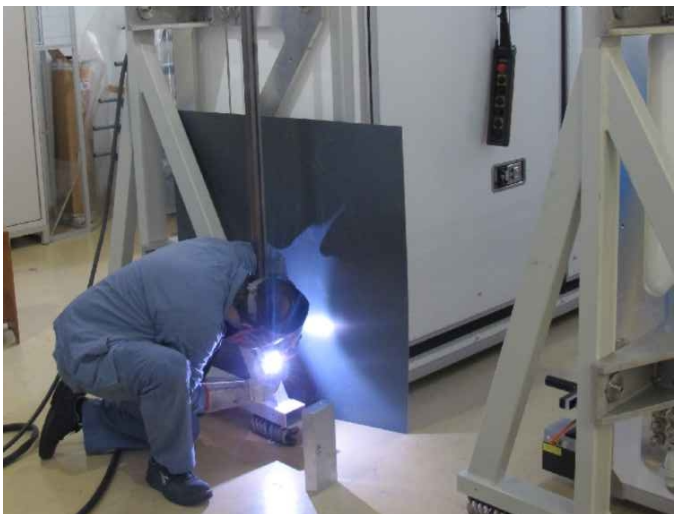

FIG. 15.8 – Welding work for reinforcement of the transportation frame done directly on a FlashCam camera body.

- CTA Cherenkov Telescope Array (Sec. 6)
  The mechanical workshop has contributed towards the finalization of two FlashCam camera bodies with the production of different mechanical parts as well as with help and personnel support during the whole assembly phase.

- Disordered and Biological Soft Matter (Sec. 14)
  We produced various moulds for fins of zebra fish in order to optimally make use of the integrated swimming channel which was built for the group of Christof Aegerter in the previous year.

- Phase Transitions, Materials and Applications (Sec. 12)
  As in previous years we've manufactured various sample holders to be used inside the cryostats for the group of Andreas Schilling . A lead coating was applied to protect against leakage of X-ray.

- Demonstration experiments for the lectures
  In order to guarantee excellent demonstration experiments for the student lectures we designed and produced some new devices and revised and maintained several older parts.

- External orders
  As in previous years many orders were placed from external institutions, universities and private companies (Fig. 15.9). Our workshop is well and widly known for its competence, high quality work and the highly motivated and competent workshop team.

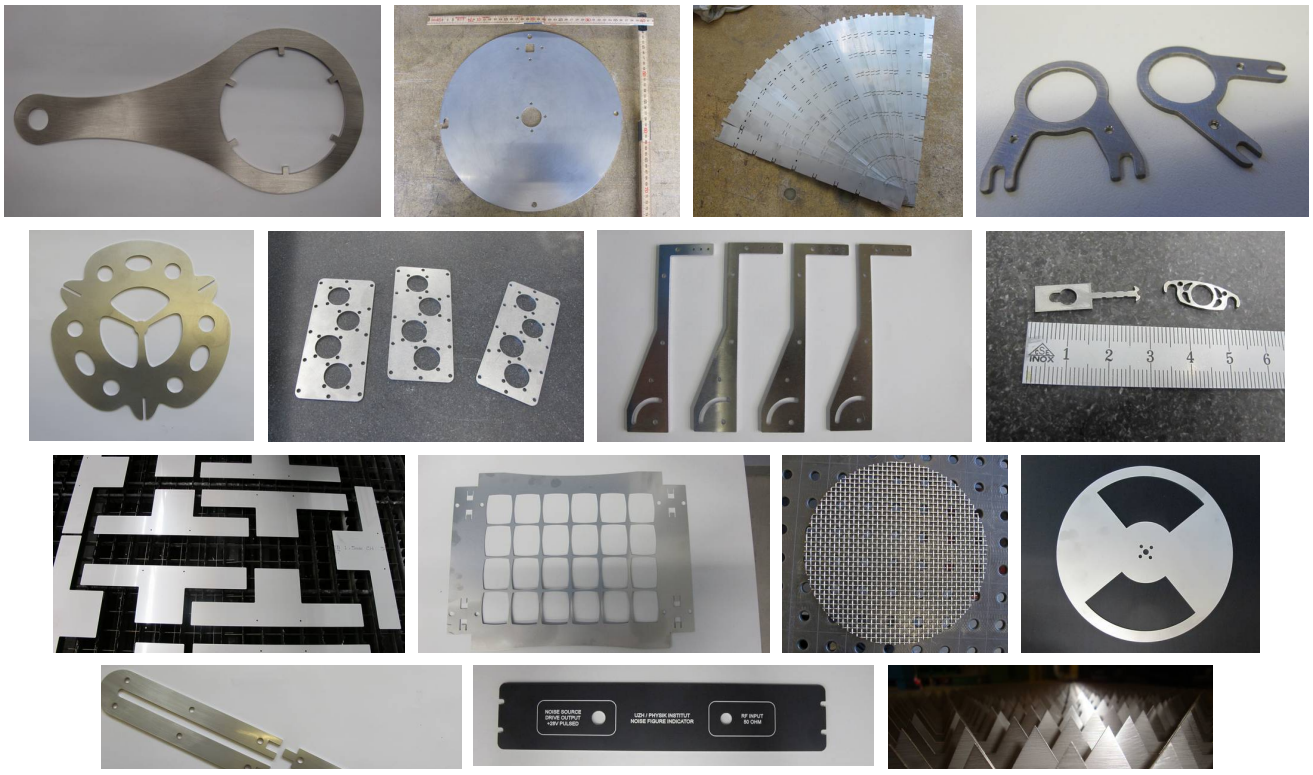

FIG. 15.9 – A selection of parts produced for external institutions, universities and private companies. All of them have been produced with the laser cutter.

16 Electronics Workshop

D. Florin, S. Karrer, A. Vollhardt, and D. Wolf

During the past year the electronics workshop supported the scientists during all phases of conception, design, purchasing and commissioning of various experimental setups. In the following sections the contributions to selected projects are highlighted.

For the CTA group of Prof. Canelli and Prof. Straumann (Sec. 6), staff of the workshop assisted in final construction and outfitting of two camera bodies of the CTA Flashcam project. This included electric and electronic wiring and testing as well as assembly and commissioning of the liquid cooling system of the camera bodies. Particular emphasis was put on the development, commissioning and verification of the fully redundant electric power system and its control hardware together with the required documentation. Another task has been the reduction of electronic noise in the Flashcam frontend boards in the photon detection plane to improve the signal-to-noise ratio of the photomultiplier signals. In parallel, 220 mirror actuator sets produced for the CTA Large Scale Telescope prototype were shipped to La Palma (Canary Islands, Spain). As the actuator system of the Physik-Institut has been selected as the common mirror actuator system for the complete CTA project, additional upgrades are integrated into a next D-series design, of which 60 sets will be prototyped in 2018. The upgrade includes improved electronics package as well as improved mechanical reliability. Figure 16.1 shows the two CTA FlashCam camera bodies in the assembly hall.

Based on a design from the University of Santa Cruz, we produced four test-boards for silicon photomultiplier detectors for the group of Prof. Serra (Sec. 8). Featuring a high speed, low-noise preamplifier directly next to the detector position allows for easy adaption to multiple sensor types and future applications. For the LHCb-UT project, we developed an interface board to connect a needle card for SALT128 readout chip wafers to an FPGA board (see Fig. 16.2). This interface board provides level translators for programming signals and general input/output-lines in addition to regulated voltages for operation of the SALT128 chip.

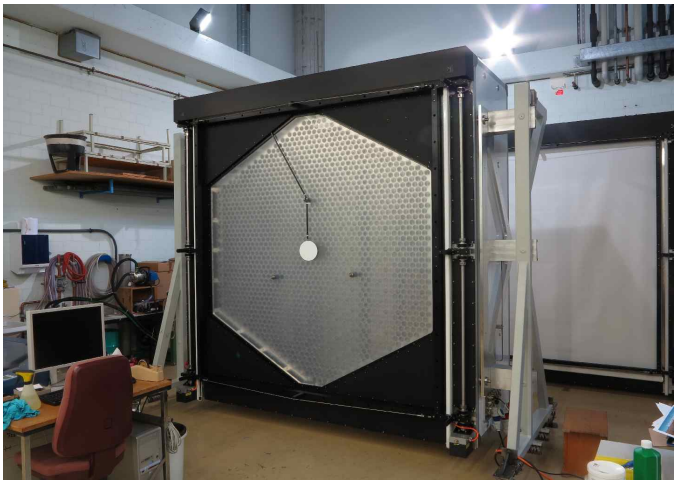

FIG. 16.1 – The two CTA FlashCam camera bodies in the assembly hall. The front camera has its lid opened and the optical calibration target extended.

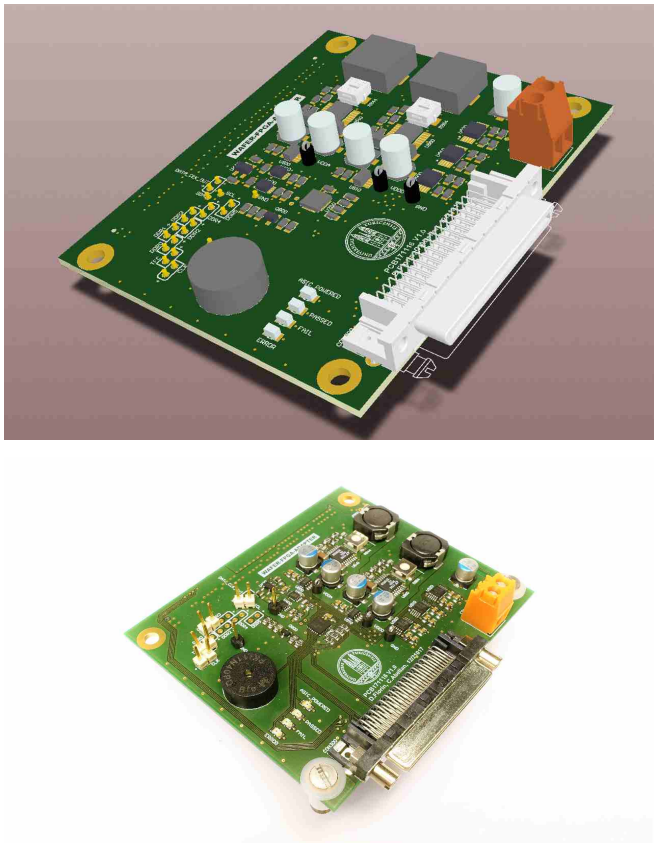

FIG. 16.2 – SALT128 wafer-FPGA adapter board: simulated CAD view and real hardware.

FIG. 16.3 – New remote control for the WALKUERE manipulator next to its old and larger version.

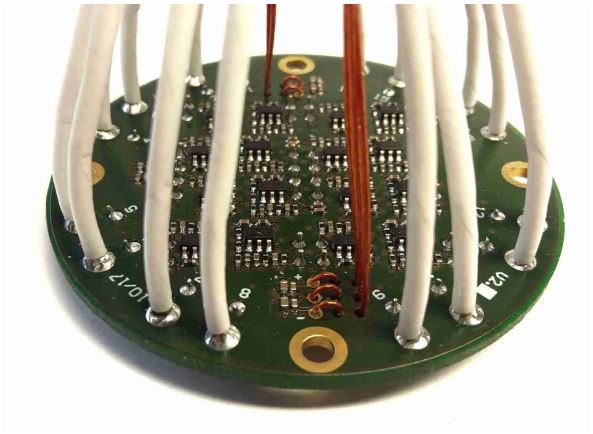

FIG. 16.5 – 16-channel preamplifier for the XENOSCOPE experiment.

For the group of Prof. Osterwalder (Sec. 13), the current joystick controller for the WALKUERE manipulator has proven to be not precise enough and too bulky. An improved version featuring a better control of positioning motor speeds and much reduced overall size was developed. The new remote control for the WALKUERE manipulator is shown in Fig. 16.3 together with the old version. Another setup required a new set of two PID temperature controllers (Fig 16.4), which were assembled and wired into a lab-compatible box with the correct external connectors.

For the Xenoscope project of the group of Prof. Baudis (Sec. 5), a compact 16-channel Silicon Photomultiplier amplifier was developed, which directly interfaces to the detector (see Fig. 16.5). In addition to amplifying the detector signals, the circuit also connects the required bias voltage to each individual channel.

A 100 MHz phase detector was built for the group of Prof. Aegerter (Sec. 14). Based on an IQ-mixer with appropriate filtering, the input signal is mixed with a reference signal and the phase information can be measured via DC-levels at the I- and Q-channel outputs (Fig. 16.6). Compared to the previous scope-based solution, this approach has the potential to significantly speed up the data taking process without compromising on signal quality.

FIG. 16.4 – Dual PID controller for the Group Osterwalder.

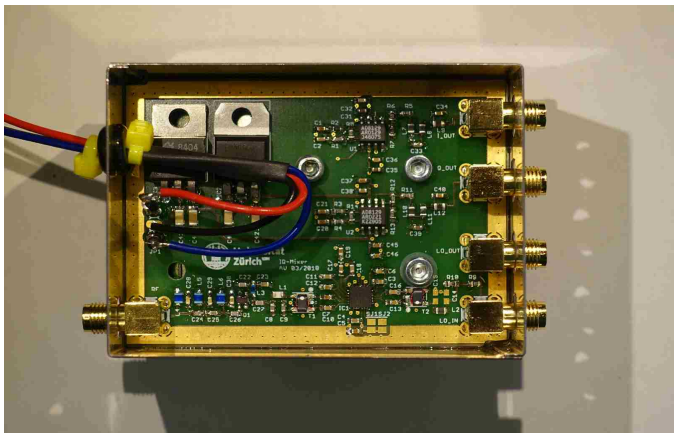

FIG. 16.6 – 100 MHz phase detector for the Group Aegerter.

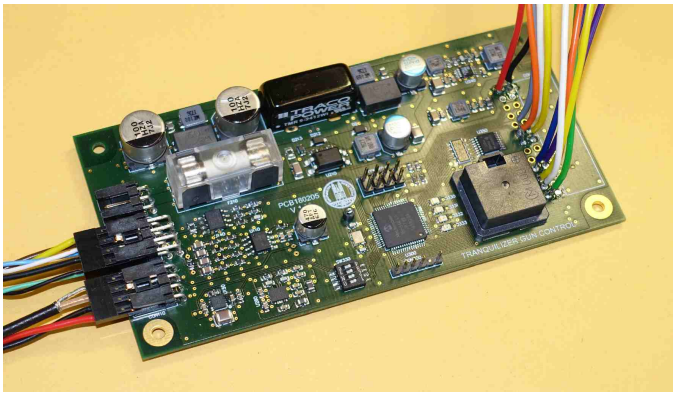

FIG. 16.7 – Control board for the tranquilizer gun remote control unit.

FIG. 16.8 – Microcontroller board for the electronics apprentice training program.

For an external project from the mechanical workshop, we assisted in the design and construction of control boards for a tranquilizer gun for wildlife animals. This control board handles the steering of the 2-axis gun turret together with a video channel for precise aiming and motion sensor to alert the operator if a potential target approaches the bait. The remote control unit for the operator is separated with a 100 m long network cable to allow the animals to approach the bait undisturbed.

A dedicated microcontroller board has been developed for the education of our electronics apprentice, together with the required training documentation and programming environment. This allows for an efficient introduction into microcontroller system development based on the C programming language. Starting on August 1st, 2018 the workshop will welcome a second electronics apprentice starting her 4-year higher education with the Physik-Institut.

The electronics workshop also organized and coordinated emergency power outlets in various laboratories. This work over the last years has been proven effective during an unplanned power cut in January 2018 which had little to no effect on the Physik-Institut.

17 Publications

17.1 Elementary particles and their interactions

17.1.1 Theory of Elementary particles

Articles

- A new method for one-loop amplitude generation and reduction in OpenLoops
F. Buccioni, S. Pozzorini and M. Zoller, Proceedings, 13th International Symposium on Radiative Corrections: Application of Quantum Field Theory to Phenomenology (RADCOR2017): St. Gilgen, Austria, September 24-29, 2017, arXiv:1801.03772

- On-the-fly reduction of open loops
F. Buccioni, S. Pozzorini and M. Zoller, Max, Eur. Phys. J. C **78** (2018) no.1, 70, arXiv:1710.11452

- NLO QCD+EW predictions for HV and HV +jet production including parton-shower effects
F. Granata, J. M. Lindert, C. Oleari and S. Pozzorini, JHEP **1709** (2017) 012, arXiv:1706.03522

- Precise predictions for $V+$ jets dark matter backgrounds
J. M. Lindert *et al.*, Eur. Phys. J. C **77** (2017) no.12, 829, arXiv:1705.04664

- NLO QCD+EW predictions for $2\ell 2\nu$ diboson signatures at the LHC
S. Kallweit, J. M. Lindert, S. Pozzorini and M. Schönherr, JHEP **1711** (2017) 120,arXiv:1705.00598

- Four-loop renormalization of QCD with a reducible fermion representation of the gauge group: anomalous dimensions and renormalization constants
K. G. Chetyrkin and M. F. Zoller, JHEP **1706** (2017) 074, arXiv:1704.04209

- An automated subtraction of NLO EW infrared divergences
M. Schönherr, Eur. Phys. J. C **78** (2018) no.2, 119, arXiv:1712.07975

- LHC Data and its Impact on nCTEQ15 PDFs
D. B. Clark *et al.* [nCTEQ Collaboration], PoS DIS **2017** (2018) 204, arXiv:1712.08199

- LHC lead data and nuclear PDFs
A. Kusina *et al.*, Acta Phys. Polon. B **48** (2017) 1035, arXiv:1705.06704

- Vector boson production in pPb and PbPb collisions at the LHC and its impact on nCTEQ15 PDFs
A. Kusina *et al.*, Eur. Phys. J. C **77** (2017) no.7, 488, arXiv:1610.02925

- NLO electroweak corrections in extended Higgs Sectors with RECOLA2
A. Denner, J. N. Lang and S. Uccirati, JHEP **1707** (2017) 087, arXiv:1705.06053

- Recola2: REcursive Computation of One-Loop Amplitudes 2
A. Denner, J. N. Lang and S. Uccirati, Comput. Phys. Commun. **224** (2018) 346, arXiv:1711.07388

- Azimuthal asymmetries in QCD hard scattering: infrared safe but divergent
S. Catani, M. Grazzini and H. Sargsyan, JHEP **1706** (2017) 017, arXiv:1703.08468

- $W^{\pm}Z$ production at the LHC: fiducial cross sections and distributions in NNLO QCD
M. Grazzini, S. Kallweit, D. Rathlev and M. Wiesemann, JHEP **1705** (2017) 139, arXiv:1703.09065

- Higgs boson pair production at NNLO in QCD including dimension 6 operators
D. de Florian, I. Fabre and J. Mazzitelli, JHEP **1710** (2017) 215, arXiv:1704.05700

- Graviton resonance phenomenology and a pseudo-Nambu-Goldstone boson Higgs at the LHC
E. Alvarez, L. Da Rold, J. Mazzitelli and A. Szynkman, Phys. Rev. D **95** (2017) no.11, 115012, arXiv:1610.08451

- Higgs boson pair production at NNLO with top quark mass effects
M. Grazzini, G. Heinrich, S. Jones, S. Kallweit, M. Kerner, J. M. Lindert and J. Mazzitelli, JHEP **1805** (2018) 059, arXiv:1803.02463

- Next-to-Next-to-Leading-Order QCD Corrections to the Transverse Momentum Distribution of Weak Gauge Bosons
  A. Gehrmann-De Ridder, T. Gehrmann, E. W. N. Glover, A. Huss and D. M. Walker, Phys. Rev. Lett. **120** (2018) no.12, 122001, arXiv:1712.07543

- Determination of the strong coupling constant $\alpha_s(m_Z)$ in next-to-next-to-leading order QCD using H1 jet cross section measurements
  V. Andreev *et al.* [H1 Collaboration], Eur. Phys. J. C **77** (2017) no.11, 791, arXiv:1709.07251

- NNLO QCD corrections to event orientation in e^+e^- annihilation
  T. Gehrmann, E. W. N. Glover, A. Huss, J. Niehues and H. Zhang, Phys. Lett. B **775** (2017) 185, arXiv:1709.01097

- Precise predictions for the angular coefficients in Z-boson production at the LHC
  R. Gauld, A. Gehrmann-De Ridder, T. Gehrmann, E. W. N. Glover and A. Huss, JHEP **1711** (2017) 003, arXiv:1708.00008

- Precise predictions for dijet production at the LHC
  J. Currie, A. Gehrmann-De Ridder, T. Gehrmann, E. W. N. Glover, A. Huss and J. Pires, Phys. Rev. Lett. **119** (2017) no.15, 152001, arXiv:1705.10271

- Precise predictions for $V+$ jets dark matter backgrounds
  J. M. Lindert *et al.*, Eur. Phys. J. C **77** (2017) no.12, 829, arXiv:1705.04664

- Single Jet Inclusive Production for the Individual Jet p_{T} Scale Choice at the LHC
  J. Currie, E. W. N. Glover, T. Gehrmann, A. Gehrmann-De Ridder, A. Huss and J. Pires, Acta Phys. Polon. B **48** (2017) 955, arXiv:1704.00923

- Transverse-momentum resummation for the signal-background interference in the $H \to \gamma\gamma$ channel at the LHC
  L. Cieri, F. Coradeschi, D. de Florian and N. Fidanza, Phys. Rev. D **96** (2017) no.5, 054003, arXiv:1706.07331

- Single top-quark production with SHERPA
  E. Bothmann, F. Krauss and M. Schönherr, Eur. Phys. J. C **78** (2018) no.3, 220, arXiv:1711.02568

- NLO QCD+EW corrections to diphoton production in association with a vector boson
  N. Greiner and M. Schönherr, JHEP **1801** (2018) 079, arXiv:1710.11514

- Electroweak corrections to diphoton plus jets
  M. Chiesa, N. Greiner, M. Schönherr and F. Tramontano, JHEP **1710** (2017) 181, arXiv:1706.09022

- Diphoton production in association with two bottom jets
  D. Fäh and N. Greiner, Eur. Phys. J. C **77** (2017) no.11, 750, arXiv:1706.08309

- To d, or not to d: recent developments and comparisons of regularization schemes
  C. Gnendiger *et al.*, Eur. Phys. J. C **77** (2017) no.7, 471, arXiv:1705.01827

- Fully differential NLO predictions for the radiative decay of muons and taus
  G. M. Pruna, A. Signer and Y. Ulrich, Phys. Lett. B **772** (2017) 452, arXiv:1705.03782

- Correlating lepton flavor universality violation in B decays with $\mu \to e\gamma$ using leptoquarks
  A. Crivellin, D. Müller, A. Signer and Y. Ulrich, Phys. Rev. D **97** (2018) no.1, 015019, arXiv:1706.08511

- High-p_T dilepton tails and flavor physics
  A. Greljo and D. Marzocca, Eur. Phys. J. C **77** (2017) no.8, 548, arXiv:1704.09015

- Probing Lepton Flavour Universality with $K \to \pi\nu\bar{\nu}$ decays
  M. Bordone, D. Buttazzo, G. Isidori and J. Monnard, Eur. Phys. J. C **77** (2017) no.9, 618, arXiv:1705.10729

- B-physics anomalies: a guide to combined explanations
  D. Buttazzo, A. Greljo, G. Isidori and D. Marzocca, JHEP **1711** (2017) 044, arXiv:1706.07808

- Gauge leptoquark as the origin of B-physics anomalies
  L. Di Luzio, A. Greljo and M. Nardecchia, Phys. Rev. D **96** (2017) no.11, 115011, arXiv:1708.08450

- Electroweak Higgs production with HiggsPO at NLO QCD
  A. Greljo, G. Isidori, J. M. Lindert, D. Marzocca and H. Zhang, Eur. Phys. J. C **77** (2017) no.12, 838, arXiv:1710.04143

- A three-site gauge model for flavor hierarchies and flavor anomalies
  M. Bordone, C. Cornella, J. Fuentes-Martin and G. Isidori, Phys. Lett. B **779** (2018) 317, arXiv:1712.01368

Articles in press

- Fully differential NNLO computations with MATRIX
  M. Grazzini, S. Kallweit and M. Wiesemann, arXiv:1711.06631

- Diphoton production at the LHC: a QCD study up to NNLO
  S. Catani, L. Cieri, D. de Florian, G. Ferrera and M. Grazzini, arXiv:1802.02095

- Differential single jet inclusive production at Next-to-Next-to-Leading Order in QCD
  J. Currie, A. Gehrmann-De Ridder, T. Gehrmann, E. W. N. Glover, A. Huss and J. Pires, arXiv:1705.08205

- NLO QCD corrections to jet production in deep inelastic scattering
  J. Currie, T. Gehrmann, A. Huss and J. Niehues, arXiv:1703.05977

- γ_5 in the four-dimensional helicity scheme
  C. Gnendiger and A. Signer, Phys. Rev. D **97** (2018) no.9, 096006, arXiv:1710.09231

- PSI/UZH Workshop: Impact of $B \to \mu^+\mu^-$ on New Physics Searches
  A. Crivellin *et al.*, arXiv:1803.10097

Oral Presentations

- M. Bordone: On the QED effects on R_K and R_K^*
  Instant Workshop on B meson anomalies, CERN, 18.05.2017.

- M. Bordone: Lepton Favour Universality Violation in $\Lambda_b \to \Lambda_c^* \tau \bar{\nu}_\tau$ decay
  2nd LHCb open semitauonic workshop, Orsay, 13.05.2017.

- M. Bordone: A three-site gauge model for flavor hierarchies and flavor anomalies
  Epiphany Conference, Cracow, 10.01.2018.

- F. Buccioni: OpenLoops2. A new method to generate and reduce one-loop amplitudes
  LoopFest XVI, Argonne National Laboratory, 1.6.2017.

- F. Buccioni: On-the-fly reduction of open loops
  Milan Christmas Meeting 2017, Universita degli studi di Milano, 21.12.2017.

- D. Buttazzo: On the breaking of Lepton Flavour Universality in B meson decays
  Seminar at Scuola Normale Superiore, Pisa, 16.06.2017.

- X. Chen: High Precision Phenomenology for Higgs Boson at LHC
  Seminar at ZheJiang University, HangZhou, China, 25.5.2017.

- X. Chen: High Precision Phenomenology for Higgs Boson at LHC
  Seminar at NanJing University, NanJing, China, 14.6.2017.

- X. Chen: Higgs p_T distributions at LHC
  Sinergia Meeting 2017, Lausanne, Switzerland, 08.12.2017.

- X. Chen: Higgs p_T distribution at NNLO + N3LL
  The XVth annual workshop on Soft-Collinear Effective Theory (SCET workshop 2018) ,
  Amsterdam, Netherlands, 20.3.2018.

- J. Fuentes-Martin: A model for B anomalies and flavor hierarchies
  II CAFPE Christmas workshop, Granada, Spain, 20.12.2017.

- J. Fuentes-Martin: UV-complete model for B anomalies and SM flavor hierarchies
  53rd Rencontres de Moriond EW18, La Thuile, 11.03.2018.

- L. Cieri: News on NNLO photon production
  ATLAS Standard Model Workshop 2017, Thessaloniki, 19.09.2017.

- T. Gehrmann: Fixed-order predictions for precision observables
  LHC Run II Gordon research conference, Hong Kong, 25.07.2017.

- T. Gehrmann: Jet cross sections and transverse momentum distributions with NNLOJET
  RADCOR 2017, St. Gilgen, 29.09.2017.

- M. Grazzini: NNLO calculations with MATRIX
  Loopfest 2017, Argonne, USA, 01.06.2017.

- M. Grazzini: Theory improvements for Run 2 and beyond
  Higgs Hunting, Paris, 26.07.2017.

- M. Grazzini: Azimuthal asymmetries in QCD hard scattering: infrared safe but divergent
  Old and New Strong Interactions from LHC to Future Colliders, Trento ECT meeting, 12.09.2017.

- M. Grazzini: Azimuthal asymmetries in QCD hard scattering: infrared safe but divergent
  Higgstools final meeting, Durham, 13.09.2017.

- M. Grazzini: Azimuthal asymmetries in hard-scattering processes
  Seminar, Wurzburg, 25.01.2018.

- A. Greljo : Collider constraints on NP models aimed to address B-anomalies
  Standard Model at the LHC, Amsterdam, 04.05.2017.

- A. Greljo: LFU and the interplay of low- and high-energy physics
  Invisibles17, Zurich, 12.06.2017.

- A. Greljo: Collider constraints on NP models aimed to address B-anomalies
  EPS-HEP, Venice, 06.07.2017.

- A. Ilnicka : Chapter 2: Pseudoobservables for LHC
  Third Annual Meeting and Young Editors School 2017, Turin, 17.05.2017.

- A. Ilnicka : Modeling BSM effects on Higgs transverse-momenta in EFT
  HEFT 2017, Lumley Castle, 22.05.2017.

- A. Ilnicka : Modeling BSM effects on Higgs transverse-momenta spectrum in an EFT approach
  QCD@LHC 2017, Debrecen, 29.08.2017.

- A. Ilnicka : Modeling BSM effects on Higgs transverse-momenta spectrum in an EFT approach
  Final HiggsTools Network Meeting, Durham, 13.09.2017.

- G. Isidori : Pseudo-observables: developments and tools
  Standard Model at the LHC, Amsterdam, 4.05.2017.

- G. Isidori: On the breaking of Lepton Flavor Universality in B decays
  Planck 2017 Conference, Warsaw, 26.05.2017.

- G. Isidori : EFT for Flavor Physics and BSM
  Lectures at the Summer School on Methods for EFT and Lattice, Munich, 29-30.06.2017.

- G. Isidori : Model building on flavour anomalies and implications for high-p_T searches
  Keynote talk at the LHCb Implication Workshop 2018, CERN, 10.11.2018.

- T. Jezo : NLO matching for $t\bar{t}b\bar{b}$ production with massive b-quarks
  25th International Workshop on Deep Inelastic Scattering and Related Topics, University of Birmingham, 04.04.2017.

- T. Jezo : A Study of the Top Mass Determination Using New NLO+PS generators
  25th International Workshop on Deep Inelastic Scattering and Related Topics, University of Birmingham, 06.04.2017.
- T. Jezo : NLO+PS matching for coloured resonances
  Seminar as a part of Seminario Teorico INFN at UniversitÃă di Roma âĂIJLa SapienzaâĂİ, 29.05.2017.
- T. Jezo : A Powheg generator for $t\bar{t}b\bar{b}$ production in the 4F scheme
  Meeting of the ttH/tH HXSWG subgroup, CERN, 06.06.2017.
- T. Jezo : SM modelling, updates on the simulation tools: POWHEG
  4th CMS Single Top Workshop, KIT Karlsruhe, 09.06.2017.
- T. Jezo : NLO+PS with decaying resonances using POWHEG
  Physics Modelling Group Plenary in ATLAS week, CERN, 20.06.2017.
- T. Jezo : Resonance aware matching at NLOW
  Seminar at Automated, Resummed and Effective: Precision Computations for the LHC and Beyond, MIAPP Munich, 01.08.2017.
- T. Jezo : NLO matching for $t\bar{t}b\bar{b}$ production with massive b-quarks
  QCD@LHC University of Debrecen, 29.08.2017.
- T. Jezo : A Study of the Top Mass Determination Using New NLO+PS generators
  QCD@LHC University of Debrecen, 31.08.2017.
- T. Jezo : WbWb production with POWHEG BOX RES
  ATLAS Higgs & B-tagging Workshop, Simons Center for Geometry and Physics Stony Brook, 05.09.2017.

- T. Jezo : Top Quark Production: modeling and tuning in Powheg
  Top workshop, Bom Jesus, Braga, 19.09.2017.
- T. Jezo : NLO+PS $t\bar{t}b\bar{b}$ in Powheg+OpenLoops
  Common meeting on $t\bar{t}+b$-jet backgrounds to $t\bar{t}H(b\bar{b})$, CERN, 06.11.2017.
- T. Jezo : $W^+W^-b\bar{b}$ 4FS NLO+PS
  Top! Hammertime (a CMS top quark workshop), CERN, 15.11.2017.
- T. Jezo : Top precision at the LHC
  Seminar as a part of Seminar of Institute of Physics of the Czech Academy of Sciences, Charles University Prague, 14.12.2017.
- T. Jezo : New four-flavour POWHEG predictions for $t\bar{t}+b$-jet production at the LHC
  CMS physics fest, CERN, 20.02.2018.
- A. Karlberg : Central jet veto and parton showers in VBF
  LHCHXSWG Meeting, CERN, 15.06.2017.
- A. Karlberg : WG1 VBF report
  13th Workshop of the LHC Higgs Cross Section Working Group, CERN, 14.07.2017.
- A. Karlberg : proVFBH: An NNLO Monte Carlo generator for VBF Higgs production
  Higgs Hunting 2017, Paris, 26.07.2017.
- A. Karlberg: Parton Shower matching for VBS
  Monte Carlo description of VBS, Amsterdam, 16.11.2017.
- A. Karlberg: Vector Boson Fusion and Scattering
  Sinergia 2017, Lausanne, 08.12.2017.
- A. Karlberg: Theoretical comparison for VBF production of W^+W^+
  VBSCAN mid-term meeting, CERN, 07.02.2018.

- A. Karlberg: VBF Higgs Production at the HL/HE-LHC
  HL/HE-LHC WG1 Meeting, CERN, 01.03.2018.

- J.-N. Lang: Automation of NLO Calculations for BSM
  MITP Workshop, Mainz, Germany, 8.3.2018.

- J.-N. Lang: One-loop amplitudes in extended Higgs sectors with RECOLA2
  seminar, Freiburg, Germany, 5.12.2017.

- D. Marzocca: BSM/EFT interpretation of precision EW measurements at the LHC
  Standard Model at the LHC, Amsterdam, 04.05.2017.

- D. Marzocca: STXT-PO complementarity
  LHC Higgs XS working group 2, CERN, 08.05.2017.

- D. Marzocca: Higgs physics and Effective Field Theories
  LHCP 2017, Shanghai, 15.05.2017.

- J. Mazzitelli: Precise QCD predictions for Higgs boson pair production
  Seminar at Max Plank Institute, Munich, 12.03.2018.

- J. Mazzitelli: Precise QCD predictions for Higgs boson pair production
  Seminar at University of Milano-Bicocca, Milan, 15.03.2018.

- J. Mazzitelli: HH production at NNLO including Mt effects
  LHC Higgs Cross Section Working Group General Meeting, Geneva, 26.03.2018.

- S. Pozzorini : ttH theory activities
  14th Workshop of the LHC Higgs Cross Section Working Group, CERN, Geneva, 26.03.2018.

- S. Pozzorini: Theory precision for V+jet backgrounds to dark matter searches at the LHC
  Seminar at the Technical University Munich, Germany, 02.11.2017.

- S. Pozzorini : Off-shell WWbb production
  Seminar at the Workshop Heavy-flavour production at the LHC, IPPP Durham, UK, 06.09.2017.

- S. Pozzorini: ttH theory activities
  13th Workshop of the LHC Higgs Cross Section Working Group, CERN, Geneva, 14.07.2017.

- S. Pozzorini: tt+HF: theory status
  Meeting of the ttH/tH HXSWG subgroup, CERN, Geneva, 06.07.2017.

- S. Pozzorini: tt+HF and ttH(bb): status and ideas from theory
  CMS week, CERN, Geneva, 21.06.2017.

- S. Pozzorini: Diboson production at the LHC
  Large Hadron Collider Physics Conference (LCHP 2017), Shanghai, China, 19.5.2017.

- S. Pozzorini: Summary of electroweak sessions
  Standard Model at the LHC 2017, NIKHEF, Amsterdam, 02.05.2017.

- S. Pozzorini : State of the Art V+jet Backgrounds for DM@LHC
  Dark Matter at the LHC 2017, UC Irvine, USA, 03.04.2017.

- A. Primo: Two-loop master integrals for μe-scattering in QED
  Workshop: The evaluation of the leading hadronic contribution to the muon anomalous magnetic moment, Mainz, Germany, 20.02.2018.

- A. Primo: NNLO virtual corrections to μe-scattering in QED
  Particleface 2018, the working group meeting of the COST Action CA16201, Valencia, Spain, 27.02.2017.

- M. Schönherr: Sherpa for V+jets
  Illuminating standard candles at the LHC - V+jets, London, United Kingdom, 25.04.2017.

- M. Schönherr: Sherpa-2.2.3 – status and prospects
  ATLAS and CMS Monte-Carlo Workshop, CERN, 02.05.2017.

- M. Schönherr: NNLOPS and higher-order EW corrections
  ATLAS and CMS Monte-Carlo Workshop, CERN, 03.05.2017.

- M. Schönherr: Parton shower uncertainties
  Les Houches WorkshopPhysics at TeV Colliders Les Houches, France, 07.06.2017.

- M. Schönherr: Issues at NLO EW
  Les Houches WorkshopPhysics at TeV Colliders Les Houches, France, 09.06.2017.

- M. Schönherr: Higher orders and parton showers
  BOOST 2017, Buffalo, USA, 18.07.2017.

- M. Schönherr: Higher-order corrections in Monte-Carlo event generators
  Lectures at the CTEQ School, Pittsburgh, USA, 22. & 24.07.2017.

- M. Schönherr: Parton shower matching and merging
  TOOLS 2017, Corfu, Greece, 10.09.2017.

- A. Signer: Lepton-flavour violating processes
  BLV 2017, Cleveland USA, 15.05.2017.

- A. Signer: Charged lepton flavour violation with effective theories
  HEFT 2017, Durham U.K, 22.05.2017.

- A. Signer: Charged lepton flavour violation
  ACFI Workshop, UMass Amherst, USA, 19.07.2017.

- A. Signer: Muon decay at NNLO, plans and interim results
  Theory Kickoff Workshop Muon Electron Scattering, Padova, Italy, 04.10.2017.

- A. Signer: Lepton flavour violation in muon decays
  SHiP open colloquium, CERN, Switzerland, 09.11.2017.

- A. Signer: Muon decay at NNLO
  MITP Workshop, Mainz, Germany, 20.02.2018.

- S. Trifinopoulos: Revisiting flavour constraints on high-scale SUSY
  25th International Conference on Supersymmetry and the Unification of Fundamental Interactions (SUSY17), Mumbai, 14.12.2017.

- D. van Dyk: Systematic approach to non-local charm contributions in exclusive $b \to s\ell\ell$ decays
  Standard Model at the LHC, Amsterdam, 02.05.2017.

- M. Zoller: Four-loop QCD renormalization group functions with different fermion representations of the gauge group
  LoopFest XVI, Argonne National Laboratory, 2.6.2017.

- M. Zoller: A new method to generate and reduce one-loop amplitudes in OpenLoops 2
  RADCOR 2017, St. Gilgen, 26.09.2017.

- M. Zoller: A new method to generate and reduce one-loop amplitudes in OpenLoops 2
  Particle Theory Seminar, PSI Villigen, 4.10.2017.

17.1.2 Astrophysics and General Relativity

Short-authorlist Articles

- Solving post-Newtonian accurate Kepler equation
  Y. Boetzel, A. Susobhanan, A. Gopakumar, A. Klein, and Ph. Jetzer, Phys. Rev. D **96**, 044011 (2017). arXiv:1707.02088

- Prospects for Measuring Planetary Spin and Frame-Dragging in Spacecraft Timing Signals
  A. Schärer, R. Bondarescu, P. Saha, R. Angélil, R. Helled, and Ph. Jetzer, Front. Astron. Space Sci. **4**, 11 (2017). arXiv:1707.00319

- Messier 81's Planck view versus its halo mapping
  V. G. Gurzadyan, F. De Paolis, A. A. Nucita, A. L. Kashin, A. Amekhyan, S. Sargsyan, G. Yegorian, A. Qadir, G. Ingrosso, Ph. Jetzer, and D. Vetrugno, Astron. Astrophys. **609**, A131 (2018). arXiv:1710.04166

- Low-frequency gravitational wave detection via double optical clocks in space
  J. Su, Q. Wang, Q. Wang, and Ph. Jetzer, Class. Quantum Grav. **35**, 085010 (2018). arXiv:1711.07730

- Post-Newtonian parameters γ and β of scalar-tensor gravity for a homogeneous gravitating sphere
  M. Hohmann, and A. Schärer, Phys. Rev. D **96**, 104026 (2017). arXiv:1708.07851

- Probing the Spinning of the Massive Black Hole in the Galactic Center via Pulsar Timing: A Full Relativistic Treatment
  F. Zhang, and P. Saha, Astrophys. J. **849**, 33 (2017). arXiv:1709.08341

- Models of gravitational lens candidates from Space Warps CFHTLS
  R. Küng, P. Saha, I. Ferreras, E. Baeten, J. Coles, C. Cornen, C. Macmillan, P. Marshall, A. More, A. Verma, O. Lucy, and J. K. Wilcox, Mon. Notices Royal Astron. Soc. **474**, 3700 (2018). arXiv:1711.0729

Articles with the LISA Pathfinder Collaboration

- Charge-induced force-noise on free-falling test masses: Results from LISA Pathfinder
  M. Armano *et al.* (The LISA Pathfinder collaboration), Phys. Rev. Lett. **118**, 171101 (2017). arXiv:1702.04633

- Capacitive sensing of test mass motion with nanometer precision over millimeter-wide sensing gaps for space-borne gravitational reference sensors
  M. Armano *et al.* (The LISA Pathfinder collaboration), Phys. Rev. D **96**, 062004 (2017).

- Measuring the Galactic Cosmic Ray Flux with the LISA Pathfinder Radiation Monitor
  M. Armano *et al.* (The LISA Pathfinder collaboration), Astropart. Phys. **98**, 28 (2018). arXiv:1711.07427

- Beyond the Required LISA Free-Fall Performance: New LISA Pathfinder Results down to 20 μHz
  M. Armano *et al.* (The LISA Pathfinder collaboration), Phys. Rev. Lett. **120**, 061101 (2018).

- Characteristics and Energy Dependence of Recurrent Galactic Cosmic-Ray Flux Depressions and of a Forbush Decrease with LISA Pathfinder
  M. Armano *et al.* (The LISA Pathfinder collaboration), Astrophys. J. **854**, 113 (2018). arXiv:1802.09374

Articles with the LIGO Scientific Collaboration

- First search for gravitational waves from known pulsars with Advanced LIGO
  B. P. Abbott *et al.* (The LIGO Scientific Collaboration and the Virgo Collaboration), Astrophys. J. **839**, no.1, 12 (2017). arXiv:1701.07709

- Search for continuous gravitational waves from neutron stars in globular cluster NGC 6544
  , B. P. Abbott *et al.* (The LIGO Scientific Collaboration and the Virgo Collaboration), Phys. Rev. D **95**, 082005 (2017). arXiv:1607.02216

- Effects of waveform model systematics on the interpretation of GW150914
  B. P. Abbott *et al.* (The LIGO Scientific Collaboration and the Virgo Collaboration), Class. Quantum Grav. **34**, 104002 (2017). arXiv:1611.07531

- Search for Gravitational Waves Associated with Gamma-Ray Bursts During the First Advanced LIGO Observing Run and Implications for the Origin of GRB 150906B
  B. P. Abbott *et al.* (The LIGO Scientific Collaboration and the Virgo Collaboration), Astrophys. J. **841**, no.2, 89 (2017). arXiv:1611.07947

- Search for gravitational waves from Scorpius X-1 in the first Advanced LIGO observing run with a hidden Markov model
  B. P. Abbott *et al.* (The LIGO Scientific Collaboration and the Virgo Collaboration), Phys. Rev. D **95**, 122003 (2017). arXiv:1704.03719

- GW170104: Observation of a 50-Solar-Mass Binary Black Hole Coalescence at Redshift 0.2
  B. P. Abbott *et al.* (The LIGO Scientific Collaboration and the Virgo Collaboration), Phys. Rev. Lett. **118**, 221101 (2017). arXiv:1706.01812

- Search for intermediate mass black hole binaries in the first observing run of Advanced LIGO
  B. P. Abbott *et al.* (The LIGO Scientific Collaboration and the Virgo Collaboration), Phys. Rev. D **96**, 022001 (2017). arXiv:1704.04628

- Search for High-energy Neutrinos from Gravitational Wave Event GW151226 and Candidate LVT151012 with ANTARES and IceCube
  B. P. Abbott *et al.* (The LIGO Scientific Collaboration and the Virgo Collaboration, ANTARES Collaboration, IceCube Collaboration), Phys. Rev. D **96**, 022005 (2017). arXiv:1703.06298

- Upper Limits on Gravitational Waves from Scorpius X-1 from a Model-Based Cross-Correlation Search in Advanced LIGO Data
  B. P. Abbott *et al.* (The LIGO Scientific Collaboration and the Virgo Collaboration),Astrophys. J. **847**, 47 (2017). arXiv:1706.03119

- All-sky Search for Periodic Gravitational Waves in the O1 LIGO Data
  B. P. Abbott *et al.* (The LIGO Scientific Collaboration and the Virgo Collaboration), Phys. Rev. D **96**, 062002 (2017). arXiv:1707.02667

- Multi-Messenger Observations of a Binary Neutron Star Merger
  B. P. Abbott *et al.* (The LIGO Scientific Collaboration and the Virgo Collaboration, Fermi Gamma-Ray Burst Monitor, INTEGRAL, IceCube Collaboration, AstroSat Cadmium Zinc Telluride Imager Team, IPN Collaboration, The Insight-Hxmt Collaboration, ANTARES Collaboration, The Swift Collaboration, AGILE Team, The 1M2H Team, The Dark Energy Camera GW-EM Collaboration, the DES Collaboration, The DLT40 Collaboration, GRAWITA: GRAvitational Wave Inaf TeAm, The Fermi Large Area Telescope Collaboration, ATCA: Australia Telescope Compact Array, ASKAP: Australian SKA Pathfinder, Las Cumbres Observatory Group, OzGrav, DWF (Deeper, Wider, Faster Program), AST3, CAASTRO Collaborations, The VINROUGE Collaboration, MASTER Collaboration, J-GEM, GROWTH, JAGWAR, Caltech- NRAO, TTU-NRAO, NuSTAR Collaborations, Pan-STARRS, The MAXI Team, TZAC Consortium, KU Collaboration, Nordic Optical Telescope, ePESSTO, GROND, Texas Tech University, SALT Group, TOROS: Transient Robotic Observatory of the South Collaboration, The BOOTES Collaboration, MWA: Murchison Widefield Array, The CALET Collaboration, IKI-GW Follow-up Collaboration, H.E.S.S. Collaboration, LOFAR Collaboration, LWA: Long Wavelength Array, HAWC Collaboration, The Pierre Auger Collaboration, ALMA Collaboration, Euro VLBI Team, Pi of the Sky Collaboration, The Chandra Team at McGill University, DFN: Desert Fireball Network, ATLAS, High Time Resolution Universe Survey, RIMAS, RATIR, SKA South Africa/MeerKAT), Astrophys. J. Lett. **848**, L12 (2017). arXiv:1710.05833

- Gravitational Waves and Gamma-rays from a Binary Neutron Star Merger: GW170817 and GRB 170817A
  B. P. Abbott *et al.* (The LIGO Scientific Collaboration and the Virgo Collaboration, Fermi Gamma-Ray Burst Monitor, INTEGRAL), Astrophys. J. Lett. **848**, L13 (2017). arXiv:1710.05834

- GW170817: Implications for the Stochastic Gravitational-Wave Background from Compact Binary Coalescences
  B. P. Abbott *et al.* (The LIGO Scientific Collaboration and the Virgo Collaboration), Phys. Rev. Lett. **120**, 091101 (2017). arXiv:1710.05837

- GW170814: A Three-Detector Observation of Gravitational Waves from a Binary Black Hole Coalescence
  B. P. Abbott *et al.* (The LIGO Scientific Collaboration and the Virgo Collaboration), Phys. Rev. Lett. **119**, 141101 (2017). arXiv:1709.09660

- GW170817: Observation of Gravitational Waves from a Binary Neutron Star Inspiral
  B. P. Abbott *et al.* (The LIGO Scientific Collaboration and the Virgo Collaboration), Phys. Rev. Lett. **119**, 161101 (2017). arXiv:1710.05832

- A gravitational-wave standard siren measurement of the Hubble constant
  B. P. Abbott *et al.* (The LIGO Scientific Collaboration and the Virgo Collaboration, The 1M2H Collaboration, The Dark Energy Camera GW-EM Collaboration and the DES Collaboration, The DLT40 Collaboration, The Las Cumbres Observatory Collaboration, The VINROUGE Collaboration and The MASTER Collaboration), Nature **551**, 85-88 (2017). arXiv:1710.05835

- Search for High-energy Neutrinos from Binary Neutron Star Merger GW170817 with ANTARES, IceCube, and the Pierre Auger Observatory
  A. Albert *et al.* (ANTARES Collaboration, IceCube Collaboration, The Pierre Auger Collaboration, and LIGO Scientific Collaboration and Virgo Collaboration), Astrophys. J. Lett. **850**, L35 **2017** arXiv:1710.05839

- Estimating the Contribution of Dynamical Ejecta in the Kilonova Associated with GW170817
  B. P. Abbott *et al.* (The LIGO Scientific Collaboration and the Virgo Collaboration), Astrophys. J. Lett. **850**, L39 (2017). arXiv:1710.05836

- On the progenitor of binary neutron star merger GW170817
  B. P. Abbott *et al.* (The LIGO Scientific Collaboration and the Virgo Collaboration), Astrophys. J. Lett. **850**, L40 (2017). arXiv:1710.05838

- Erratum: "First Search for Gravitational Waves from Known Pulsars with Advanced LIGO" (2017, ApJ, 839, 12)
  B. P. Abbott *et al.* (The LIGO Scientific Collaboration and the Virgo Collaboration), Astrophys. J. **851**, 71 (2017).

- Search for Post-merger Gravitational Waves from the Remnant of the Binary Neutron Star Merger GW170817
  B. P. Abbott *et al.* (The LIGO Scientific Collaboration and the Virgo Collaboration), Astrophys. J. Lett. **851**, L16 (2017). arXiv:1710.09320

- GW170608: Observation of a 19 Solar-mass Binary Black Hole Coalescence
  B. P. Abbott *et al.* (The LIGO Scientific Collaboration and the Virgo Collaboration), Astrophys. J. Lett. **851**, L35 (2017). arXiv:1711.05578

- First low-frequency Einstein@Home all-sky search for continuous gravitational waves in Advanced LIGO data
  B. P. Abbott *et al.* (The LIGO Scientific Collaboration and the Virgo Collaboration), Phys. Rev. D **96**, 122004 (2017). arXiv:1707.02669

- First narrow-band search for continuous gravitational waves from known pulsars in advanced detector data
  B. P. Abbott *et al.* (The LIGO Scientific Collaboration and the Virgo Collaboration), Phys. Rev. D **96**, 122006 (2017). arXiv:1710.02327

- First Search for Nontensorial Gravitational Waves from Known Pulsars
  B. P. Abbott *et al.* (The LIGO Scientific Collaboration and the Virgo Collaboration), Phys. Rev. Lett. **120**, 031104 (2018). arXiv:1709.09203

- All-sky search for long-duration gravitational wave transients in the first Advanced LIGO observing run
  B. P. Abbott *et al.* (The LIGO Scientific Collaboration and the Virgo Collaboration), Class. Quantum Grav. **35**, 065009 (2018). arXiv:1711.06843

- Effects of data quality vetoes on a search for compact binary coalescences in Advanced LIGO's first observing run
  B. P. Abbott *et al.* (The LIGO Scientific Collaboration and the Virgo Collaboration), Class. Quantum Grav. **35**, 065010 (2018). arXiv:1710.02185

Conference proceedings and other articles

- General relativity tests with space clocks in highly elliptic orbits
  Ph. Jetzer, Proceedings of the V Italian-Pakistani meeting (Lecce, July 2016), Int. J. Mod. Phys. D **26**, 1741014 (2017).

- Gravitational wave polarization modes in f(R) theories
  H. Rizwana Kausar, L. Philippoz, and Ph. Jetzer, Proceedings of the MG14 Meeting on General Relativity (Rome, July 2015), World Scientific, p.1220-1226 (2017).

- Prospects for testing general relativity and alternative theories with clocks on satellites in Earth orbit
  A. Schärer, R. Bondarescu, Ph. Jetzer, P. Saha, R. Angélil, and A. Lundgren, Proceedings of the MG14 Meeting on General Relativity (Rome, July 2015), World Scientific, p.3471-3475 (2017).

- Detecting additional polarization modes with LISA
  L. Philippoz, and Ph. Jetzer, Proceedings of the 11th LISA Symposium, J. Phys. Conf. Ser. **840**, 012057 (2017).

- Detecting additional polarization modes with LISA
  L. Philippoz, and Ph. Jetzer, Proceedings of the 52nd Rencontres de Moriond, ARISF, 69-72 (2017).

- On solving post-Newtonian accurate Kepler Equation
  Y. Boetzel, Proceedings of the 52nd Rencontres de Moriond, ARISF, 69-72 (2017).

- Proceedings, 11th International LISA Symposium (Zurich, September 5-9, 2016)
  D. Giardini (ed.), and Ph. Jetzer (ed.), J. Phys. Conf. Ser. **840**, no.1 (2017).

- Gravitational waves: a new window to explore the Universe
  Ph. Jetzer, Swiss Physical Society Mitteilungen **53**, p.30-32 (2017).

Oral Presentations

- Gravitational waves: A new window to explore the universe
  Philippe Jetzer, Swiss Physical Society Meeting, Geneva, 22 August 2017.

- Gravitational waves: A new window to explore the universe
  Philippe Jetzer, Gurukula Kangri University, Haridwar (India), 30 October 2017.

- Tests of General Relativity with high performance clocks in space
  Philippe Jetzer, 29th International Texas Symposium on Relativistic Astrophysics, Cape Town, 6 December 2017.

- Gravitational waves: A new window to explore the universe
  Philippe Jetzer, Universidad Autónoma de Madrid, Madrid, 15 December 2017.

- Gravitational waves and Multi-Messenger Astronomy
  Philippe Jetzer, Swiss Academy of Sciences, Bern, 22 March 2018.

- Gravitational waves from eccentric binary black hole coalescence
  Maria Haney, Max Planck Institute for Gravitational Physics (Albert Einstein Institute), Hannover, 5 October 2017.

- Gravitational waves from eccentric binary black hole coalescence
  Maria Haney, GWverse: black holes, gravitational waves and fundamental physics, Valletta, 23 January 2017.

- Fourier domain gravitational waveforms for precessing eccentric binaries
  Yannick Boetzel, GWverse: black holes, gravitational waves and fundamental physics, Valletta, 23 January 2017.

- Fourier domain gravitational waveforms for precessing eccentric binaries
  Yannick Boetzel, Tata Institute of Fundamental Research, Mumbai, 6 March 2018.

Outreach activities

- Gravitationswellen: Ein neues Fenster zur Erforschung des Universums (von LISA Pathfinder zu LISA)
  Philippe Jetzer, Naturforschende Gesellschaft in Zürich, Zürich, 23 October 2017.

- Onde Gravitazionali
  Philippe Jetzer, Liceo di Bellinzona, Bellinzona,13 March 2018.

- 100 years after Einstein - The dawn of gravitational wave astronomy
  Maria Haney, nanoTalks Nobel Prize Special, Zürich, 26 October 2017.

- Nobel 2017 et ondes gravitationnelles
  Lionel Philippoz, Société Valaisanne de Physique, Sion, 25 November 2017.

17.1.3 GERDA

Articles

- Improved limit on neutrinoless double beta decay of ^{76}Ge from GERDA Phase II
  M.Agostini *et al.* (GERDA Collaboration), Phys. Rev. Lett. **120**, 132503.
- Background free search for neutrinoless double beta decay with GERDA Phase II
  M.Agostini *et al.* (GERDA Collaboration), Nature 544 (2017) 47, arXiv:1703.00570

Oral Presentations

- L. Baudis: A Background-Free Search for the Neutrinoless Double Beta Decay with GERDA
  13th Patras Workshop on Axions, WIMPs and WISPs, Thessaloniki, May 18, 2017.
- C. Ransom: Studies of a PMT with magnesium fluoride window for direct detection of liquid argon scintillation light
  Joint SPS and OePG meeting 2017, Geneva, 25 August 2017.
- R.Hiller: Background free search for neutrinoless double beta decay with the GERDA experiment
  Joint SPS and OePG meeting 2017, Geneva, 24 August 2017.
- C. Ransom: Direct observation of liquid argon scintillation light: Studies of a magnesium fluoride (MgF_2) PMT for neutrinoless double-beta decay experiments
  Invisibles17 workshop, Zurich, 31 May 2017.
- R. Mingazheva: Search for keV-scale dark matter candidates with the Gerda experiment
  Invisibles17 workshop, Zurich, 31 May 2017

17.1.4 XENON/DARWIN

Articles

- The Search for Dark Matter
  Laura Baudis, European Review, Volume 26, Issue 1 February 2018, pp. 70-81, arXiv:1801.08128
- A Dual-phase Xenon TPC for Scintillation and Ionisation Yield Measurements in Liquid Xenon
  Laura Baudis, Yanina Biondi, Chiara Capelli, Michelle Galloway, Shingo Kazama, Alexander Kish, Payam Pakarha, Francesco Piastra, Julien Wulf, Eur. Phys. J. C**78** (2018) no.5, 351, arXiv:1712.08607
- Search for Bosonic Super-WIMP Interactions with the XENON100 Experiment
  E. Aprile *et al.* (XENON Collaboration), Phys.Rev. D**96** (2017) no.12, 122002, arXiv:1709.02222
- The XENON1T dark matter experiment
  E. Aprile *et al.* (XENON Collaboration), Eur. Phys. J. C**77** (2017) no.12, 881, arXiv:1705.01828
- First Dark Matter Search Results from the XENON1T Experiment
  E. Aprile *et al.* (XENON Collaboration), Phys. Rev. Lett. **119** (2017) no. 18, 181301, arXiv:1705.06655
- Effective field theory search for high-energy nuclear recoils using the XENON100 dark matter detector
  E. Aprile *et al.* (XENON Collaboration), Phys. Rev. D**96** (2017) no.4, 042004, arXiv:1705.02614
- Material radioassay and selection for the XENON1T dark matter experiment
  E. Aprile *et al.* (XENON Collaboration), Eur. Phys. J. C**77** (2017) no.12, 890, arXiv:1705.01828
- Search for WIMP Inelastic Scattering off Xenon Nuclei with XENON100
  E. Aprile *et al.* (XENON Collaboration), Phys. Rev. D**96** (2017) no.2, 022008, arXiv:1705.05830

- Search for magnetic inelastic dark matter with XENON100
  E. Aprile *et al.* (XENON Collaboration), JCAP **1710** (2017) no.10, 039, arXiv:1704.05804

Oral Presentations

- L. Baudis: Illuminating the dark side: direct searches for cold dark matter in the Milky Way
  Elisabeth Spreadbury Lecture, UCL, London, March 14, 2018.
- L. Baudis: Illuminating the dark side: direct searches for cold dark matter in the Milky Way
  General Physics Colloquium, Chalmers Gothenburg Physics Centre, January 25, 2018.
- S.Kazama: First Dark Matter Search Results XENON1T
  CosPA 2017, Kyoto University, December 13, 2017.
- M. Galloway: Dark Matter Searches with Xenon TPCs and First Results from XENON1T
  Vistas on Detector Physics, Heidelberg University, Germany, 11 Dec 2017.
- L. Baudis: The state-of-the art in the direct search for dark matter
  The dark Universe 2017, Munich, October 10, 2017.
- L. Baudis: Status of the XENON experiment
  XLVIII LNGS Scientific Committee meeting, LNGS, October 2, 2017.
- L. Baudis: Status and future prospects of direct dark matter detection experiments
  Dark matter, neutrinos and their connections, Odense, August 29, 2017.
- S. Reichard: Supernova Neutrino Physics with XENON1T and Beyond
  NuEclipse, Knoxville, USA, 22 August 2017.
- L. Baudis: Illuminating the dark side: direct searches for cold dark matter in the Milky Way
  Discovery Physics Colloquium, Niels Bohr Institute, Copenhagen, July 27, 2017.
- M. Galloway: First Results from the XENON1T Dark Matter Experiment
  European Physical Society (EPS-HEP), Venice, Italy, 6 July 2017.
- L. Baudis: Illuminating the dark: searches for dark matter in the Milky Way
  Passion for Physics, SIF, Varenna, June 24, 2017.
- L. Baudis: Illuminating the dark side: direct searches for cold dark matter in the Milky Way
  Physics Colloquium, EPFL, Lausanne, May 22, 2017.
- L. Baudis: The Future of WIMP Searches
  The future of WIMP Dark Matter, Chicheley Hall, Royal Society, May 2, 2017.
- L. Baudis: Dark matter detection with XENON and DARWIN
  Physics Seminar, Oxford University, Oxford, April 25, 2017.
- L. Baudis: Illuminating the dark side: searches for dark matter in the Milky Way
  Conference-Debat, Academie des Sciences, Paris, April 18, 2017.
- L. Baudis: Licht ins Dunkel: Die direkte Suche nach kalter dunkler Materie in der Milchstrasse
  Berliner Physikalisches Kolloquium, Berlin, April 6, 2017.

17.1.5 SHiP

Oral presentations

- Christopher Betancourt: A timing detector for the SHiP experiment (Poster)
  11th International Hiroshima Symposium on the Development and Application of Semiconductor Tracking Detectors (HSTD11) / 2nd Workshop on SOI Pixel Detectors (SOIPIX2017) (2017), Okinawa, Japan, December 10, 2017.

- Elena Graverini: Search for hidden Particles
  7 March, Seminar at Birmingham University, Birmingham, UK, March 7, 2018.

17.1.6 H1

The 2015 H1 Collaboration has 141 members including K. Müller, P. Robmann, U. Straumann and P. Truöl.
Articles

- Measurement of D^* production in diffractive deep inelastic scattering at HERA
  H1 Collaboration, V. Andreev *et al.*, Eur. Phys. J. C **77** (2017) no.5, 340, arXiv:1703.09476.

- Determination of the strong coupling constant $\alpha_s(m_Z)$ in next-to-next-to-leading order QCD using H1 jet cross section measurements
  H1 Collaboration, V. Andreev *et al.*, Eur. Phys. J. C **77** (2017) no.11, 791, arXiv:1709.07251.

17.1.7 CMS

Articles

- Test beam demonstration of silicon microstrip modules with transverse momentum discrimination for the future CMS tracking detector
  W. Adam *et al.* [CMS Tracker Collaboration], JINST **13** (2018) no.03, P03003.

- Jet properties in PbPb and pp collisions at $\sqrt{s_{\mathrm{NN}}} = 5.02$ TeV
  A. M. Sirunyan *et al.* [CMS Collaboration], JHEP **1805** (2018) 006 arXiv:1803.00042.

- Search for a heavy resonance decaying to a pair of vector bosons in the lepton plus merged jet final state at $\sqrt{s} = 13$ TeV
  A. M. Sirunyan *et al.* [CMS Collaboration], JHEP **1805** (2018) 088 arXiv:1802.09407.

- Search for narrow resonances in the b-tagged dijet mass spectrum in proton-proton collisions at $\sqrt{s} = 8$ TeV
  A. M. Sirunyan *et al.* [CMS Collaboration], Phys. Rev. Lett. **120** (2018) no.20, 201801 arXiv:1802.06149.

- Measurement of the Λ_b polarization and angular parameters in $\Lambda_b \to J/\psi\,\Lambda$ decays from pp collisions at $\sqrt{s} = 7$ and 8 TeV
  A. M. Sirunyan *et al.* [CMS Collaboration], Phys. Rev. D **97** (2018) no.7, 072010 arXiv:1802.04867.

- Search for natural and split supersymmetry in proton-proton collisions at $\sqrt{s} = 13$ TeV in final states with jets and missing transverse momentum
  A. M. Sirunyan *et al.* [CMS Collaboration], JHEP **1805** (2018) 025 arXiv:1802.02110.

- Search for lepton-flavor violating decays of heavy resonances and quantum black holes to eμ final states in proton-proton collisions at $\sqrt{s} = 13$ TeV
  A. M. Sirunyan *et al.* [CMS Collaboration], JHEP **1804** (2018) 073 arXiv:1802.01122.

- Comparing transverse momentum balance of b jet pairs in pp and PbPb collisions at $\sqrt{s_{\mathrm{NN}}} = 5.02$ TeV
  A. M. Sirunyan *et al.* [CMS Collaboration], JHEP **1803** (2018) 181 arXiv:1802.00707.

- Combined search for electroweak production of charginos and neutralinos in proton-proton collisions at $\sqrt{s} = 13$ TeV
  A. M. Sirunyan *et al.* [CMS Collaboration], JHEP **1803** (2018) 160 arXiv:1801.03957.

- Radioactive source calibration test of the CMS Hadron Endcap Calorimeter test wedge with Phase I upgrade electronics
  B. .Bilki *et al.* [CMS HCAL Collaboration], JINST **12** (2017) no.12, P12034.

- Identification of heavy-flavour jets with the CMS detector in pp collisions at 13 TeV
  A. M. Sirunyan *et al.* [CMS Collaboration], JINST **13** (2018) no.05, P05011 arXiv:1712.07158.

- Search for the X(5568) state decaying into $\mathrm{B}_\mathrm{s}^0\pi^\pm$ in proton-proton collisions at $\sqrt{s} = 8$ TeV
  A. M. Sirunyan *et al.* [CMS Collaboration], Phys. Rev. Lett. **120** (2018) no.20, 202005 arXiv:1712.06144.

- Measurement of the associated production of a single top quark and a Z boson in pp collisions at $\sqrt{s} =$ TeV
A. M. Sirunyan *et al.* [CMS Collaboration], Phys. Lett. B **779** (2018) 358 arXiv:1712.02825.

- Constraints on the double-parton scattering cross section from same-sign W boson pair production in proton-proton collisions at $\sqrt{s} = 8$ TeV
A. M. Sirunyan *et al.* [CMS Collaboration], JHEP **1802** (2018) 032 arXiv:1712.02280.

- Search for pair production of excited top quarks in the lepton + jets final state
A. M. Sirunyan *et al.* [CMS Collaboration], Phys. Lett. B **778** (2018) 349 arXiv:1711.10949.

- Search for new long-lived particles at $\sqrt{s} = 13$ TeV
A. M. Sirunyan *et al.* [CMS Collaboration], Phys. Lett. B **780** (2018) 432 arXiv:1711.09120.

- Search for gauge-mediated supersymmetry in events with at least one photon and missing transverse momentum in pp collisions at $\sqrt{s} = 13$ TeV
A. M. Sirunyan *et al.* [CMS Collaboration], Phys. Lett. B **780** (2018) 118 arXiv:1711.08008.

- Search for excited quarks of light and heavy flavor in $\gamma+$ jet final states in proton-proton collisions at $\sqrt{s} = 13$TeV
A. M. Sirunyan *et al.* [CMS Collaboration], Phys. Lett. B **781** (2018) 390 arXiv:1711.04652.

- Search for ZZ resonances in the $2\ell 2\nu$ final state in proton-proton collisions at 13 TeV
A. M. Sirunyan *et al.* [CMS Collaboration], JHEP **1803** (2018) 003 arXiv:1711.04370.

- Measurement of the inclusive $\mathrm{t\bar{t}}$ cross section in pp collisions at $\sqrt{s} = 5.02$ TeV using final states with at least one charged lepton
A. M. Sirunyan *et al.* [CMS Collaboration], JHEP **1803** (2018) 115 arXiv:1711.03143.

- Measurement of associated Z + charm production in proton-proton collisions at $\sqrt{s} = 8$ TeV
A. M. Sirunyan *et al.* [CMS Collaboration], Eur. Phys. J. C **78** (2018) no.4, 287 arXiv:1711.02143.

- Search for top squarks and dark matter particles in opposite-charge dilepton final states at $\sqrt{s} = 13$ TeV
Phys. Rev. D **97** (2018) no.3, 032009 A. M. Sirunyan *et al.* [CMS Collaboration], arXiv:1711.00752.

- Search for new physics in events with a leptonically decaying Z boson and a large transverse momentum imbalance in proton-proton collisions at $\sqrt{s} = 13$ TeV
A. M. Sirunyan *et al.* [CMS Collaboration], Eur. Phys. J. C **78** (2018) no.4, 291 arXiv:1711.00431.

- Search for supersymmetry in proton-proton collisions at 13 TeV using identified top quarks
A. M. Sirunyan *et al.* [CMS Collaboration], Phys. Rev. D **97** (2018) no.1, 012007 arXiv:1710.11188.

- Measurement of quarkonium production cross sections in pp collisions at $\sqrt{s} = 13$ TeV
A. M. Sirunyan *et al.* [CMS Collaboration], Phys. Lett. B **780** (2018) 251 arXiv:1710.11002.

- Search for standard model production of four top quarks with same-sign and multilepton final states in proton-proton collisions at $\sqrt{s} = 13$ TeV
A. M. Sirunyan *et al.* [CMS Collaboration], Eur. Phys. J. C **78** (2018) no.2, 140 arXiv:1710.10614.

- Pseudorapidity distributions of charged hadrons in proton-lead collisions at $\sqrt{s_{\mathrm{NN}}} = 5.02$ and 8.16 TeV
A. M. Sirunyan *et al.* [CMS Collaboration], JHEP **1801** (2018) 045 arXiv:1710.09355.

- Search for supersymmetry in events with at least three electrons or muons, jets, and missing transverse momentum in proton-proton collisions at $\sqrt{s} = 13$ TeV
A. M. Sirunyan *et al.* [CMS Collaboration], JHEP **1802** (2018) 067 arXiv:1710.09154.

- Measurement of differential cross sections in the kinematic angular variable ϕ^* for inclusive Z boson production in pp collisions at $\sqrt{s} = 8$ TeV
A. M. Sirunyan *et al.* [CMS Collaboration], JHEP **1803** (2018) 172 arXiv:1710.07955.

- Search for a massive resonance decaying to a pair of Higgs bosons in the four b quark final state in proton-proton collisions at $\sqrt{s} = 13$ TeV
A. M. Sirunyan *et al.* [CMS Collaboration], Phys. Lett. B **781** (2018) 244 arXiv:1710.04960.

- Measurement of angular parameters from the decay $B^0 \to K^{*0}\mu^+\mu^-$ in proton-proton collisions at $\sqrt{s} = 8$ TeV
A. M. Sirunyan *et al.* [CMS Collaboration], Phys. Lett. B **781** (2018) 517 arXiv:1710.02846.

- Study of dijet events with a large rapidity gap between the two leading jets in pp collisions at $\sqrt{s} = 7$ TeV
A. M. Sirunyan *et al.* [CMS Collaboration], Eur. Phys. J. C **78** (2018) no.3, 242 arXiv:1710.02586.

- Search for pair production of vector-like quarks in the bW$\bar{\text{b}}$W channel from proton-proton collisions at $\sqrt{s} = 13$ TeV
A. M. Sirunyan *et al.* [CMS Collaboration], Phys. Lett. B **779** (2018) 82 arXiv:1710.01539.

- Search for low mass vector resonances decaying into quark-antiquark pairs in proton-proton collisions at $\sqrt{s} = 13$ TeV
A. M. Sirunyan *et al.* [CMS Collaboration], JHEP **1801** (2018) 097 arXiv:1710.00159.

- Search for supersymmetry in events with one lepton and multiple jets exploiting the angular correlation between the lepton and the missing transverse momentum in proton-proton collisions at $\sqrt{s} = 13$ TeV
A. M. Sirunyan *et al.* [CMS Collaboration], Phys. Lett. B **780** (2018) 384 arXiv:1709.09814.

- Observation of Correlated Azimuthal Anisotropy Fourier Harmonics in pp and $p + Pb$ Collisions at the LHC
A. M. Sirunyan *et al.* [CMS Collaboration], Phys. Rev. Lett. **120** (2018) no.9, 092301 arXiv:1709.09189 .

- Search for new phenomena in final states with two opposite-charge, same-flavor leptons, jets, and missing transverse momentum in pp collisions at $\sqrt{s} = 13$ TeV
A. M. Sirunyan *et al.* [CMS Collaboration], JHEP **1803** (2018) 076 arXiv:1709.08908.

- Brightness and uniformity measurements of plastic scintillator tiles at the CERN H2 test beam
S. Chatrchyan *et al.* [CMS HCAL Collaboration], JINST **13** (2018) no.01, P01002 arXiv:1709.08672.

- Measurements of the $\text{pp} \to \text{ZZ}$ production cross section and the $\text{Z} \to 4\ell$ branching fraction, and constraints on anomalous triple gauge couplings at $\sqrt{s} = 13$ TeV
A. M. Sirunyan *et al.* [CMS Collaboration], Eur. Phys. J. C **78** (2018) 165 arXiv:1709.08601.

- Evidence for the Higgs boson decay to a bottom quark-antiquark pair
A. M. Sirunyan *et al.* [CMS Collaboration], Phys. Lett. B **780** (2018) 501 arXiv:1709.07497.

- Observation of top quark production in proton-nucleus collisions
A. M. Sirunyan *et al.* [CMS Collaboration], Phys. Rev. Lett. **119** (2017) no.24, 242001 arXiv:1709.07411.

- Observation of electroweak production of same-sign W boson pairs in the two jet and two same-sign lepton final state in proton-proton collisions at $\sqrt{s} = 13$ TeV
A. M. Sirunyan *et al.* [CMS Collaboration], Phys. Rev. Lett. **120** (2018) no.8, 081801 arXiv:1709.05822.

- Inclusive search for a highly boosted Higgs boson decaying to a bottom quark-antiquark pair
A. M. Sirunyan *et al.* [CMS Collaboration], Phys. Rev. Lett. **120** (2018) no.7, 071802 arXiv:1709.05543.

- Search for electroweak production of charginos and neutralinos in multilepton final states in proton-proton collisions at $\sqrt{s} = 13$ TeV
A. M. Sirunyan *et al.* [CMS Collaboration], JHEP **1803** (2018) 166 arXiv:1709.05406.

- Combination of inclusive and differential $\text{t}\bar{\text{t}}$ charge asymmetry measurements using ATLAS and CMS data at $\sqrt{s} = 7$ and 8 TeV
M. Aaboud *et al.* [ATLAS and CMS Collaborations], JHEP **1804** (2018) 033 arXiv:1709.05327.

- Search for Higgsino pair production in pp collisions at $\sqrt{s} = 13$ TeV in final states with large missing transverse momentum and two Higgs bosons decaying via $H \to b\bar{b}$
A. M. Sirunyan *et al.* [CMS Collaboration], Phys. Rev. D **97** (2018) no.3, 032007 arXiv:1709.04896.

- Search for supersymmetry with Higgs boson to diphoton decays using the razor variables at $\sqrt{s} = 13$ TeV
A. M. Sirunyan *et al.* [CMS Collaboration], Phys. Lett. B **779** (2018) 166 arXiv:1709.00384.

- Measurement of the Splitting Function in pp and Pb-Pb Collisions at $\sqrt{s_{\text{NN}}} = 5.02$ TeV
A. M. Sirunyan *et al.* [CMS Collaboration], Phys. Rev. Lett. **120** (2018) no.14, 142302 arXiv:1708.09429.

- Search for heavy resonances decaying to a top quark and a bottom quark in the lepton+jets final state in proton-proton collisions at 13 TeV
  A. M. Sirunyan *et al.* [CMS Collaboration], Phys. Lett. B **777** (2018) 39 arXiv:1708.08539.

- Search for Evidence of the Type-III Seesaw Mechanism in Multilepton Final States in Proton-Proton Collisions at $\sqrt{s} = 13$ TeV
  A. M. Sirunyan *et al.* [CMS Collaboration], Phys. Rev. Lett. **119** (2017) no.22, 221802 arXiv:1708.07962.

- Measurement of normalized differential $\mathrm{t\bar{t}}$ cross sections in the dilepton channel from pp collisions at $\sqrt{s} = 13$ TeV
  A. M. Sirunyan *et al.* [CMS Collaboration], JHEP **1804** (2018) 060 arXiv:1708.07638.

- Principal-component analysis of two-particle azimuthal correlations in PbPb and pPb collisions at CMS
  A. M. Sirunyan *et al.* [CMS Collaboration], Phys. Rev. C **96** (2017) no.6, 064902 arXiv:1708.07113.

- Search for massive resonances decaying into WW, WZ, ZZ, qW, and qZ with dijet final states at $\sqrt{s} = 13$ TeV
  A. M. Sirunyan *et al.* [CMS Collaboration], Phys. Rev. D **97** (2018) no.7, 072006 arXiv:1708.05379.

- Search for resonant and nonresonant Higgs boson pair production in the $\mathrm{b\bar{b}}\ell^{\circ}\ell^{\circ}$ final state in proton-proton collisions at $\sqrt{s} = 13$ TeV
  A. M. Sirunyan *et al.* [CMS Collaboration], JHEP **1801** (2018) 054 arXiv:1708.04188.

- Measurement of prompt D^0 meson azimuthal anisotropy in Pb-Pb collisions at $\sqrt{s_{NN}} = 5.02$ TeV
  A. M. Sirunyan *et al.* [CMS Collaboration], Phys. Rev. Lett. **120** (2018) no.20, 202301 arXiv:1708.03497.

- Measurement of vector boson scattering and constraints on anomalous quartic couplings from events with four leptons and two jets in proton-proton collisions at $\sqrt{s} = 13$ TeV
  A. M. Sirunyan *et al.* [CMS Collaboration], Phys. Lett. B **774** (2017) 682 arXiv:1708.02812.

- Search for vectorlike light-flavor quark partners in proton-proton collisions at $\sqrt{s}$ =8 TeV
  A. M. Sirunyan *et al.* [CMS Collaboration], Phys. Rev. D **97** (2018) 072008 arXiv:1708.02510.

- Constraints on the chiral magnetic effect using charge-dependent azimuthal correlations in pPb and PbPb collisions at the CERN Large Hadron Collider
  A. M. Sirunyan *et al.* [CMS Collaboration], Phys. Rev. C **97** (2018) no.4, 044912 arXiv:1708.01602.

- Search for single production of a vector-like T quark decaying to a Z boson and a top quark in proton-proton collisions at $\sqrt{s} = 13$ TeV
  A. M. Sirunyan *et al.* [CMS Collaboration], Phys. Lett. B **781** (2018) 574 arXiv:1708.01062.

- Observation of the Higgs boson decay to a pair of τ leptons with the CMS detector
  A. M. Sirunyan *et al.* [CMS Collaboration], Phys. Lett. B **779** (2018) 283 arXiv:1708.00373.

- Search for a light pseudoscalar Higgs boson produced in association with bottom quarks in pp collisions at $\sqrt{s} = 8$ TeV
  A. M. Sirunyan *et al.* [CMS Collaboration], JHEP **1711** (2017) 010 arXiv:1707.07283.

- Search for the pair production of third-generation squarks with two-body decays to a bottom or charm quark and a neutralino in proton-proton collisions at $\sqrt{s} = 13$ TeV
  A. M. Sirunyan *et al.* [CMS Collaboration], Phys. Lett. B **778** (2018) 263 arXiv:1707.07274.

- Search for supersymmetry in events with at least one photon, missing transverse momentum, and large transverse event activity in proton-proton collisions at $\sqrt{s} = 13$ TeV
  A. M. Sirunyan *et al.* [CMS Collaboration], JHEP **1712** (2017) 142 arXiv:1707.06193.

- Measurement of the differential cross sections for the associated production of a W boson and jets in proton-proton collisions at $\sqrt{s} = 13$ TeV
  A. M. Sirunyan *et al.* [CMS Collaboration], Phys. Rev. D **96** (2017) no.7, 072005 arXiv:1707.05979.

- Search for natural supersymmetry in events with top quark pairs and photons in pp collisions at $\sqrt{s} = 8$ TeV
  A. M. Sirunyan *et al.* [CMS Collaboration], JHEP **1803** (2018) 167 arXiv:1707.03325.

- Search for direct production of supersymmetric partners of the top quark in the all-jets final state in proton-proton collisions at $\sqrt{s} = 13$ TeV
A. M. Sirunyan *et al.* [CMS Collaboration], JHEP **1710** (2017) 005 arXiv:1707.03316.

- Search for Higgs boson pair production in events with two bottom quarks and two tau leptons in proton-proton collisions at $\sqrt{s}$ =13TeV
A. M. Sirunyan *et al.* [CMS Collaboration], Phys. Lett. B **778** (2018) 101 arXiv:1707.02909.

- Search for heavy resonances that decay into a vector boson and a Higgs boson in hadronic final states at $\sqrt{s} = 13$ TeV
A. M. Sirunyan *et al.* [CMS Collaboration], Eur. Phys. J. C **77** (2017) no.9, 636 arXiv:1707.01303.

- Constraints on anomalous Higgs boson couplings using production and decay information in the four-lepton final state
A. M. Sirunyan *et al.* [CMS Collaboration], Phys. Lett. B **775** (2017) 1 arXiv:1707.00541.

- Search for Higgs boson pair production in the $bb\tau\tau$ final state in proton-proton collisions at $\sqrt{(s)} = 8$ TeV
A. M. Sirunyan *et al.* [CMS Collaboration], Phys. Rev. D **96** (2017) no.7, 072004 arXiv:1707.00350.

- Measurement of charged pion, kaon, and proton production in proton-proton collisions at $\sqrt{s} = 13$ TeV
A. M. Sirunyan *et al.* [CMS Collaboration], Phys. Rev. D **96** (2017) no.11, 112003 arXiv:1706.10194.

- Measurements of properties of the Higgs boson decaying into the four-lepton final state in pp collisions at $\sqrt{s} = 13$ TeV
A. M. Sirunyan *et al.* [CMS Collaboration], JHEP **1711** (2017) 047 arXiv:1706.09936.

- Search for electroweak production of charginos and neutralinos in WH events in proton-proton collisions at $\sqrt{s} = 13$ TeV
A. M. Sirunyan *et al.* [CMS Collaboration], JHEP **1711** (2017) 029 arXiv:1706.09933.

- P-Type Silicon Strip Sensors for the new CMS Tracker at HL-LHC
W. Adam *et al.* [CMS Collaboration], JINST **12** (2017) no.06, P06018.

- Search for a heavy composite Majorana neutrino in the final state with two leptons and two quarks at $\sqrt{s} = 13$ TeV
A. M. Sirunyan *et al.* [CMS Collaboration], Phys. Lett. B **775** (2017) 315 arXiv:1706.08578.

- Measurement of the semileptonic $\mathrm{t\bar{t}} + \gamma$ production cross section in pp collisions at $\sqrt{s} = 8$ TeV
A. M. Sirunyan *et al.* [CMS Collaboration], JHEP **1710** (2017) 006 arXiv:1706.08128.

- Suppression of Excited Υ States Relative to the Ground State in Pb-Pb Collisions at $\sqrt{s_{\mathrm{NN}}}$=5.02 TeV
A. M. Sirunyan *et al.* [CMS Collaboration], Phys. Rev. Lett. **120** (2018) no.14, 142301 arXiv:1706.05984.

- Measurements of jet charge with dijet events in pp collisions at $\sqrt{s} = 8$ TeV
A. M. Sirunyan *et al.* [CMS Collaboration], JHEP **1710** (2017) 131 arXiv:1706.05868.

- Particle-flow reconstruction and global event description with the CMS detector
A. M. Sirunyan *et al.* [CMS Collaboration], JINST **12** (2017) no.10, P10003 arXiv:1706.04965.

- Search for top squark pair production in pp collisions at $\sqrt{s} = 13$ TeV using single lepton events
A. M. Sirunyan *et al.* [CMS Collaboration], JHEP **1710** (2017) 019 arXiv:1706.04402.

- Searches for W′ bosons decaying to a top quark and a bottom quark in proton-proton collisions at 13 TeV
A. M. Sirunyan *et al.* [CMS Collaboration], JHEP **1708** (2017) 029 arXiv:1706.04260.

- Search for new physics in the monophoton final state in proton-proton collisions at $\sqrt{s} = 13$ TeV
A. M. Sirunyan *et al.* [CMS Collaboration], JHEP **1710** (2017) 073 arXiv:1706.03794.

- Search for pair production of vector-like T and B quarks in single-lepton final states using boosted jet substructure in proton-proton collisions at $\sqrt{s} = 13$ TeV
A. M. Sirunyan *et al.* [CMS Collaboration], JHEP **1711** (2017) 085 arXiv:1706.03408.

- Search for dark matter produced in association with heavy-flavor quark pairs in proton-proton collisions at $\sqrt{s} = 13$ TeV
A. M. Sirunyan *et al.* [CMS Collaboration], Eur. Phys. J. C **77** (2017) no.12, 845 arXiv:1706.02581.

- Search for top quark partners with charge 5/3 in proton-proton collisions at $\sqrt{s} = 13$ TeV
A. M. Sirunyan *et al.* [CMS Collaboration], JHEP **1708** (2017) 073 arXiv:1705.10967.

- Search for Low Mass Vector Resonances Decaying to Quark-Antiquark Pairs in Proton-Proton Collisions at $\sqrt{s} = 13$ TeV
A. M. Sirunyan *et al.* [CMS Collaboration], Phys. Rev. Lett. **119** (2017) no.11, 111802 arXiv:1705.10532.

- Measurements of $t\bar{t}$ cross sections in association with b jets and inclusive jets and their ratio using dilepton final states in pp collisions at $\sqrt{s} = 13$ TeV
A. M. Sirunyan *et al.* [CMS Collaboration], Phys. Lett. B **776** (2018) 355 arXiv:1705.10141.

- Combination of searches for heavy resonances decaying to WW, WZ, ZZ, WH, and ZH boson pairs in proton-proton collisions at $\sqrt{s} = 8$ and 13 TeV
A. M. Sirunyan *et al.* [CMS Collaboration], Phys. Lett. B **774** (2017) 533 arXiv:1705.09171.

- Measurement of the $B^{\pm}$ Meson Nuclear Modification Factor in Pb-Pb Collisions at $\sqrt{s_{NN}} = 5.02$ TeV
A. M. Sirunyan *et al.* [CMS Collaboration], Phys. Rev. Lett. **119** (2017) no.15, 152301 arXiv:1705.04727.

- Search for Supersymmetry in pp Collisions at $\sqrt{s} = 13$ TeV in the Single-Lepton Final State Using the Sum of Masses of Large-Radius Jets
A. M. Sirunyan *et al.* [CMS Collaboration], Phys. Rev. Lett. **119** (2017) no.15, 151802 arXiv:1705.04673.

- Search for new phenomena with the M_{T2} variable in the all-hadronic final state produced in proton-proton collisions at $\sqrt{s} = 13$ TeV
A. M. Sirunyan *et al.* [CMS Collaboration], Eur. Phys. J. C **77** (2017) no.10, 710 arXiv:1705.04650.

- Search for Charged Higgs Bosons Produced via Vector Boson Fusion and Decaying into a Pair of W and Z Bosons Using pp Collisions at $\sqrt{s} = 13$ TeV
A. M. Sirunyan *et al.* [CMS Collaboration], Phys. Rev. Lett. **119** (2017) no.14, 141802 arXiv:1705.02942.

- Measurement of the triple-differential dijet cross section in proton-proton collisions at $\sqrt{s} = 8$ TeV and constraints on parton distribution functions
A. M. Sirunyan *et al.* [CMS Collaboration], Eur. Phys. J. C **77** (2017) no.11, 746 arXiv:1705.02628.

- Search for black holes in high-multiplicity final states in proton-proton collisions at $\sqrt{s}$ =13 TeV
A. M. Sirunyan *et al.* [CMS Collaboration], Phys. Lett. B **774** (2017) 279 arXiv:1705.01403.

- Search for supersymmetry in multijet events with missing transverse momentum in proton-proton collisions at 13 TeV
A. M. Sirunyan *et al.* [CMS Collaboration], Phys. Rev. D **96** (2017) no.3, 032003 arXiv:1704.07781.

- Search for physics beyond the standard model in events with two leptons of same sign, missing transverse momentum, and jets in proton-proton collisions at $\sqrt{s} = 13$ TeV
A. M. Sirunyan *et al.* [CMS Collaboration], Eur. Phys. J. C **77** (2017) no.9, 578 arXiv:1704.07323.

- Measurement of the top quark mass in the dileptonic $t\bar{t}$ decay channel using the mass observables $M_{b\ell}$, M_{T2}, and $M_{b\ell\nu}$ in pp collisions at $\sqrt{s} = 8$ TeV
A. M. Sirunyan *et al.* [CMS Collaboration], Phys. Rev. D **96** (2017) no.3, 032002 arXiv:1704.06142.

- Search for $\mathrm{t\bar{t}}$ resonances in highly boosted lepton+jets and fully hadronic final states in proton-proton collisions at $\sqrt{s} = 13$ TeV
A. M. Sirunyan *et al.* [CMS Collaboration], JHEP **1707** (2017) 001 arXiv:1704.03366.

- Measurements of the pp $\to W\gamma\gamma$ and pp $\to Z\gamma\gamma$ cross sections and limits on anomalous quartic gauge couplings at $\sqrt{s} = 8$ TeV
A. M. Sirunyan *et al.* [CMS Collaboration], JHEP **1710** (2017) 072 arXiv:1704.00366.

- Search for new physics with dijet angular distributions in proton-proton collisions at $\sqrt{s} = 13$ TeV
A. M. Sirunyan *et al.* [CMS Collaboration], JHEP **1707** (2017) 013 arXiv:1703.09986.

- Search for a heavy resonance decaying to a top quark and a vector-like top quark at $\sqrt{s} = 13$ TeV
A. M. Sirunyan *et al.* [CMS Collaboration], JHEP **1709** (2017) 053 arXiv:1703.06352.

- Measurement of the jet mass in highly boosted $\mathrm{t\bar{t}}$ events from pp collisions at $\sqrt{s} = 8$ TeV
A. M. Sirunyan *et al.* [CMS Collaboration], Eur. Phys. J. C **77** (2017) no.7, 467 arXiv:1703.06330.

- Search for anomalous couplings in boosted WW/WZ $\to \ell\nu q\bar{q}$ production in proton-proton collisions at $\sqrt{s} = 8$ TeV
A. M. Sirunyan *et al.* [CMS Collaboration], Phys. Lett. B **772** (2017) 21 arXiv:1703.06095.

- Search for associated production of dark matter with a Higgs boson decaying to $b\bar{b}$ or $\gamma\gamma$ at $\sqrt{s} = 13$ TeV
A. M. Sirunyan *et al.* [CMS Collaboration], JHEP **1710** (2017) 180 arXiv:1703.05236.

- Search for third-generation scalar leptoquarks and heavy right-handed neutrinos in final states with two tau leptons and two jets in proton-proton collisions at $\sqrt{s} = 13$ TeV
A. M. Sirunyan *et al.* [CMS Collaboration], JHEP **1707** (2017) 121 arXiv:1703.03995.

- Measurement of the top quark mass using single top quark events in proton-proton collisions at $\sqrt{s} = 8$ TeV
A. M. Sirunyan *et al.* [CMS Collaboration], Eur. Phys. J. C **77** (2017) no.5, 354 arXiv:1703.02530.

- Search for dark matter produced with an energetic jet or a hadronically decaying W or Z boson at $\sqrt{s} = 13$ TeV
A. M. Sirunyan *et al.* [CMS Collaboration], JHEP **1707** (2017) 014 arXiv:1703.01651.

- Measurement of double-differential cross sections for top quark pair production in pp collisions at $\sqrt{s} = 8$ TeV and impact on parton distribution functions
A. M. Sirunyan *et al.* [CMS Collaboration], Eur. Phys. J. C **77** (2017) no.7, 459 arXiv:1703.01630.

- Search for standard model production of four top quarks in proton-proton collisions at $\sqrt{s} = 13$ TeV
A. M. Sirunyan *et al.* [CMS Collaboration], Phys. Lett. B **772** (2017) 336 arXiv:1702.06164.

- Results from CMS on Higgs boson physics
P. Azzurri [CMS Collaboration], J. Phys. Conf. Ser. **878** (2017) 012010.

- Measurement of the cross section for electroweak production of $Z\gamma$ in association with two jets and constraints on anomalous quartic gauge couplings in proton-proton collisions at $\sqrt{s} = 8$ TeV
V. Khachatryan *et al.* [CMS Collaboration], Phys. Lett. B **770** (2017) 380 arXiv:1702.03025.

- Measurement of prompt and nonprompt J/ψ production in pp and pPb collisions at $\sqrt{s_{NN}} = 5.02$ TeV
A. M. Sirunyan *et al.* [CMS Collaboration], Eur. Phys. J. C **77** (2017) no.4, 269 arXiv:1702.01462.

- Search for associated production of a Z boson with a single top quark and for tZ flavour-changing interactions in pp collisions at $\sqrt{s} = 8$ TeV
A. M. Sirunyan *et al.* [CMS Collaboration], JHEP **1707** (2017) 003 arXiv:1702.01404.

- Study of Jet Quenching with $Z+$jet Correlations in Pb-Pb and pp Collisions at $\sqrt{s_{NN}} = 5.02$ TeV
A. M. Sirunyan *et al.* [CMS Collaboration], Phys. Rev. Lett. **119** (2017) no.8, 082301 arXiv:1702.01060.

- Azimuthal anisotropy of charged particles with transverse momentum up to 100 GeV/ c in PbPb collisions at $\sqrt{s_{NN}}$=5.02 TeV
A. M. Sirunyan *et al.* [CMS Collaboration], Phys. Lett. B **776** (2018) 195 arXiv:1702.00630.

- Measurement of the inclusive energy spectrum in the very forward direction in proton-proton collisions at $\sqrt{s} = 13$ TeV
A. M. Sirunyan *et al.* [CMS Collaboration], JHEP **1708** (2017) 046 arXiv:1701.08695.

- Search for single production of vector-like quarks decaying into a b quark and a W boson in proton-proton collisions at $\sqrt{s} = 13$ TeV
A. M. Sirunyan *et al.* [CMS Collaboration], Phys. Lett. B **772** (2017) 634 arXiv:1701.08328.

- Search for single production of vector-like quarks decaying to a Z boson and a top or a bottom quark in proton-proton collisions at $\sqrt{s} = 13$ TeV
A. M. Sirunyan *et al.* [CMS Collaboration], JHEP **1705** (2017) 029 arXiv:1701.07409.

- Search for new phenomena with multiple charged leptons in proton-proton collisions at $\sqrt{s} = 13$ TeV
V. Khachatryan *et al.* [CMS Collaboration], Eur. Phys. J. C **77** (2017) no.9, 635 arXiv:1701.06940.

- Measurement of the $t\bar{t}$ production cross section using events with one lepton and at least one jet in pp collisions at $\sqrt{s}$ = 13 TeV
A. M. Sirunyan *et al.* [CMS Collaboration], JHEP **1709** (2017) 051 arXiv:1701.06228.

- Search for light bosons in decays of the 125 GeV Higgs boson in proton-proton collisions at $\sqrt{s} = 8$ TeV
  V. Khachatryan *et al.* [CMS Collaboration], JHEP **1710** (2017) 076 arXiv:1701.02032.

- Mechanical stability of the CMS strip tracker measured with a laser alignment system
  A. M. Sirunyan *et al.* [CMS Collaboration], JINST **12** (2017) no.04, P04023 arXiv:1701.02022.

- Search for supersymmetry in the all-hadronic final state using top quark tagging in pp collisions at $\sqrt{s} = 13$ TeV
  V. Khachatryan *et al.* [CMS Collaboration], Phys. Rev. D **96** (2017) no.1, 012004 arXiv:1701.01954.

- Search for leptophobic Z' bosons decaying into four-lepton final states in proton-proton collisions at $\sqrt{s}$ =8TeV
  V. Khachatryan *et al.* [CMS Collaboration], Phys. Lett. B **773** (2017) 563 arXiv:1701.01345.

Oral presentations

- Thea Aarrestad: W/Z/H tagging in CMS
  BOOST 2017, Buffalo, USA, 17 July 2017.

- Lea Caminada: Particle detection with CMS at the LHC
  PSI Lille Art Program, PSI, Villigen, Switzerland, 7 November 2017.

- Lea Caminada: Status of the CMS Experiment
  CERN LHCC Open Session, CERN, Geneva, Switzerland, 28 February 2018.

- Florencia Canelli: Exploring new physics with top quarks
  Seminar, DESY Zeuthen, Zeuthen, Germany, 28 June 2017.

- Florencia Canelli: Exploring new physics with top quarks
  Seminar, DESY Hamburg, Hamburg, Germany, 27 June 2017.

- Florencia Canelli: Top quark mass measurements from CMS
  LHCP 2017, Shangai, China, 15 May 2017.

- Florencia Canelli: High energy searches beyond the standard model
  Invisibles 2017, Zurich, Switzerland, 12 June 2017.

- Annapaola de Cosa: DM searches in CMS
  International Conference on new Frontiers in Physics 2017, Kolymbari, Greece, 17-26 August 2017.

- Silvio Donato: Overview talk on trigger performances (CMS)
  International Conference on new Frontiers in Physics 2017, Kolymvari, Greece, 17 August 2017.

- Silvio Donato : H(125) decay to bb at CMS
  Higgs Hunting 2017, Paris, France, 24 July 2017.

- Silvio Donato : ttH at CMS
  Higgs Coupling 2017, Heildelberg, Germany, 6 November 2017.

- Silvio Donato : Measurement of Higgs production cross-sections and couplings
  Les Rencontres de Physique de la Vall'ee d'Aoste, La Thuile, Italy, 25 February 2018.

- Camilla Galloni: Searches for new heavy resonances decaying into two Higgs bosons or a W/Z and a Higgs bosons at CMS
  Workshop on the Standard Model and Beyond, Corfu, Greece, 4 September 2017.

- Ben Kilminster: Coherent Neutrino Nucleus interaction Experiment in CCDs
  17th International Workshop on Next Generation Nucleon Decay and Neutrino Detectors (NNN2017), Warwick, U.K., 26 October 2017.

- Ben Kilminster: CCDs for dark matter and neutrino searches
  VERTEX 2017, Asturias, Spain, 11 September 2017.

- Ben Kilminster: Higgs productions and decays
  Physics in Collisions (PIC), Prague, Czech Republic, 5 September 2017.

- Ben Kilminster: Small particles, big data
  Scientifica 2017, Zurich, Switzerland, 2 September 2017.

- Deborah Pinna: Two is not always better than one: Single Top Quarks and Dark Matter
  DM@LHC 2017, Irvine, USA., 3 April 2017.

- Deborah Pinna: Searches for dark matter in hadronic final states with CMS
  EPS-HEP 2017, Venice, Italy, 5 July 2017.

- Giorgia Rauco: Search for vector-like quarks and excited quarks at CMS
  European Physical Society Conference on High Energy Physics, Lido di Venezia, Italy, 5 - 12 July 2017.

- Giorgia Rauco: Search for a single produced vector-like quark B decaying to a b quark and a Higgs boson in a full hadronic final state using boosted topologies
  Joint Annual Meeting of SPS and ÖPG, Geneva, Switzerland, 12 - 25 August 2017.

- Giorgia Rauco: Search for single production of vector-like quarks decaying to a b quark and a Higgs boson
  Les Rencontres de Physique de la Valle d'Aoste, La Thuile, Italy, 25 February - 03 March 2018.

- Daniel Salerno : Latest results on ttH,(Hbb) production at CMS
  EPS-HEP 2017, Palazzo del Cinema, Lido, Venice, Italy, 7 July 2017.

- Claudia Seitz: Review of RPV in SUSY and EXO
  CMS SUSY workshop, Ghent, Belgium, 11 April 2017.

- Claudia Seitz: Searches for strong production of SUSY with ATLAS and CMS
  LHCP 2017, Shanghai, China, 18 May 2017.

- Claudia Seitz: Searches for strong production of SUSY in CMS
  Experimental particle physics seminar University of Zurich, Zurich, Switzerland, 9 October 2018.

- Claudia Seitz: SUSY searches in the context of R parity violation with CMS data
  53 Rencontre de Moriond Electroweak, La Thuile, Italy, 13 March 2018.

- Yuta Takahashi: Discriminating quark and gluon jets at CMS
  BOOST 2017 conference, Buffalo, USA, 17 July 2017.

- Yuta Takahashi: Search for singly produced third generation LQ to τ and b final state
  CMS Exotica Workshop 2017, Brussels, Belgium, 30 November 2017.

- Yuta Takahashi: Flavor anomalies & direct searches at CMS
  Tera-scale research workshop, Tokyo, Japan, 25 December 2017.

- Yuta Takahashi: Leptoquark and Z' searches at CMS
  Zurich Phenomenology Workshop (ZPW) 2018, Zurich, Switzerland, 15 January 2018.

- Yuta Takahashi: Leptoquark searches in CMS
  53 Rencontre de Moriond Electroweak, La Thuile, Italy, 10 March 2018.

- Alberto Zucchetta: Search for new resonances decaying into W, Z and H bosons at CMS
  XXV International Workshop on Deep-Inelastic Scattering and Related Subjects (DIS2017), Birmingham, UK, 5 April 2017.

- Alberto Zucchetta: Two is not always better than one: Single Top Quarks and Dark Matter
  ALPS2017, Obergurgl, Austria, 20 April 2017.

- Alberto Zucchetta: Single Top and Dark Matter: Two is not always better than one
  EPS-HEP2017, Venezia, Italy, 6 July 2017.

- Alberto Zucchetta: Search for heavy resonances decaying to boosted bosons
  Sinergia workshop meeting, Lausanne, Switzerland, 7 December 2017.

17.1.8 LHCb

- First measurement of the CP-violating phase $\phi_s^{d\bar{d}}$ in $B_s^0 \to (K^+\pi^-)(K^-\pi^+)$ decays
  LHCb-Collaboration, R. Aaij *et al.*, JHEP **1803** (2018) 140 arXiv:1712.08683
- Search for weakly decaying b-flavored pentaquarks
  LHCb-Collaboration, R. Aaij *et al.*, Phys. Rev. D **97** (2018) no.3, 032010 arXiv:1712.08086
- Measurement of CP asymmetry in $B_s^0 \to D_s^{\mp}K^{\pm}$ decays
  LHCb-Collaboration, R. Aaij *et al.*, JHEP **1803** (2018) 059 arXiv:1712.07428
- Search for excited B_c^+ states
  LHCb-Collaboration, R. Aaij *et al.*, JHEP **1801** (2018) 138 arXiv:1712.04094
- Updated determination of D^0-$\overline{D}^0$ mixing and CP violation parameters with $D^0 \to K^+\pi^-$ decays
  LHCb-Collaboration, R. Aaij *et al.*, Phys. Rev. D **97** (2018) no.3, 031101 arXiv:1712.03220
- First observation of $B^+ \to D_s^+K^+K^-$ decays and a search for $B^+ \to D_s^+\phi$ decays
  LHCb-Collaboration, R. Aaij *et al.*, JHEP **1801** (2018) 131 arXiv:1711.05637
- Measurement of the ratio of branching fractions $\mathcal{B}(B_c^+ \to J/\psi\tau^+\nu_\tau)/\mathcal{B}(B_c^+ \to J/\psi\mu^+\nu_\mu)$
  LHCb-Collaboration, R. Aaij *et al.*, Phys. Rev. Lett. **120** (2018) no.12, 121801 arXiv:1711.05623

- Measurement of branching fractions of charmless four-body Λ_b^0 and Ξ_b^0 decays
  LHCb-Collaboration, R. Aaij *et al.*, JHEP **1802** (2018) 098 arXiv:1711.05490
- Measurements of the branching fractions of $\Lambda_c^+ \to p\pi^-\pi^+$, $\Lambda_c^+ \to pK^-K^+$, and $\Lambda_c^+ \to p\pi^-K^+$
  LHCb-Collaboration, R. Aaij *et al.*, JHEP **1803** (2018) 043 arXiv:1711.01157
- Measurement of the $B^{\pm}$ production cross-section in pp collisions at $\sqrt{s} = 7$ and 13 TeV
  LHCb-Collaboration, R. Aaij *et al.*, JHEP **1712** (2017) 026 arXiv:1710.04921
- Search for the lepton-flavour violating decays $B^0_{(s)} \to e^{\pm}\mu^{\mp}$
  LHCb-Collaboration, R. Aaij *et al.*, JHEP **1803** (2018) 078 arXiv:1710.04111
- Search for Dark Photons Produced in 13 TeV pp Collisions
  LHCb-Collaboration, R. Aaij *et al.*, Phys. Rev. Lett. **120** (2018) no.6, 061801 arXiv:1710.02867
- Measurement of CP observables in $B^{\pm} \to DK^{*\pm}$ decays using two- and four-body D final states
  LHCb-Collaboration, R. Aaij *et al.*, JHEP **1711** (2017) 156 arXiv:1709.05855
- χ_{c1} and χ_{c2} Resonance Parameters with the Decays $\chi_{c1,c2} \to J/\psi\mu^+\mu^-$
  LHCb-Collaboration, R. Aaij *et al.*, Phys. Rev. Lett. **119** (2017) no.22, 221801 arXiv:1709.04247
- Measurement of CP violation in $B^0 \to J/\psi K_S^0$ and $B^0 \to \psi(2S)K_S^0$ decays
  LHCb-Collaboration, R. Aaij *et al.*, JHEP **1711** (2017) 170 arXiv:1709.03944
- First observation of forward $Z \to b\bar{b}$ production in pp collisions at $\sqrt{s} = 8$ TeV
  LHCb-Collaboration, R. Aaij *et al.*, Phys. Lett. B **776** (2018) 430 arXiv:1709.03458
- Measurement of the shape of the $\Lambda_b^0 \to \Lambda_c^+\mu^-\overline{\nu}_\mu$ differential decay rate
  LHCb-Collaboration, R. Aaij *et al.*, Phys. Rev. D **96** (2017) no.11, 112005 arXiv:1709.01920
- Bose-Einstein correlations of same-sign charged pions in the forward region in pp collisions at $\sqrt{s} = 7$ TeV
  LHCb-Collaboration, R. Aaij *et al.*, JHEP **1712** (2017) 025 arXiv:1709.01769
- Measurement of the Υ polarizations in pp collisions at $\sqrt{s} = 7$ and 8 TeV
  LHCb-Collaboration, R. Aaij *et al.*, JHEP **1712** (2017) 110 arXiv:1709.01301

- First Observation of the Rare Purely Baryonic Decay $B^0 \to p\bar{p}$
  LHCb-Collaboration, R. Aaij *et al.*, Phys. Rev. Lett. **119** (2017) no.23, 232001 arXiv:1709.01156

- Measurement of CP observables in $B^\pm \to D^{(*)}K^\pm$ and $B^\pm \to D^{(*)}\pi^\pm$ decays
  LHCb-Collaboration, R. Aaij *et al.*, Phys. Lett. B **777** (2018) 16 arXiv:1708.06370

- Study of $b\bar{b}$ correlations in high energy proton-proton collisions
  LHCb-Collaboration, R. Aaij *et al.*, JHEP **1711** (2017) 030 arXiv:1708.05994

- Search for Baryon-Number Violating Ξ_b^0 Oscillations
  LHCb-Collaboration, R. Aaij *et al.*, Phys. Rev. Lett. **119** (2017) no.18, 181807 arXiv:1708.05808

- Observation of D^0 meson decays to $\pi^+\pi^-\mu^+\mu^-$ and $K^+K^-\mu^+\mu^-$ final states
  LHCb-Collaboration, R. Aaij *et al.*, Phys. Rev. Lett. **119** (2017) no.18, 181805 arXiv:1707.08377

- Study of prompt D^0 meson production in pPb collisions at $\sqrt{s_{\mathrm{NN}}} = 5$ TeV
  LHCb-Collaboration, R. Aaij *et al.*, JHEP **1710** (2017) 090 arXiv:1707.02750

- Updated branching fraction measurements of $B^0_{(s)} \to K^0_{\mathrm{S}}h^+h'^-$ decays
  LHCb-Collaboration, R. Aaij *et al.*, JHEP **1711** (2017) 027 arXiv:1707.01665

- Observation of the doubly charmed baryon Ξ_{cc}^{++}
  LHCb-Collaboration, R. Aaij *et al.*, Phys. Rev. Lett. **119** (2017) no.11, 112001 arXiv:1707.01621

- Prompt and nonprompt J/ψ production and nuclear modification in pPb collisions at $\sqrt{s_{\mathrm{NN}}} = 8.16$ TeV
  LHCb-Collaboration, R. Aaij *et al.*, Phys. Lett. B **774** (2017) 159 arXiv:1706.07122

- Study of charmonium production in b-hadron decays and first evidence for the decay $B_s^0 \to \phi\phi\phi$
  LHCb-Collaboration, R. Aaij *et al.*, Eur. Phys. J. C **77** (2017) no.9, 609 arXiv:1706.07013

- Improved limit on the branching fraction of the rare decay $K^0_{\mathrm{S}} \to \mu^+\mu^-$
  LHCb-Collaboration, R. Aaij *et al.*, Eur. Phys. J. C **77** (2017) no.10, 678 arXiv:1706.00758

- Updated search for long-lived particles decaying to jet pairs
  LHCb-Collaboration, R. Aaij *et al.*, Eur. Phys. J. C **77** (2017) no.12, 812 arXiv:1705.07332

- Test of lepton universality with $B^0 \to K^{*0}\ell^+\ell^-$ decays
  LHCb-Collaboration, R. Aaij *et al.*, JHEP **1708** (2017) 055 arXiv:1705.05802

- Measurement of B_s^0 and D_s^- meson lifetimes
  LHCb-Collaboration, R. Aaij *et al.*, Phys. Rev. Lett. **119** (2017) no.10, 101801 arXiv:1705.03475

- Observation of charmless baryonic decays $B^0_{(s)} \to p\bar{p}h^+h'^-$
  LHCb-Collaboration, R. Aaij *et al.*, Phys. Rev. D **96** (2017) no.5, 051103 arXiv:1704.08497

- Resonances and CP violation in B_s^0 and $\overline{B}_s^0 \to J/\psi K^+K^-$ decays in the mass region above the $\phi(1020)$
  LHCb-Collaboration, R. Aaij *et al.*, JHEP **1708** (2017) 037 arXiv:1704.08217

- First observation of a baryonic B_s^0 decay
  LHCb-Collaboration, R. Aaij *et al.*, Phys. Rev. Lett. **119** (2017) no.4, 041802 arXiv:1704.07908

- Observation of the decays $\Lambda_b^0 \to \chi_{c1}pK^-$ and $\Lambda_b^0 \to \chi_{c2}pK^-$
  LHCb-Collaboration, R. Aaij *et al.*, Phys. Rev. Lett. **119** (2017) no.6, 062001 arXiv:1704.07900

- Observation of the $B^+ \to D^{*-}K^+\pi^+$ decay
  LHCb-Collaboration, R. Aaij *et al.*, Phys. Rev. D **96** (2017) no.1, 011101 arXiv:1704.07581

- Measurement of B^0, B_s^0, B^+ and Λ_b^0 production asymmetries in 7 and 8 TeV proton-proton collisions
  LHCb-Collaboration, R. Aaij *et al.*, Phys. Lett. B **774** (2017) 139 arXiv:1703.08464

- Measurement of the $B_s^0 \to \mu^+\mu^-$ branching fraction and effective lifetime and search for $B^0 \to \mu^+\mu^-$ decays
  LHCb-Collaboration, R. Aaij *et al.*, Phys. Rev. Lett. **118** (2017) no.19, 191801 arXiv:1703.05747

- Observation of five new narrow Ω_c^0 states decaying to $\Xi_c^+ K^-$
  LHCb-Collaboration, R. Aaij *et al.*, Phys. Rev. Lett. **118** (2017) no.18, 182001 arXiv:1703.04639

- Search for the decays $B_s^0 \to \tau^+\tau^-$ and $B^0 \to \tau^+\tau^-$
  LHCb-Collaboration, R. Aaij *et al.*, Phys. Rev. Lett. **118** (2017) no.25, 251802 arXiv:1703.02508

- Observation of the decay $\Lambda_b^0 \to pK^-\mu^+\mu^-$ and a search for *CP* violation
  LHCb-Collaboration, R. Aaij *et al.*, JHEP **1706** (2017) 108 arXiv:1703.00256

- Observation of the decay $B_s^0 \to \eta_c\phi$ and evidence for $B_s^0 \to \eta_c\pi^+\pi^-$
  LHCb-Collaboration, R. Aaij *et al.*, JHEP **1707** (2017) 021 arXiv:1702.08048

- Measurement of the *CP* violation parameter A_Γ in $D^0 \to K^+K^-$ and $D^0 \to \pi^+\pi^-$ decays
  LHCb-Collaboration, R. Aaij *et al.*, Phys. Rev. Lett. **118** (2017) no.26, 261803 arXiv:1702.06490

- Observation of the suppressed decay $\Lambda_b^0 \to p\pi^-\mu^+\mu^-$
  LHCb-Collaboration, R. Aaij *et al.*, JHEP **1704** (2017) 029 arXiv:1701.08705

- Study of the D^0p amplitude in $\Lambda_b^0 \to D^0p\pi^-$ decays
  LHCb-Collaboration, R. Aaij *et al.*, JHEP **1705** (2017) 030 arXiv:1701.07873

- Observation of the $\Xi_b^- \to J/\psi\Lambda K^-$ decay
  LHCb-Collaboration, R. Aaij *et al.*, Phys. Lett. B **772** (2017) 265 arXiv:1701.05274

- Study of J/ψ Production in Jets
  LHCb-Collaboration, R. Aaij *et al.*, Phys. Rev. Lett. **118** (2017) no.19, 192001 arXiv:1701.05116

- Measurement of *CP* asymmetries in $D^\pm \to \eta'\pi^\pm$ and $D_s^\pm \to \eta'\pi^\pm$ decays
  LHCb-Collaboration, R. Aaij *et al.*, Phys. Lett. B **771** (2017) 21 arXiv:1701.01871

- Search for long-lived scalar particles in $B^+ \to K^+\chi(\mu^+\mu^-)$ decays
  LHCb-Collaboration, R. Aaij *et al.*, Phys. Rev. D **95** (2017) no.7, 071101 arXiv:1612.07818

- Measurement of the J/ψ pair production cross-section in pp collisions at $\sqrt{s} = 13$ TeV
  LHCb-Collaboration, R. Aaij *et al.*, JHEP **1706** (2017) 047 Erratum: [JHEP **1710** (2017) 068] arXiv:1612.07451

- Search for *CP* violation in the phase space of $D^0 \to \pi^+\pi^-\pi^+\pi^-$ decays
  LHCb-Collaboration, R. Aaij *et al.*, Phys. Lett. B **769** (2017) 345 arXiv:1612.03207

- Search for massive long-lived particles decaying semileptonically in the LHCb detector
  LHCb-Collaboration, R. Aaij *et al.*, Eur. Phys. J. C **77** (2017) no.4, 224 arXiv:1612.00945

- Evidence for the two-body charmless baryonic decay $B^+ \to p\overline{\Lambda}$
  LHCb-Collaboration, R. Aaij *et al.*, JHEP **1704** (2017) 162 arXiv:1611.07805

- New algorithms for identifying the flavour of B^0 mesons using pions and protons
  LHCb-Collaboration, R. Aaij *et al.*, Eur. Phys. J. C **77** (2017) no.4, 238 arXiv:1610.06019

- Measurements of prompt charm production cross-sections in pp collisions at $\sqrt{s} = 5$ TeV
  LHCb-Collaboration, R. Aaij *et al.*, JHEP **1706** (2017) 147 arXiv:1610.02230

Conference proceedings

- Olaf Steinkamp: The Early Career, Gender and Diversity Office at the LHCb experiment
  2017 European Physical Society Conference on High Energy Physics, 2017, PoS(EPS-HEP2017)569.

- Albert Puig Navarro: Rare B decays at LHCb
  2017 European Physical Society Conference on High Energy Physics, 2017, PoS(EPS-HEP2017)236.

- Albert Puig Navarro: The LHCb Starterkit initiative
  2017 European Physical Society Conference on High Energy Physics, 2017, PoS(EPS-HEP2017)565.

Oral presentations on behalf of the LHCb collaboration

- Rafael Silva Coutinho: Non-leptonic three body decays at LHCb
  Pion-Kaon Interactions Workshop, Newport News, United States, 14 - 15 February, 2018.
- Rafael Silva Coutinho: Non-leptonic three body decays at LHCb
  Pion-Kaon Interactions Workshop, Newport News, United States, 14 - 15 February, 2018.
- Rafael Silva Coutinho: Heavy flavour physics at LHCb
  XXIV Cracow Epiphany Conference on Advances in Heavy Flavour Physics, Cracow, Poland, 9 - 12 January, 2018.
- Patrick Owen: LHCb Jamboree
  Symposium 25 Years of LHC Experimental Programme , CERN, Geneva, December 15, 2017.
- Davide Lancierini: Rare semileptonic B decays at LHCb
  The 25th International Conference on Supersymmetry and the Unification of Fundamental Interactions, Mumbai, India, 11 - 15 December, 2017.
- Andreas Weiden: Recent results with heavy ion and fixed target collisions at LHCb
  9th International Workshop on Multiple Partonic Interactions at the LHC, Shimla, India, 11 - 15 December, 2017.
- Katharina Müller: Recent results with heavy ion and fixed target collisions at LHCb
  Resonance Workshop , Bergamo, Italie, 10 - 13 October, 2017.
- Rafael Silva Coutinho: CP violation in b -baryons at LHCb
  2017 European Physical Society Conference on High Energy Physics, Venice, Italy, 5 - 12 July, 2017.
- Albert Puig Navarro: Rare B decays at LHCb
  2017 European Physical Society Conference on High Energy Physics, Venice, Italy, 5 - 12 July, 2017.
- Andrea Mauri: Search for long-lived scalar particles in B decays at LHCb
  2017 European Physical Society Conference on High Energy Physics, Venice, Italy, 5 - 12 July, 2017.
- Albert Puig Navarro: The LHCb Starterkit initiative
  2017 European Physical Society Conference on High Energy Physics, Venice, Italy, 5 - 12 July, 2017.
- Olaf Steinkamp: Updated LHCb measurements on pentaquark and tetraquark states
  2017 European Physical Society Conference on High Energy Physics, Venice, Italy, 5 - 12 July, 2017.
- Olaf Steinkamp: Early Career, Gender and Diversity Office at the LHCb experiment
  2017 European Physical Society Conference on High Energy Physics, Venice, Italy, 5 - 12 July, 2017.
- Katharina Müller: Central exclusive production at LHCb
  Low x 2017, Bari, Italy, 12 - 18 June, 2017.
- Katharina Müller: Production measurements at LHCb: Electroweak Bosons, Jets and Heavy Flavor
  Low x 2017, Bari, Italy, 12 - 18 June, 2017.
- Carlos Abellan Beteta: The Silicon Micro-strip Upstream Tracker for the LHCb Upgrade
  International Conference on Technology and Instrumentation in Particle Physics 2017, Beijing, China, 21 - 26 May, 2017.
- Albert Puig Navarro: Rare radiative decays at LHCb
  International Conference on the Structure and the Interactions of the Photon, including the 22th International Workshop on Photon-Photon Collisions, Geneva, Switzerland, 22 - 26 May, 2017.
- Patrick Owen: Lepton flavour universality
  Flavour Physics at LHC run II, Benasque, Spain, 21 - 27 May, 2017.
- Olaf Steinkamp: Flavour Physics Reach after Upgrade
  5th Conference on Large Hadron Collider Physics 2017, Shanghai, China, 15 - 20 May, 2017.

- Marcin Chrzaszcz: Rare decays at LHCb
  5th Conference on Large Hadron Collider Physics 2017, Shanghai, China, 15 - 20 May, 2017.

Oral presentations not on behalf of the LHCb collaboration

- Elena Graverini: Search for Hidden Particles
  Seminar at University of Birmingham, March 7, 2018.
- Rafael Silva Coutinho: Reconstructing final states with electrons at LHCb and interplay with QED corrections
  $b \to sll$ 2018: 6th Workshop on Rare Semileptonic B Decays, Munich, 20 - 22 February 2018.
- Andrea Mauri: Direct measurements of Wilson coefficients and LFU test in $B \to K^* \ell\ell$ decays
  $b \to sll$ 2018: 6th Workshop on Rare Semileptonic B Decays, Munich, 20 - 22 February 2018.
- Andrea Mauri: Prospects for data-driven determination of hadronic matrix element in $B \to K^* \mu\mu$ decays
  $b \to sll$ 2018: 6th Workshop on Rare Semileptonic B Decays, Munich, 20 - 22 February 2018.
- Rafael Silva Coutinho: Disentangling Charmonia in the Threshold Region
  Joint BESIII-LHCb workshop, IHEP, Beijing, China, 8 - 9 February, 2018.
- Elena Graverini: $\Lambda_b \to \Lambda_c \ell\nu$ as a probe of lepton flavour nonuniversality
  Implications of LHCb measurements and future prospects, CERN, 8 - 10 November 2017.
- Andrea Mauri: Prospects for data-driven analyses of the decay $B \to K^* \ell\ell$
  Implications of LHCb measurements and future prospects, CERN, 8 - 10 November 2017.
- Rafael Silva Coutinho: CP violation in b-baryons at LHCb
  Joint Annual Meeting of the SPS/APS, Geneva, Switzerland, 21 - 25 August, 2017.
- Olaf Steinkamp: Event Selection and Data Analysis in Particle Physics
  Young Physicist Forum, UZH, April 22, 2017

17.2 Condensed matter

17.2.1 Condensed matter theory group

Articles

- Numerical investigation of gapped edge states in fractional quantum Hall-superconductor heterostructures
  C. Repellin, A. M. Cook, T. Neupert, N. Regnault,npj Quantum Materials **3**, 14 (2018)
- Weyl-type topological phase transitions in fractional quantum Hall like systems
  St. Kourtis, T. Neupert, Ch. Mudry, M. Sigrist, W. Chen, Phys. Rev. B **96**, 205117 (2017)
- Competing orders in the Hofstadter t-J model
  W. Tu, F. Schindler, T. Neupert, D. Poilblanc, Phys. Rev. B **97**, 035154 (2017)
- Spin-Orbital Excitations in Ca_2RuO_4 Revealed by Resonant Inelastic X-ray Scattering
  L. Das, F. Forte, R. Fittipaldi, C. G. Fatuzzo, V. Granata, O. Ivashko, M. Horio, F. Schindler, M. Dantz, Yi Tseng, D. E. McNally, H. M. Ronnow, W. Wan, N. B. Christensen, J. Pelliciari, P. Olalde-Velasco, N. Kikugawa, T. Neupert, A. Vecchione, T. Schmitt, M. Cuoco and J. Chang, Phys. Rev. X **8**, 011048 (2018)
- Magnetic and noncentrosymmetric Weyl fermion semimetals in the RAlX family of compounds (R=rare earth, Al=aluminium, X=Si, Ge)
  G. Chang, B. Singh, S.-Y. Xu, G. Bian, S.-M. Huang, C.-H. Hsu, I. Belopolski, N. Alidoust, D. S. Sanchez, H. Zheng, H. L., Xiao Zhang, Y. B., T.-R. Chang, H.-T. Jeng, A. Bansil, H. H., S. J., T. Neupert, H. L., M. Z. Hasan, Phys. Rev. B **97**, 041104(R) (2018)
- Mirror Protected Dirac Fermions on a Weyl Semimetal NbP Surface
  H. Zheng *et al.*, Phys. Rev. Lett. **119**, 196403 (2017)

- Ultraquantum magnetoresistance in the Kramers-Weyl semimetal candidate β-Ag_2Se
  H. Zheng, G. Chang, S. Huang, Ch. Guo, X. Zhang, S. Zhang, J. Yin, S. Xu, I. Belopolski, N. Alidoust, D. Sanchez, G. Bian, T. Chang, T. Neupert, H. Jeng, S. Jia, H. Lin, M. Hasan, Phys. Rev. B **96**, 165148 (2017)

- Type-II Symmetry-Protected Topological Dirac Semimetals
  T.-R. Chang, S.-Y. Xu, D. S. Sanchez, W.-F. Tsai, S.-M. Huang, G. Chang, C.-H. Hsu, G. Bian, I. Belopolski, Z.-M. Yu, S. A. Yang, T Neupert, H.-T. Jeng, H. Lin, and M. Hasan, Phys. Rev. Lett. **119**, 026404, (2017)

- Nexus fermions in topological symmorphic crystalline metals
  G. Chang, S.-Y. Xu, S.-M. Huang, D. S. Sanchez, C.-H. Hsu, G. Bian, Z. M. Yu, I. Belopolski, N. Alidoust, H. Zheng, T.R. Chang, H. T. Jeng, S. Yang, T. Neupert, H. Lin, M. Z. Hasan, Scientific Reports **7**, 1688 (2017)

- Magnetic-tunnelling-induced Weyl node annihilation in TaP
  C.-L. Zhang, S.-Y. Xu, C. M. Wang, Z. Lin, Z. Z. Du, C. Guo, C.-C. Lee, H. Lu, Y. Feng, S.-M. Huang, G. Chang, C.-H. Hsu, H. Liu, H. Lin, L. Li, C. Zhang, J. Zhang, X.-C. Xie, T. Neupert, M. Z. Hasan, H.-Z. Lu, J. Wang and S. Jia, Nature Physics **13**, 979986 (2017)

- Probing many-body localization with neural networks
  F. Schindler, N. Regnault, T. Neupert, Phys. Rev. B **95**, 245134 (2017)

Conference talks and colloquia

- Titus Neupert: Higher-order topological insulators
  Peking University, Beijing, China, 18.04.2017

- Titus Neupert: Higher-order topological insulators
  Institute of Physics, Beijing, China, 20.04.2017

- Titus Neupert: Probing Many-body Localization with Neural Networks
  University of Cologne, Cologne, Germany, 25.04.2017

- Titus Neupert: Higher-order topological insulators
  ETH Zurich, Zurich, Switzerland, 08.05.2017

- Titus Neupert: Higher-order topological insulators
  Spin Dynamics in the Dirac Systems, Mainz, Germany, 06.06.2017

- Titus Neupert: Higher-order topological insulators
  Augsburg University, Augsburg, Germany, 13.06.2017

- Titus Neupert: Higher-order topological insulators
  Karlsruhe Institute of Technology, Karlsruhe, Germany, 06.07.2017

- Titus Neupert: Probing Many-body Localization with Neural Networks
  Symposium on Quantum Matter, Corfu, Greece, 13.07.2017

- Titus Neupert: Higher-order topological insulators
  New Trends in Topological Insulators, Monte Verita, Switzerland, 16.07.2017

- Titus Neupert: Topological crystalline insulators
  Topological Matter School, Donostia-San Sebastian, Spain, 21.08.–25.08.2017

- Titus Neupert: Big data in der Quantenmechanik: Wie ein Dutzend Elektronen eine Festplatte füllt
  Wissenschaftsmesse Scientifica, Zurich, Switzerland, 03.09.2017

- Titus Neupert: Higher-order topological insulators
  New Generation in Strongly Correlated Electron Systems, Castelldefels, Spain, 06.09.2017

- Frank Schindler: Probing Many-body Localization with Neural Networks
  New Generation in Strongly Correlated Electron Systems, Castelldefels, Spain, 06.09.2017

- Titus Neupert: Higher-order topological insulators
  Korrelationstage, Dresden, Germany, 12.09.2017

- Frank Schindler: Higher-Order Topological Insulators
  Trends in Theory of Correlated Materials, Tsukuba, Japan, 12.09.2017

- Frank Schindler: Probing Many-body Localization with Neural Networks
  Seminar in the group of Akira Furusaki, RIKEN, Japan, 14.09.2017

- Titus Neupert: Higher-order topological insulators
  Yukawa Institute, Kyoto, Japan, 01.10.2017

- Ashley Cook: Higher-order topological insulators
  Kali Institute for Theoretical Physics, Santa Barbara, USA, 3.10.2017

- Ashley Cook: Higher-order topological insulators
  Freie Universitaet Berlin, Berlin, Germany, 12.10.2017

- Frank Schindler: Probing Many-body Localization with Neural Networks
  Condensed matter theory seminar, Paul Scherrer Institute, Switzerland, 21.11.2017

- Ashley Cook: Magnetic Weyl and Dirac Kondo semimetal phases in heterostructures
  Yukawa Institute, Kyoto, Japan, 21.11.2017

- Frank Schindler: Topolectrical Circuit Realization of Topological Corner Modes
  Condensed matter theory seminar, University of Cologne, Germany, 28.11.2017

- Titus Neupert: Weyl semimetals
  Zurich Physics Colloquium, Zurich, Switzerland, 13.12.2017

- Titus Neupert: Higher-order topological insulators
  Weizmann Institute, Tel Aviv, Israel, 03.01.2018

- Titus Neupert: Talk im Turm
  University of Zurich, Zurich, Switzerland, 15.01.2018

- Titus Neupert: Axiomatic topological quantum field theory
  School on topological states of quantum matter, SISSA, Trieste, Italy, 23.01.–25.01.2018

- Titus Neupert: Higher-order topological insulators
  Workshop on Relativistic fermions in Condensed Matter, Banff, Canada, 12.02.2018

- Ashley Cook: Magnetic Weyl and Dirac Kondo semimetal phases in heterostructures
  Workshop on Relativistic fermions in Condensed Matter, Banff, Canada, 15.02.2018

- Ashley Cook: Higher-order topological insulators
  Concordia University, Montreal, Canada, 21.02.2018

Poster

- Frank Schindler: Kramers-Weyl Fermions
  Spin Dynamics in the Dirac Systems, Mainz, Germany, 06.06.2017

- Frank Schindler: Kramers-Weyl Fermions
  New Trends in Topological Insulators, Monte Verita, Switzerland, 16.07.2017

17.2.2 Superconductivity and Magnetism

Articles

- Spin-Orbital Excitations in Ca2RuO4 Revealed by Resonant Inelastic X-Ray Scattering
L. Das, F. Forte, R. Fittipaldi, C. G. Fatuzzo, V. Granata, O. Ivashko, M. Horio, F. Schindler, M. Dantz, Yi Tseng, D. E. McNally, H. M. Rønnow, W. Wan, N. B. Christensen, J. Pelliciari, P. Olalde-Velasco, N. Kikugawa, T. Neupert, A. Vecchione, T. Schmitt, M. Cuoco, and J. Chang, Physical Review X **8**, 11048 (2018).

- Direct observation of orbital hybridisation in a cuprate superconductor
C. E. Matt, D. Sutter, A. M. Cook, Y. Sassa, M. Månsson, O. Tjernberg, L. Das, M. Horio, D. Destraz, C. G. Fatuzzo, K. Hauser, M. Shi, M. Kobayashi, V. N. Strocov, T. Schmitt, P. Dudin, M. Hoesch, S. Pyon, T. Takayama, H. Takagi, O. J. Lipscombe, S. M. Hayden, T. Kurosawa, N. Momono, M. Oda, T. Neupert, and J. Chang,
Nature Communications **9**, 972 (2018).

- Pseudogap temperature T* of cuprate superconductors from the Nernst effect
O. Cyr-Choinière, R. Daou, F. Laliberté, C. Collignon, S. Badoux, D. LeBoeuf, J. Chang, B. J. Ramshaw, D. A. Bonn, W. N. Hardy, R. Liang, J.-Q. Yan, J.-G. Cheng, J.-S. Zhou, J. B. Goodenough, S. Pyon, T. Takayama, H. Takagi, N. Doiron-Leyraud, and Louis Taillefer, Physical Review B 97, 64502 (2018).

- Dispersive magnetic and electronic excitations in iridate perovskites probed by oxygen K-edge resonant inelastic x-ray scattering
Xingye Lu, Paul Olalde-Velasco, Yaobo Huang, Valentina Bisogni, Jonathan Pelliciari, Sara Fatale, Marcus Dantz, James G. Vale, E. C. Hunter, Johan Chang, Vladimir N. Strocov, R. S. Perry, Marco Grioni, D. F. McMorrow, Henrik M. Rønnow, and Thorsten Schmitt, Physical Review B **97**, 041102(R) (2018).

- Charge-Stripe Order and Superconductivity in $Ir_{1-x}Pt_xTe_2$
O. Ivashko, L. Yang, D. Destraz, E. Martino, Y. Chen, C. Y. Guo, H. Q. Yuan, A. Pisoni, P. Matus, S. Pyon, K. Kudo, M. Nohara, L. Forró, H. M. Rønnow, M. Hücker, M. v. Zimmermann, and J. Chang,
Scientific Reports **7**, 17157 (2017).

- Pressure tuning of structure, superconductivity, and novel magnetic order in the Ce-underdoped electron-doped cuprate T'-$Pr_{1.3-x}La_{0.7}Ce_xCuO_4$ (x=0.1)
Z. Guguchia, T. Adachi, Z. Shermadini, T. Ohgi, J. Chang, E. S. Bozin, F. von Rohr, A. M. dos Santos, J. J. Molaison, R. Boehler, Y. Koike, A. R. Wieteska, B. A. Frandsen, E. Morenzoni, A. Amato, S. J. L. Billinge, Y. J. Uemura, and R. Khasanov, Physical Review B **96**, 94515 (2017).

- Damped spin excitations in a doped cuprate superconductor with orbital hybridization
O. Ivashko, N. E. Shaik, X. Lu, C. G. Fatuzzo, M. Dantz, P. G. Freeman, D. E. McNally, D. Destraz, N. B. Christensen, T. Kurosawa, N. Momono, M. Oda, C. E. Matt, C. Monney, H. M. Rønnow, T. Schmitt, and J. Chang,
Physical Review B **95**, 214508 (2017).

- Superconducting fluctuations in a thin NbN film probed by the Hall effect
Daniel Destraz, Konstantin Ilin, Michael Siegel, Andreas Schilling, and Johan Chang,
Physical Review B **95**, 224501 (2017).

- Hallmarks of Hunds coupling in the Mott insulator Ca_2RuO_4
D. Sutter, C. G. Fatuzzo, S. Moser, M. Kim, R. Fittipaldi, A. Vecchione, V. Granata, Y. Sassa, F. Cossalter, G. Gatti, M. Grioni, H. M. Rønnow, N. C. Plumb, C. E. Matt, M. Shi, M. Hoesch, T. K. Kim, T-R Chang, H-T Jeng, C. Jozwiak, A. Bostwick, E. Rotenberg, A. Georges, T. Neupert, and J. Chang, Nature Communications **8**, 15176 (2017).

Conferences

- Johan Chang: X-ray diffraction in extreme magnetic fields: Day-One Experiments
Satellite meeting to the DESY Users meeting 2018, 22th January 2018, Hamburg, Germany (Invited).

- Johan Chang: 3D-COMPETITION: SC versus CDW order in YBCO
Intertwined Order and Fluctuations in Quantum Materials, 31th July – 4th Aug 2017, Santa Barbara, USA (Invited).

- Johan Chang: Oxide - Electronics: From Mott Physics to high-temperature superconductivity
  The 14th Int. Conf. on Muon Spin Rotation, Relaxation and Resonance 25 – 30th June 2017, Sapporo, Japan (Invited).
- Johan Chang: Nature of the Mott insulator Ca_2RuO_4
  Superstripe conference, 5 – 9th of June 2017, Ischia, Italy (Invited).
- Masafumi Horio: Three Dimensional Fermi Surface of Overdoped La-based Cuprates
  JPS annual meeting, 22 – 25th of March 2018, Tokyo, Japan.
- Denys Sutter: Hallmarks of Hund's coupling in the Mott insulating state of Ca2RuO4
  To-Be Spring meeting 2017, 1st of April 2017, Luxembourg.
- Daniel Destraz: Superconducting fluctuations in a thin NbN film probed by the Hall effect
  Superstripes une 4–10, 2017, Ischia, Italy.
- Oleh Ivashko: Anisotropic dispersion of the spin-excitations in a cuprate superconductor
  International workshop on strong correlations and angle-resolved photoemission spectroscopy(CORPES17), July 2-7, 2017, Hiroshima, Japan.
- Oleh Ivashko: Charge-Stripe Order and Superconductivity in $Ir_{1x}Pt_xTe_2$
  Workshop on Bulk Scattering in Condensed Matter Physics and Chemistry (CMPC), February 22 – 23, 2018, DESY, Hamburg.

17.2.3 Phase transitions, materials and applications

Articles

- Single-crystal growth and study of the mixed spin-dimer system $Ba_{3-x}Sr_xCr_{2O8}$
  A. Gazizulina, D.L. Quintero-Castro, A. Schilling, Phys. Rev. B **96**, 184201 (2017).
- Bose-Einstein condensation of triplons with a weakly broken U(1) symmetry
  A. Khudoyberdiev, A. Rakhimov, A. Schilling, New. J. Phys. **19** 13002 (2017)
- Design of NbN superconducting nanowire single-photon detectors with enhanced infrared detection efficiency
  Q. Wang, J.J. Renema, A.Engel, and M.J.A. de Dood, Phys. Rev. Applied 8, 034004 (2017)
- Superconducting fluctuations in a thin NbN film probed by the Hall effect
  D. Destraz, K. Ilin, M. Siegel, A. Schilling, J. Chang, Phys. Rev. B **95**, 22450 (2017)

Conference contributions

- Qiang Wang: Design of NbN superconducting nanowire single photon detectors with enhanced infrared photon detection efficiency (Poster)
  16th International Superconductive Electronics Conference, ISEC 2017, June 12 – 16, Sorrento, Italy.
- Alsu Gazizulina: Single crystal growth and study of the magnetic properties of the diluted system $Ba_{3-x}Sr_xCr_2O_8$ (Poster)
  International Conference on Strongly Correlated Electron Systems (SCES 2017), 17–21 July 2017, Prague.
- Alsu Gazizulina: Crystal growth and and magnetic properties of spin-1/2-dimer system $Ba_{0.1}Sr_{2.9}Cr_2O_8$ (Poster)
  The European School on Magnetism, 9 – 21 October 2017, Cargese, Corsica, France.
- Alsu Gazizulina: Single crystal growth and study of the magnetic properties of the mixed system $Ba_{3-x}Sr_xCr_2O_8$ (Poster)
  APS March Meeting 2018, 5 – 9 March 2018, Los Angeles, USA.
- Alsu Gazizulina: High Magnetic Field Investigations of the Dimerized System $Ba_{0.1}Sr_{2.9}Cr_2O$
  APS March Meeting 2018, 5 – 9 March 2018, Los Angeles, USA.
- Andreas Schilling: Triplonen in magnetischen Isolatoren
  Physikalische Gesellschaft Zürich, 4. Mai 2017.

17.2.4 Surface Physics

Articles

- The impact of metalation on adsorption geometry, electronic level alignment and UV-stability of organic macrocycles on TiO_2(110)
  M. Graf, G. Mette, D. Leuenberger, Y. Gurdal, M. Ianuzzi, W-D Zabka, S. Schnidrig, B. Probst, J. Hutter, R. Alberto, J. Osterwalder, Nanoscale, 9, 8756 (2017).

- Single molecule magnet with an unpaired electron trapped between two lanthanide ions inside a fullerene
  F. Liu, D. S. Krylov, L. Spree, S. M. Avdoshenko, N. A. Samoylova, M. Rosenkranz, A. Kostanyan, T. Greber, A. U. B. Wolter, B. Büchner and A. A. Popov, Nature Comm. 8, 16098 (2017).

- Atomically Resolved Band Bending Effects in a p-n Heterojunction of Cu_2O and a Cobalt Macrocycle
  D. Leuenberger, W-D. Zabka, O-F. R. Shah, S. Schnidrig, B. Probst, R. Alberto, J. Osterwalder,
  Nano Letters 17, 6620 (2017).

- Optical Control of Young/s Type Double-slit Interferometer for Laser-induced Electron Emission from a Nano-tip
  H. Yanagisawa, M. Ciappina, C. Hafner, J. Schötz, J. Osterwalder, M. F. Kling, Sci. Rep. 7, 12661 (2017).

- From two- to three-dimensional alumina: Interface templated films and formation of γ-Al_2O_3(111) nuclei
  W.-D. Zabka, D. Leuenberger, G. Mette, and J. Osterwalder, Phys. Rev. B 96, 155420 (2017).

- Fermi surface map of large-scale single-orientation graphene on SiO_2
  E. Miniussi, C. Bernard, H. Y. Cun, B. Probst , D. Leuenberger, G. Mette, W-D. Zabka, M. Weinl, M. Haluska, M. Schreck, J. Osterwalder and T. Greber, J. Phys.: Condens. Matter 29, 475001 (2017).

- Atomically dispersed hybrid nickel-iridium sites for photoelectrocatalysis
  C. Cui, M. Heggen, W-D. Zabka, W. Cui, J. Osterwalder, B. Probst, R. Alberto, Nature Comm. 8, 1341 (2017).

- Imaging Chemical Reactions One Molecule at a Time
  Z. Novotny, Z. Zhang, Z. Dohnalek, Reference Module in Chemistry,
  Molecular Sciences and Chemical Engineering.

- Tau Zero: In the cockpit of a Bussard ramjet
  H. Blatter, T. Greber, Am. J. Phys. 85, 12 (2017).

- Effective mass effect in attosecond electron transport
  L. Kasmi, M. Lucchini, L. Castiglioni, P. Kliuiev, J. Osterwalder, M. Hengsberger, L. Gallmann, P. Krueger, and U. Keller, Optica, 4, 1492 (2017).

- Switching Molecular Conformation with the Torque on a Single Magnetic Moment
  A. Kostanyan, R. Westerstrøm, Y. Zhang, D. Kunhardt, R. Stania, B. Büchner, A. A. Popov, and T. Greber,
  Phys. Rev. Lett. 119, 237202 (2017).

- Photoemission and photoionization time delays and rates
  L. Gallmann, I. Jordan, H. J. Wörner, L. Castiglioni, M. Hengsberger, J. Osterwalder, C. A. Arrell, M. Chergui, E. Liberatore, U. Rothlisberger, and U. Keller, Struct. Dyn. 4, 061502 (2017).

- Femtosecond manipulation of spins, charges, and ions in nanostructures, thin films, and surfaces
  F. Carbone, M. Hengsberger, L. Castiglioni, and J. Osterwalder, Struct. Dyn. 4, 061504 (2017).

- Strong field transient manipulation of electronic states and bands
  I. Crassee, L. Gallmann, G. Gäumann, M. Matthews, H. Yanagisawa, T. Feurer, M. Hengsberger, U. Keller, J. Osterwalder, H. J. Wörner, and J. P. Wolf, Struct. Dyn. 4, 061505 (2017).

- Watching ultrafast responses of structure and magnetism in condensed matter with momentum-resolved probes
  S. L. Johnson, M. Savoini, P. Beaud, G. Ingold, U. Staub, F. Carbone, L. Castiglioni, M. Hengsberger, and J. Osterwalder, Struct. Dyn. 4, 061506 (2017).

- Centimeter-Sized Single-Orientation Monolayer Hexagonal Boron Nitride With or Without Nanovoids
  H. Cun, A. Hemmi, E. Miniussi, C. Bernard, B. Probst, K. Liu, D. T. L. Alexander, A. Kleibert, G. Mette, M. Weinl, M. Schreck, J. Osterwalder, A. Radenovic, and T. Greber, Nano Letters, 18, 1205 (2018).

- Robustness of the charge-ordered phases in $IrTe_2$ against photoexcitation
  C. Monney, A. Schuler, T. Jaouen, M.-L. Mottas, Th. Wolf, M. Merz, M. Muntwiler, L. Castiglioni, P. Aebi, F. Weber, and M. Hengsberger, Phys. Rev. B 97, 075110 (2018).

- Remote doping of graphene on SiO_2 with 5 keV x-rays in air
  B. Salzmann, C. Bernard, A. Hemmi and T. Greber, J. Vac. Sci. Technol. A 36, 020603 (2018).

- Polarization-sensitive pulse reconstruction by momentum-resolved photoelectron streaking
  K. Waltar, J. Haase, M. Lucchini, J. A. van Bokhoven, M. Hengsberger, J. Osterwalder, and L. Castiglioni, Opt. Express 26, 8364 (2018).

Contributed conference presentations

- P. Kliuiev: Reconstruction of molecular wave functions with iterative phase retrieval algorithms (Poster)
  Interdisciplinary Surface Science Conference (ISSC-21) by the IOP Thin Films and Surfaces Group, Manchester, UK, 10.04.2017.

- A. Kostanyan: Effect of in-field cooling on $HoLu_2N@C_{80}$ (Poster)
  First Sino Swiss Science and Technology (SSSTC) workshop on endohedral single molecule magnets, Castasegna, Switzerland, 24.06.2017.

- M. Hotz: Co-Pyrphyrin on $Cu_2O(111)$ and $TiO_2(110)$: Properties and Stability under Near Operando Conditions
  SPS Joint Annual Meeting 2017, Geneva, Switzerland, 24.08.2017.

- W.-D. Zabka: From 2D to 3D Alumina: Interface Templated Growth of γ-$Al_2O_3(111)$-like Films
  ECOSS 2017, Szeged, Hungary, 29.08.2017.

- A. Kostanyan: An isotropic ion inside an exchange stabilized endohedral single-molecule magnet (Poster)
  QMol 2017, Monte VeritÂĹ, Ascona, Switzerland, 10.09.2017.

- L. Castiglioni: Prospects and limitations of THz pump-XUV probe experiments in condensed matter
  Future of Science at FLASH Workshop DESY, Hamburg, Germany, 25.09.2017.

- Z. Novotny: Co-Pyrphyrin on $Cu_2O(111)$ and TiO2(110): Properties and Stability under Near-Operando Conditions
  64th Meeting of the American Vacuum Society, Tampa, FL, 02.11.2017.

- W.-D. Zabka: Functionalization of Ultrathin Alumina Films with Rhenium Photosensitizers
  AVS 64th International Symposium, Tampa, USA, 03.11.2017.

- Z. Novotny: Co-Pyrphyrin on $Cu_2O(111)$ and $TiO_2(110)$: Bridging the Pressure Gap (Poster)
  URPP LightChEC Symposium, Universität ZÂ§rich-Irchel Theatersaal Y21 F-65, 10.11.2017.

- W.-D. Zabka: Towards Charge Carrier Dynamics in Re-Photosensitizers on Alumina Thin Films (Poster)
  LightChEC Symposium 2017, Zürich, Switzerland, 10.11.2017.

- W.-D. Zabka: Photosensitizers on Ultrathin Alumina Films: Comparison of Photosensitizer Coverage and Band Alignment (Poster)
  34th SAOG Meeting, Fribourg, Switzerland, 01.02.2018.

- A. Hemmi: Single Layer Boron Nitride from UZH: A Status Report
  Workshop Graphene Flagship WP3, Fuertaventura, Spain, 20.02.2018.

Invited lectures

- T. Greber: Single layer boron nitride membranes
  EMCMRE-4, Marrakech, Moroco, 09.05.2017.

- T. Greber: Magnetism inside C_{80}
  Kolloquium Universität Regensburg, Regensburg, Germany, 22.05.2017.

- T. Greber: Endohedral Single Molecule Magnets
  Electrochemical Society, New Orleans, USA, 29.05.2017.

- L. Castiglioni: Attosecond Dynamics in Photoemission from Noble Metal Surfaces
  Ultrafast Surface Dynamics, USD 10, Inzell, Germany, 16.06.2017.

- M. Hengsberger: From attoseconds to picoseconds - dynamics in surfaces studied by photoemission
  International Workshop on Surface Physics IWSP 2017, Trzebnica, Poland, 28.06.2017.

- T. Greber: The smallest compass
  IWNN, Beijing, China, 05.07.2017.

- L. Castiglioni: Temporal aspects of photoemission from metal surfaces
  International Workshop on Strong Correlations and Angle-Resolved Photoemission Spectroscopy, CORPES17, Hiroshima, Japan, 07.07.2017.

- T. Greber: Smart Membranes
  IWNN, Xian, China, 07.07.2017.

- L. Castiglioni: Molecular tomography and photoelectron diffraction: initial vs. final state effects in ARPES from molecules
  Chiba University, Chiba, Japan, 11.07.2017.

- T. Greber: Shaping the nanomesh with an ion gun
  Workshop on Advanced Scanning Probe Microscopy ASPM , Konjiam, Korea, 18.08.2017.

- T. Greber: Creating non random nanostructures with ions near the penetration threshold of single layer material
  Workshop on Inelastic Ion Surface Collisions IISC-22, Dresden, Germany, 19.09.2017.

- T. Greber: Shaping single layer materials with slow ions
  TUM-CAS Workshop, Fraueninsel Chiemsee, Germany, 10.10.2017.

- M. Hengsberger: Coherent collective modes studied with time-resolved photoelectron diffraction
  International Conference on Novel Nanomaterials ICON2, Synchrotron SOLEIL, St. Aubin, France, 19.10.2017.

- T. Greber: Dünner wär dümmer: 2D 4 the future
  TecDay, Aarau, Switzerland, 09.11.2017.

- T. Greber: The inside of C_{80}: A cornucopia for molecular magnetism
  Kolloquium, Martin Luther Universität Halle, Halle, Germany, 30.11.2017.

- T. Greber: Taming 4f electrons in endohedral single molecule magnets
  Atomic Level Characterisation ALC17, Kauai, USA, 07.12.2017.

- T. Greber: Is C_{80} a Faraday cage?
  SSNS18, Furano, Japan, 12.01.2018.

17.2.5 Disordered and Biological Soft Matter

Articles

- Coherent multiple light scattering in Faraday active materials.
  L. Schertel, G.J. Aubry, C.M. Aegerter, and G. Maret, Europ. Phys J. ST **226** 1409 (2017).

- Free-standing photonic glasses fabricated in a centrifugal field.
  M. Chen, D. Fischli, L. Schertel, G.J. Aubry, B. Häusele, S. Polarz, G. Maret, and H. Cölfen,
  Small **13** 1701392 (2017).

- Challenging FRET-based force measurements in Drosophila
  D. Eder, K. Basler, and C.M. Aegerter, Nature Scientific Reports **7**, 13692 (2017).

- Resonant Near-Field Effects in Photonic Glasses
  G.J. Aubry, L. Schertel, M. Chen, H. Weyer, C.M. Aegerter, S. Polarz, H. Cölfen, and G. Maret, Phys. Rev. A **96**, 043871 (2017).

- In-vivo determination of bending-stiffness of caudal fins in adult zebrafish.
  S. Puri, T. Aegerter-Wilmsen, A. Jazwinska and C.M. Aegerter, J. of Exp. Biol. **221**, 17077 (2018).

- Dynamic generation of light sheets behind turbid media.
  J. Schneider and C.M. Aegerter, J. Europ. Opt Soc. **14**, 7 (2018).

Articles in press

- A magnetic tweezer for application in Drosophila embryos.
  L.Selvaggi, L. Pasykarnakis, D. Brunner, and C.M. Aegerter, Review of Scientific Instruments (2018).

Conference reports

- Explorative mechanochemical modelling of dorsal closure reveals emergent cell patterning and tissue shaping
  F. Atzeni; EMBO/EMBL Symposium: "Tissue Self-Organisation: Challenging the Systems", EMBL Heidelberg, March 14th, 2018.

- Mechanochemical modelling as an explorative tool to study tissue morphogenesis
  F. Atzeni; Life Sciences Switzerland Annual Meeting, "Metabolism and Signaling in the Life Sciences", University of Lausanne, February 12, 2018.

- Mechanochemical modelling as an explorative tool to study Drosophila dorsal closure
  F. Atzeni; Symposium on Emergence and Self-Organization in Living Systems, Careum Auditorium, Zürich. November 7th, 2017 (poster).

- Mechanochemical modelling as an explorative tool to study Drosophila dorsal closure
  F. Atzeni; 3rd International SystemsX.ch Conference, ETH Zurich. September 4-7th, 2017 (poster).

- Hydrodynamic stress and bone growth regulation in the zebrafish caudal fin
  P. Dagenais; Mechanical Forces in Biology, EMBL Heidelberg, Germany. July 12-15th, 2017 (poster).

- Establishment of lepidotrichial branching networks in Zebrafish caudal fins
  S. Puri; Mechanical Forces in Biology, EMBL Heidelberg, Germany. July 12-15th, 2017 (poster).

- Resonant Near-Field Effects in Photonic Glasses
  L. Schertel; Complex Nanophotonics (Cumberland Lodge, Winsdor, GB), July 2017 (poster).

- Near field effected resonant light transport
  L. Schertel; DINAMO 2017 (Siglufjördur, Iceland), May 2017 (poster).

Invited lectures

- C.M. Aegerter: Von Wirbelkanonen, Magnusgleitern und Elephanten im Zimmer
  Kinderuniversität Zürich, Zürich, Switzerland (17.03.2018).

- C.M. Aegerter: Firlefax der Wettermacher
  Gemeindezentrum Loogarten, Zürich, Switzerland (14.01.2018).

17.3 PhD, Master and Bachelor Theses

PhD Theses

- Search for Diboson Resonances with CMS and Pixel Barrel Detector Calibration and Upgrade
  Jennifer Ngadiuba, PhD thesis, April 2017.

- Response of liquid xenon to low-energy neutron interactions, and PMT calibration system for the XENON1T dark matter search experiment
  Payam Pakarha, PhD thesis, April 2017.

- General Relativity: Alternatives, Tests and Applications
  Andreas Schärer, PhD thesis, June 2017.

- Materials Radioassay for the XENON1T Dark Matter Experiment with Gamma Ray Spectrometry and Development of a Projection Time Chamber for the Study of Low-energy Neutron Interactions in Liquid Xenon
  Francesco Piastra, PhD thesis, June 2017.

- Probing the Universe with Citizen Science and Gravitational Lensing
  Rafael Küng, PhD thesis, September 2017.

- Higher-Order QCD Corrections to Jet Production in Deep Inelastic Scattering
  Jan Niehues, PhD thesis, September 2017.

- Out-of-Field Dose in Photon Radiotherapy: Models and Measurements
  Pascal Hauri, PhD thesis, October 2017.

- Unveiling New Physics Hints through the Higgs Sector
  Andrea Pattori, PhD thesis, November 2017.

- Post-growth Intercalation for Electronic Characterization of On-surface Synthesized Graphene Nanoribbons
  Okan Deniz, PhD thesis, November 2017.

- Uncovering the Mechanical Properties of /Drosophila's/ Wing Disc
  Flavio Lanfranconi, PhD thesis, November 2017.

- Search for the Standard Model Higgs Boson Produced in Association with Top Quarks in the Fully Hadronic Final State at the CMS Experiment
  Daniel Salerno, PhD thesis, February 2018.

- Characteristics of Tungsten Silicide and Its Application for Single X-ray Photon Detection
  Xiaofu Zhang, PhD thesis, March 2018.

- Measurement of angular observables of $B_0 \to K_0^* ee$ and $B_0 \to K_0^* \mu\mu$ decays and the upgrade of LHCb
  Federica Lionetto, PhD thesis, March 2018.

- Higher-Order Corrections to Higgs Boson Amplitudes with Full Quark Mass Dependence in Quantum Chromodynamics
  Dominik Kara, PhD thesis, March 2018.

- Flavour Physics with (semi)leptonic decays at forward spectrometers
  Elena Graverini, PhD thesis, March 2018.

- C80 Endohedral Fullerenes: Rearranging Atoms in a Magnetic Field and Exploring the Interplay of their Spins with Subkelvin Magnetometry and X-rays
  Aram Kostanyan, PhD thesis, March 2018.

17.3.1 Master theses

- SiPM Readout for SHiP Timing Detector
  Ruth Bründler, Master thesis, April 2017.

- Search for electroweak production of a vector-like quark T' decaying to a top quark and a Z boson
  Giulia Giannini, Master thesis, June 2017.

- Characterisation of parallel interconnected silicon photomultipliers
  Christian Huber, Master thesis, June 2017.

- Background predictions for double Higgs production at the LHC
  Daniel Fäh, Master thesis, July 2017.

- Investigation of Adsorption Geometry and Electronic Structure of Cobalt-Pyrphyrin on $Cu_2O(111)$ and $TiO_2(110)$
  Michael Hotz, Master thesis, July 2017.

- Search for a low mass ditau resonance at CMS in 2016 data
  Izaak Neutelings, Master thesis, August 2017.

- A Study of Coatings with Breath Figure Structures on Silicon Photomultipliers and the Effect on the Photon Detection Efficiency
  Timothy Widmer, Master thesis, Auigust 2017.

- Dynamical Yukawa in the context of SU(5) Grand Unification
  Julie Pages, Master thesis, September 2017.

- Higgs Pseudo-Observables for New Physics Searches
  Hantian Zhang, Master thesis, September 2017.

- h-BN Nanomesh Islands on PtRh Alloys: dI/dV Microscopy on Clean and Near-Ambient hydrogen Intercalated Surfaces
  Hubert Nussbaumer, Master thesis, November 2017.

- (Time resolved) Photoluminescence of single layer MoS_2 and WSe_2
  Kevin Kramer, Master thesis, November.

- Development of a fractionation scheme optimisation algorithm and implementation in a Graphical User Interface for radiotherapy planning
  Nicoletta Farabullini, Master thesis, January 2018.

- Asymmetric Dependence of Dark Count Rates on Magnetic Field in differently shaped Superconducting Nanowire Single-Photon Detectors based on Niobium Nitride
  Jessica Britschgi, Master thesis,February 2018.

- Timing detector based on scintillators and SiPMs for SHiP
  Alexander Dätwyler, Master thesis, March 2018.

- Characterization of Novel VUV-Silicon Photomultipliers and their Application in Xenon-Based Dual-Phase TPCs
  Chris Marentini, Master thesis, March 2018.

- The boundary terms of the Einstein-Hilbert action
  Simone Bavera, Master thesis, March 2018.

- Gravitational wave polarization from future detector measurements
  Adrian Boîtier, Master thesis, March 2018.

- Gravitational waves from binaries on hyperbolic trajectories
  Oliver Fischer, Master thesis, March 2018.

17.3.2 Bachelor theses

- Towards Planckian SI Units (beyond CODATA 18)
  Michael Ebersold, Bachelor thesis, April 2017.

- Time-Resolved Multi-Photon-Photoemission on Gallium Arsenide
  Matthias Meier, Bachelor thesis, May 2017.

- Studies of Bu -> Kpipiee decays at LHCb
  Jonas Eschle, Bachelor thesis, June 2017.

- GPU Accelerated Photodynamic Modeling
  Remo Furrer, Bachelor thesis, September 2017.

- Characterization of the local velocity field with TGAS-RAVE
  Mauro Bernardini, Bachelor thesis, September 2017.

- Two-orbital band structure of the high-T_c superconductor $La_{2-x}Sr_xCuO_4$ - - An ARPES perspective
  Kevin Hauser, Bachelor thesis, September 2017.

- Drosophila-Wing-Disc-Zellen unter Spannung: Gewebeveränderungen im Grossen vs. Kleinen
  Andrina Bernhard, Bachelor thesis, September 2017.

- 1030 nm cw-Laser for muonic hydrogen hyperfine splitting spectroscopy
  Céline Nauer, Bachelor thesis, November 2017.

- Reconstruction of tau lepton pair invariant mass using an artificial neural network
  Pascal Bärtschi, Bachelor thesis, November 2017.

- The Thomas-Fermi theory
  Filippo Gaia, Bachelor thesis, December 2017.

- Optimizing the search for DM in association with top quarks at the CMS experiment
  Rico Buergler, Bachelor thesis, January 2018.

- Pressure Induced Rotational Symmetry Breaking in URu_2Si_2
  Nik Dennler, Bachelor thesis, February 2018.

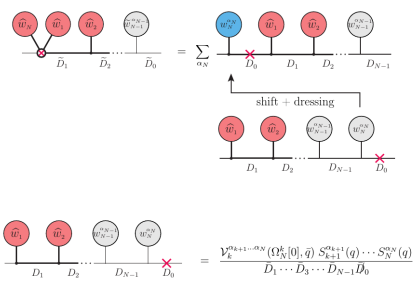
shift + dressing